Electronic Phenomena in Two-Dimensional Topological Insulators

Electronic Phenomena in Two-Dimensional Topological Insulators

A DISSERTATION PRESENTED
BY
SEAN HART
TO
THE DEPARTMENT OF PHYSICS

IN PARTIAL FULFILLMENT OF THE REQUIREMENTS
FOR THE DEGREE OF
DOCTOR OF PHILOSOPHY
IN THE SUBJECT OF
PHYSICS

HARVARD UNIVERSITY
CAMBRIDGE, MASSACHUSETTS

MAY 2016

Thesis advisor: Professor Amir Yacoby Sean Hart

Electronic Phenomena in Two-Dimensional Topological Insulators

Abstract

In recent years, two-dimensional electron systems have played an integral role at the forefront of discoveries in condensed matter physics. These include the integer and fractional quantum Hall effects, massless electron physics in graphene, the quantum spin and quantum anomalous Hall effects, and many more. Investigation of these fascinating states of matter brings with it surprising new results, challenges us to understand new physical phenomena, and pushes us toward new technological capabilities. In this thesis, we describe a set of experiments aimed at elucidating the behavior of two such two-dimensional systems: the quantum Hall effect, and the quantum spin Hall effect.

The first experiment examines electronic behavior at the edge of a two-dimensional electron system formed in a GaAs/AlGaAs heterostructure, under the application of a strong perpendicular magnetic field. When the ratio between the number of electrons and flux quanta in the system is tuned near certain integer or fractional values, the electrons in the system can form states which are respectively known as the integer and fractional quantum Hall effects. These states are insulators in the bulk, but carry gapless excitations at the edge. Remarkably, in certain fractional quantum Hall states, it was predicted that even as charge is carried downstream along an edge, heat can be carried upstream in a neutral edge channel.

By placing quantum dots along a quantum Hall edge, we are able to locally monitor the edge temperature. Using a quantum point contact, we can locally heat the edge and use the quantum dot thermometers to detect heat carried both downstream and upstream. We find that heat can be carried upstream when the edge contains structure related to the $\nu = 2/3$ fractional quantum Hall state. We

further find that this fractional edge physics can even be present when the bulk is tuned to the $\nu = 1$ integer quantum Hall state. Our experiments also demonstrate that the nature of this fractional reconstruction can be tuned by modifying the sharpness of the confining potential at the edge.

In the second set of experiments, we focus on an exciting new two-dimensional system known as a quantum spin Hall insulator. Realized in quantum well heterostructures formed by layers of HgTe and HgCdTe, this material belongs to a set of recently discovered topological insulators. Like the quantum Hall effect, the quantum spin Hall effect is characterized by an insulating bulk and conducting edge states. However, the quantum spin Hall effect occurs in the absence of an external magnetic field, and contains a pair of counter propagating edge states which are the time-reversed partners of one another. It was recently predicted that a Josephson junction based around one of these edge states could host a new variety of excitation called a Majorana fermion. Majorana fermions are predicted to have non-Abelian braiding statistics, a property which holds promise as a robust basis for quantum information processing.

In our experiments, we place a section of quantum spin Hall insulator between two superconducting leads, to form a Josephson junction. By measuring Fraunhofer interference, we are able to study the spatial distribution of supercurrent in the junction. In the quantum spin Hall regime, this supercurrent becomes confined to the topological edge states. In addition to providing a microscopic picture of these states, our measurement scheme generally provides a way to investigate the edge structure of any topological insulator.

In further experiments, we tune the chemical potential into the conduction band of the HgTe system, and investigate the behavior of Fraunhofer interference as a magnetic field is applied parallel to the plane of the quantum well. By theoretically analyzing the interference in a parallel field, we find that Cooper pairs in the material acquire a tunable momentum that grows with the magnetic field strength. This finite pairing momentum leads to the appearance of triplet pair correlations at certain locations within the junction, which we are able to control with the external magnetic field.

Our measurements and analysis also provide a method to obtain information about the Fermi surface properties and spin-orbit coupling in two-dimensional materials.

Contents

Author List

Chapter 3 is adapted from reference [121]:

Vivek Venkatachalam, Sean Hart, Loren Pfeiffer, Ken West, and Amir Yacoby.

Local thermometry of neutral modes on the quantum Hall edge. *Nature Physics*, 8:676-681, 2012.

Chapter 5 is adapted from reference [43]:

Sean Hart, Hechen Ren, Timo Wagner, Philipp Leubner, Mathias Mühlbauer, Christoph Brüne, Hartmut Buhmann, Laurens W. Molenkamp, and Amir Yacoby.

Induced superconductivity in the quantum spin Hall edge. *Nature Physics*, 10:638-643, 2014.

Chapter 6 is adapted from reference [44]:

Sean Hart, Hechen Ren, Michael Kosowsky, Gilad Ben-Shach, Philipp Leubner, Christoph Brüne, Hartmut Buhmann, Laurens W. Molenkamp, Bertrand I. Halperin, and Amir Yacoby.

Controlled finite momentum pairing and spatially varying order parameter in HgTe quantum wells. `http://arxiv.org/abs/1509.02940`, 2015.

Listing of figures

To Lindsay, and to my parents.

Acknowledgments

These acknowledgements are in one sense difficult to write, because they signify the end of an intensely exciting period of time. On the other hand, it is a pleasure to thank the many people who have contributed to this work, and I hope that I will not inadvertently leave anyone out. First and foremost, I would like to thank my advisor, Amir Yacoby. Amir is a brilliant physicist, with a great enthusiasm for science. He is always ready with new insight or a new approach to a difficult problem, and he has set up an amazing lab where scientists can easily thrive. I am grateful that I have had the opportunity to work with Amir during my time in graduate school.

I would also like to thank Bert Halperin. In addition to serving on my committee, he has been available throughout my PhD for numerous illuminating conversations, about physics or otherwise. It is largely because of Bert, for example, that I ended up learning about foraging for mushrooms, and then eating said mushrooms. Much more importantly, Bert's theoretical insight led to an explanation of my experiments on Josephson junctions in a parallel magnetic field. It has been a privilege to collaborate with such an amazing physicist.

Over the course of my PhD, I have had the pleasure of working with many talented students. During my first years of graduate school, I was fortunate to be able to study fractional quantum Hall edge states with Vivek Venkatachalam, who is an excellent scientist. Even as a new student joining the project, Vivek immediately provided me with copious opportunities to learn, for which I am grateful. Later on, Hechen Ren joined Team Topology, and I thank her for her contributions to our work together. Despite many challenges which confronted us, her dedication and talent were important to the eventual success of our experiments. Now two new students, Michael Kosowsky and Andrew Pierce, have joined our effort, and I am certain that the future of Team Topology is bright.

I am also happy that I was able to work with Fokko de Vries and Timo Wagner, both visiting students who made great contributions despite their time here being all too short. Lan Luan, probably the most cheerful person I have ever met, instilled in me a unique perspective on our research as we worked together on new approaches to device fabrication. It was exciting to work with Gilad Ben-Shach on the parallel field experiments. I have also benefited from conversations with theorists including Anton Akhmerov, Jay Deep Sau, Ewelina Hankiewicz, and Falko Pientka.

Our collaboration with Laurens Molenkamp and his lab at Würzburg enabled the experiments on HgTe quantum wells. Working with this group has been a fantastic and fruitful experience. I am grateful to Mathias Mühlbauer for helping us get started with this material, especially with regard to fabrication strategies. Working with Christoph Brüne has been a great pleasure, and I thank him for sharing his knowledge of HgTe heterostructures over the years. I will miss our conversations at the 'usual time.'

I have also benefited from interactions with a number of individuals with whom I did not directly work. I have learned a lot from talking with Shannon Harvey, both about the care and well-being of

dilution refrigerators and about general lab organization. I thank John Nichol for numerous insightful physics conversations. Angela Kou always had time to talk through perplexing physics problems, for which I am grateful. Pat Gumann is a force to be reckoned with when it comes to cryogenic techniques. In addition to improving just about every experiment in the lab, he also found time to be a great friend. I thank all of the members of the Yacoby lab, all of whom in one way or another have influenced this work.

I am grateful to all of my tennis partners over the years - Seth Herbst, Vivek Venkatachalam, Mikey Shulman, Doug McClure, Kristiaan de Greve, Marc Warner, Yuliya Dovzhenko, and Tony Zhou. I also want to thank Ben Feldman, who taught me a thing or two about playing Starcraft, and about the scanning probe microscope. The times spent playing Mario Kart 64 with Mikey *et. al.* were also a welcome diversion. I thank Andrew Yarmola for putting up with me as a roommate.

I have benefited tremendously from technical interactions with a number of people. At CNS, Jiangdong Deng was always happy to help troubleshoot a problematic process or to brainstorm new nanofabrication ideas. The CNS staff in general have maintained an efficient and productive cleanroom, and I am particularly grateful to Yuan Lu, John Tsakirgis, and Steve Paolini for keeping the machines in working order. At Oxford Instruments, Nick Dent was an excellent source of help and advice with respect to the Oxford dilution refrigerators in the lab. At AJA, Joel Moore generously lent his expertise when I had questions about our new sputtering system. Mike McKenna and his shop, and also Stan Cotreau, were great resources whenever our experiment required machining a new part. Jim MacArthur provided electronics expertise, as well as the famed DecaDac voltage sources. Frank Morrissey and his team were extremely helpful and responsive when we needed to install or move large equipment around the lab.

Organizationally, both the lab and myself owe great thanks to Carolyn Moore. She was always willing to take on work to ensure that I was able to focus first on science, and for that I am grateful. More recently, Hannah Belcher has done an excellent job filling this role. I also thank Lisa Cacciabaudo for helping things go smoothly with the administrative side of my PhD, particularly in the face of several missed deadlines on my part. I would also like to thank the Department of Energy SCGF program for their generous financial support.

Finally, I would like to thank my family. In particular, I thank my parents, without whom none of this would have been possible. I also thank Lindsay, who has been there for me in all of the times when I needed her most.

1 Introduction

1.1 Electrons in two dimensions

Two-dimensional electron systems occupy a central position in condensed matter physics, and for good reason. A vast array of interesting behaviors are possible when electrons are confined to a plane, depending on many factors such as their crystalline environment, the electron density, the presence of external electric or magnetic fields, and electron-electron interactions. This diversity of possibilities opens the potential to realize new states of matter, discover exciting physical phenomena, and imagine devices which previously were not possible. The exploration of such an immense space of possibilities is uniquely facilitated in two dimensions, where a variety of rather simple experimental inputs provide a large degree of control.

Because a two-dimensional electron system (2DES) is planar, it is possible to alter the electron density electrostatically by placing a metal gate over the sample. Then the behavior of the system can be explored over a range of electron density. By patterning the gates using nanolithography techniques, it is even possible to realize structures such as quantum point contacts (QPCs) and quantum dots (QDs) inside a 2DES. These basic structures are interesting in their own right, allowing investigation of one-dimensional electron physics [117] or precise control over a small number of electrons [108]. Moreover, it is possible to use such structures as tools to probe the physics of their parent 2DES. For example, one can use a QPC to locally inject charge into a 2DES and quantum dots can in principle

function as electrometers, spectrometers, or thermometers.

Another benefit of 2DESs is that external magnetic and electric fields can be used to significantly manipulate the system. In two dimensions, applying a perpendicular magnetic field discretizes the spectrum of the system into a series of energy levels known as Landau levels. The physics associated with these levels is fascinating and can provide a window into the properties unique to a given system. Since the 2DES is a planar system, it is also possible to place metal gates on either side of the 2DES with relatively small spatial separation. Then, one can experimentally apply significant electric fields perpendicular to the system without the need for excessive voltage applied to the gates. Depending on the particular system under consideration, such an electric field can have profound effects on the electronic structure [73, 124].

Even with these powerful tools for manipulating the behavior of a two-dimensional electron system, there remains a striking diversity of behavior. As alluded to previously, these behaviors depend on many factors. For example, in graphene, a two-dimensional honeycomb lattice of carbon atoms, the electronic spectrum is gapless and disperses linearly with momentum [87]. In contrast, semiconducting heterostructures such as GaAs/AlGaAs quantum wells have a band gap and parabolic dispersion. In both of these systems, application of a magnetic field perpendicular to the system leads to a diverse variety of states known as the quantum Hall effect, with the underlying properties of each material influencing the detailed nature of these states.

In this thesis, we describe a set of experiments aimed at elucidating the behavior of two different two-dimensional systems: the quantum Hall effect in GaAs/AlGaAs quantum wells, and the quantum spin Hall effect in HgTe/HgCdTe quantum wells. Both of these are examples of a class of material called a topological insulator. Topological insulators are characterized by an energy gap in bulk of the material, while the boundary contains gapless conducting states. In two dimensions, these boundary states consist of one-dimensional channels with unique electronic properties. As we will see throughout this thesis, the edge states of a two-dimensional topological insulator are a fruitful ground for investigating new physical phenomena.

In the following chapters, we will explore the physics underlying the quantum Hall effect and the quantum spin Hall effect, as well as the techniques we have used in order to control and investigate their behavior. The following is a brief overview of the contents of each chapter.

1.2 Organization of this document

In Chapter 2, we review the physics which arises when a strong magnetic field is applied perpendicular to the plane of a 2DES. When the ratio between the number of electrons and flux quanta in the system

is tuned near certain integer or fractional values, the electrons in the system can form states which are respectively known as the integer and fractional quantum Hall effects. We review the single-particle physics behind the integer quantum Hall effect, followed by an overview of the fractional quantum Hall effect. In particular, we describe the formation of a neutral mode at the edge of the $\nu = 2/3$ state. Reconstruction of quantum Hall edges due to electrostatic screening is also discussed.

Chapter 3 describes our study of the edge of a quantum Hall system, realized in a heterostructure composed of layered GaAs and AlGaAs. Using a quantum point contact, we are able to inject charge into the outermost component of a quantum Hall edge. Using a local measurement of the downstream chemical potential, we find that physics associated with the $\nu = 2/3$ fractional quantum Hall effect can exist even when the bulk of the 2DES is tuned into an integer quantum Hall state. By placing quantum dots along the edge, both downstream and upstream of the quantum point contact, we are able to monitor how heat is carried by the quantum Hall edge states.

Chapter 4 contains an overview of a recently discovered topological insulator, the quantum spin Hall insulator. We provide a general overview of the quantum spin Hall effect, and how this effect arises in quantum wells composed of a layer of HgTe sandwiched by layers of HgCdTe. We examine the model proposed by Bernevig, Hughes, and Zhang, which predicts that this material should become a quantum spin Hall insulator when the well width exceeds 6.3 nm. Following this, we review several experiments which have elucidated the nature of charge transport in the quantum spin Hall effect. Finally, we discuss an exciting theoretical proposal, in which coupling superconductors to the quantum spin Hall edge leads to the appearance of new topological excitations called Majorana fermions.

In Chapter 5, we present experiments in which a section of HgTe quantum well is placed between two superconducting leads to form a Josephson junction. Using Fraunhofer interferometry, we are able to monitor the spatial distribution of supercurrent in the quantum well. In wells that are 7.5 nm wide, we find that supercurrents are confined to the sample edges as the bulk density is depleted using a top gate, as expected for a quantum spin Hall insulator. Our interference measurements provide microscopic information about the quantum spin Hall edge states. We also examine the behavior when the quantum well width decreases to 4.5 nm, in which case the edge supercurrents cannot be distinguished from those in the bulk.

Chapter 6 details further experiments on Josephson junctions based around HgTe quantum wells wider than 6.3 nm, and with the chemical potential tuned into the conduction band. In these experiments, application of a magnetic field in the plane of the system leads to an unusual evolution of the Fraunhofer interference. Based on our measurements and theoretical analysis, we find that Cooper pairs in the quantum well acquire a tunable momentum that grows with the magnetic field strength.

This finite momentum shift leads to triplet pairing of electrons at certain locations within the junction, which we are able to control with the external magnetic field. The details of the interference behavior provide a means to probe the nature of spin-orbit coupling within the quantum well, as well as a measure of geometric properties of the junction. The density dependence of our measurements also allows us to extract the value of $\tilde{g}/v_F$, where $\tilde{g}$ is the effective g-factor and v_F is the Fermi velocity.

2

Quantum Hall effects in GaAs quantum wells

2.1 Two-dimensional electron system in GaAs quantum wells

When a system of electrons is confined in one direction (say, the z direction) but free to move in the remaining directions (x and y), it is referred to as a two-dimensional electron system (2DES). This is the situation that one encounters in certain layered semiconductor heterostructures, where bandgap engineering in the z direction is used to confine electrons. A particularly clean 2DES arises in heterostructures in which a layer of GaAs is sandwiched by layers of AlGaAs. Since the conduction band of GaAs typically lies approximately 300 meV below that of AlGaAs[23], such a heterostructure approximately realizes a square well confinement in one spatial direction.

Numerous technological advances over the preceding decades have made it possible for the GaAs/AlGaAs 2DES to achieve electron mobilities exceeding 30×10^6 cm^2/Vs, a feat which has yet to be surpassed by any other 2DES. Many of these developments, including in some cases their experimental benefits and pitfalls, are described in [23, 66, 92].

In order to understand the basic properties of a 2DES, it is often a good approximation to ignore electron-electron interactions. In this case one can treat each electron individually, so that the Hamil-

tonian for a single electron is written as

$$H = -\frac{\hbar^2}{2m}\nabla^2 + V(z). \tag{2.1}$$

Here $V(z)$ is the confining energy, and m is the effective mass of electrons. When we solve the Schrödinger equation with this Hamiltonian, we find solutions with energies equal to

$$E_i(k_x, k_y) = E_i + \frac{\hbar^2}{2m}\left(k_x^2 + k_y^2\right). \tag{2.2}$$

The index i labels different quantum well states, or sub-bands. For convenience, we set the energy of the lowest sub-band $E_1 = 0$. In a system with in-plane dimensions $L_x \times L_y$, the in-plane momentum will take discrete values $\hbar\vec{k} = \hbar\left(\frac{2\pi N_x}{L_x}, \frac{2\pi N_y}{L_y}\right)$, where N_x and N_y are integers. Here we have assumed periodic boundary conditions.

Due to Pauli exclusion, each of the states described above can only be occupied by two electrons with opposite spin. At zero temperature, in a 2DES with areal density n, states will be occupied from the lowest energy up to a maximum energy called the Fermi energy $E_F = \hbar^2 k_F^2/2m$. Here we have also defined the Fermi momentum $\hbar k_F$, the maximum occupied in-plane momentum. It is straightforward to show that the Fermi wave vector and density are related by $k_F = \sqrt{2\pi n}$, and that the density of states is independent of energy and equal to $g(E) = \frac{m}{\pi\hbar^2}$ (see Figure 2.2). As long as the Fermi energy and temperature are both small compared to the sub-band splitting $E_2 - E_1$, it remains valid to treat the system as effectively two-dimensional. One can easily verify that these conditions are satisfied under typical experimental conditions (see [79], for example).

In the following sections we will review the response of a 2DES to a magnetic field applied in the z direction. We will find that the application of a strong magnetic field not only strongly modifies the properties derived above, but also leads to many new and unexpected behaviors.

2.2 Integer quantum Hall effect

In 1980, von Klitzing, Dorda, and Pepper reported measurements on a 2DES located within a silicon metal-oxide-semiconductor field-effect transistor [115]. They applied a strong magnetic field (18 T) oriented perpendicular to their Hall-bar device (shown in Figure 2.1), and varied the electron density in the device using a top gate. By doing this they were able to make two striking observations. First, under the strong magnetic field the Hall resistance R_{xy} evolved through many precisely quantized

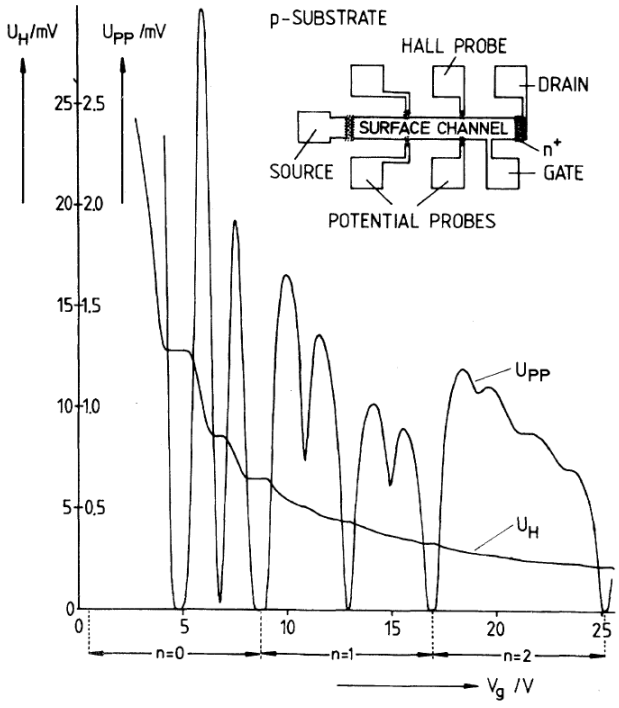

Figure 2.1: Observation of the integer quantum Hall effect, from [115]. Under a perpendicular magnetic field of 18 T, sweeping the voltage on a top gate causes the Hall resistance to evolve through a series of plateaus given by $R_{xy} = \frac{h}{Ne^2}$ (N is an integer). Plateaus in R_{xy} are associated with zeros in the longitudinal resistance R_{xx}.

plateaus, given by

$$R_{xy} = \frac{h}{Ne^2}, \tag{2.3}$$

where N is an integer (hence the name integer quantum Hall effect). A given plateau $R_{xy} = \frac{h}{Ne^2}$ occurred in the vicinity of $\nu = \frac{n}{B/\Phi_0} = N$, where the number ν is equal to the ratio between the electron number and the number of flux quanta penetrating the 2DES. The second important observation was that when the Hall resistance R_{xy} was on a quantized plateau, the longitudinal resistance R_{xx} was found to be zero. The measurement of zero longitudinal resistance indicates that transport associated with the quantized plateaus occurs without dissipation.

2.2.1 Landau levels

To understand the integer quantum Hall effect (IQHE), we must analyze the behavior of a 2DES under a perpendicular magnetic field $\vec{B} = B\hat{z}$. This problem is greatly simplified by neglecting interactions between electrons, so that one need only consider one electron at a time. The Hamiltonian for an electron confined to two-dimensions, under a perpendicular magnetic field, is:

$$H = \frac{1}{2m}\left(\vec{p} + e\vec{A}\right)^2. \tag{2.4}$$

Here, the charge of an electron is $-e$, and we use the kinetic momentum $\vec{p} + e\vec{A}$. To solve the Schrödinger equation, we must choose a gauge. A commonly used gauge is the Landau gauge:

$$\vec{A} = B\,(-y, 0, 0) \tag{2.5}$$

which gives $\vec{B} = \nabla \times \vec{A} = B\hat{z}$. Already we can see that because the vector potential is linear in the spatial coordinate y, this system should in essence behave as a harmonic oscillator. Substituting equation (2.5) into equation (2.4), we find:

$$H = \frac{p_y^2}{2m} + \frac{1}{2m}\omega_c^2\left(y - l_B^2 k_x\right)^2. \tag{2.6}$$

Here we have made the substitution $p_x = \hbar k_x$, since the Hamiltonian commutes with p_x. We have also defined the cyclotron frequency $\omega_c = \frac{eB}{m}$ and the magnetic length $l_B = \sqrt{\frac{\hbar}{eB}}$. Equation (2.6) indeed has the form of a harmonic oscillator, with the y position shifted by the distance $l_B^2 k_x$.

When we solve the Schrödinger equation with the Hamiltonian in equation (2.6), the solutions have the standard energy eigenvalues of a quantum harmonic oscillator:

$$E(N, k_x) = \left(N + \frac{1}{2}\right)\hbar\omega_c. \tag{2.7}$$

In effect, the perpendicular magnetic field quenches the kinetic energy of electrons, reducing the density of states to a set of equally spaced levels, often referred to as Landau levels (Figure 2.2). The Landau levels are highly degenerate, with different eigenstates within a level having different quantum numbers k_x. Within a Landau level, the degeneracy per unit area is equal to $1/2\pi l_B^2 = B/\Phi_0$[1]. In other words, there is one state per flux quantum $\Phi_0 = h/e$ within any given Landau level.

We can define a filling factor $\nu = \frac{n}{B/\Phi_0}$. Since ν is equal to the ratio between the number of

[1] If we account for the spin degree of freedom and neglect Zeeman splitting, this degeneracy is multiplied by 2.

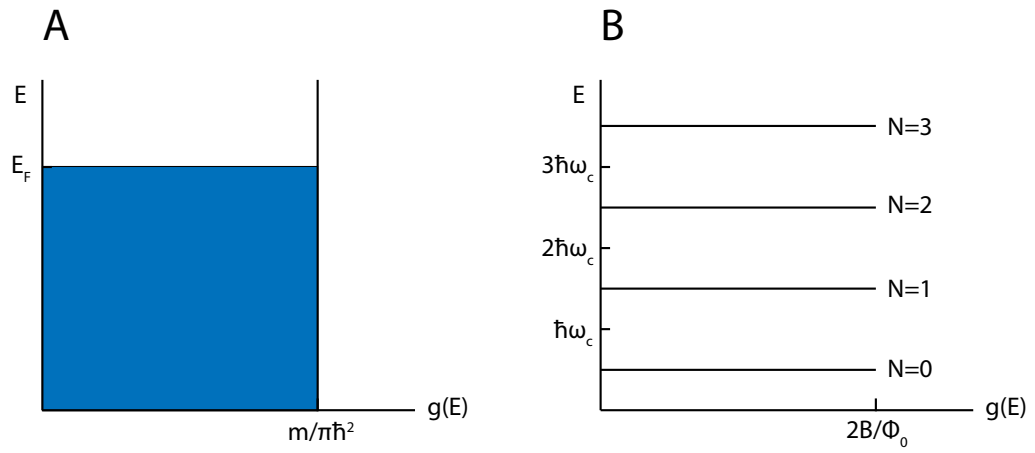

Figure 2.2: The density of states in a two-dimensional electron system. **(A)** In the absence of an external magnetic field, the density of states is independent of energy and given by $g(E) = \frac{m}{\pi\hbar^2}$. States are filled up to the maximum occupied energy, the Fermi energy E_F. **(B)** When a magnetic field B is applied perpendicular to the plane of the 2DES, the kinetic energy becomes quantized into highly degenerate Landau levels. The energy of these levels is given by $E = \left(N + \frac{1}{2}\right)\hbar\omega_c$. Accounting for the electronic spin degree of freedom, each level holds $2B/\Phi_0$ electrons, where $\Phi_0 = h/e$ is the magnetic flux quantum.

electrons in the sample and the number of flux quanta penetrating the sample, it counts the number of Landau levels which are filled. For example, a filling factor of $\nu = 1$ would mean that there is one electron per flux quantum, so that the lowest Landau level is completely filled. In discussing the original observation of the IQHE, we noted that plateaus in the Hall resistance R_{xy} occurred near integer values of the filling factor ν. We can now understand that Landau levels play an important role in this relationship, but in order to see how this plays out in a transport experiment we must now consider what happens at the edge of the sample.

2.2.2 Edge states

Suppose that our electron system is confined by a potential $V(y)$, which is zero for $|y| < W/2$ and increases for $|y| \geq W/2$. The increasing confinement at the edges means that Landau level energies will bend upward at the edges of the sample. For illustrative purposes, we can assume that the potential $V(y)$ increases slowly enough at the edges that locally it can be approximated as constant [2]. Then the solutions to equation (2.6) will be modified only by the addition of a position-dependent energy shift,

[2] We will revisit the physics associated with a smooth confining potential in Section 2.4.

so that we can write the following dispersion relation [52]:

$$E(N, k_x) = \left(N + \frac{1}{2}\right)\hbar\omega_c + V(l_B^2 k_x). \tag{2.8}$$

When the chemical potential lies between Landau levels in the bulk, the levels which are fully occupied in the bulk will necessarily intersect the chemical potential at the edges of the sample (Figure 2.3) [41]. We can see from equation (2.8) that the group velocity $v = \frac{1}{\hbar}\frac{\partial E(N,k_x)}{\partial k_x}$ will have opposite sign at opposite edges of the sample. Hence, charge will be carried in a chiral sense through one-dimensional channels at the boundary of the sample. We can see that the number of channels that we expect at the edge of the sample is equal to the number N of completely filled Landau levels.

It is straightforward to show that the conductance of a ballistic one-dimensional channel is e^2/h. The quantum Hall effect can in essence be viewed as a set of N one-dimensional wires, with the left and right movers located at opposing edges of the sample. If we impose a current through a Hall bar device such as the one in Figure 2.3B and measure the Hall resistance R_{xy}, we therefore expect, on the basis of this analysis, to find that $R_{xy} = \frac{h}{Ne^2}$. Furthermore, since the left and right movers are well-separated, if we measure the longitudinal resistance R_{xx} along an edge, we expect to find that $R_{xx} = 0$. This protection against backscattering underlies the extremely precise quantization of the IQHE[3].

In the presence of disorder, localized states appear in the spectrum of the system (Figure 2.3A). Then, when the chemical potential lies between Landau levels, changing either the external magnetic field or the density results in a change in the occupation of these localized states. Since localized states do not contribute to transport, we expect that in the vicinity of integer filling factors ν we should find plateaus in R_{xy} concomitantly with zeros of R_{xx}. This matches what was originally observed by von Klitzing, *et. al.* When the chemical potential lies within a Landau level, however, changes in density or magnetic field will modify the occupation of extended states which percolate throughout the sample and are able to scatter. Under these conditions, we do not necessarily expect to find plateaus in R_{xy} or zero longitudinal resistance R_{xx}. These expectations also match the behavior observed by von Klitzing, *et. al.*

2.3 Fractional quantum Hall effect

The behavior of samples away from integer filling factor ν is extremely interesting. In clean samples where electron-electron interactions play an important role, an entirely new set of states develops at

[3]The quantized Hall resistance is now known to within 2 parts in 10^7 [122].

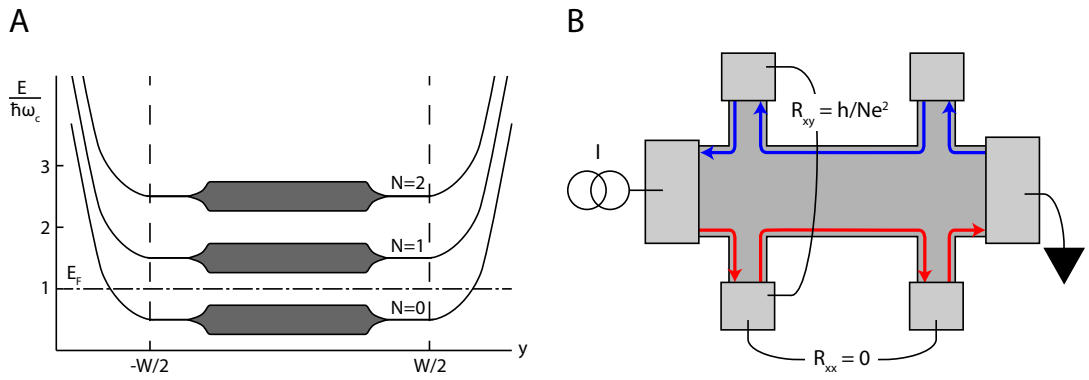

Figure 2.3: Current-carrying edge states in the IQHE. **(A)** Energy bands as a function of position y, in a sample with a confining potential that increases for $|y| \geq W/2$ (adapted from [41]). Landau levels at the edge of a 2DES are raised to higher energies by the confining potential. Levels which are completely filled in the bulk intersect the chemical potential at the edge of the system, leading to the formation of conducting one-dimensional edge channels. The center of the sample contains a disordered region (shaded gray). **(B)** Schematic of transport through chiral edge states in a Hall bar geometry, with the red edge having a higher chemical potential than the blue edge. Dark gray areas are the 2DES, and light gray areas are metallic contacts. When current flows through a Hall bar in the IQH regime as shown, a measurement of the Hall resistance R_{xy} will be quantized to $\frac{h}{Ne^2}$, where N is the number of edge channels. A measurement of R_{xx} will be zero, since backscattering is prohibited along the edge.

certain fractional values of the filling factor. In this section, we present a brief overview of these states, which are collectively known as the fractional quantum Hall effect.

2.3.1 Overview of the Fractional quantum Hall effect

In 1982, Tsui, Stormer, and Gossard reported an extraordinary result [114]. Near $1/3$ filling of the lowest Landau level, they observed a quantized plateau in the Hall resistance equal to $R_{xy} = 3h/e^2$, accompanied by a minimum in the longitudinal resistivity R_{xx}. Dubbed the fractional quantum Hall effect (FQHE) at filling $\nu = 1/3$, this new state of matter cannot be explained in terms of Landau levels arising from non-interacting electrons under a strong magnetic field. Instead, it is necessary to consider Coulomb interactions between electrons, leading to the Hamiltonian

$$H = \sum_j \frac{1}{2m}\left(\vec{p}_j + e\vec{A}(\vec{r}_j)\right)^2 + \sum_{j>k} \frac{e^2}{|\vec{r}_j - \vec{r}_k|}. \tag{2.9}$$

Here we sum over all electrons, with the momentum and position of the jth electron respectively given by $\vec{p}_j$ and $\vec{r}_j$.

In general it is not known how to solve the Hamiltonian (2.9) exactly. However, in 1983 Laughlin

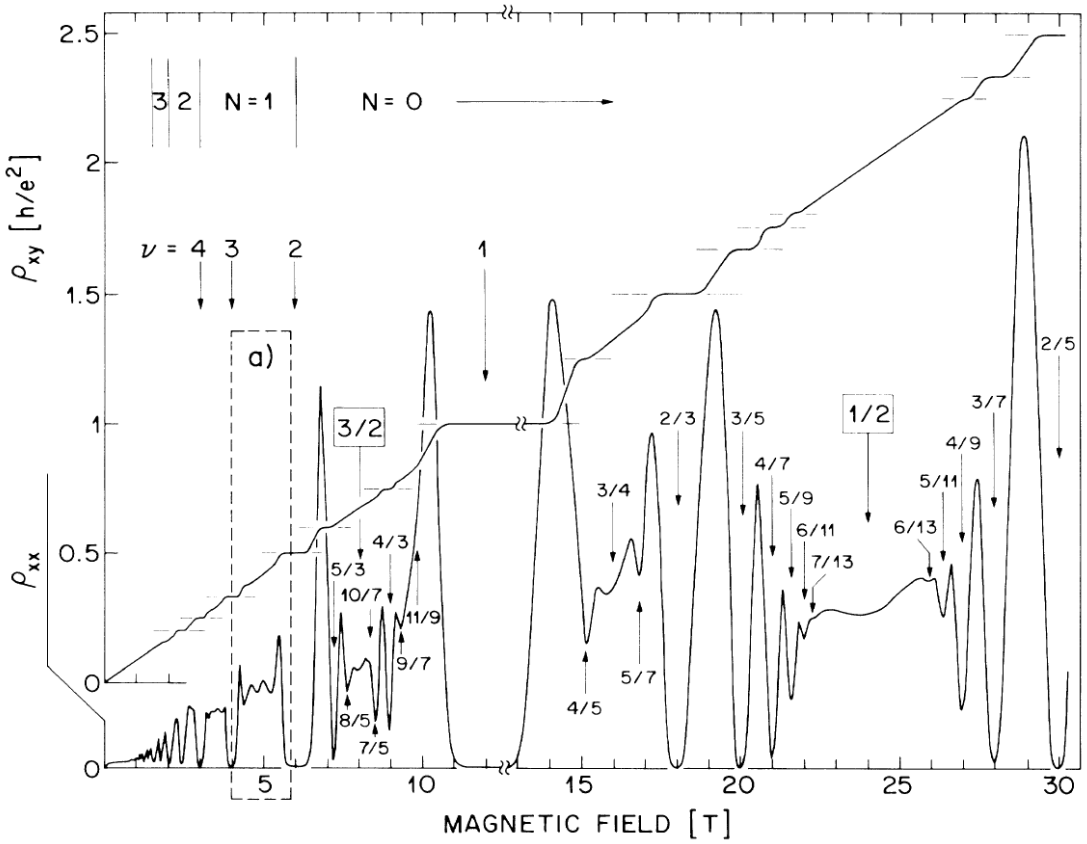

Figure 2.4: A plethora of quantum Hall states, from [126]. In addition to integer quantum Hall states, a wide variety of fractional quantum Hall states are observed. The strongest of these occur at certain filling factors given by $\nu = \frac{p}{2fp\pm1}$, where where f and p are positive integers.

made significant headway toward understanding the $\nu = 1/3$ FQHE with an astute *ansatz* for the ground state wave function. Using the variational approach, he arrived at a correlated state with Hall conductance $(1/m) \times (e^2/h)$ [69]. Remarkably, the elementary excitations of Laughlin's state were shown to have the fractional charge e/m, which has now been observed experimentally at filling factor $\nu = 1/3$ [77].

Using modern heterostructures, it is now possible to observe a large variety of FQH states. A representative measurement, shown in Figure 2.4, reveals that many of the observed fractions follow a specific sequence,

$$\nu = \frac{p}{2fp \pm 1}, \tag{2.10}$$

where f and p are positive integers.

The above sequence of FQH states is often understood in the bulk of the system using a mean-field approach called the composite fermion (CF) theory (see [49] for a detailed overview). Within this theory, each electron becomes attached to $2f$ magnetic flux quanta[4], to form a composite fermion. These composite fermions will then experience an effective magnetic field B_{eff}, which differs from the external magnetic field B by the relation $B_{\text{eff}} = B - 2fn\Phi_0$, where n is the electron density. If the filling factor is tuned so that $\nu = \frac{p}{2fp\pm1}$, it is then possible to show that the composite fermion filling factor $\nu_{CF} = n\Phi_0/B_{\text{eff}}$ is simply equal to the integer p. Hence, FQH states which fall into the sequence (2.10) can be understood in terms of the IQHE of composite-fermions.

At filling $\nu = 1/2$[5], the system of composite fermions effectively feels zero magnetic field. It is then possible to view the system as a Fermi sea[42]. In order to have a fractional quantum Hall state with even denominator, one possibility would then be for composite fermions in this Fermi sea to interact and condense into an entirely new state. Fractional quantum Hall states are in fact observed at certain even-denominator fillings, most notably at $\nu = 5/2$. It is widely hoped that the ground state of the $\nu = 5/2$ state is well-described by a wave function proposed by Moore and Read, in which pairing interactions between composite fermions lead to a state analogous to a superconductor [84]. The fundamental excitations of this Moore-Read state are theoretically predicted to have non-Abelian braiding statistics, a property which could be useful for quantum information processing. For good theoretical and experimental overviews of progress in this area, see [79, 86].

[4]Note that the true magnetic field remains uniform in the sample.

[5]More generally, $\nu = 1/2f$.

2.3.2 Edge states in the fractional quantum Hall effect

In the IQHE, we were able to formulate a picture in which the formation of edge channels leads to quantization of the Hall conductance. In the FQHE, although it is not immediately clear that such a picture should be possible, the sharp quantization of the Hall conductance might lead one to suspect that edge channels with fractionally quantized conductance can form. In 1990, X. G. Wen showed theoretically that the edge of a Laughlin $1/m$ state indeed hosts such a one-dimensional channel, which carries fractionally charged excitations in one direction with conductance e^2/mh [125]. In more complex fractional quantum Hall states, such as the CF sequence in (2.10), this picture can be generalized to include multiple fractionally quantized edge channels [52].

A peculiar situation arises, however, when considering even an ostensibly simple case such as the $\nu = 2/3$ state. A naïve view would have this state be composed of a $\nu = 1/3$ hole state embedded in an integer $\nu = 1$ state, so that the bulk filling factor is $2/3$ ([74], Figure 2.5A). At the edge, there would then be two counter propagating states, one associated with the $\nu = 1/3$ state and having conductance $e^2/3h$, and the other associated with the $\nu = 1$ state and having conductance e^2/h. Depending on the details of scattering between these two edges, one would then expect in an experiment to measure a non-universal two-terminal conductance of $\frac{2}{3} \times \frac{e^2}{h} \leq G_{2T} \leq \frac{4}{3} \times \frac{e^2}{h}$. In fact, in experiments the conductance is universally found to be quantized to $G_{2T} = \frac{2}{3} \times \frac{e^2}{h}$, in conflict with this simple theoretical picture. Moreover, a time-domain experiment found only a single charge mode propagating downstream at the $\nu = 2/3$ edge, with no evidence for upstream charge transport [6]. Clearly, some ingredient is lacking from this simple theoretical picture.

In attempting to resolve this apparent contradiction, Kane, Fisher, and Polchinski considered the possibility of random tunneling between the $\nu = 1/3$ and $\nu = 1$ edges [56]. They found that the addition of this random tunneling leads to a phase transition into a new disorder-dominated edge phase. Remarkably, the eigenstates of this new edge phase are predicted to consist of a mode carrying charge downstream with conductance $\frac{2}{3} \times \frac{e^2}{h}$, and a neutral mode which carries energy upstream (Figure 2.5B). In addition to resolving the problem with the two-terminal conductance, this analysis predicts that locally exciting the neutral mode of a $\nu = 2/3$ edge should lead to upstream propagation of heat from the point of excitation. In Chapter 3, we use a thermometer placed along the edge of a quantum Hall system to detect such upstream flow of heat.

2.4 Electrostatics and reconstruction of edge channels

In Section 2.2.2, we describe edge channels as relatively featureless one-dimensional channels, which occur when Landau levels intersect the chemical potential (Figure 2.6A-C). In reality, the properties of

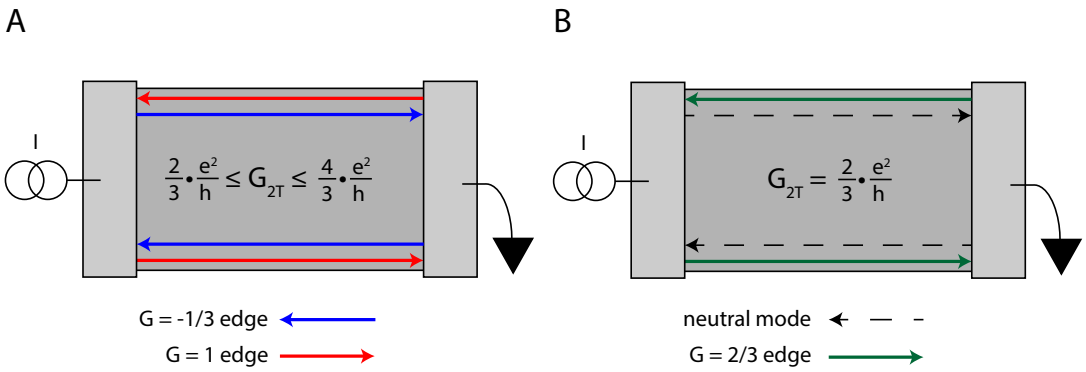

Figure 2.5: Possible edge channel configurations at bulk filling $\nu = 2/3$. Dark gray areas are the 2DES, and light gray areas are metallic contacts. **(A)** A simple pictures of the $\nu = 2/3$ state consists of a $\nu = 1/3$ hole state embedded in an integer $\nu = 1$ state. In this picture, the two-terminal conductance G_{2T} depends on the details of scattering between the edge states and would not be universally quantized. **(B)** Kane, *et. al.* considered the presence of random tunneling between the $\nu = 1/3$ and $\nu = 1$ edges. They found that this leads to a transition to a new edge phase, where the eigenstates are a charge-carrying mode with conductance $\frac{2}{3} \times \frac{e^2}{h}$, and a neutral mode which carries energy upstream. The two-terminal conductance in this situation is quantized to $G_{2T} = \frac{2}{3} \times \frac{e^2}{h}$.

edge channels will be determined by the interplay between Coulomb interactions, magnetic confinement, the smoothness of the electrostatic confining potential, and even disorder (as mentioned in the previous section). In formulating a more realistic picture of the edge modes, Chklovskii, Shklovskii, and Glazman considered the problem of a two-dimensional electron system with an edge defined electrostatically by an electrode [20]. In the absence of an external magnetic field, they found that as one approaches the edge the electron density screens the electric field from the gate and smoothly decreases to zero.

With an external perpendicular magnetic field, however, the local density of states becomes a series of delta functions due to the formation of Landau levels. Now, at the edge of the system, it becomes necessary to pay an additional energy $\hbar\omega_c$ whenever the density exceeds a particular integer filling $\nu = N$. Thus, it is no longer always energetically favorable to locate electrons farther from the gate electrode. The system can instead reach a lower energy state by relocating some electrons from the $\nu = N + 1$ Landau level into the $\nu = N$ level. Although there will be a penalty for moving these electrons closer to the gate, the net decrease in energy through this process leads the system to form a series of compressible and incompressible strips, as shown in Figure 2.6D-F.

In clean enough samples, even further reconstruction is possible. As the electron density decreases near the edge of a sample, it is in principle possible to stabilize incompressible strips associated with FQH states, in addition to the IQH strips. In our measurements in Chapter 3, for example, we provide

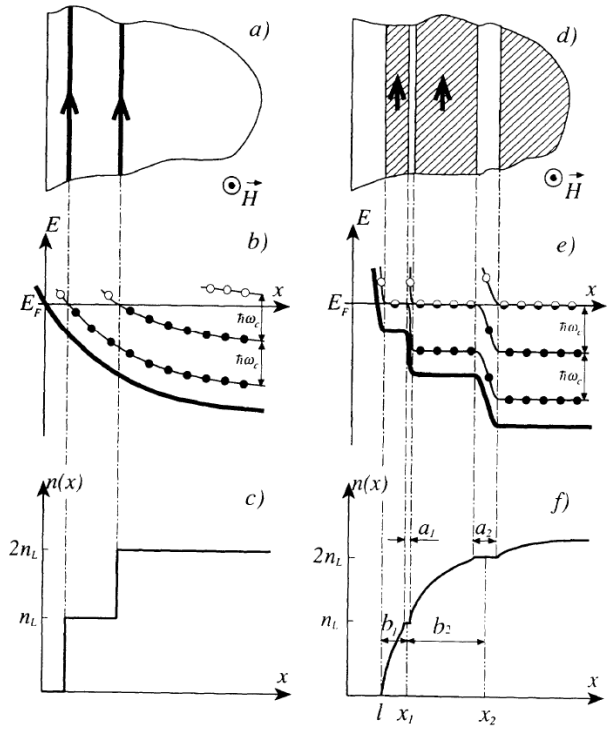

Figure 2.6: Electrostatics of edge channels, from [20]. **(A-C)** In a single-electron picture, the Landau levels bend upward at the edge of the sample due to the confining potential. Edge states occur where Landau levels intersect the chemical potential, and the electron density drops in sharp steps as Landau levels are depleted. **(D-F)** In a more realistic self-consistent electrostatic picture, the 2DES screens the electric field from the gate. The presence of Landau levels influences this screening, so that the system forms a series of alternating compressible and incompressible strips at the edge of the sample.

evidence for the formation of a $\nu = 2/3$ strip located outside of a bulk $\nu = 1$ state. By injecting electrons into the $\nu = 2/3$ edge associated with this strip, and measuring the resulting upstream edge temperature, we are able to provide evidence for the upstream neutral mode predicted by Kane, *et. al.* Moreover, by probing both gate-defined and etch-defined edges, we find evidence that the sharpness of the edge confinement indeed modifies the edge structure.

3

Local thermometry of neutral modes on the quantum Hall edge

When a two-dimensional electron system (2DES) is subject to a strong perpendicular magnetic field and tuned such that the ratio of electrons to magnetic flux quanta in the system (ν) is near certain integer or fractional values, the bulk of the system develops a gap due to either quantization of kinetic energy (the integer quantum Hall, or IQH, effect) or strong correlations arising from non-perturbative Coulomb interactions (the fractional quantum Hall, or FQH, effect) [37]. While the bulk (2D) is gapped and incompressible, the edge (1D) of the system contains compressible regions with gapless excitations that carry charge chirally around the system, in a direction determined by the external magnetic field. Compressible edge states have gained more attention recently due to their ability to serve as a bus for quasiparticles that exist in exotic FQH phases[15, 110]. These edges, however, can have considerable internal structure that is not apparent from bulk transport measurements.

The spatial structure of edges is dictated by the interplay between the external confining potential that defines the edge, an additional harmonic confinement from the magnetic field, and Coulomb interactions. It was predicted [20] and verified [48, 128, 132] that for a smooth, topgate-defined confining potential, it is energetically favorable for the electron density to redistribute slightly to create alternating compressible and incompressible strips. This has the effect of spatially separating edges corresponding to transitions between different filling factors. Such an effect is not present in sharper

edges [47].

Perhaps more surprising than this spatial structure is the possibility of modes that carry energy (or heat) upstream, even as the magnetic field carries the injected charge downstream. The edge of the $\nu = 2/3$ FQH state was originally predicted to consist of a $\nu = 1$ edge of electrons traveling downstream with a $\nu = 1/3$ edge of holes propagating upstream [74, 125]. This edge structure would suggest a two-terminal conductance of $G_{2T} = \frac{4}{3}\frac{e^2}{h}$. Scattering between the edges would lead to non-universal values in the range of $\frac{2}{3}\frac{e^2}{h} \leq G_{2T} \leq \frac{4}{3}\frac{e^2}{h}$. Experimentally, however, no such two terminal conductance has been measured. Direct approaches to look for upstream charge transport in the time domain have similarly found no evidence [6]. This motivated a picture in which disorder induces scattering and equilibration between the edges, forcing the charge to travel exclusively downstream. Heat, however, would be allowed to travel diffusively upstream and downstream, leading to a nonzero thermal Hall conductivity and partial upstream heat transport at $\nu = 2/3$ [53, 56].

Evidence for upstream heat transport in a $\nu = 2/3$ edge was recently obtained by performing modified shot noise measurements [14]. Our approach studies the same state by directly placing thermometers upstream and downstream of a current-source heater to observe charge and heat transport along the edge. We will focus on low-energy transport properties, in contrast to another recent measurement with a high degree of charge imbalance along the edge [26].

As our heater, we use a lithographically fabricated quantum point contact (QPC), tuned to the tunneling regime (Figure 3.1C). Tunneling of electrons through this QPC at elevated energy locally excites the outermost compressible component of a gate-defined edge [116]. This edge, in general, may have many spatially separated compressible components (dark gray regions in Figure 3.1A). We then place quantum dots 20 μm upstream and downstream of the QPC to measure charge and heat transport (blue and red gates in Figure 3.1A). The edge itself is defined by a separate pair of gates (green in Figure 3.1A), and the perpendicular magnetic field defines a clockwise charge-propagation direction (with respect to Figure 3.1). All measurements were carried out in a dilution refrigerator with a minimum electron temperature of 20 mK, measured with Coulomb blockade thermometry.

3.1 Charge signatures of edge reconstruction

To first characterize the structure of the edge that we are tunneling charge into, we energize a subset of gates upstream (blue) and downstream (red) of the central QPC to create two more point contacts that serve as imperfect voltage probes ($R \sim 100$ kΩ). This ensures that we only measure the chemical potential of the outermost edge component alone [116]. Current is injected through the central QPC (10 pA sourced through O3 and drained at O6). The upstream chemical potential, $V1 - V7$, was

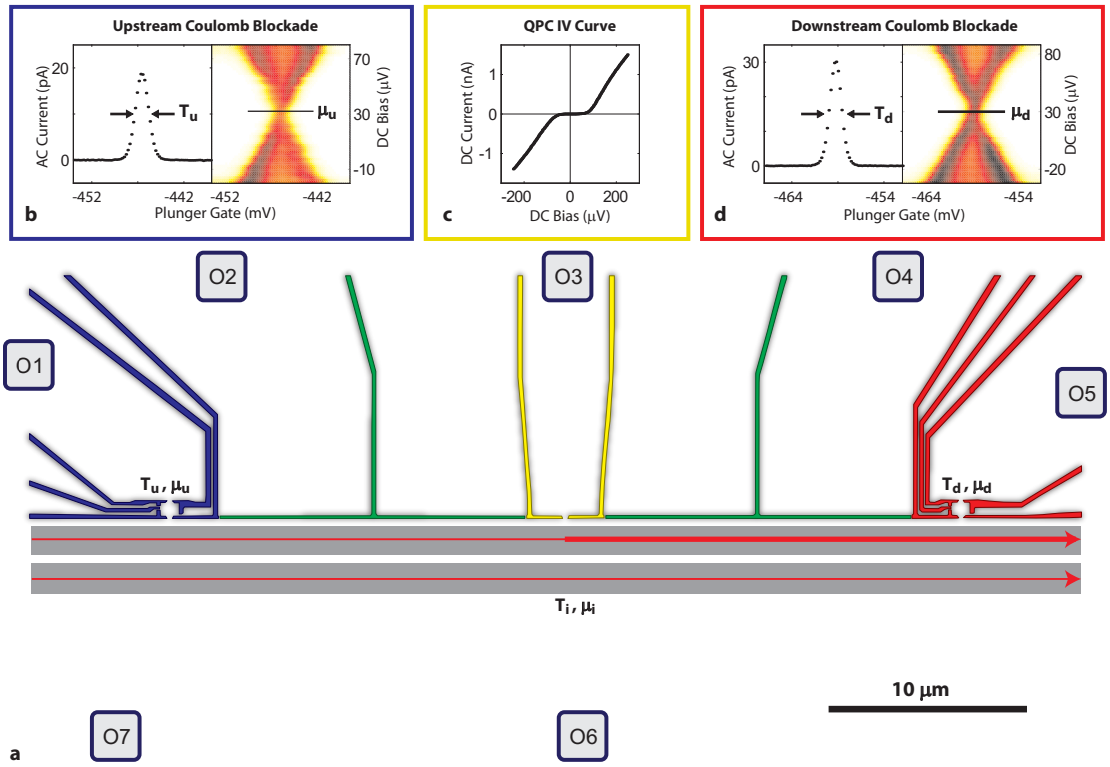

Figure 3.1: Measurement overview. **(a)** Scanning electron micrograph with colored gates. O1-7 denote ohmic contacts. Injection of current through the central QPC (yellow) populates and heats the outermost quantum Hall edge channel. Deflector gates (green) adjacent to the injection site define the edge or can be de-energized to direct edge channels to floating ohmic contacts (O2 and O4). A quantum dot (red) located 20 μm downstream of the injection site is used to measure the temperature T_d and chemical potential μ_d of the outer edge channel. Similarly, an upstream dot (blue) measures T_u and μ_u. Inner edges may be present at a different temperature (T_i) and chemical potential (μ_i). Our measurements cannot determine edge widths, but there is some evidence that edge reconstruction may occur over several micrometers in these device (see Figure 3.18). **(b, d)** Coulomb blockade peaks and diamonds for the quantum dots. The temperature is determined from the Coulomb blockade peak width. The chemical potential is determined by zeroing the voltage bias across the quantum dot. **(c)** The IV characteristic of the QPC. For charge transport (Figure 3.2), the QPC was biased just beyond blockade. Heat transport measurements (Figure 3.3) were taken at all points of the IV curve.

observed to be immeasurably small in all measurements, indicating that no charge is transported upstream on a 20 μm scale. The downstream chemical potential, $V5 - V7$, can be used to determine the resistance of the edge connecting the source to the probe (the local Hall resistance R_L). This resistance is plotted in blue in Figure 3.2. Further measurement details can be found in Section3.5.

For magnetic fields (B) between 2 T and 8 T, the measured value $R_L = 1\frac{h}{e^2}$ indicates that the charge is carried between the injector and detector by electronic modes that behave similarly to an IQH $\nu = 1$ edge. Inner edges can (and must, at fields below 6 T) be present, as can be seen by comparing R_{xy} with R_L. These inner edges, however, do not carry any of the injected charge. Above 8 T, we find that R_L is quantized to $R_L = \frac{3}{2}\frac{h}{e^2}$ even though the bulk is at $\nu = 1$[67]. This suggests that the edge has additional structure consisting of alternating compressible and incompressible regions that are spatially separated, as indicated in Fig. 3.2 (IV). In this situation, we only access the outermost edge of the incompressible $\nu = 2/3$ strip located outside the $\nu = 1$ bulk. The robust quantization that we observe indicates that no charge leaks out of this outermost $\nu = 2/3$ edge over the 20 μm separating the injector from the detector.

The edge-deflecting gates (green in Figure 3.1A) can be de-energized to deflect the edges into floating ohmic contacts located 250 μm away (O2 and O4), where they will chemically equilibrate and thermally cool (although some equilibration and cooling may occur before the edges reach the ohmic contacts). If we repeat this charge transport measurement with the deflector gates de-energized, we continue to monitor no upstream charge transport. However, the downstream resistance is observed to match exactly the bulk value of R_{xy}, plotted in black in Figure 3.2. This indicates that our deflection process does, indeed, force all edges to fully equilibrate their chemical potentials in ohmic contacts O2 and O4, providing an important control for the heat transport measurements discussed below.

3.2 Heat Transport at $\nu = 2$ and $\nu = 3$

To characterize heat transport, we energize all of the gates upstream and downstream of the central QPC to form quantum dots, which serve as thermometers to measure the temperature of the edge. This is similar to another recent spectroscopic approach [3, 4, 111]. The width of the Coulomb blockade peak as a function of gate voltage can be translated into the temperature of the leads (Figure 3.1B, details in Section 3.5).

With the thermometers active, we inject current through the QPC set to an average transmission of 15% to create a non-equilibrium population in the outermost edge (Figure 3.1C). The low transmission ensures that we inject solely electrons into the edge (no FQH edges are fully transmitted). These energetic electrons, however, are not necessarily the elementary excitations of the edge and will

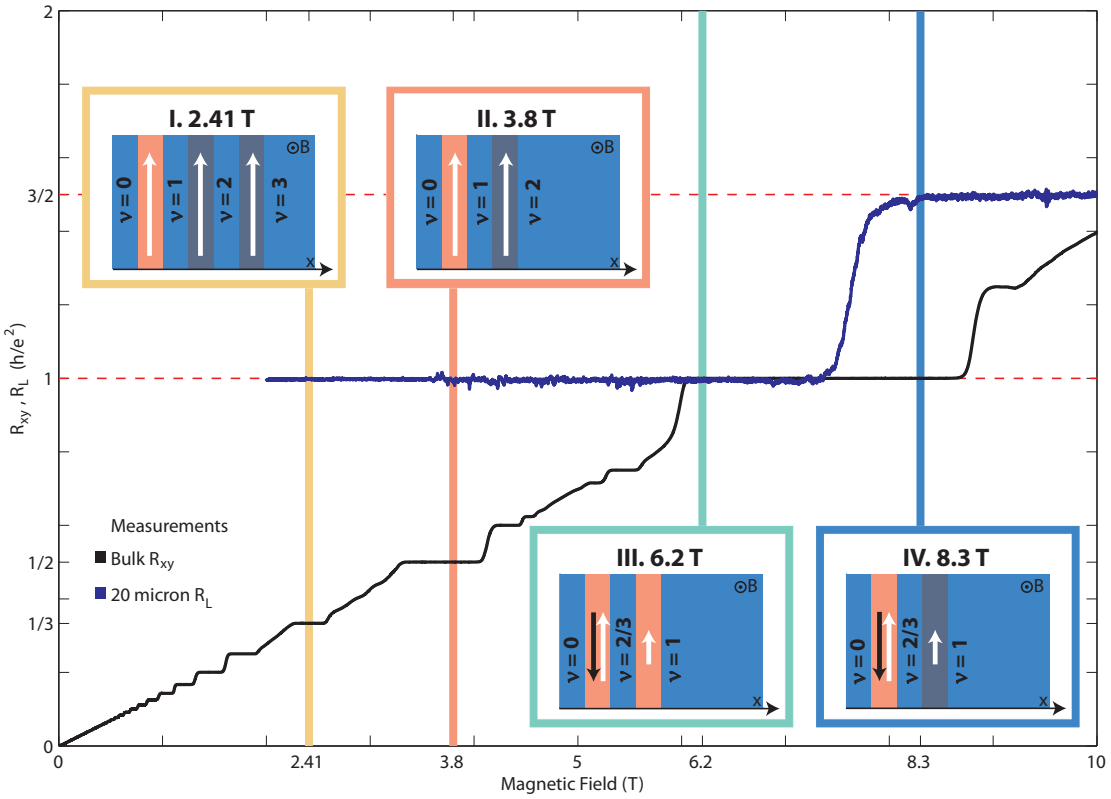

Figure 3.2: Local charge transport. Plateaux in R_{xy} (black) indicate bulk quantum Hall states. Plateaux in R_L (blue) reveal the structure of the edge. The insets depict the qualitative structure of the sample edge at various magnetic fields, with incompressible regions shown in light blue and labelled by filling factor. In the intervening compressible channels, white arrows point in the direction of charge flow. The arrow length specifies a charge conductance of G=1, 2/3, or 1/3 in units of e^2/h. Black arrows indicate neutral modes that carry energy upstream. The channels highlighted in red contribute to charge transport at the voltage probe. **(I), (II)** When the bulk filling factor is ν=2 or ν=3, the edge is composed of integer channels with the outermost channel having conductance G=1. At the voltage probe, the excess current is carried solely by the outermost channel. **(III), (IV)** Outside the bulk ν=1 state the edge is reconstructed, resulting in an outermost G=2/3 charge channel. The remaining 1/3 conductance can be found on a spatially separated inner edge located in the compressible region between the ν=2/3 and ν=1 incompressible regions. At 8.3 T, the excess current is carried to the voltage probe only by the outermost channel. At 6.2 T, the edge channels come to the same potential before reaching the voltage probe, resulting in R_L=1. Dashed red lines indicate quantized values of R_L.

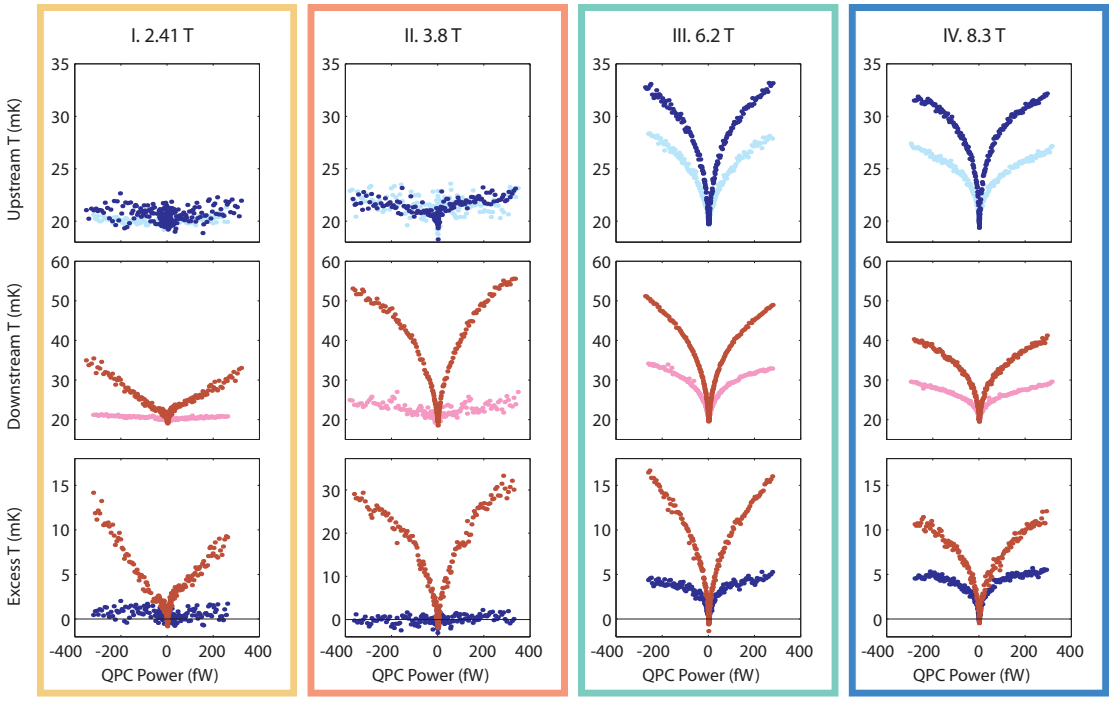

Figure 3.3: Local edge temperature versus QPC power dissipation at different magnetic fields. Negative (positive) QPC powers correspond to the injection of holes (electrons). For each magnetic field, the upstream and downstream temperatures were measured with (blue, red) and without (cyan, magenta) the deflector gates energized. The difference between temperatures with and without the deflectors energized is plotted across the bottom row for the downstream (red) and upstream (blue) dots. For I and II, corresponding to an integer outermost edge, heat is carried chirally downstream with no upstream heat transport. For IV, where we measure a 2/3 outermost edge, the heat is carried downstream and upstream. For III, heat is also carried in both directions, while R_L=1. We attribute this behavior to reconstruction outside the bulk ν=1 edge, which allows upstream heat transport without 2/3 charge transport.

therefore excite the natural edge modes as they decompose. By increasing the bias across the QPC, we vary the current (and therefore the power) being delivered to the edge. We monitor both the chemical potential and temperature of the edge at the upstream and downstream dots (Figure 3.1B and 3.1D).

Measurements are first performed with the deflector gates energized, to measure heat transport associated with the edge (red and blue curves in rows 1 and 2 of Figure 3.3). We then repeat the procedure with the deflector gates off, to measure any background heating not associated with the edge (cyan and magenta curves in rows 1 and 2 of Figure 3.3). The difference between these two temperatures gives us a measure of the excess heat carried by the edge (bottom row in Figure 3.3, red is downstream and blue is upstream temperature).

At the two lowest fields that were measured (2.41 T and 3.8 T), our charge transport measurements

indicate that we are injecting charge into a $\nu = 1$ edge sitting outside an incompressible bulk at filling $\nu = 3$ or $\nu = 2$ respectively. This is depicted schematically in Figure 3.2 (I,II) and in Figure 3.4 (II). By monitoring the chemical potential as we vary the injected power, we find that charge is carried exclusively by the outermost $\nu = 1$ edge over the entire range of measurement (Section 3.5).

At 2.41 T, when the bulk is at $\nu = 3$, there is no measurable background heating either upstream or downstream. When the deflectors are turned on, we find heating downstream but none upstream. When the bulk is at $\nu = 2$, we find about $2 - 3$ mK of background heating that is perfectly cancelled in the upstream direction. Thus, in both cases, we find that heat carried by edge modes is transported exclusively downstream. While this strict downstream heat transport in the IQH regime is expected and matches previous measurements [14, 38], surprisingly, the magnitude of the temperature observed does not agree with what one would expect from quantized thermal transport (assuming an equilibrated edge):

$$K_H \equiv \frac{\partial J_E}{\partial T} = n\frac{\pi^2}{3}\frac{k_B^2}{h}T \implies T = \frac{\sqrt{6hJ_E/n}}{\pi k_B},$$

where J_E is the power carried by the edge and n is the number of IQH edges participating in transport [53]. At $\nu = 2$, for an injected power of 350 fW, we expect an edge temperature between 430 mK and 608 mK, depending on how well the two edges thermally equilibrate ($n = 2$ or $n = 1$). Our measured temperature of 30 mK indicates that a substantial quantity of heat is transferred out of the edge[4]. We can model the behavior of heat transport for out-of-equilibrium Fermi systems (Section 3.6), which indicates a similar temperature deficiency. Both models, however, give the correct shape for the temperature versus power curves presented in Figure 3.3.

3.3 Neutral modes associated with the $\nu = 2/3$ and $\nu = 1$ edges

At the highest measured field, 8.3 T, charge transport (Figure 3.2) indicates that we have an incompressible $\nu = 2/3$ strip outside a $\nu = 1$ bulk, depicted schematically in Figure 3.2 (IV). Here we see substantially more background heating, both upstream and downstream. This bulk heating at $\nu = 1$ is unexpected and has not previously been observed, although a similar result at $\nu = 4/3$ has recently been reported [5]. Further details can be found in Section 3.7. After subtracting contributions from the bulk (deflectors energized) we still find an upstream temperature rise of 5 mK at 300 fW, compared with a downstream rise of 11 mK. Such upstream heating is consistent with the predicted upstream thermal conductivity of the outer $\nu = 2/3 \to 0$ edge[53], although the asymmetry between upstream and downstream temperatures suggests that the inner $\nu = 1 \to 2/3$ edge (which is expected to carry heat preferentially downstream) is partially participating in heat transport.

At the second highest measured field, 6.2 T, one would expect, based on charge transport, behavior similar to what we find when the bulk is at $\nu = 2$ or $\nu = 3$, with all heat being carried downstream by the integer $\nu = 1$ edge. Instead, we find a behavior similar to what was observed at 8.3 T, with heating both upstream and downstream and a slight asymmetry between the two. This surprising result can be understood if we allow for the presence of additional structure in the $\nu = 1$ edge that does not affect charge transport. Perhaps the simplest such structure would be the presence of an incompressible strip of $\nu = 2/3$, much like what we see at 8.3 T, but with charge equilibrating between the two separated edges of this strip (Figure 3.2 (III)). With these edges equilibrated, we measure a local Hall resistance of $R_L = \frac{h}{e^2}$. However, the diffusive heat transport provided by the outer $\nu = 2/3 \rightarrow 0$ edge could still carry heat to the upstream thermometer (edge IV in Figure 3.4). Importantly, this mechanism of upstream heating by an apparent $\nu = 1$ edge would not be universal and would depend sensitively on the spatial reconstruction of the edge. A sharper mesa-defined edge with a larger density gradient [14, 38] or a lower-mobility 2DES may not allow an incompressible strip of $\nu = 2/3$ to form outside the $\nu = 1$ bulk. To clarify this, we will now consider a device with a mesa-defined edge.

3.4 Sharp confinement modifies edge structure

Here, we will present data from a sample in which we physically removed material to define the boundary of the 2DES, creating a steeper confining potential when compared to the device in Figure 3.1. As a result of the steeper confinement, we find edges of type III and IV (from Figure 3.4) when the bulk is at $\nu = 1$. The gate-defined edge, as a reminder, had edges of type IV and V at bulk filling $\nu = 1$. From the table in Figure 3.4, we see that charge transport (R_{xy} and R_L) cannot discriminate between the type III and type IV edges. We will now present evidence that both of these edges can exist in a single sample, and that they can be distinguished by monitoring upstream heat transport.

In Figure3.5, we present a scanning electron micrograph of the device under consideration. The device geometry and substrate used are identical to those used for the device presented in Figure 3.1. Instead of using deflector gates to define the edge, we used a chemical etch to remove material between the QPC heater and the quantum dot thermometer. This creates a physical boundary to the sample along which the edge propagates. The density in the 2DES must drop to zero across this edge, which can happen over a shorter length scale than for an edge created by depleting the 2DES through electrostatic gating.

To demonstrate that this edge is sharper, we can repeat our local charge transport measurements (Figure 3.5b, R_L in red). The observed enhanced conductance at any given field (red compared with blue) is a result of either more edges participating in transport, or a greater conductance of participat-

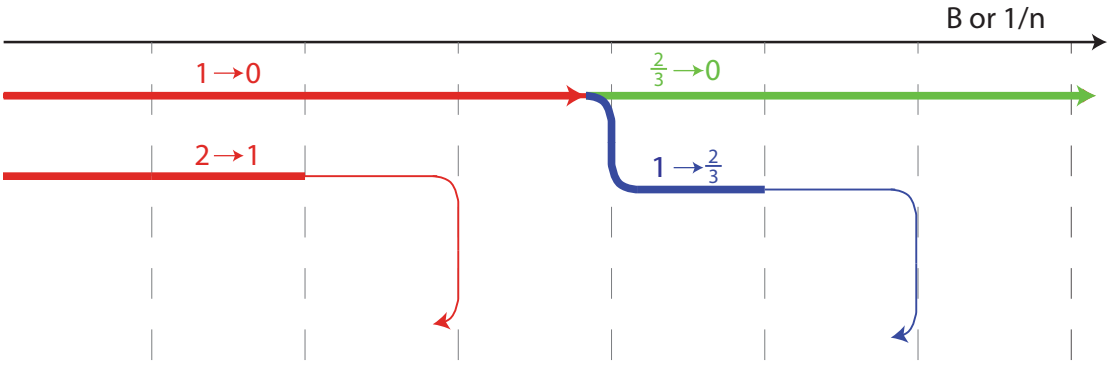

	(I)	(II)	(III)	(IV)	(V)	(VI)
R_{xy}^{-1}	2	2	1	1	1	2/3
R_{L}^{-1}	2	1	1	1	2/3	2/3
upstream heat	no	no	no	yes	yes	yes

Figure 3.4: Possible edge structures at different magnetic fields. The width (and existence) of each given region will depend on details of the sample and the sharpness of the edge. Three types of edge are present in this experiment, denoted by different colors, with the topmost edge being the outer edge. Only edge structures II, IV, and V are present in the device in Figure 3.1. Edge III is present in the device in Figure 3.5. All resistances are given in units of h/e^2. A measurement of R_L allows one to determine which edges chemically equilibrate when charge is injected into the outer edge (denoted by bold lines in the figure). Only the (2/3)⟶0 edge transports heat upstream, and can be identified by thermometry measurements. Detecting upstream heat allows us to discriminate between edges III and IV.

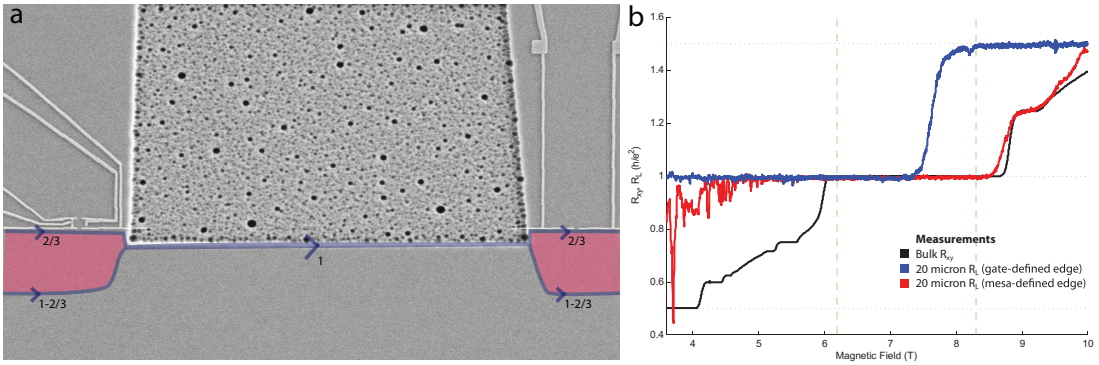

Figure 3.5: Modified device to study heat transport along a sharper edge. The gate-defined edge (Figure 3.1) allowed for a ν=2/3 edge to form outside the ν=1 bulk (blue trace in **b**). The mesa-defined edge here is sharper, and the sharp density gradient may preclude FQH edge structure outside the ν=1 bulk. **(a)** Scanning electron micrograph of a device with 40 μm between the heater and the thermometer. The device measured had 20 μm between the heater and the thermometer, to match the device presented in Figure 3.1. **(b)** R_L (red) for the device in **a**. The reduced resistance of the edge (red versus blue) at 8.3 T when switching from a gate-defined to a mesa-defined edge suggests that the originally separated FQH (ν=2/3 and ν=1$\rightarrow$2/3) channels are brought close together, allowing charge to equilibrate between them. Although the device is drawn with and edge of type III (from Figure 3.4), an edge of type IV cannot be ruled out from charge transport, either locally (R_L) or globally (R_{xy}). Dotted red lines indicate quantized values of R_L. Dashed green lines indicate fields at which thermometry measurements were made.

ing edges. This is precisely what is expected if the edges are confined with a steeper potential. Here we will focus on behavior on the edge of the $\nu = 1$ bulk (6.2 and 8.3 T). From the charge transport measurements, we cannot distinguish the exact structure at either field (see edges III and IV in Figure 3.4).

To distinguish between these two possible edge structures, we can perform upstream thermometry measurements. As we created our edge in this sample by etching the mesa, we cannot control for bulk heating by energizing and de-energizing deflection gates. However, by using an identical geometry to the gate-defined device, we can still identify the presence or absence of excess heating due to the edge. This thermometry measurement is presented in Figure 3.6, with data from the edge-defined device in red. For comparison, data from the gate-defined device taken at the same fields are reproduced in dark blue and light blue (identical to upstream data in columns III and IV of Figure 3.3).

At 6.2 T, we see that the temperature detected upstream (red in Figure 3.6a) closely matches the temperature associated with bulk heating in the original device (light blue). This is consistent with no heat being transported by the edge. The lack of upstream heat carried by the edge allows us to classify it as a simple IQH $\nu = 1$ edge (type III in Figure 3.4), similar to what was observed at bulk fillings of $\nu = 2$ and $\nu = 3$ in the original device.

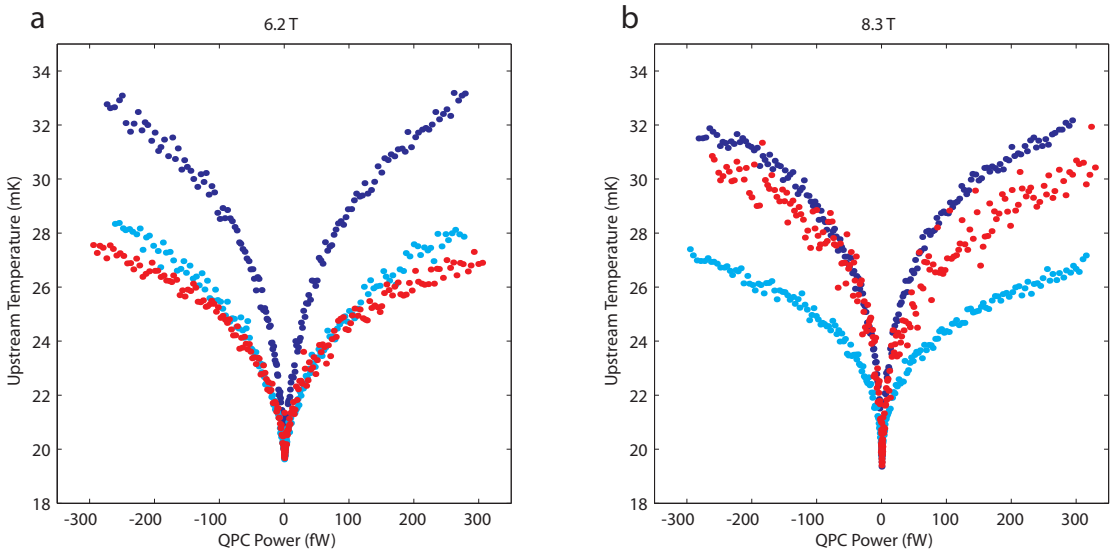

Figure 3.6: Upstream thermometry to identify FQH structure in the ν=1 edge. Light blue curves depict background upstream heating, which we attribute to the bulk. The dark blue curves depict the heat observed with a gate-defined edge connecting the heater and the thermometer. The red curves depict upstream heat observed with a sharper mesa-defined edge connecting the heater and the thermometer. **(a)** At low fields, the upstream heating from the mesa-defined edge closely matches the background, suggesting no excess heat is carried by the edge. **(b)** At high fields, there is a similar amount of upstream heating by both sharp and shallow edges, both appreciably above the background.

At 8.3 T, the temperature measured upstream (red in Figure 3.6b) seems to be elevated, closely matching the temperature seen when a $\nu = 2/3$ edge connects the heater to the upstream thermometer. Recall that in the original device, this $\nu = 2/3$ edge was detectable through measurement of R_L (blue curve in Figure 3.2). Here the charge signature has vanished ($R_L = R_{xy}$, but the nearly identical upstream heating strongly suggests that the $\nu = 2/3$ edge is still present (edge IV in Figure 3.4). These measurements increase our confidence in assigning edge IV to our observations at 6.2 T in the original device.

By studying the charge and heat transport properties of the outermost component of a gate-defined quantum Hall edge, these measurements suggest that such edges contain considerable structure. Charge transport along the edge shows that correlated FQH modes can exist outside an IQH bulk. Even when these charge signatures are not present (Fig. 3.2 (III) and edge IV in Fig. 3.4), heat transport suggests that density reconstructions can still create edge components that carry heat upstream. The presence of such edge structure could have strong implications for the behavior of quantum Hall interferometers, where integer edges are conventionally treated as featureless electron beams [25].

In addition to this, by separating bulk and edge contributions, we have been able to observe bulk heat transport at $\nu = 1$ that is absent at $\nu = 2$ and $\nu = 3$, the origin of which remains an open question.

More generally, our system provides a framework to extract quantitative information about charge and heat transport at the boundary of any two-dimensional topological insulator. Such a system can be essential to discriminate between topological states of matter that have identical charge transport behavior. For example, with the $\nu = 5/2$ FQH state, the presence or absence of these neutral modes would allow us to discriminate between distinct ground states that are particle-hole conjugates of each other [28, 71, 72].

3.5 Chemical Potential Measurements and Thermometry

I. Chemical Potential Measurement

As the DC current I injected through the QPC increases, the downstream chemical potential of the outermost edge component must correspondingly rise. Unless a DC voltage bias V_{ZB} is applied to O5 to exactly compensate this altered chemical potential, a DC current will flow through the dot whenever the Coulomb blockade is lifted. Tuning the dot to this zero bias condition allows us to measure the chemical potential of the outermost edge component. In principle an upstream charge current may cause a similar rise in chemical potential at the upstream dot. For all measurements, the upstream chemical potential was indistinguishable from that of the ground contact (O7), suggesting that upstream charge transport does not occur on a 20 μm scale.

The dependence of V_{ZB} on the current I, at a particular value of magnetic field, measures the total conductance of the edge channels participating in charge transport at the quantum dot. For the deflector gates energized, this conductance matches $1/R_L$. When the deflector gates are at zero voltage, however, all edges carry charge and the total conductance matches the Hall conductance. These observations corroborate the assertion that the deflector gates are able to direct the flow of edge channels. When the deflector gates are energized, the data also show that charge remains in the outermost edge on a 20 μm scale even during thermometry measurements. An example of edge resistances determined using the quantum dot zero bias condition is presented in Figure 3.7.

II. Coulomb Blockade Thermometry

At each value of the magnetic field, quantum dots were tuned to the Coulomb blockade (CB) regime. The typical charging energy was 50 μeV, while the typical spacing between CB peaks corresponded to 20 mV on the plunger gate. We calibrated each dot individually for thermometry measurements by extracting the slopes m_1 and m_2 of CB diamonds adjacent to the conductance peak of interest, as shown in Figure 3.8. The lever arm $\alpha = C_G/C$ was then determined by

$$\alpha = \frac{|m_1 m_2|}{|m_1| + |m_2|}, \tag{3.1}$$

where C_G is the capacitance between the dot and the plunger gate, and C is the total capacitance. Knowing α allows the use of the conductance peak width as a sensitive thermometer. Our dots are in the metallic regime $\Delta E \ll k_B T \ll e^2/C$, where the temperature exceeds the dot level spacing ΔE. Note that thermometry in the metallic regime is slightly different than thermometry with a single level,

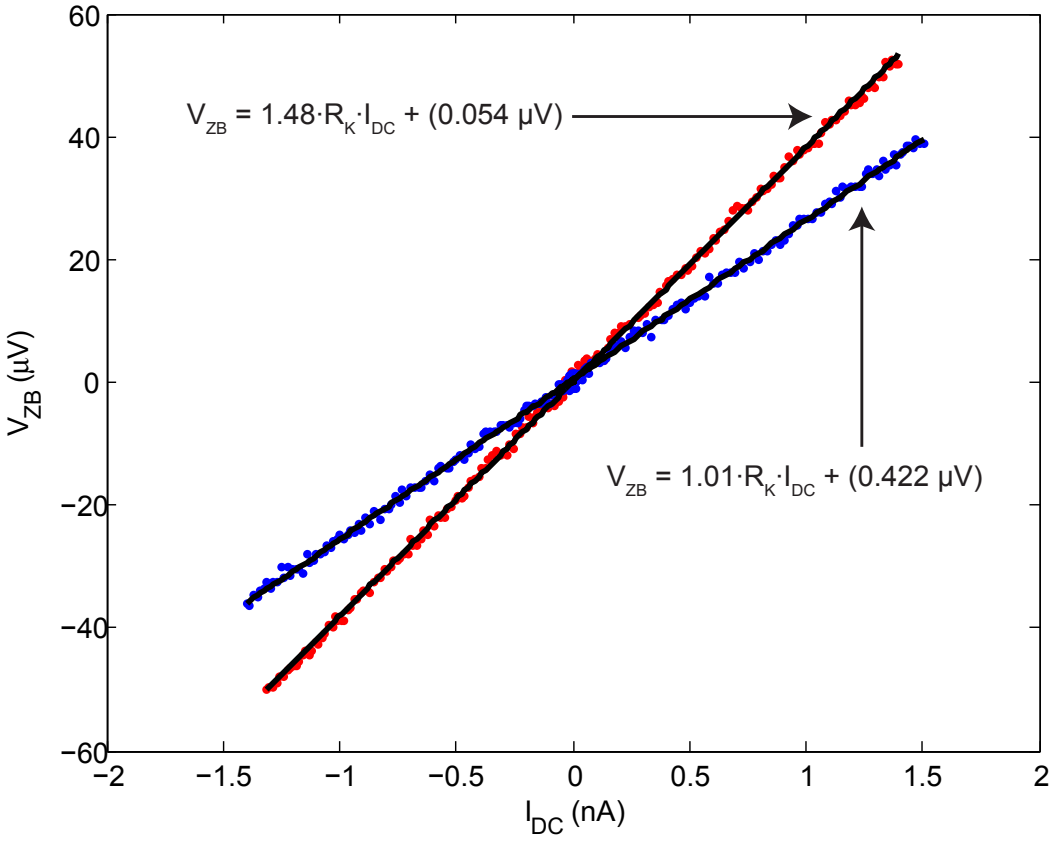

Figure 3.7: The voltage V_{ZB} applied to O5 in order to zero the bias across the downstream quantum dot, as a function of the current I_{DC} injected through the QPC. Data were acquired at a magnetic field of 8.3 T. For the deflector gates energized, V_{ZB} is shown in red, with a slope corresponding to current carried by a $\nu = 2/3$ outermost edge. When the deflector gates are set to zero, V_{ZB} is shown in blue, indicating conduction of current by edges with total conductance $G = 1$.

where obtaining exact electron distributions and individual lead temperatures is possible [3, 46]. The temperature of the leads is then found through the formula for the lineshape of a conductance peak centered at gate voltage V_R [8]:

$$G \propto \cosh^{-2}\left(\frac{e \cdot \alpha \cdot |V_R - V_G|}{2.5 k_B T}\right). \tag{3.2}$$

During the experiment, we applied a fixed 4 μV AC voltage bias and a variable DC voltage bias to each dot (contacts O1 and O5 in Fig. 3.1). The different AC frequencies used for each dot were typically 215 and 315 Hz. To determine the temperature T of the leads coupled to a single dot, we first tuned the DC voltage bias V_{DC} applied to the dot so that the chemical potentials of the two leads were equal, as described above. Then the plunger gate voltage V_G was swept through a conductance peak while the resulting AC current was monitored using lockin techniques. The typical AC dot resistance was > 100 kΩ, resulting in AC currents of ~ 10 pA. For each DC current I injected through the QPC, the temperature of the leads was extracted using equation 3.2. Representative scans over conductance peaks in the downstream dot, for two different injected currents, are plotted in Fig. 3.9.

A data set consisted of one sweep of the DC voltage bias V_{bias} applied to the QPC (contact O3), between -250 μV and 250 μV. At each value of V_{bias} we recorded the injected current I, as well as the temperature T and chemical potential μ for both dots. The QPC power was defined as the vector $P_{QPC} = I \cdot V_{bias} - I^2(h/\nu e^2)$, where ν was the bulk filling factor. For each sweep, the electron temperatures found using equation (3.2) were normalized such that the minimum electron temperature was always 20 mK, equivalent to an effective rescaling of α. This minimum electron temperature of 20 mK was measured at the base temperature of our dilution refrigerator via Coulomb blockade thermometry, for quantum dots with cold leads sourced directly from ohmic contacts. We assume in our experiment that all edges are at this minimum temperature when $V_{bias} = 0$. For a dot coupled to a fractional edge, electronic correlations may alter the temperature extracted using equation 3.2. As long as the peak width remains linear in temperature as a result of such behavior, our procedure accurately reports relative edge temperatures. The absolute fractional edge temperatures may then differ from our reported data by an overall normalization.

While all of our reported Coulomb blockade temperatures use the above rescaling to normalize the base temperature to 20 mK, it is also possible to calibrate temperatures using the resistive RuO thermometer on the mixing chamber. In Fig. 3.11 such a calibration is plotted, showing how the temperature deduced from Coulomb blockade peaks corresponds to the mixing chamber temperature. The behavior is linear at high temperatures and saturates to the minimum dot temperature of 20 mK at low temperatures due to the decoupling of the electronic system from the lattice. Because the

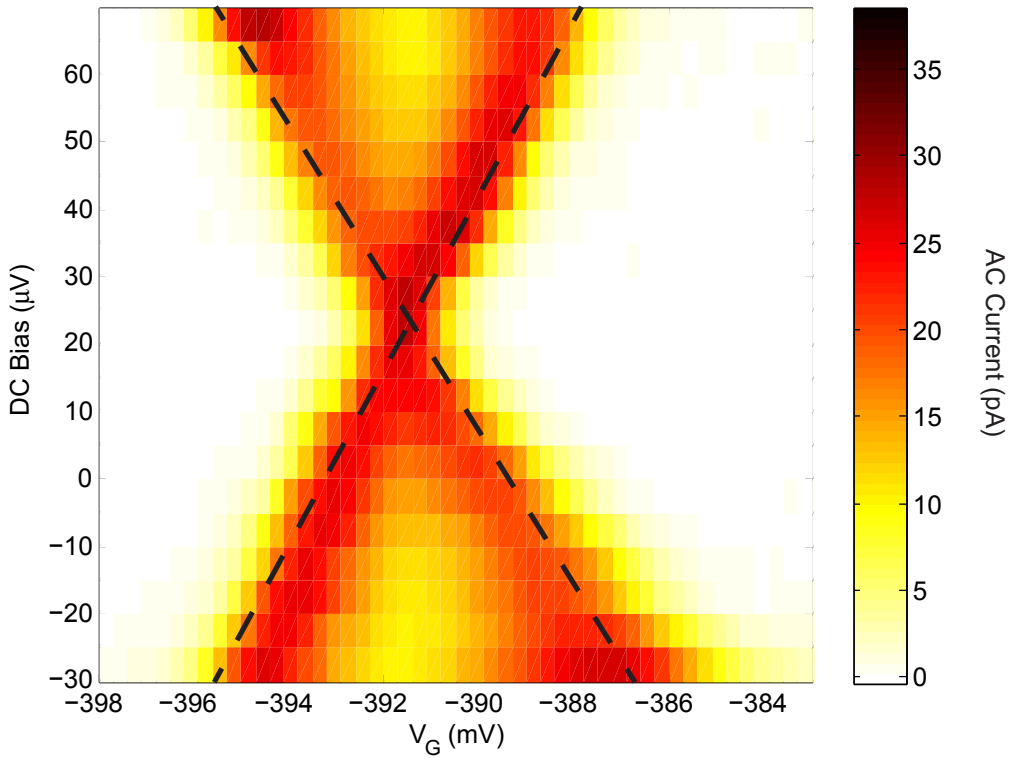

Figure 3.8: Coulomb blockade data used to calibrate the downstream quantum dot at a magnetic field of 8.3 T. The lever arm α is calculated from the slopes of the zero-conductance regions, marked by dashed lines.

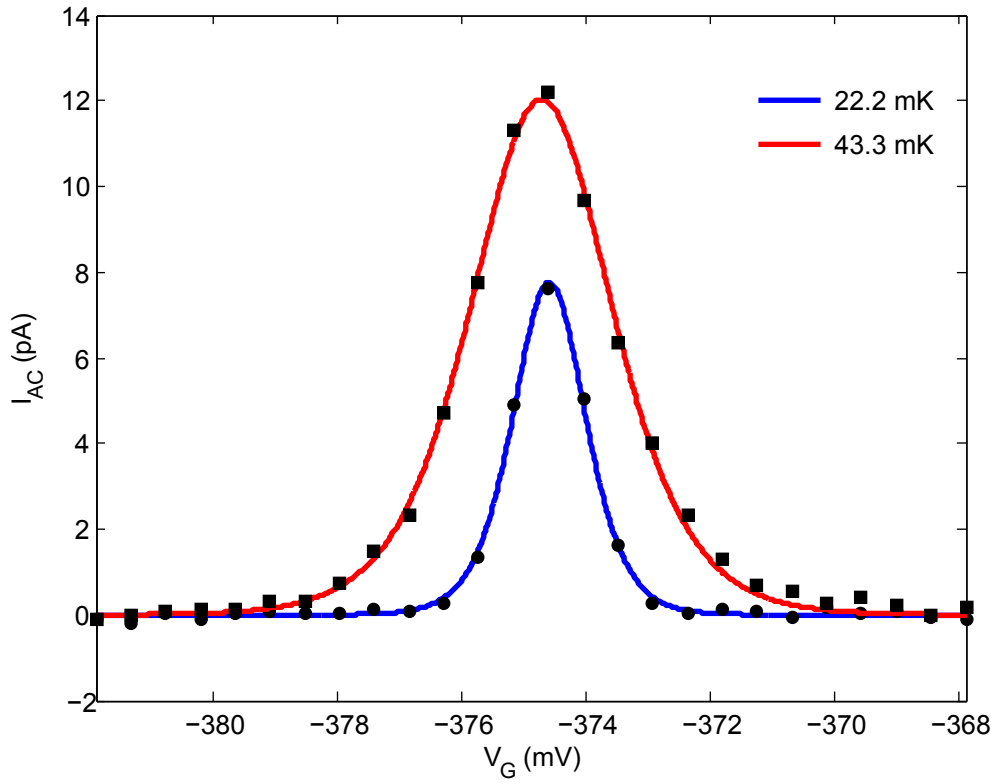

Figure 3.9: AC current I_{AC} through the downstream quantum dot as a function of the plunger gate voltage V_G, measured at a magnetic field of 8.3 T. Black circles (squares) correspond to data taken for an injected QPC current $I = 0$ nA ($I = 1.5$ nA). The best fits of the data to equation (2) are shown in blue and red, and give temperatures of $T = 22.2$ mK for $I = 0$ nA and 43.3 mK for $I = 1.5$ nA.

mixing chamber thermometer is not directly coupled to the two-dimensional electronic system, we have chosen to normalize minimum temperatures to 20 mK rather than calibrate using the mixing chamber. From this data we see that a calibration using the mixing chamber thermometer does not significantly alter our results beyond a 140% temperature rescaling at the highest reported temperatures. This rescaling may be due to electron correlations in the leads, which are known to broaden Coulomb blockade peaks (tunneling between $g = 1/3$ Luttinger wires should result in a 130% higher effective temperature) [36]. None of our qualitative claims are changed by such a rescaling, and this temperature increase cannot explain the temperature deficiency discussed in the main text and Section 3.6.

We accumulated several normalized data sets at each value of magnetic field, both with the deflector gates energized and at zero voltage. To determine the increase in temperature at the downstream dot due to heat carried by the outermost edge component, we first separated the data sets into two groups, depending on whether the deflectors were energized or at zero voltage while the data was taken. For each group, the normalized downstream temperatures were then averaged to obtain two vectors containing the mean downstream temperatures for both deflector settings. The QPC powers were similarly averaged, resulting in the power-dependent mean temperatures plotted in Fig. 3.3. The pre-averaged data from 8.3 T with deflectors off is presented in Figure 3.10.

The difference between the mean downstream temperatures, for equal QPC power, was reported as the excess downstream dot temperature. This procedure was also used for the upstream dot, and for all reported values of the magnetic field. The excess temperatures determined in this way are plotted in the third row of Fig. 3.3 of the main paper.

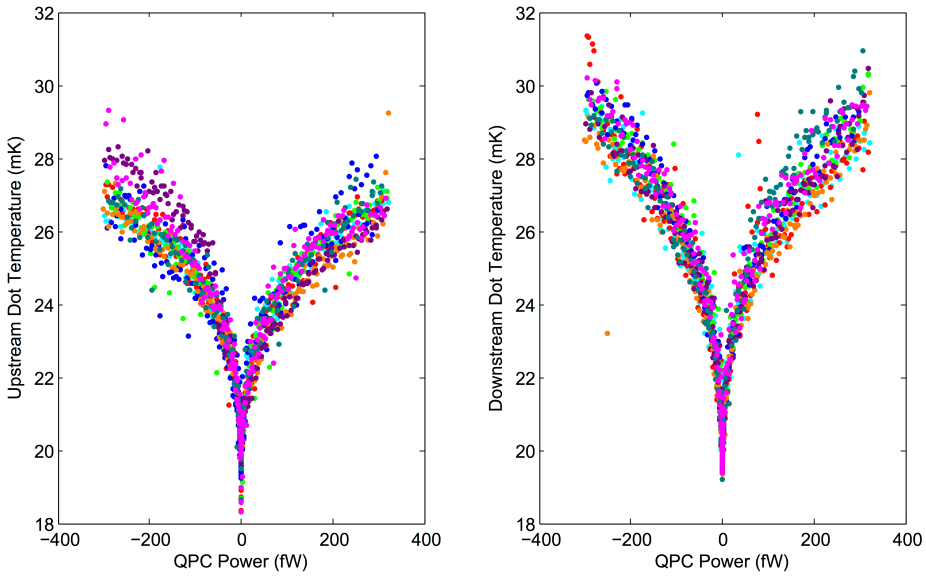

Figure 3.10: Full dataset taken at 8.3 T with deflectors off. These curves were averaged to produce the cyan and magenta curves in Figure 3.3(IV).

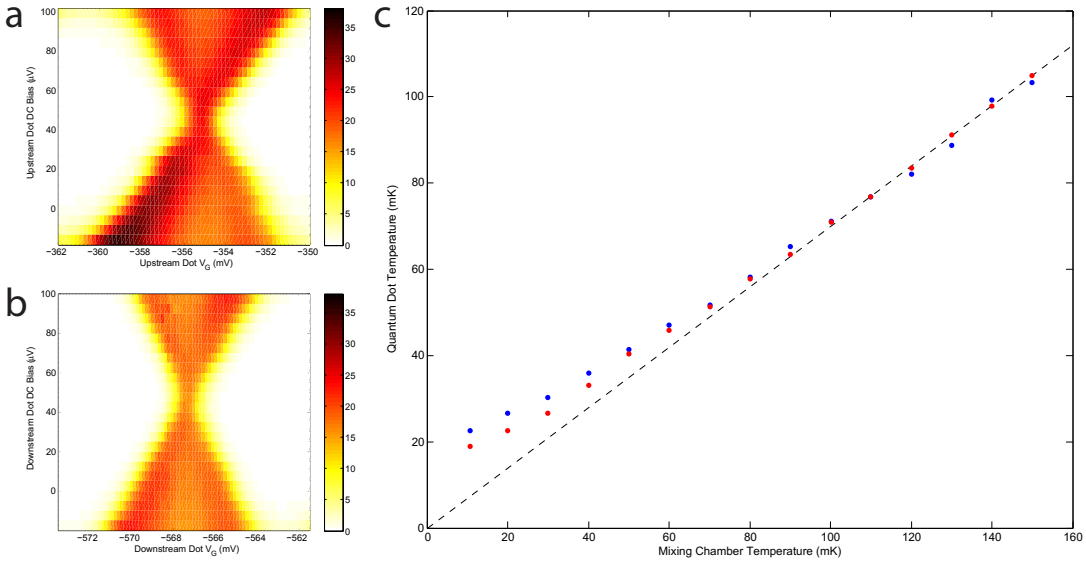

Figure 3.11: Comparison of Mixing Chamber and Coulomb Blockade Thermometry, at 6.15 T. Heat is applied to the mixing chamber and temperatures are measured using a resistive RuO thermometer attached to the mixing chamber along with the two patterned quantum dots. **(a,b)** Widths for the CB thermometers are calibrated using the diamonds. **(c)** The widths of our CB peaks are linear in temperature, except for a saturation at 20 mK as the mixing chamber is cooled to 10 mK.

3.6 Power carried by Non-Equilibrium Edges

In our experiment, we tune the bulk quantum Hall state to filling factor ν, and apply a voltage V between ohmic contacts O3 and O6. These two contacts are separated by a QPC tuned to have resistance $R \sim 100$ kΩ. When a net current I is injected through the QPC, the electronic occupation of the outermost compressible edge channel deviates locally from its equilibrium distribution. Quantum dots placed 20 μm upstream and downstream of the QPC probe the chemical potential and temperature of this outermost edge. The form of Coulomb blockade peaks monitored during our heat transport measurements suggests that the outer edge internally reaches thermal equilibrium over a distance smaller than 20 μm. However, our charge measurements indicate that chemical equilibration of the outer edge with inner edge channels starts to occur at a distance greater than 20 μm. Thus, at the downstream measurement point the outermost edge has a Fermi occupation function and carries all of the injected current I. For the measurements at magnetic fields of 2.41 T and 3.8 T (bulk ν = 3 and ν = 2), the electrical conductance of this edge is consistent with downstream charge transport by a single integer quantum Hall (IQH) edge. Furthermore, our thermometry measurements show strict downstream heat transport, also consistent with the IQH regime. To determine the expected quantitative outcome of our measurements in the IQH regime, we analyze charge and heat transport by IQH edges in the experimental system described above.

The chemical potential μ of an IQH edge is related to the current I_E that it carries:

$$I_E = \frac{e}{h}\mu. \tag{3.3}$$

In our model, the total number of edge channels on each side of the QPC is equal to the bulk filling ν. However, since only the outermost channel contributes to charge transport on a 20 μm scale, we treat inner channels as inert and consider only the behavior of the outer channel. The two outer edges that carry charge toward the QPC originate in ohmic contacts O3 and O6. The occupations of these incoming edges are therefore Fermi functions,

$$\begin{aligned} f_{in}^{O3}(E) &= f(E - \mu_{in}^{O3}, T_{base}) \\ f_{in}^{O6}(E) &= f(E - \mu_{in}^{O6}, T_{base}), \end{aligned} \tag{3.4}$$

where $\mu_{in}^{O3} = \mu + eV$ and $\mu_{in}^{O6} = \mu$ are the chemical potentials of O3 and O6 and $T_{base} = 20$ mK is the electron base temperature. At the QPC, the electronic occupations of the outgoing edge modes are forced out of equilibrium. At a distance 20 μm from the QPC these outgoing edges reach thermal equilibrium, with chemical potentials $\mu_{out}^{O3} = \mu + eV - (h/e)I$ and $\mu_{out}^{O6} = \mu + (h/e)I$ determined

using equation 3.3. While these chemical potentials can be found simply by considering charge transport, a more detailed analysis of scattering at the QPC is necessary to determine the temperatures of the outgoing edges.

The equilibrium temperature T of an IQH edge is related to the power J_E carried by its excitations according to [53]

$$J_E = \frac{(\pi k_B)^2}{6h} T^2. \tag{3.5}$$

In general J_E can also be calculated from the occupation $n(E)$ and chemical potential μ of an edge, by integrating the power:

$$J_E = \frac{1}{h}\int_0^{\mu} dE \cdot (\mu - E) \cdot (1 - n(E)) + \frac{1}{h}\int_{\mu}^{\infty} dE \cdot (E - \mu) \cdot n(E). \tag{3.6}$$

Here the first integral corresponds to the contribution of hole-like excitations, while the second integral corresponds to particle-like excitations. The 1D relation $g(E) \cdot v(E) = 1/h$ between the velocity $v(E)$ and density of states $g(E)$ was used to simplify the integrals.

Since the outgoing edges in our model have non-equilibrium distributions $n_{out}^{O3}(E)$ and $n_{out}^{O6}(E)$ immediately after the injection of current I, their respective energy currents are determined using equation 3.6. At a distance 20 μm from the QPC, the outgoing edges are in equilibrium. If no energy escapes from the edge as it equilibrates, equation 3.5 then provides a calculation of the expected edge temperatures. With the goal of ultimately finding these temperatures, we therefore consider the forms of the non-equilibrium edge distributions, which depend on the energy-dependent QPC transmission probability $\tau(E)$. This transmission is determined by the differential conductance dI/dV of the QPC, as follows:

$$I = \int_0^{\infty} dE \cdot \tau(E) \cdot (f_{in}^{O3}(E) - f_{in}^{O6}(E)). \tag{3.7}$$

Using τ and the distributions of the incoming edges (equation 3.4), we find expressions for the non-equilibrium distributions:

$$\begin{aligned} n_{out}^{O3} &= (1 - \tau) \cdot f_{in}^{O3} + \tau \cdot f_{in}^{O6} \\ n_{out}^{O6} &= (1 - \tau) \cdot f_{in}^{O6} + \tau \cdot f_{in}^{O3}. \end{aligned} \tag{3.8}$$

From these distributions we can then deduce the partitioning of power among the outgoing edges, as well as the outgoing equilibrium temperatures T_{out}^{O3} and T_{out}^{O6}. We find that each outgoing edge carries

an equal energy current. Conservation of energy provides a constraint on the total outgoing power:

$$I \cdot V - I^2(h/e^2) = \frac{(\pi k_B T_{out}^{O3})^2}{6h} + \frac{(\pi k_B T_{out}^{O6})^2}{6h} - \frac{(\pi k_B T_{base})^2}{3h}. \tag{3.9}$$

This relationship holds as long as the inner edges remain decoupled from the outermost edge modes. Here the left-hand side specifies the power dissipated by the QPC, while the right-hand side represents the net power carried away by edge excitations. The term $I^2(h/e^2)$ refers to energy dissipated at ohmic contacts, and does not contribute to heating the edge. For completeness, the distributions of the outgoing edges, 20 μm from the QPC, are given below:

$$\begin{aligned} f_{out}^{O3}(E) &= f(E - \mu_{out}^{O3}, T_{out}^{O3}) \\ f_{out}^{O6}(E) &= f(E - \mu_{out}^{O6}, T_{out}^{O6}), \end{aligned} \tag{3.10}$$

In Figure 3.12, numerical calculations of the outermost edge occupation functions are plotted during each stage of scattering at the QPC, for an applied voltage $V = 175$ μV and at bulk filling $\nu = 2$. In panel B, the incoming distributions are shown with the QPC transmission τ extracted from IV data. In panels C and D, the non-equilibrium and equilibrium distributions are plotted for outgoing edges on each side of the QPC. For the equilibrium outgoing distributions, we extract the temperatures T_{out}^{O3} and T_{out}^{O6} over a range of V to determine the dependence of edge temperatures on the QPC power $P_{QPC} = I \cdot V - I^2(h/e^2)$. As shown in Figure 3.13, our model qualitatively explains the cusp in temperature that is observed at $P_{QPC} = 0$.

Using this model, we expect the downstream quantum dot to measure a maximum temperature of 560 mK for $\nu = 2$ and 545 mK for $\nu = 3$. The actual observed maximum temperatures were 55 mK for $\nu = 2$ and 35 mK for $\nu = 3$. Although we observe no charge leakage to inner edge channels on a 20 μm scale, the loss of heat to inner edges is still possible and would decrease the expected temperatures. If all edges equilibrate thermally over a distance smaller than 20 μm, we expect that the power J_E carried by the outermost edge will be divided by the filling factor ν. Using equation 3.5, it follows that the temperature will be divided by $\nu^{1/2}$. For this type of thermal equilibration we thus expect to measure 395 mK for $\nu = 2$ and 315 mK for $\nu = 3$. Whether or not heat escapes to the inner edges, it is still clear from this analysis that in our experiment the majority of the power dissipated in the QPC does not find its way to the outermost edge.

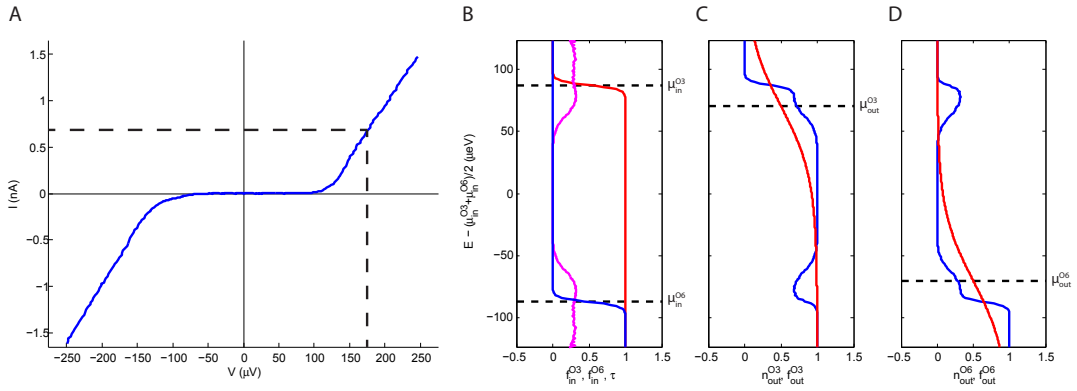

Figure 3.12: (A) The IV curve of the QPC at bulk filling $\nu = 2$. An applied voltage $V = 175\ \mu$V was used to calculate the distributions shown in (B-D). This voltage and the corresponding injected current are marked with dashed lines. **(B)** The QPC transmission probability τ, calculated from the QPC IV curve, is shown in magenta. In blue (red), the occupation f_{in}^{O6} (f_{in}^{O3}) of the incoming outer edge mode originating at ohmic contact O6 (O3). The chemical potentials differ by $eV = 175\ \mu$eV. **(C)** In blue, the non-equilibrium occupation n_{out}^{O3} of the outermost edge immediately after the injection of current through the QPC. This edge component carries charge toward O3. 20 μm from the QPC, the edge is in equilibrium with the distribution f_{out}^{O3}, shown in red. **(D)** The edge component carrying charge toward O6 has the non-equilibrium occupation n_{out}^{O6}, shown in blue, immediately after current is injected. 20 μm downstream the edge has equilibrated to the distribution f_{out}^{O6}, shown in red.

3.7 Bulk Heat Transport

As mentioned in the main text and Section 3.6, we observe temperatures well below what is expected for a system of quantum Hall edges with no energy dissipation. This necessarily means that heat diffuses out of the edges into additional modes in either the bulk of the 2D electronic system or the surrounding crystalline solid. Because we see a bulk contribution to heating when the bulk is at $\nu = 1$ (Columns III and IV of Fig. 3.3), but not when the bulk is at $\nu = 2$ or $\nu = 3$ (Columns I and II), and because we don't expect a change of magnetic field to significantly affect heat conduction through the solid, we can attribute the heating at high fields to the $\nu = 1$ electronic system. While we don't know the mechanism of this bulk heat transport in such a strongly insulating state, we suspect it may be associated with low energy spin degrees of freedom that exist at $\nu = 1$.

The presence of this bulk heat transport in the two measurements where we see upstream heat transport attributed to edges requires some additional discussion.[1] Specifically, we need to rule out the possibility that turning our deflectors on and off affects the quantity of heat transported by the

[1] In the sharp-edged sample discussed in Section 3.4, bulk heating is present without additional edge heating at 6.2 T.

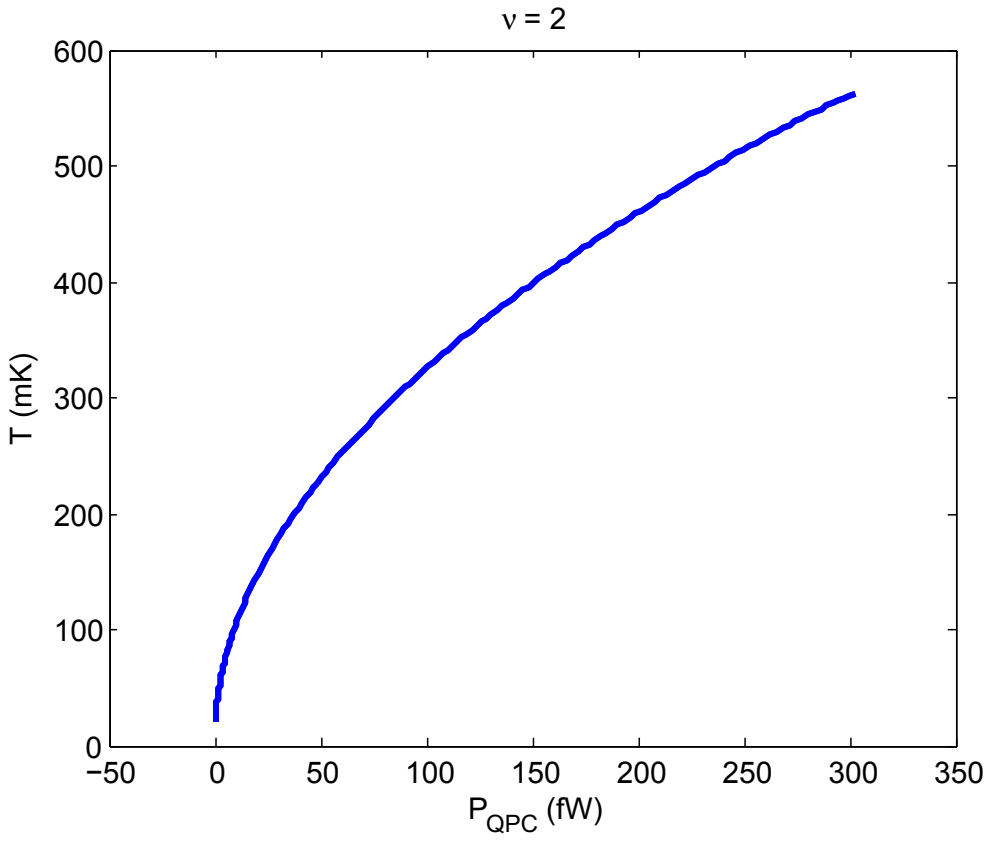

Figure 3.13: Expected equilibrium temperatures of the outgoing outermost edges, calculated using the measured QPC transmission τ at $\nu = 2$. Both outgoing edges are expected to have the same temperature. The $\nu = 3$ data give the same temperature as a function of QPC power.

bulk to the thermometers, thereby producing a signal unrelated to edge heat transport. Below we describe two experiments specifically designed to address this possibility. Our findings provide two important observations. Firstly, our gates are not completely effective at preventing the flow of heat, matching observations in [58]. We inferred this from the shape of our Coulomb blockade peaks, and checked it explicitly by attempting to block heat flow with a gate. Secondly, if we reduce the length of the deflector gates to the point where there is much less bulk $\nu = 1$ region for heat to diffuse upwards into when the deflectors are off, we observe the same qualitative and quantitative behavior that was presented in the main body of the paper. Both of these observations are discussed more carefully below.

I. Diffusion of heat through gated regions

When our topgates are energized to completely deplete carriers from the underlying 2D electron system, we would expect that energy can no longer be transported by that system. However, heat that manages to diffuse into the lattice can still propagate. Here we will present data suggesting that some heat does indeed diffuse across the depleted regions.

The first indication that such diffusion is taking place can be seen in the form of our Coulomb blockade peaks. The fits we used in the experiment assume that the temperatures of the two quantum dot leads are identical. However, since we are only explicitly heating one side of the dot, a simple model suggests that we should expect leads with different temperatures. This temperature asymmetry should show up as an increased kurtosis in the CB peak shape. In Figure 3.14, we show the one-temperature fit that was used in the main body of this paper along with two alternatives that allow for asymmetric lead temperatures. This particular peak corresponds to the downstream measurement at a magnetic field of 6.2 T and an injected power of 274 fW. The deflector gates are energized, so this peak includes both edge and bulk contributions.

Figure 3.14b presents an alternative fit with an additional fit parameter that allows for different temperatures in the two leads. While the one-temperature fit suggests lead temperatures of 51 mK, the two temperature fit suggests that one of the leads is hotter (60 mK) and the other is colder (39 mK). However, even though the fits are consistently better with the extra parameter, the residuals are not systematically cleaner. Figure 3.15 presents a comparison of the one-temperature and two-temperature fits for the entire range of injected powers that we studied. Below 50 fW of injected power, the one-temperature and two-temperature fits agree exactly, suggesting equal temperature leads. At higher powers, the two temperature fit does suggest a difference in the lead temperatures. Even this asymmetry, however, has to be considered carefully. Because there are nearby peaks (roughly 800 mK away

from the peak center, when translated from gate voltage as in Figure 3.14), at high temperatures we can expect them to artificially distort our peak and increase the quality of an asymmetric-temperature fit.

Figure 3.14c presents yet another fit which assumes that the cold lead has the naively expected temperature of 20 mK, corresponding to the observed base temperature for electrons with no intentional heating. The temperature of the hot lead is allowed to vary. With this constraint, the best fit suggests a hot lead temperature of 59 mK. Here, however, the residuals have a pronounced trend that persists for all fits with the 20 mK constraint.

Without strong evidence that a two-temperature fit better describes our measurements, we opted to use a single-temperature fit for the main data presented. None of the qualitative observations of bulk heat transport or upstream heat transport by a neutral edge mode are affected by using the hotter temperature from two-temperature fits. Furthermore, the two-temperature fit doesn't solve the temperature deficiency alluded to in the main text or Section 3.6.

We can go further and explicitly test for heat transport across depleted regions by placing a strip of such a region between our heater and our thermometers, as in the device pictured in Figure 3.16. Any heat detected at the thermometers would necessarily have to diffuse through the depleted region beneath the vertical gates. Results of this test are depicted in Figure 3.17. Here, we can clearly see that some heat flows through these narrow depleted regions. At the highest injected power, we see the temperature rise from 20 mK to 28 mK with an uninterrupted 2D and a temperature rise to 22 mK with the 2D depleted beneath the vertical gates. This small heat diffusion through gated regions is qualitatively consistent with our observation of heating in the cold leads of our quantum dots, as mentioned above. The fact that the temperature is reduced from the ungated value (22 mK versus 28 mK) provides additional evidence that the 2D electron system is responsible for the observed bulk heat transport at high fields.

II. Geometric Diffusion Considerations

Because we only detect neutral mode heating when there is a bulk contribution to the heating signal, we have to ensure that there is no significant change in the bulk contribution as we energize and deenergize the deflector gate. It would appear plausible, for instance, that by turning on the deflector gate we reduce the area over which the bulk heat can diffuse. Specifically, with the deflector gate on, heat can no longer diffuse up into the 2D region between our heater and our thermometers. As a result, one may conjecture that more heat will be directed towards the thermometers resulting in a higher temperature unassociated with quantum Hall edge physics. The first indication that this redirection of heat isn't relevant is the above observation (from CB peak shapes and direct measurements) that heat

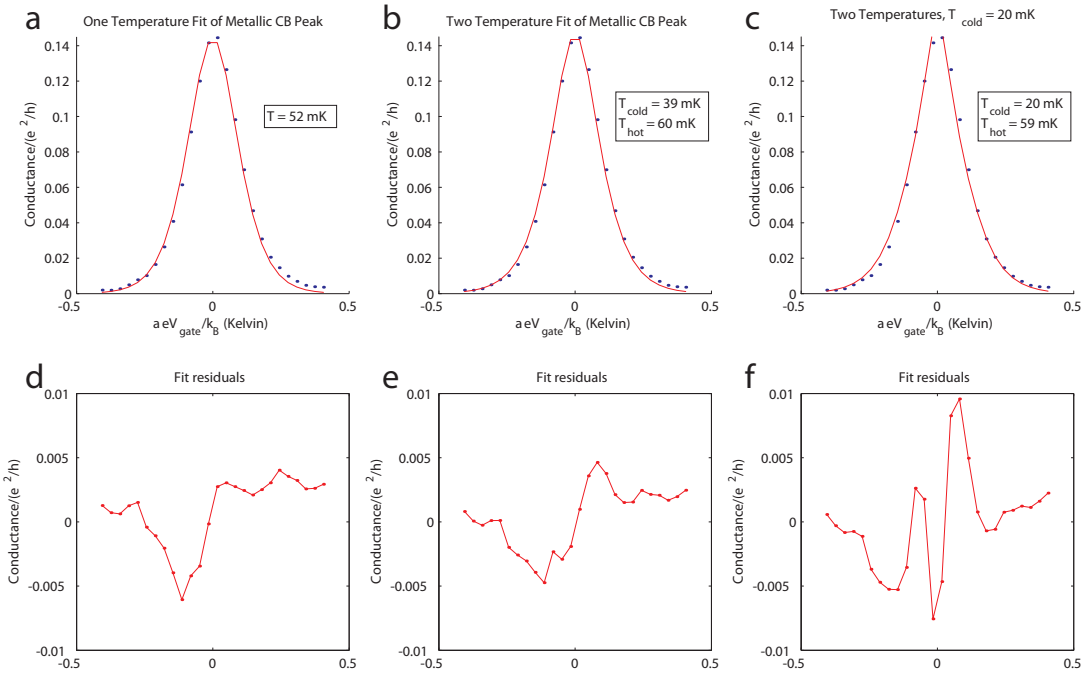

Figure 3.14: (a) One temperature fit of the CB peak seen downstream at 6.2 T and 274 mW of injected power. The deflector gates are energized, so this peak includes both edge and bulk contributions. Additional peaks are centered roughly 800 mK to the left and right of the center of this peak. **(b)** Fit obtained by adding an additional parameter allowing for asymmetric lead temperatures. There is no systematic improvement in the residual trend by using such a fit (though the quality of fit obviously improves slightly). **(c)** Fit obtained using the same form as panel b, but fixing the cold lead to a 20 mK distribution. This produces a low quality of fit and certainly doesn't describe our data well. **(d,e,f)** Fit residuals plotted below the associated fit.

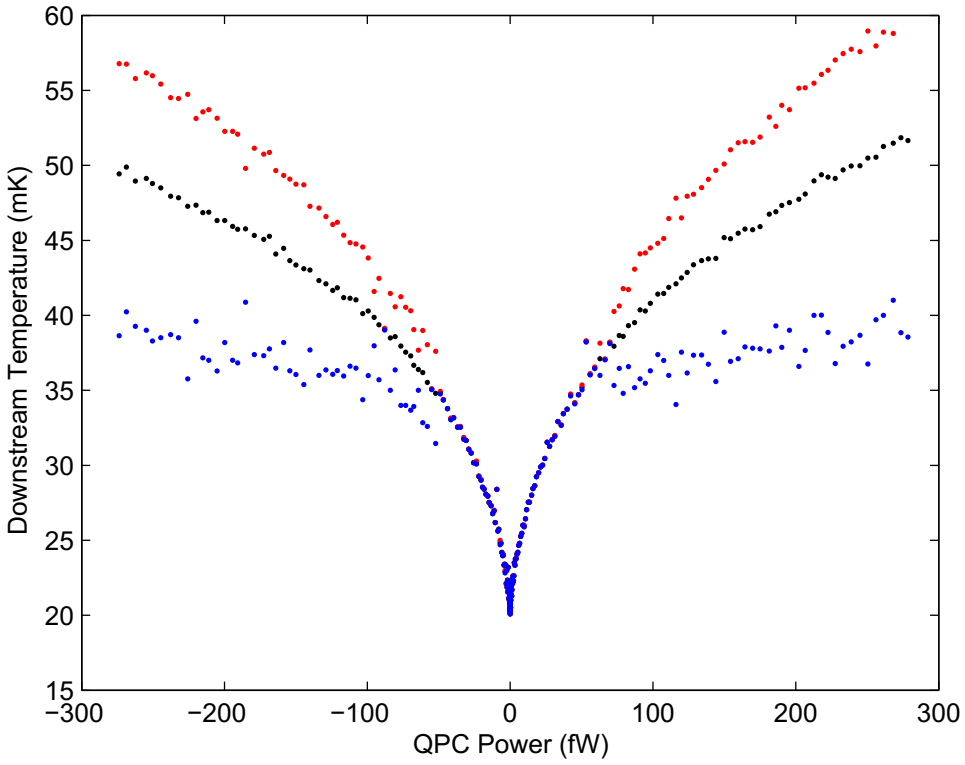

Figure 3.15: Temperature fit of the CB peak seen downstream at 6.2 T as a function of injected power. Black denotes the one-temperature fit (as in Figure 3.14a), and red and blue denote the hot and cold temperatures of a two-temperature fit (as in Figure 3.14b). They agree perfectly at low injected powers, but begin to diverge beyond 50 fW.

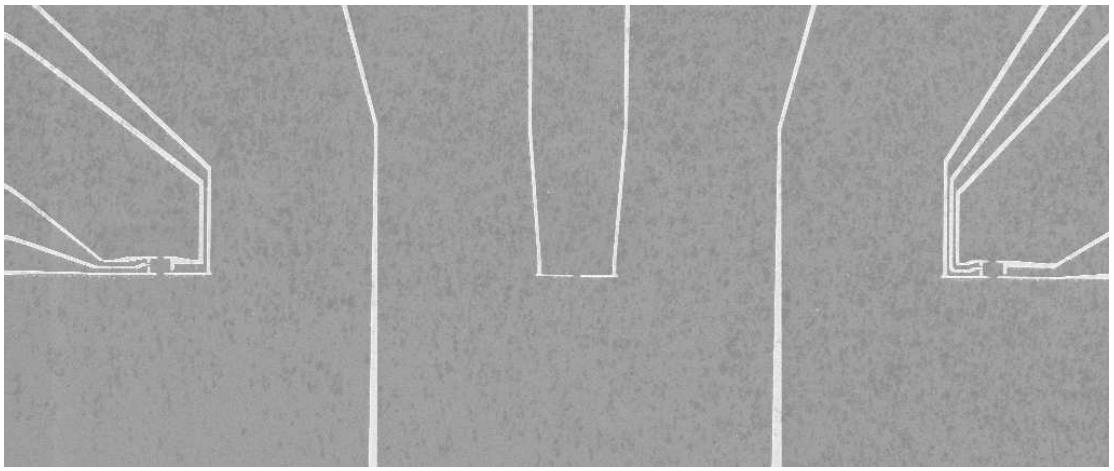

Figure 3.16: Device designed to explicitly test for heat leakage across a depleted barrier. When the vertical gates are energized, the 2D systems on the left and right are completely isolated (electrically) from the 2D system with the heater in the center.

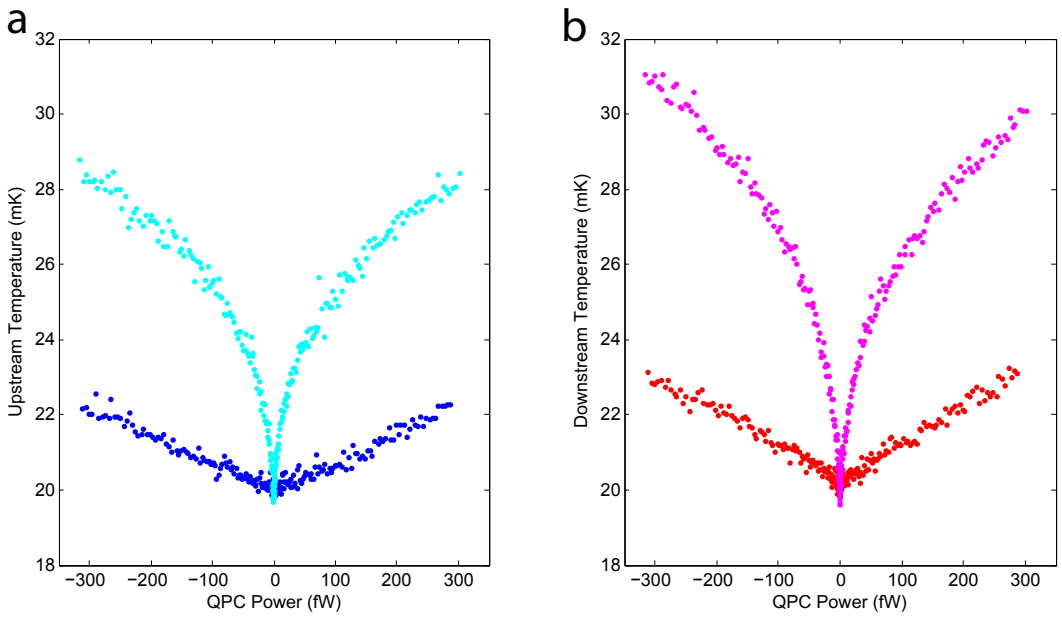

Figure 3.17: Heat transport across a depleted barrier. The cyan curve depicts temperature measured upstream from the heater when the vertical gates are deenergized. The blue curve depicts the temperature when the vertical gate is energized, so heat must diffuse across a depleted region. The magenta and red curves are the corresponding traces for the downstream dot. All data was taken at 8.3 T, corresponding to column IV in Fig. 3.3.

does indeed partially diffuse through depleted regions. A more convincing test, however, consists of altering the geometry of the bulk to reduce the effect of this geometric distortion.

To this end, consider the device shown in Figure 3.18b. It is identical to the devices used for measurements in the main body of the paper, but with a shorter deflector gate length (8 μm instead of 15 μm). At 8.3 T, we expect an edge structure as shown in Figure 3.18, with two separated edges: one corresponding to the boundary between vacuum and $\nu = \frac{2}{3}$ and the other corresponding to the boundary between $\nu = \frac{2}{3}$ and $\nu = 1$, as $\nu = 1$ is the bulk filling factor and $\nu = \frac{2}{3}$ is the edge that we detect with our local injection measurements. In the 8 μm deflector device, with the deflector de-energized, we measure a slightly elevated resistance ($1.19\, R_K$), indicating that the inner edge corresponding to the transition from $\nu = \frac{2}{3}$ to $\nu = 1$ is being backscattered (transmission coefficient of 52% for that inner edge). This indicates that the $\nu = 1$ bulk is largely closed off in this deflected region, so we would expect very little bulk heat to diffuse upwards through this narrow constriction. If the difference in upstream heating displayed in Figure 3.3(IV) of the main paper is due to a redirection of bulk heat flow, we would expect almost the same difference between the temperature measured in the 15 um deflector device (Figure 3.18a) and the 8 um deflector device (Figure 3.18b).

The data from these measurements are presented in Figure 3.19. The blue and red points correspond to temperatures measured in the device from Figure 3.18a with deflectors off. The cyan and magenta points correspond to temperatures measured in the device from Figure 3.18b, also with deflectors off. These undeflected temperatures in the two devices are very close, to within the data spread. For reference, the temperature associated with turning on the deflectors (which results in the same geometry for the two devices) is displayed in green and orange.

From these, we can infer that the excess temperature found in the green and orange traces is indeed associated with a hot $\nu = \frac{2}{3}$ edge, as this edge is the only component of the system that is significantly altered as deflector gates are turned on in the device from Figure 3.18b.

In Section 3.4, we present yet another device, where the gate-defined edge is replaced by a sharp mesa-defined edge. If the excess upstream heat was due to a redirection of bulk heating, we would expect an elevated temperature in that situation, given that the device possesses a nearly identical bulk geometry compared with the gate-defined edge. Here, however, we don't see any heat associated with the edge at 6.2 T (Fig. 3.13a). This provides even further evidence that the observed upstream heat is due to FQH edge structure and is independent of the measured bulk heat transport at $\nu = 1$.

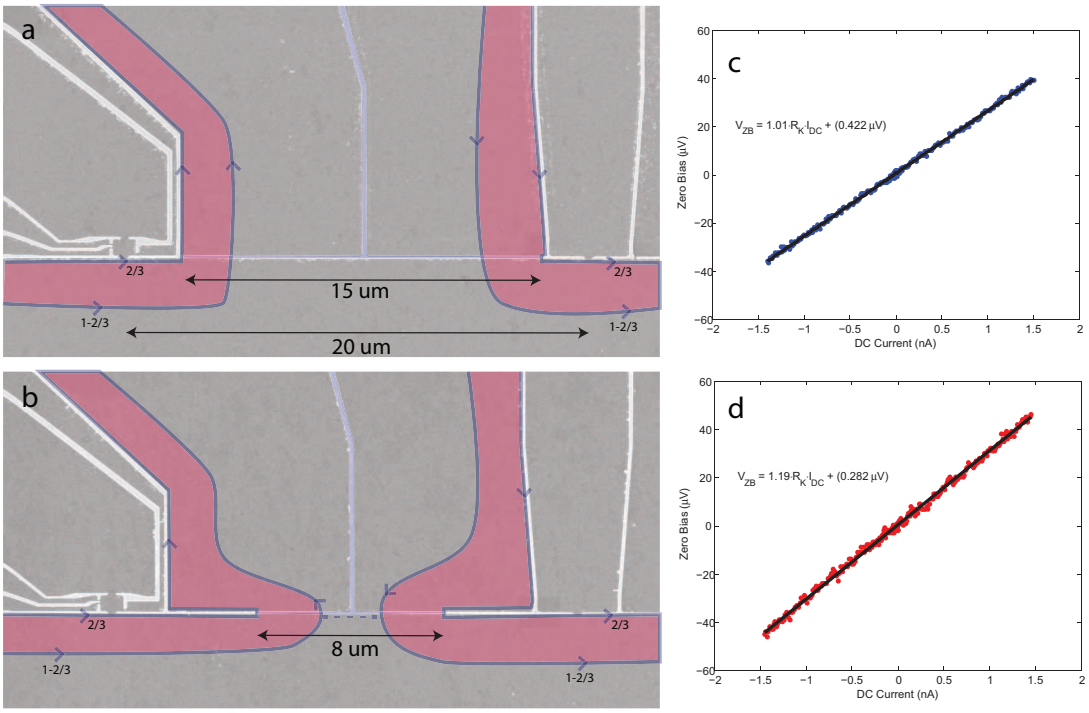

Figure 3.18: A device to test the effect of geometric diffusion considerations. **(a)** SEM image of device identical to that used for data in the main paper. Edge labels correspond to what is expected at a field of 8.3 T, based on our local and global R_{xy} measurements. **(b)** SEM image of a device with a narrower region through which edges can be deflected. From the elevated resistance shown in panel d, we know that the inner edge is partially backscattered. **(c)** Copy of the ΔV_{ZB} versus I_{DC} curve from Fig. 3.7, demonstrating that the resistance in the deflector channel is the same as the bulk value ($1.01R_K$), indicating that the $\nu = 1$ state is fully connected from the top to the bottom of the image in panel a. **(d)** A corresponding ΔV_{ZB} versus I_{DC} curve for the device in panel b. The elevated resistance ($1.19R_K$) indicates that the inner edge, which has a conductance of $\frac{e^2}{3h}$ is 52% transmitted. This suggests that the $\nu = 1$ state is connected through a narrow channel in this device, providing much less room for heat to diffuse upwards compared to the device in panel **a**.

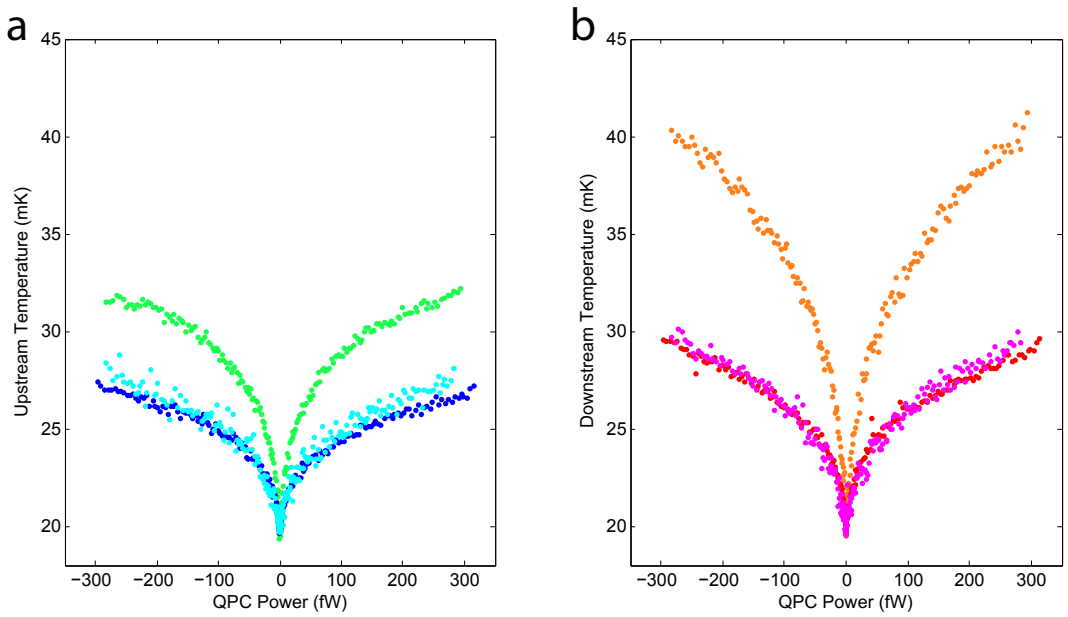

Figure 3.19: The blue and red points correspond to temperatures measured in the device from Fig. 3.18a with deflectors off. The cyan and magenta points correspond to temperatures measured in the device from Fig. 3.18b, also with deflectors off. These undeflected temperatures in the two devices are very close, to within the data spread. For reference, the temperature associated with turning on the deflectors (which results in the same geometry for the two devices) is displayed in green and orange. From this we can conclude that the observed upstream heating is not due to a redirection of bulk heating upon energizing of deflector gates. **a)** Upstream. **b)** Downstream.

3.8 Length Dependence of R_L

If two separated co-propagating edge channels are filled to different chemical potentials, we expect charge to slowly equilibrate between them. By varying the length between injector (the central QPC), and detector (a downstream QPC), we can learn how this equilibration takes place.

Data from 3 separate samples, all from the same wafer, are shown in Figure 3.20. At 6.2 T, R_L is always found to be quantized to 1 (though it isn't so clear for the 1 μm device due to large conductance fluctuations). Focusing on data from sample 3 only, we see that a transition from $R_L = 1$ to $R_L = 3/2$ occurs at 7.2 T, for lengths between 10 μm and 40 μm. The fact that all the R_L curves from sample 3 lie on top of each other indicates that the edges can maintain different chemical potentials over 10s of microns without equilibrating.

The slightly higher transition field for sample 1 (20 μm) compared to sample 3 is likely due to a slightly different density frozen in beneath the gates during sample cooldown. From the difference in transition fields (7.2 T versus 7.6 T) we can estimate that there is 5% more density frozen in near the gates in sample 1 compared to sample 3. Bulk R_{xy} values do not vary by such a large amount between samples in this wafer.

3.9 Molecular Beam Epitaxy Information

All samples used in this experiment were obtained from the wafer LP 11-18-08.1, grown at Bell Laboratories in Murray Hill, NJ, by Loren Pfeiffer and Kenneth West. Figure 3.21 has the details of the growth.

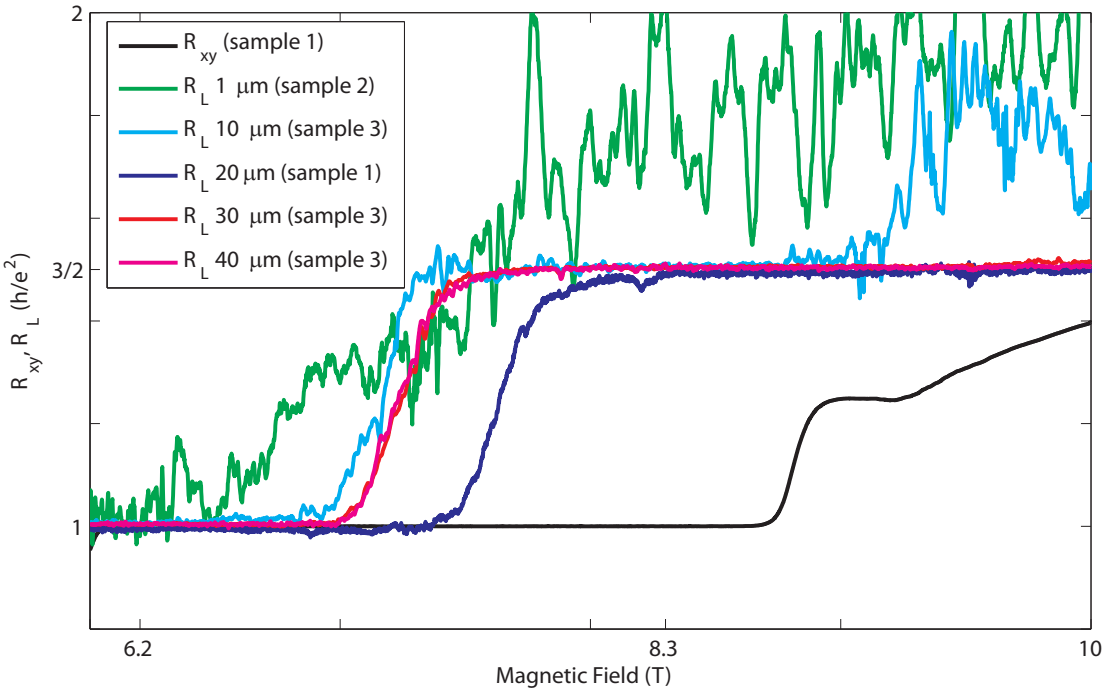

Figure 3.20: Length dependence of R_L using data obtained from 3 different samples. No evidence of charge equilibration is observed over 10s of microns.

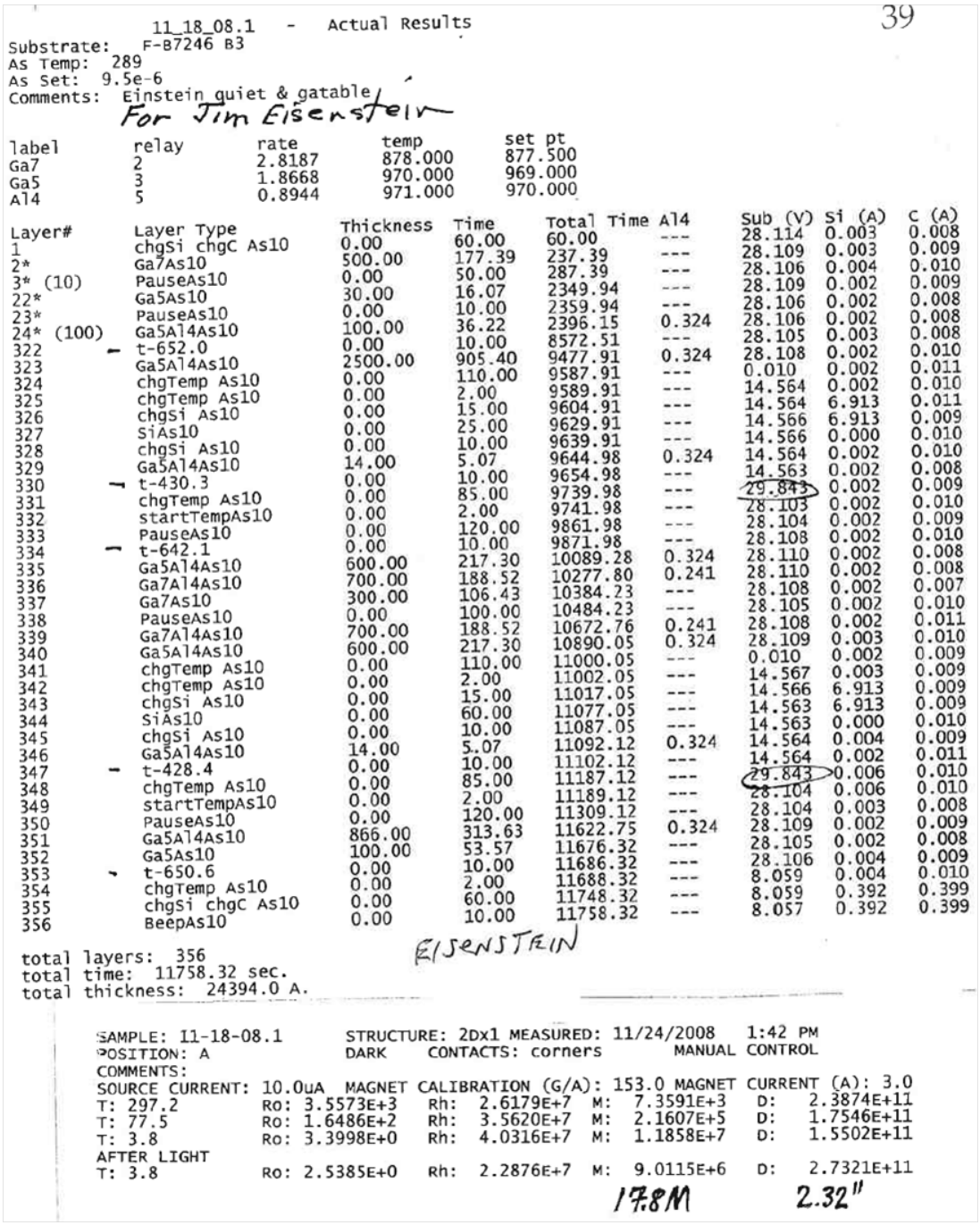

11_18_08.1 - Actual Results

39

Substrate: F-B7246 B3
As Temp: 289
As Set: 9.5e-6
Comments: Einstein quiet & gatable
For Jim Eisenstein

label	relay	rate	temp	set pt
Ga7	2	2.8187	878.000	877.500
Ga5	3	1.8668	970.000	969.000
Al4	5	0.8944	971.000	970.000

Layer#	Layer Type	Thickness	Time	Total Time	Al4	Sub (V)	Si (A)	C (A)
1	chgSi chgC As10	0.00	60.00	60.00	---	28.114	0.003	0.008
2*	Ga7As10	500.00	177.39	237.39	---	28.109	0.003	0.009
3* (10)	PauseAs10	0.00	50.00	287.39	---	28.106	0.004	0.010
22*	Ga5As10	30.00	16.07	2349.94	---	28.109	0.002	0.009
23*	PauseAs10	0.00	10.00	2359.94	---	28.106	0.002	0.008
24* (100)	Ga5Al4As10	100.00	36.22	2396.15	0.324	28.106	0.002	0.008
322	t-652.0	0.00	10.00	8572.51	---	28.105	0.003	0.008
323	Ga5Al4As10	2500.00	905.40	9477.91	0.324	28.108	0.002	0.010
324	chgTemp As10	0.00	110.00	9587.91	---	0.010	0.002	0.011
325	chgTemp As10	0.00	2.00	9589.91	---	14.564	0.002	0.010
326	chgSi As10	0.00	15.00	9604.91	---	14.564	6.913	0.011
327	SiAs10	0.00	25.00	9629.91	---	14.566	6.913	0.009
328	chgSi As10	0.00	10.00	9639.91	---	14.566	0.000	0.010
329	Ga5Al4As10	14.00	5.07	9644.98	0.324	14.564	0.002	0.010
330	t-430.3	0.00	10.00	9654.98	---	14.563	0.002	0.008
331	chgTemp As10	0.00	85.00	9739.98	---	29.843	0.002	0.009
332	startTempAs10	0.00	2.00	9741.98	---	28.103	0.002	0.010
333	PauseAs10	0.00	120.00	9861.98	---	28.104	0.002	0.009
334	t-642.1	0.00	10.00	9871.98	---	28.108	0.002	0.010
335	Ga5Al4As10	600.00	217.30	10089.28	0.324	28.110	0.002	0.008
336	Ga7Al4As10	700.00	188.52	10277.80	0.241	28.110	0.002	0.008
337	Ga7As10	300.00	106.43	10384.23	---	28.108	0.002	0.007
338	PauseAs10	0.00	100.00	10484.23	---	28.105	0.002	0.010
339	Ga7Al4As10	700.00	188.52	10672.76	0.241	28.108	0.002	0.011
340	Ga5Al4As10	600.00	217.30	10890.05	0.324	28.109	0.003	0.010
341	chgTemp As10	0.00	110.00	11000.05	---	0.010	0.002	0.009
342	chgTemp As10	0.00	2.00	11002.05	---	14.567	0.003	0.009
343	chgSi As10	0.00	15.00	11017.05	---	14.566	6.913	0.009
344	SiAs10	0.00	60.00	11077.05	---	14.563	6.913	0.009
345	chgSi As10	0.00	10.00	11087.05	---	14.563	0.000	0.010
346	Ga5Al4As10	14.00	5.07	11092.12	0.324	14.564	0.004	0.009
347	t-428.4	0.00	10.00	11102.12	---	14.564	0.002	0.011
348	chgTemp As10	0.00	85.00	11187.12	---	29.843	0.006	0.010
349	startTempAs10	0.00	2.00	11189.12	---	28.104	0.006	0.010
350	PauseAs10	0.00	120.00	11309.12	---	28.104	0.003	0.008
351	Ga5Al4As10	866.00	313.63	11622.75	0.324	28.109	0.002	0.009
352	Ga5As10	100.00	53.57	11676.32	---	28.105	0.002	0.008
353	t-650.6	0.00	10.00	11686.32	---	28.106	0.004	0.009
354	chgTemp As10	0.00	2.00	11688.32	---	8.059	0.004	0.010
355	chgSi chgC As10	0.00	60.00	11748.32	---	8.059	0.392	0.399
356	BeepAs10	0.00	10.00	11758.32	---	8.057	0.392	0.399

EISENSTEIN

total layers: 356
total time: 11758.32 sec.
total thickness: 24394.0 A.

SAMPLE: 11-18-08.1 STRUCTURE: 2Dx1 MEASURED: 11/24/2008 1:42 PM
POSITION: A DARK CONTACTS: corners MANUAL CONTROL
COMMENTS:
SOURCE CURRENT: 10.0uA MAGNET CALIBRATION (G/A): 153.0 MAGNET CURRENT (A): 3.0

T: 297.2	Ro: 3.5573E+3	Rh:	2.6179E+7	M:	7.3591E+3	D:	2.3874E+11
T: 77.5	Ro: 1.6486E+2	Rh:	3.5620E+7	M:	2.1607E+5	D:	1.7546E+11
T: 3.8	Ro: 3.3998E+0	Rh:	4.0316E+7	M:	1.1858E+7	D:	1.5502E+11
AFTER LIGHT							
T: 3.8	Ro: 2.5385E+0	Rh:	2.2876E+7	M:	9.0115E+6	D:	2.7321E+11

17.8M 2.32"

Figure 3.21: Wafer Structure: LP 11-18-08

4

The quantum spin Hall effect in HgTe quantum wells

4.1 The quantum spin Hall effect

The integer quantum Hall effect (IQHE) is the prototypical example of a system which insulates in the bulk and carries gapless edge excitations. The IQHE occurs when a large magnetic field is applied perpendicular to the plane of a two-dimensional electron gas. The bulk of the system then develops a gap due to the quantization of kinetic energy into Landau levels. At the edges of the system, the confining potential bends these levels to higher energy. Levels which are completely filled with electrons in the bulk will necessarily intersect the chemical potential at the edge, forming gapless one-dimensional channels [41]. These channels carry charge chirally around the system with a quantized conductance of e^2/h per channel. A measurement of the Hall conductance σ_{xy} will therefore be quantized to Ne^2/h, where N is the number of edge channels.

The chiral nature of edge channels in the IQHE strongly suppresses backscattering, which would require electrons to tunnel through the incompressible bulk of the sample. This means that charge carriers can be carried along IQH edges essentially without dissipating energy, a very appealing technological prospect. Less appealing is the need for a strong magnetic field in order to discretize the density of states into energetically separated Landau levels. It is difficult to see how to obtain an analogous

situation to the IQHE without the need for an external magnetic field.

A breakthrough in this respect came from viewing materials with a bulk energy gap (insulators) from the perspective of topology [45]. In this approach, two insulators are said to be topologically equivalent if it is possible to continuously tune between their Hamiltonians without closing the energy gap. Insulators which are topologically equivalent to the vacuum are referred to as trivial insulators. Early on, Thouless, Kohmoto, Nightingale, and den Nijs came to the important conclusion that the IQHE is topologically distinct from the vacuum and is characterized by a topological invariant called the Chern invariant N [112]. This Chern invariant is the same as the number of edge channels at the boundary of the system, and cannot change under smooth variations of the system Hamiltonian. The Chern number also embodies a unifying feature of the topological insulators known as the bulk boundary correspondence. This correspondence relates the topology of a bulk insulator to the presence of gapless modes at the boundary. In other words, both the topology and the number of edge channels are described by a single unifying quantum number. The bulk-boundary correspondence also implies that gapless conducting states will always exist at interfaces between two insulators where the topological invariant changes.

Within this powerful framework a myriad of topological states distinct from the IQHE become possible to envision [60, 101, 105, 106]. In the vein of searching for a zero magnetic field analogue to the IQHE, we focus now on one of these states in particular: the Z_2 topological insulator, also known as the quantum spin Hall (QSH) insulator[55, 75][1]. This insulating state is characterized by a Z_2 topological invariant which counts the number of stable gapless edge states modulo 2. When the topological invariant is 0, the system is in the topologically trivial state. A topological invariant of 1 corresponds to the quantum spin Hall insulator.

The quantum spin Hall insulator is a two-dimensional state of matter with an energy gap in the bulk (Figure 4.1). It is a time-reversal symmetric state, which hosts gapless edge channels due to its nontrivial topology. Due to the time-reversal symmetry, these edge channels circulate in opposite directions and carry opposite spin. In this sense, the quantum spin Hall insulator is roughly similar to two copies of the $\nu = 1$ IQHE effect, with one copy for each spin. In a perfect system with no electron-electron interactions, as long as time-reversal symmetry is preserved the counterpropagating channels at any given edge are prevented from backscattering.

Theoretical work on obtaining a nontrivial Chern number without an external magnetic field was first done by Haldane in 1988 [40]. Following that there were several theoretical proposals to measure the QSH effect either in graphene [54] or in strained semiconductors [11], but these were both pro-

[1] Recently, another two-dimensional topological insulator, the quantum anomalous Hall insulator, has been experimentally measured under zero external magnetic field [19].

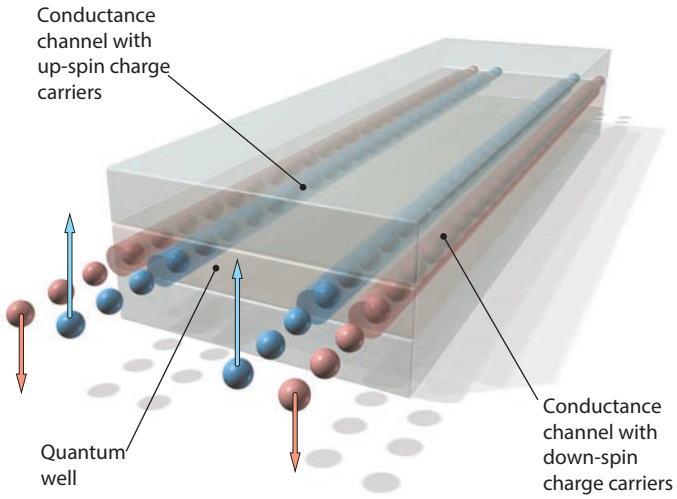

Figure 4.1: The quantum spin Hall effect, from [62].

hibitively difficult experimentally [75, 83, 129]. The first experimentally feasible scheme for realizing the quantum spin Hall insulator came in 2006, when Bernevig, Hughes, and Zhang predicted that this state should appear in quantum wells made of HgTe/HgCdTe [12]. In addition to the quantum spin Hall effect, the unconventional band structure of HgTe leads to interesting electronic behavior even outside of the quantum spin Hall state. We will explore the origins and consequences of these effects in the following sections and chapters.

4.2 Band structure of (Hg,Cd)Te quantum wells

4.2.1 General properties of bulk HgTe and CdTe

In order to understand how a HgTe/HgCdTe quantum well can become a quantum spin Hall insulator, we should first examine the bulk properties of the underlying HgTe and CdTe crystals. Both of these bulk materials have the zinc-blende lattice structure. Near the Fermi level, the important bands in each material are the s-type Γ_6 band and the p-type band which spin-orbit coupling splits into a $J = 3/2, \Gamma_8$ band and a $J = 1/2, \Gamma_7$ band. The 8-band Kane model, derived from $\mathbf{k} \cdot \mathbf{p}$ perturbation theory, approximately determines the structure of these bands near the $\Gamma-$point. The band structure of both HgTe and CdTe near the $\Gamma-$point is shown in Figure 4.2. The band ordering in CdTe is typical of zinc-blende semiconductors, with the $s-$like conduction band at higher energy than the $p-$like valence band [127].

Replacement of Cd with Hg drastically modifies the band structure. In contrast with Cd, Hg has

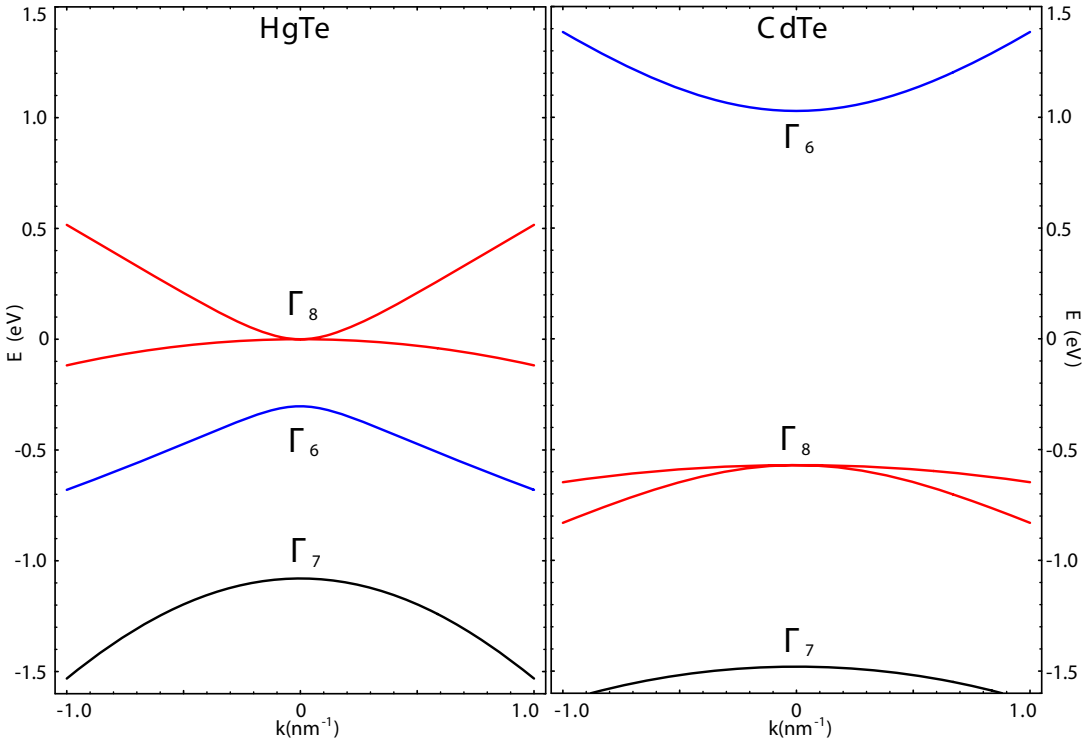

Figure 4.2: The bulk band structure of HgTe and CdTe, near the Γ point, from [63]. The band ordering in CdTe follows the normal progression of bands for zinc-blende semiconductors, with the $s-$like Γ_6 band at higher energy than the $p-$like Γ_7 and Γ_8 bands. By contrast, the band ordering in HgTe is inverted, with the Γ_8 bands at higher energy than the Γ_6 band.

many occupied shallow 5d levels which tend to be spatially delocalized, leading to a large effective positive nuclear charge [131]. This large effective charge most strongly modifies the energy of $s-$like states originating in the Hg, thus lowering the Γ_6 band below the Γ_8 band. With a negative energy gap of -300 meV, such an unusual band ordering is often referred to as an inverted band structure[2].

4.2.2 Bulk electronic properties of HgTe quantum wells

Due to its inverted band structure, one might anticipate that a quantum well based around HgTe should have some fairly unique properties. This is in fact the case, and in the following sections we will explore an array of interesting consequences for the electronic structure that directly arise from band inversion.

Before delving into the detailed peculiarities of HgTe quantum wells, however, an heuristic overview is beneficial. To that end, when a layer of HgTe is sandwiched on either side by CdTe, the resulting spectrum of energy levels is to a large extent determined by the interplay between bulk band structure and the zero point motion resulting from confinement. Within this picture there are then two basic behaviors which are controlled by the width d of the HgTe layer, as shown in Figure 4.3. If d is sufficiently large, we can expect that the confinement energy will be small enough that the quantum well subbands remain inverted, as in bulk HgTe. As d becomes smaller, the confinement energy increases, pushing the subbands closer together until at a critical thickness d_C the bands touch. For thicknesses $d < d_C$, the band structure will then be 'uninverted.' With these basic considerations, we can expect that the quantum well thickness d should be a powerful experimental input for tuning between inverted and uninverted regimes, and that wells thicker than a critical thickness should have interesting electronic properties associated with an inverted band structure.

To describe the above scenario quantitatively requires a model with at least four bands (including spin). The four-band model proposed by Bernevig, Hughes, and Zhang succeeds in describing the most interesting behaviors of this system, including the band inversion and topological phase transition. Their model can be derived perturbatively using $\mathrm{k}\cdot\mathrm{p}$ theory, and its form can be deduced by considerations of both symmetry and energy.

In reducing the 8-band Kane model down to the BHZ model, the bulk split-off Γ_7 band is neglected, since it has only small effects on the quantum well band structure[3]. There are then six remaining bands which combine to form the opposite-spin states of three sets of subbands, labeled E

[2] Although there is an energy gap between the Γ_6 and Γ_8 bands, HgTe is a semi-metal. This is due to the degeneracy between the heavy- and light-hole bands at the Γ point.

[3] The contribution of the Γ_7 band to the quantum well energies is $< 5\%$.

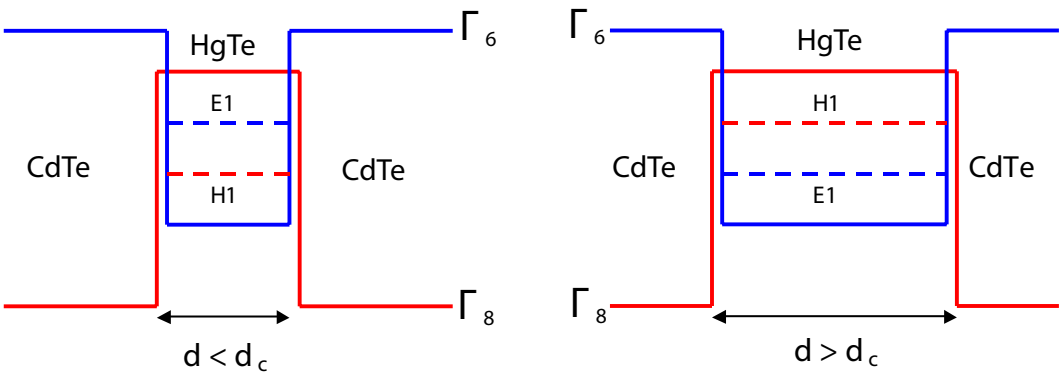

Figure 4.3: Schematic diagrams of energy levels in quantum wells formed by a layer of HgTe sandwiched on each side by CdTe, from [12]. The ordering of energy levels inside the quantum well is tuned by the well thickness d. When the thickness d is larger than a critical thickness d_C, the energy levels in the well are inverted. As the thickness d becomes smaller, zero point motion in the well becomes more pronounced. Eventually when $d < d_C$, the band ordering switches.

(electron-like), H (heavy hole-like), and L (light hole-like) [93]. Since the L bands are separated energetically by ≈ 100 meV from the other bands, they are neglected, leaving only the E and H bands.

There is good reason not to neglect these E and H bands, and in particular the first subbands $E1$ and $H1$. At the Γ point with zero in-plane momentum, the $|E1, m_J\rangle$ state is formed from a linear combination of the $|\Gamma_6, m_J = \pm 1/2\rangle$ and $|\Gamma_8, m_J = \pm 1/2\rangle$ states. Because the $E1$ state then has angular momentum $1/2$, it is analogous to states which normally form the conduction band in a two-dimensional electron system (hence the designation as 'electron-like'). Under these same conditions, the $|H1, m_J\rangle$ state is formed from the $|\Gamma_8, m_J = \pm 3/2\rangle$ state. With angular momentum $3/2$, the $H1$ state is similar to states which normally form the valence band, and is referred to as 'hole-like.' The energies of these states, calculated using k · p theory, are shown in Figure 4.4 as a function of the quantum well thickness [89, 93]. Near a critical well thickness, $d_C = 6.3$ nm, we see that the electron-like $E1$ state crosses the hole-like $H1$ state, as anticipated from the heuristic discussion above.

By considering the symmetry properties of the $E1$ and $H1$ states, Bernevig, Hughes, and Zhang arrived at their model for the behavior of the $E1$ and $H1$ states near the critical well thickness. Written in the basis $|E1, m_J = +1/2\rangle$, $|H1, m_J = +3/2\rangle$, $|E1, m_J = -1/2\rangle$, and $|H1, m_J = -3/2\rangle$, the Hamiltonian is:

$$H_{\text{BHZ}} = \begin{pmatrix} H(k) & \\ & H^*(-k) \end{pmatrix}, \; H = \epsilon(k) + d_i(k)\sigma_i, \text{ where} \tag{4.1}$$

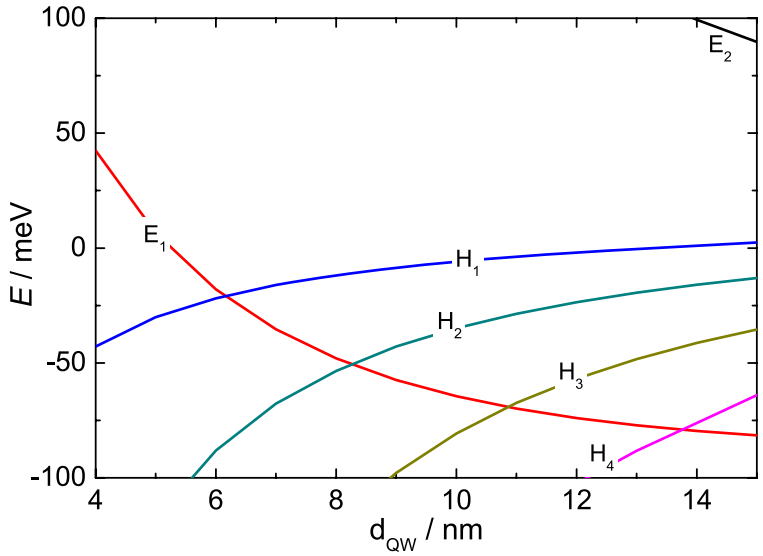

Figure 4.4: Evolution of electron- and hole-like energy levels in HgTe quantum wells, as a function of the quantum well thickness d, from [63]. In this plot the in-plane wave vectors $k_x = k_y = 0$. At the critical thickness $d_C = 6.3$ nm, the $E1$ and $H1$ bands cross. For wells thinner than 6.3 nm, the bands are ordered normally, with electron-like bands at higher energy than hole-like bands. For wells thicker than 6.3 nm, the band ordering inverts.

$$d_1 + id_2 = A(k_x + ik_y), \tag{4.2}$$

$$d_3 = M - B\left(k_x^2 + k_y^2\right), \text{ and} \tag{4.3}$$

$$\epsilon = C - D\left(k_x^2 + k_y^2\right). \tag{4.4}$$

The most important parameter in this model is the mass term M, which changes sign at the critical well thickness d_C and gives the energy difference between the $E1$ and $H1$ bands at zero in-plane wave vector. Using this model and the parameters listed in Table 4.1, one can calculate the expected band structure for quantum well widths less than, equal to, and greater than d_C (Figure 4.5). With the well thickness is equal to 5.8 nm, the system has an energy gap, a dominantly hole-like valence band, and a dominantly electron-like conduction band. Increasing the well width to the critical thickness, $d_C = 6.3$ nm, causes the gap to close. With the thickness set to 7.0 nm, the gap again opens. Now, however, the character of states near the bottom of the conduction band is dominantly hole-like due

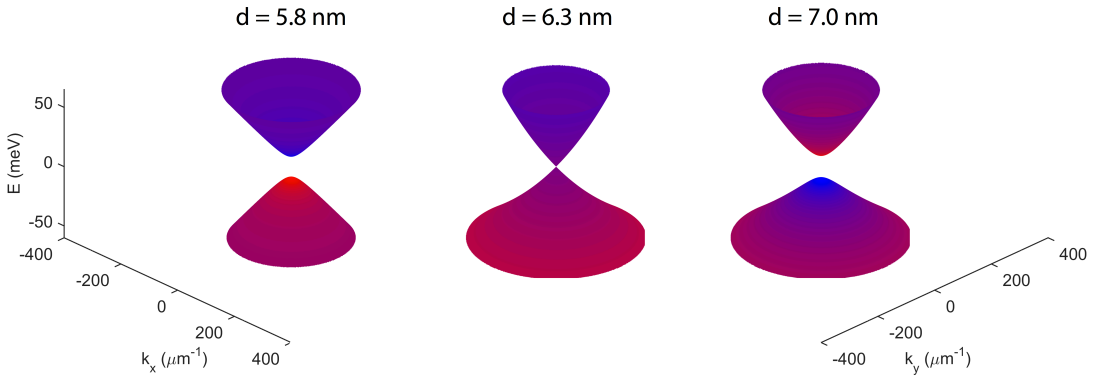

Figure 4.5: Dispersion relations calculated for three different quantum well thicknesses, using the BHZ model with parameters listed in Table 4.1. The energy bands are colored according to projection onto the $E1$ (blue) and $H1$ (red) bands, after Bernevig, Hughes, and Zhang. The energy range is 125 meV for all plots. When the well thickness is equal to 5.8 nm, the system has an energy gap, a dominantly hole-like valence band, and a dominantly electron-like conduction band. Increasing the well width to the critical thickness, $d_C = 6.3$ nm, causes the gap to close. With a thickness equal to 7.0 nm, the gap again opens. Now, however, the character of states near the bottom of the conduction band is dominantly hole-like due to the band inversion. Similarly, states near the top of the valence band are dominantly electron-like.

to the band inversion. Similarly, states near the top of the valence band are dominantly electron-like.

In the conduction band of the 7.0 nm quantum well, the evolution from hole-like to electron-like character with increasing in-plane wave vector $\vec{k}$ carries ramifications for the effective in-plane g-factor $\tilde{g}$. Since hole-like states have angular momentum $3/2$ and are therefore not first-order coupled by magnetic fields, the effective g-factor near $\vec{k} = 0$ is expected to be zero. As $|k|$ increases, the character of states becomes more electron-like, and therefore the effective g-factor should evolve away from zero. A calculation of the theoretically expected g-factor,

$$\tilde{g} = g_{||}\sqrt{\langle\sigma_x(1+s_z)/2\rangle^2 + \langle\sigma_y(1+s_z)/2\rangle^2 + \langle\sigma_z(1+s_z)/2)\rangle^2}, \tag{4.5}$$

is shown in Figure 4.6. Here σ and s are Pauli matrices operating in spin space and pseudo spin ($E1$,$H1$) space respectively, and $g_{||} = -20.5$ [63]. As expected, $\tilde{g}$ is zero at $\vec{k} = 0$, and evolves toward $g_{||}$ as $|k|$ increases. This theoretically expected behavior will become important in Chapter 6, where we describe experiments in which a magnetic field is applied parallel to the plane of HgTe quantum wells in the inverted regime.

d (nm)	A (eV·Å)	B (eV·Å^2)	D (eV·Å^2)	M (eV)
5.8	-3.62	-18.0	-0.594	0.00922
6.3	3.73	-85.7	-68.2	0
7.0	3.645	-68.6	-51.2	-0.010

Table 4.1: List of parameters used to model band structure in the BHZ model. For the 5.8 nm quantum well, parameters were taken from [12]. For the 6.3 nm quantum well, parameters were taken from [16]. For the 7.0 nm quantum well, parameters were taken from [63].

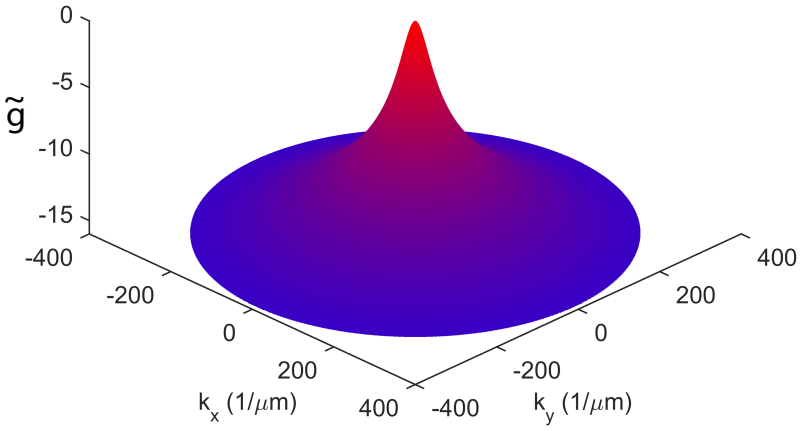

Figure 4.6: Calculation of the effective g-factor in the conduction band of 7.0 nm-wide HgTe quantum well. Since such a well is in the inverted regime, the character of states near the bottom of the conduction band is dominantly $H1$ (hole-like). Moving away from the band edge, mixing in of $E1$ (electron-like) states becomes more pronounced. Since the $H1$ states have angular momentum $3/2$ and are not first-order coupled by magnetic fields, the effective g-factor is expected to evolve dramatically as a function of the in-plane wave vector $\vec{k}$. As depicted, the effective g-factor is zero at $\vec{k} = 0$. As $|k|$ increases, the effective g-factor evolves to more negative values.

4.2.3 Topological edge states in wide HgTe quantum wells

In addition to having interesting bulk electronic properties, the BHZ Hamiltonian (equation (4.1)) carries spectacular implications at the edges of a finite system. When the Fermi energy is tuned into the bulk band gap, the physical edges of an inverted quantum well should always host two counter propagating channels with opposite spin, realizing the quantum spin Hall effect. An heuristic argument for this is often used, and we describe it here. One imagines placing the edge of an inverted HgTe quantum well system in contact with the edge of an insulator with normal band ordering. Then, on moving spatially from the HgTe quantum well into the conventional insulator, the inverted bands should switch to the normal ordering. The crossing of these bands is protected by time-reversal symmetry, and we therefore expect that the edge of the HgTe should always host a pair of time-reversal symmetric edge states. Of course, for thin HgTe wells where the bands are ordered normally, one expects that no such crossing should occur at the edge, and therefore there should be no quantum spin Hall effect.

There is a better argument based on topology. Just as the Chern invariant n counts the number of edge channels and therefore the Hall conductance σ_{xy} in the IQHE, an analogous topological invariant can be defined for the quantum spin Hall effect. Bernevig, Hughes, and Zhang calculated the Hall conductance of their model. They found that $\sigma_{xy} = 0$ for $M/2B < 0$, and $\sigma_{xy} = \pm e^2/h$ for $0 < M/2B < 2$, where the $H(k)$ and $H^*(-k)$ blocks of the Hamiltonian (4.1) have opposite values of σ_{xy}. There are then three distinct possible phases, enumerated by the possible values of the Hall conductance σ_{xy}. One of the phases, in which the quantum well is uninverted, is equivalent to a trivial insulator and is characterized by $\sigma_{xy} = 0$. The other two phases occur for an inverted quantum well and each have a pair of counter propagating edges. In time-reversal invariant two-dimensional insulators, it is possible to show that a Z_2 topological invariant distinguishes between an even and odd number of pairs of edge states [55]. Phases with an even number of edge state pairs are topologically trivial, while those with an odd number of pairs are equivalent and topologically nontrivial. The Z_2 invariant takes values of either 0 or 1, and counts the number of stable gapless edge states modulo 2. Using the bulk-boundary correspondence, simply knowing that an inverted quantum well has a Z_2 invariant of 1 is enough to say that it must be a quantum spin Hall insulator. The different topology of inverted and uninverted wells also explains the evolution of $E1$ and $H1$ states in Figure 4.4; because the bulk gap must close at a topological phase transition, the $E1$ and $H1$ states cross at the critical well thickness $d_C = 6.3$ nm.

4.3 Experimental expectations for charge transport

The BHZ model provides several clear experimental predictions for charge transport in HgTe quantum wells. The most dramatic prediction is that the system should undergo a topological phase transition when the quantum well thickness crosses through the critical thickness $d_C = 6.3$ nm. For wells thinner than the critical thickness, this means that if the chemical potential is tuned into the gap, there should be no edge channels and no quantum spin Hall effect. For wells whose width matches the critical thickness, the gap should close, and the system should realize a single-valley Dirac system [16]. Finally, for wells thicker than the critical thickness, the system should become a quantum spin Hall insulator when the chemical potential enters the bulk gap. Charge should then flow at the edges of the sample, but still not through the bulk. Although it is not possible experimentally to tune the quantum well thickness in a single sample[4], by growing samples with different thicknesses it is possible to test this expectation.

A second prediction concerns the nature of charge transport in the quantum spin Hall effect. As long as time-reversal symmetry is conserved, electrons should not be able to scatter between the counter propagating edge modes. Along any given edge of an experimental sample, one then expects to find a ballistic one-dimensional channel with conductance e^2/h. A convenient geometry with which to test this expectation is the Hall bar geometry shown in Figure 4.7. Assuming that edge channels equilibrate completely at each contact, a standard measurement of the longitudinal conductance should yield the result $G_{xx} = 2e^2/h$ in the quantum spin Hall regime. This result contrasts dramatically with what one expects for a trivial insulator, where $G_{xx} = 0$.

4.4 Experimental evidence for topological edge channels

In Chapter 5, we present measurements of Josephson junctions where a rectangular section of quantum well is contacted on opposite sides by superconducting aluminum leads. By measuring Fraunhofer interference in a device where the quantum well width exceeds 6.3 nm, we are able to spatially image the topological edge states associated with the quantum spin Hall effect. In the following sections, we discuss experimental evidence for these topological edge channels that was obtained prior to the work in Chapter 5.

[4] Not yet, anyway.

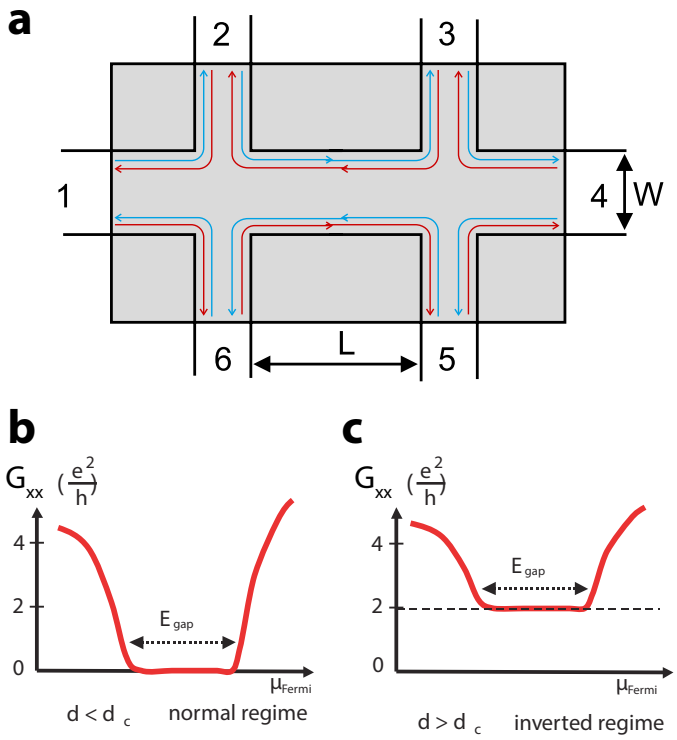

Figure 4.7: Predicted conductance of trivial and topological devices, adapted from [12, 62]. **(a)** Experimental fabrication of a Hall bar, as shown, allows a four-terminal measurement of the longitudinal conductance G_{xx}. With a top gate, the chemical potential can be tuned into the bulk band gap. Then, with the current sourced from contact 1 and drained at contact 4, the measured voltage difference between contacts 2 and 3 (and hence the conductance G_{xx}) indicates whether the device is in the trivial or topological regime. **(b)** In the trivial regime ($d < d_C$), the sample insulates when the chemical potential lies in the band gap, so that the conductance G_{xx} is expected to be zero. **(c)** In the topological regime ($d > d_C$), the presence of quantum spin Hall edge states leads to a nonzero conductance even with the chemical potential in the band gap. In the absence of backscattering, and if edge channels equilibrate perfectly in the leads, the conductance of this Hall bar configuration should then be $G_{xx} = 2e^2/h$.

4.4.1 Quantized resistance

The first experimental evidence for the quantum spin Hall effect came from the group of Laurens Molenkamp at the University of Würzburg [62]. They found that in devices where the quantum well was thinner than the critical thickness d_C, the longitudinal resistance was dramatically higher than in devices with quantum wells thicker than d_C. The layout of these devices was the same as in Figure 4.7.

The results of their measurements are shown in Figure 4.8. In the first device, which contained a 5.5 nm-thick quantum well, tuning into the bulk band gap leads to a longitudinal resistance of more than 10 Mohm. This contrasts dramatically with the measurements on 7.3 nm-thick quantum wells, where devices with micron-scale dimensions had longitudinal resistances close to $h/2e^2$. As discussed previously, this nearly quantized resistance can be interpreted as evidence for transport via quantum spin Hall edge modes. Comparing the $\approx$ 3 orders of magnitude difference in resistance between narrow and wide quantum wells strengthens this interpretation.

An additional device had dimensions 20.0×13.3 μm^2 and also contained a 7.3 nm-thick quantum well. In this device, the resistance was surprisingly somewhat larger than the expected resistance $h/2e^2$. This suggests that in HgTe samples, the scattering length for the edge states is on the order of a few microns. Even in devices that are nearly quantized, the resistance can fluctuate by several kohm. These deviations from the expected resistance are ubiquitous and have been studied both theoretically [76, 104, 118, 119] and experimentally [13, 64] with no definitive resolution to date. Regardless of whether the scattering mechanism is known, however, the dramatic difference in resistance seen on changing the quantum well width by only $\approx$ 2 nm, combined with the nearly quantized resistance of micron-scale samples, still provides strong evidence for the existence of topological edge states. In addition, the nonlocal nature of the edge conduction has also been checked by varying the geometry and arrangement of contacts in various wide-well devices [98].

In the Yacoby lab, we sought to replicate the original observation of quantum spin Hall behavior, using a wide quantum well grown by the group of Laurens Molenkamp. The growth structure of the wafer that we used is shown in Figure 4.9, and the mobility and density of this intrinsically doped sample were $\mu = 94,000$ cm^2/Vs and $n = 3.78 \times 10^{11}$/cm^2.

The device that we fabricated is shown in Figure 4.10. A mesa, created with argon etching, is shown in green and also lies under blue and red regions. Blue regions define ohmic contacts made by depositing titanium and gold. The red areas define the top gate, which is used to tune the electron density.

Due to the intrinsic doping of this wafer, ungated areas of the device will have a metallic two-dimensional electron system and can be treated as extensions of the ohmic contacts. On energizing

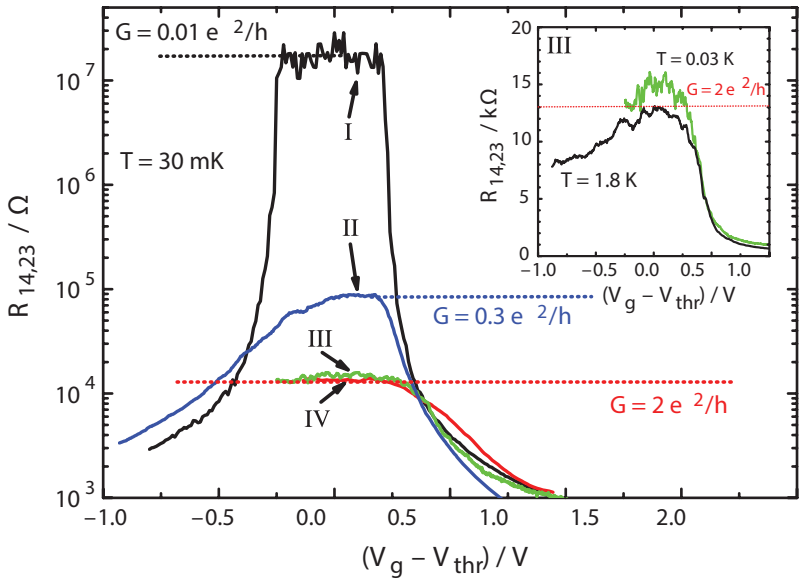

Figure 4.8: Experimental evidence for the quantum spin Hall effect in HgTe quantum wells, adapted from [62]. The longitudinal four-terminal resistance of four different devices was measured, as a function of the voltage on a global top gate. The devices were all in the configuration discussed in Figure 4.7. Device I contained a 5.5 nm-thick quantum well, while Devices II-IV contained a 7.3 nm-thick quantum well. Devices I and II had dimensions $20.0 \times 13.3\,\mu\text{m}^2$, while devices III and IV were smaller with dimensions $1.0 \times 1.0\,\mu\text{m}^2$ and $1.0 \times 0.5\,\mu\text{m}^2$ respectively. In device I, tuning the chemical potential into the band gap resulted in a measured resistance that was orders of magnitude larger than $h/2e^2$, as expected for a trivial sample. In the smallest samples with wide wells (devices III and IV), tuning into the band gap yielded a resistance close to $h/2e^2$, as expected when quantum spin Hall edges are present.

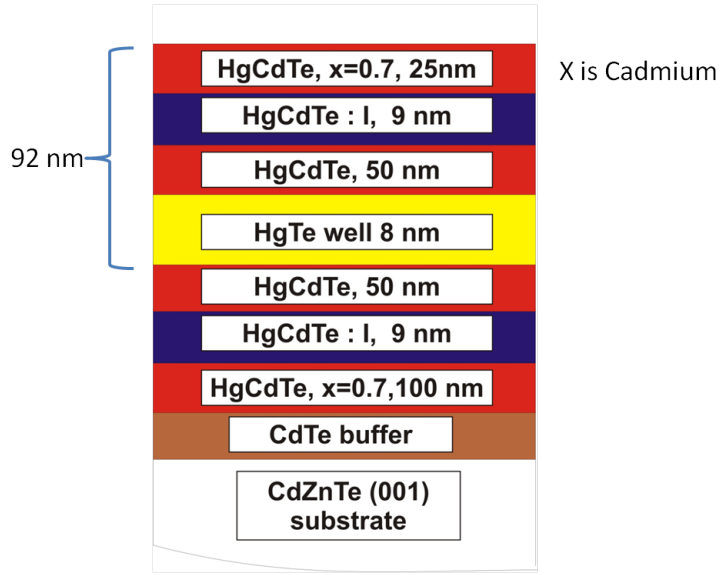

Figure 4.9: Schematic of the heterostructure used to measure resistance consistent with the quantum spin Hall effect. The quantum well thickness was 8 nm. The wafer was also intrinsically doped.

the top gate, regions underneath the gate can be tuned into the topologically insulating regime. Since the gate only overlaps the mesa in short (2 micron) lengths, the quantum spin Hall edge states only traverse this short length between the contacts, even in a device with large overall dimensions.

To mimic the contact arrangement used in the measurements by the Molenkamp group, we measure current from three adjacent grounded contacts, and source current from the appropriate remaining contact. On repeating the measurement in Figure 4.8, we find that as the chemical potential is tuned into the band gap, the longitudinal resistance approaches the expected value of $h/2e^2$ (Figure 4.10). This measurement provides further evidence for the existence of topological edge states in the quantum spin Hall effect.

In all of the experiments discussed so far, the measured resistance depends not only on the resistance of the edge segment between the voltage leads, but also on the resistances of all other segments. This is not ideal, since the fundamental property that one hopes to probe in such measurements is actually the conductance of a single quantum spin Hall edge. It is therefore desirable to find a measurement strategy which would allow us to examine each edge resistance individually.

Figure 4.11 depicts our scheme for accomplishing this goal. We model the system as a ring, with each of the edge segments replaced by a resistor R_i. Electrical contacts are then placed between the resistors. We will be interested in a pair of measurements which allows us to find the value of one of

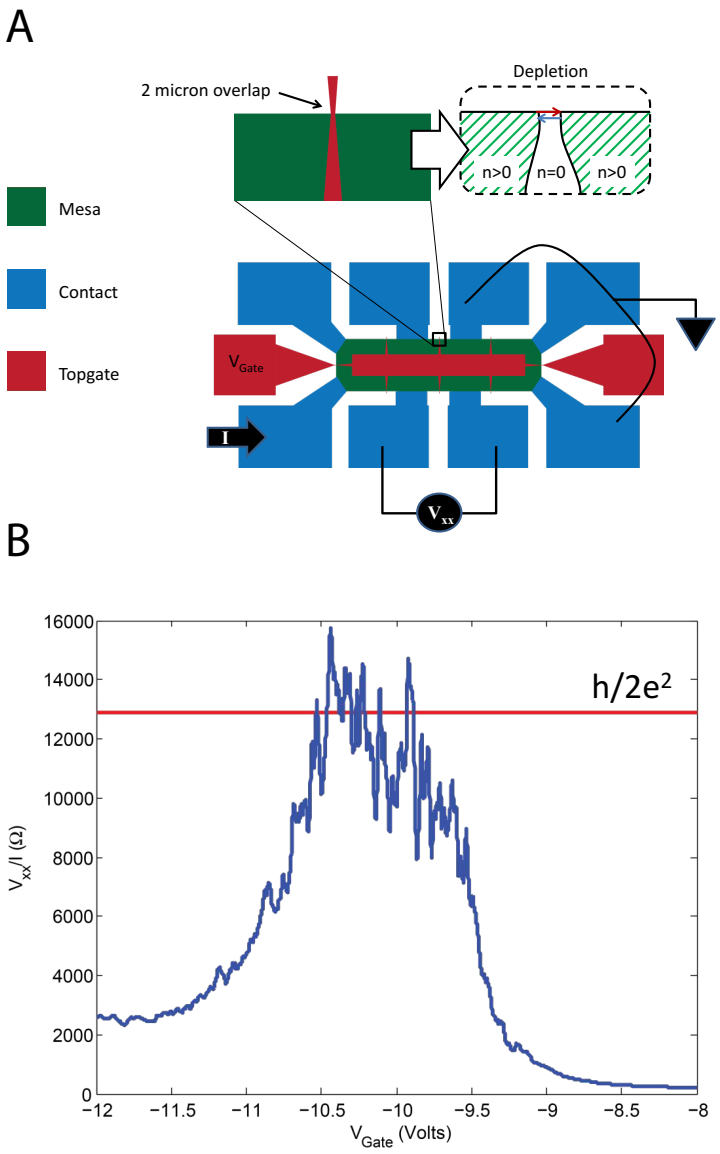

Figure 4.10: Measuring resistance consistent with the quantum spin Hall effect. **(A)** The device used for the measurements. The top gate overlapped the edge only in small (2 micron long) segments. Upon depleting the electron density under the top gate, this gate design results in short quantum spin Hall edges. **(B)** The longitudinal resistance, as a function of the gate voltage. With the chemical potential tuned into the gap underneath the top gate, this resistance becomes close to the expected resistance for transport through quantum spin Hall edges (red line).

these resistances R_1. In each of the two measurements, a current I flows between two of the contacts, and voltages are measured across the resistors R_1 and R_4. Using the first measurement (Figure 4.11a), one finds

$$I = \frac{V_1}{R_1} + \frac{V_4}{R_4}. \tag{4.6}$$

The second measurement (Figure 4.11b) allows one to measure the ratio r_{14} between the resistances R_1 and R_4, expressed in terms of measured quantities as

$$r_{14} \equiv \frac{R_1}{R_4} = \frac{U_1}{U_4}. \tag{4.7}$$

When we combine these two measurements, we find an expression for R_1 which depends only on experimentally measured quantities:

$$R_1 = \frac{V_1 + r_{14} \cdot V_4}{I}. \tag{4.8}$$

Many schemes of this type are possible, allowing experimental extraction of all eight edge resistances.

Figure 4.12 shows the resistance of all eight edge segments, extracted using this method. In each plot, the expected edge resistance h/e^2 appears as a green line. The mean edge resistance, calculated using data highlighted in red, is plotted as a dark gray line. The area shaded in light gray falls within one standard deviation of the mean resistance. Despite the usual fluctuations, one can immediately see that four of the edge resistances are very close to the expected resistance h/e^2. This provides strong evidence in favor of the quantum spin Hall effect. The remaining mean edge resistances are somewhat higher than expected, a fact which remains to be explained.

4.4.2 Current imaging with a scanning SQUID

In 2013, imaging experiments performed by the Moler group at Stanford University yielded further evidence for topological edge channels, and for a topological phase transition tuned by the quantum well thickness [90]. Using a scanning SQUID, they were able to detect magnetic fields produced by current flowing in HgTe samples. In samples with quantum wells thicker than the critical thickness d_C, upon tuning the chemical potential into the band gap they found that currents only flowed near the edges of the sample. In quantum wells thinner than d_C, they found no evidence of enhanced edge conduction. These measurements provide additional evidence, via imaging of transport currents, for the existence of topological edge states.

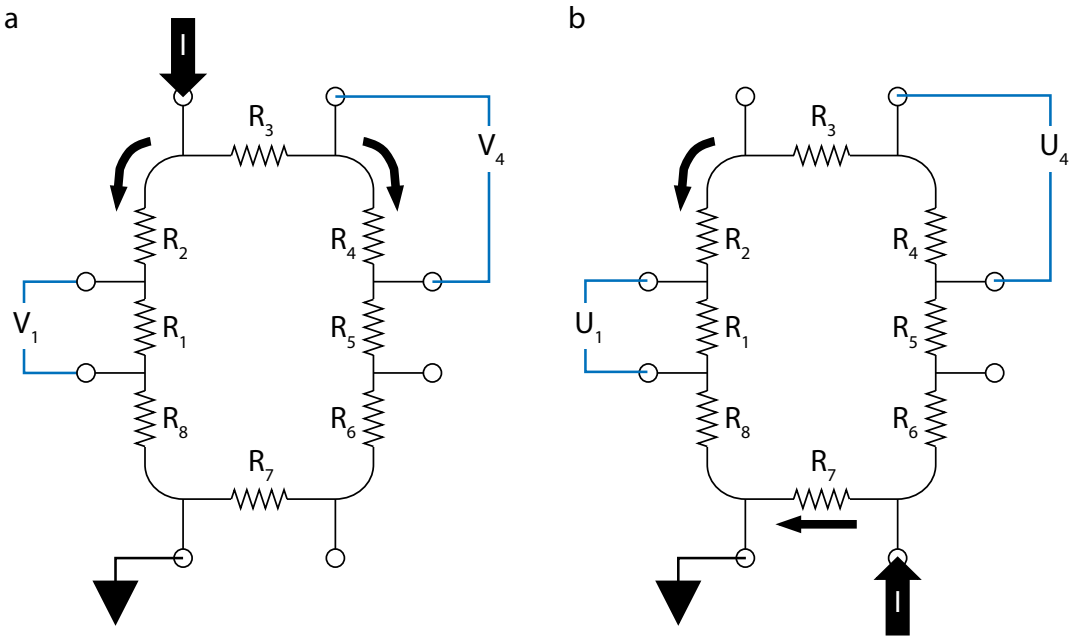

Figure 4.11: Strategy for measuring individual quantum spin Hall edge resistances. A pair of measurements allows extraction of the edge resistance R_1. **(a)** The first measurement provides a relation between R_1 and R_4, in terms of measured quantities. **(b)** The second measurement provides the ratio r_{14} between the resistances R_1 and R_4. Combining these two measurements gives an expression for R_1 in terms of only measured quantities.

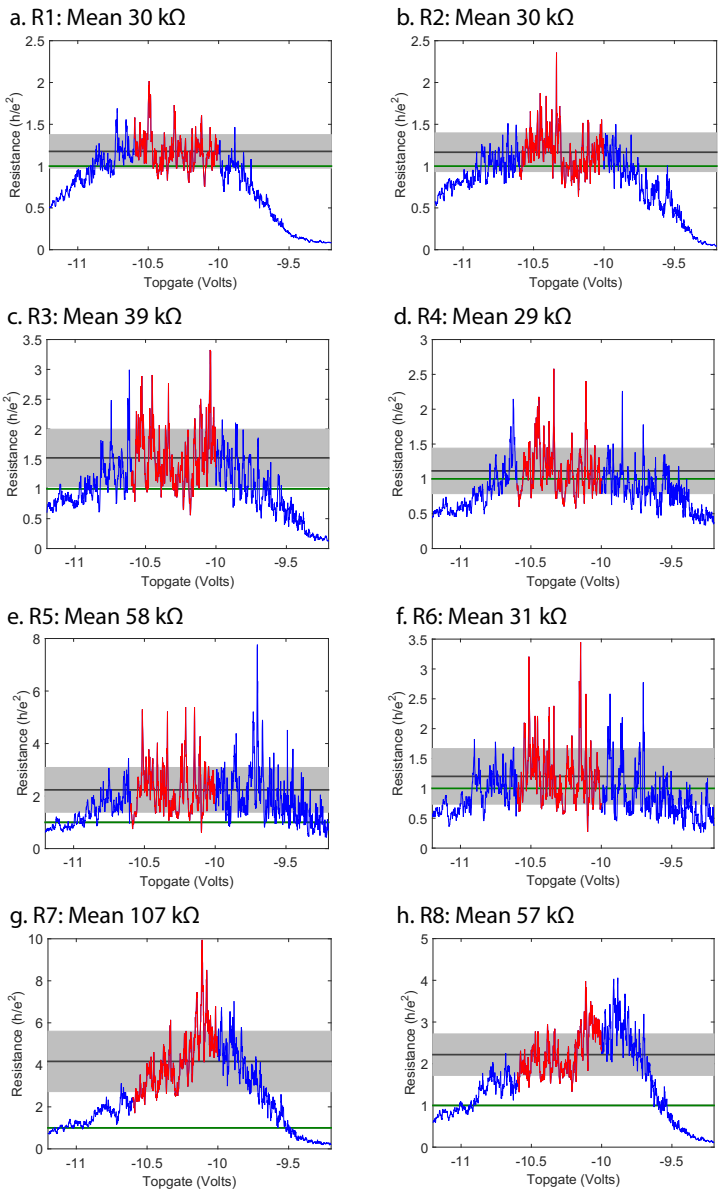

Figure 4.12: Resistances of quantum spin Hall edges, extracted using the scheme depicted in Figure 4.11. In each plot, the data in red was averaged to produce the mean resistance plotted in dark gray. The light gray area falls within one standard deviation of this mean resistance. Green lines show the expected resistance h/e^2 for a single quantum spin Hall edge. Four of the measured edge resistances lie within one standard deviation of this expected resistance, providing evidence for the quantum spin Hall effect.

4.5 Josephson effect in HgTe quantum wells

Given the preponderance of evidence in support of the quantum spin Hall effect, it is natural to ask what use this unique system might have. One answer to this question centers on combining the topological edge channels with superconductivity. The edge states of a quantum spin Hall insulator are special in that they realize a quantum wire with no spin degree of freedom. Such effectively spinless wires have been intensely researched in recent years, due to the possibility that introducing superconducting pairing into these systems could result in a completely new phase of matter called a topological superconductor [2, 9].

Topological superconductivity in this context was first examined theoretically by Alexei Kitaev [59]. He studied a one-dimensional chain of fermions with superconducting pairing but no spin degree of freedom, and found that it is possible for such a system to become a topological superconductor. Such a one-dimensional topological superconductor is characterized by the appearance of a zero-energy mode, called a Majorana fermion, at each end of the wire. Majorana fermions in this condensed matter context are fractionalized modes which pair to form conventional fermions [86]. It is interesting that a single fermonic degree of freedom can become delocalized in this way. In fact, $2n$ sufficiently separated Majorana modes define a degenerate Hilbert space of 2^n states, where the only way to rotate between states is to braid a pair of Majorana modes spatially around one another. In such an ideal system, local perturbations would not be able to change the state of the system. This profound robustness of the quantum state in a system of Majorana fermions makes them highly desirable as the building blocks for a quantum computer.

In pioneering work, Fu and Kane envisioned a system based around the quantum spin Hall effect which could host Majorana fermions [34]. They studied an annulus of quantum spin Hall insulator which is contacted by a superconductor everywhere along its outer edge except for a region of length L (Figure 4.13I). They then studied the spectrum of states inside this region as a function of the phase difference ϕ between the ends of the junction. In the short junction limit, they found that there will be two energy levels in the spectrum which cross at zero energy, due to the presence of Majorana modes in the junction (Figure 4.13IIa). Furthermore, breaking of time-reversal symmetry (for example by application of an in-plane magnetic field) opens a gap in the quantum spin Hall edge, confining the Majorana modes more tightly to the boundaries of the superconductor. Increasing the strength of the parallel magnetic field then pushes the spectrum of states closer to zero energy, as the Majorana modes become more tightly confined (Figure 4.13IIb). Finally, increasing the length of the junctions adds additional states but cannot lift the crossing at $E = 0$, which is due to the nontrivial topology of the system (Figure 4.13IIc, d). The existence of states inside the gap which cross at zero energy arises

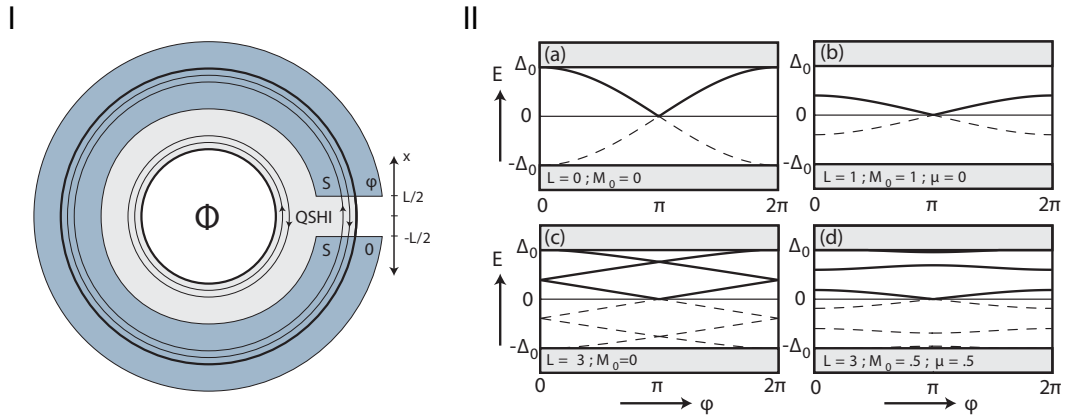

Figure 4.13: A Josephson junction based around a quantum spin Hall edge, adapted from [34]. **(I)** A superconductor/quantum spin Hall edge/superconductor junction where a single edge state connects two superconductors separated by a distance L. The annular geometry in this setup would allow control over the phase difference ϕ across the junction, via magnetic flux threaded through the center of the annulus. **(II)** a) The spectrum of states in the short-junction limit $L = 0$, featuring a degeneracy at $E = 0$ when $\phi = \pi$. b-d) Upon increasing the junction length L, introducing a non-zero Zeeman field M_0, or changing the chemical potential μ away from zero, the degeneracy at $E = 0$ and $\phi = \pi$ remains. Here L is in units of v/Δ_0, where v is the edge state velocity and Δ_0 is the amplitude of the induced pairing potential. M_0 and μ are in units of Δ_0.

due to the presence of a quantum spin Hall edge channel contacting the superconductor. In a trivial insulator, no such states should exist and the spectrum should be gapped and featureless.

With this in mind, we are motivated not only to study the microscopic properties of the quantum spin Hall effect, but also its possible role in quantum information processing. To that end, in the following chapters we study transport in junctions where a rectangular section of quantum well is located between two superconducting leads. Such an arrangement is called a Josephson junction, and in the absence of external magnetic fields ordinarily carries a supercurrent I_S determined as follows:

$$I_S = I_C \sin(\Delta\phi). \tag{4.9}$$

This relation, called the DC Josephson effect, was predicted by Brian Josephson in 1962 [51]. It specifies a definite relation between the phase difference $\Delta\phi$ between the superconducting leads and the supercurrent I_S, in terms of the maximum supercurrent I_C that can flow in the junction. This maximum supercurrent, called the critical current, is the largest value of I_S for which equation (4.9) has a solution.

If an external magnetic field is applied perpendicular to the quantum well, there will then be a flux

Φ penetrating the junction. It is then necessary to account for the Aharonov-Bohm phase accumulated by electrons traversing the junction. If supercurrent flows uniformly throughout the junction in the absence of the external magnetic field, it is possible to show that the critical current in the junction will then be modulated by this flux in the form of a Fraunhofer diffraction pattern [113]:

$$I_C(\Phi) = I_C \left|\sin(\pi\Phi/\Phi_0)/(\pi\Phi/\Phi_0)\right| . \tag{4.10}$$

Here $\Phi_0 = h/2e$ is the magnetic flux quantum. The experiments described in Chapters 5 and 6 will be concerned with this relationship, and how it is modified by certain properties of the HgTe system. In Chapter 5, we study how depletion of the electron density in the bulk of a topological sample restricts the flow of supercurrent to the quantum spin Hall edge channels. The resulting change in the Fraunhofer interference provides microscopic information about these topological edge states. In Chapter 6, we study the effect on Fraunhofer interference of a magnetic field oriented parallel to the plane of the sample. With the chemical potential tuned into the conduction band of an inverted quantum well, this experiment provides information about the interplay between superconductivity, spin-orbit coupling, and the applied magnetic field.

5

Induced superconductivity in the quantum spin Hall edge

5.1 Introduction

Topological insulators are a newly discovered phase of matter characterized by a gapped bulk surrounded by novel conducting boundary states [45, 55, 94]. Since their theoretical discovery, these materials have encouraged intense efforts to study their properties and capabilities. Among the most striking results of this activity are proposals to engineer a new variety of superconductor at the surfaces of topological insulators [33, 34]. These topological superconductors would be capable of supporting localized Majorana fermions, particles whose braiding properties have been proposed as the basis of a fault-tolerant quantum computer [86]. Despite the clear theoretical motivation, a conclusive realization of topological superconductivity remains an outstanding experimental goal. Here we present measurements of superconductivity induced in two-dimensional HgTe/HgCdTe quantum wells, a material which becomes a quantum spin Hall insulator when the well width exceeds $d_C = 6.3$ nm [63]. In wells that are 7.5 nm wide, we find that supercurrents are confined to the one-dimensional sample edges as the bulk density is depleted. However, when the well width is decreased to 4.5 nm the edge supercurrents cannot be distinguished from those in the bulk. Our results provide evidence for supercurrents induced in the helical edges of the quantum spin Hall effect, establishing this sys-

tem as a promising avenue toward topological superconductivity. In addition to directly confirming the existence of the topological edge channels, our results also provide a measurement of their widths, which range from 180 nm to 408 nm.

Topological superconductors, like topological insulators, possess a bulk energy gap and gapless surface states. In a topological superconductor, the surface states are predicted to manifest as zero-energy Majorana fermions, fractionalized modes which pair to form conventional fermions. Due to their non-Abelian braiding statistics, achieving control of these Majorana modes is desirable both fundamentally and for applications to quantum information processing. Proposals toward realizing Majorana fermions have focused on their emergence within fractional quantum Hall states [84] and spinless $p+ip$ superconductors [95], and on their direct engineering using s-wave superconductors combined with topological insulators or semiconductors [1, 102]. Particularly appealing are implementations in one-dimensional (1D) systems, where restriction to a single spin degree of freedom combined with proximity to an s-wave superconductor would provide the basis for topological superconductivity [59]. Effort in this direction has been advanced by studies of nanowire systems [21, 22, 31, 70, 85, 97] and by excess current measurements on InAs/GaSb devices [61].

An attractive route toward a 1D topological superconductor originates from the two-dimensional (2D) quantum spin Hall (QSH) insulator. This topological phase of matter was recently predicted [11, 12] and observed [62, 98] in transport measurements of HgTe/HgCdTe quantum wells thicker than a critical thickness $d_C = 6.3$ nm. Due to strong spin-orbit coupling the bulk bands of the system invert, crossing only at the edges of the system to form 1D counterpropagating helical modes. Time-reversal symmetry ensures protection of these modes against elastic backscattering over distances shorter than the coherence length [104]. The helical nature of the edge modes makes them a particularly appealing path toward topological superconductivity, due to the intrinsic elimination of their spin degree of freedom. Here we report measurements of supercurrents induced in HgTe/HgCdTe quantum well heterostructures. As the system enters the QSH regime we find that these supercurrents become confined to the topological edge modes, verifying their existence and providing a microscopic picture of the QSH state.

5.2 Measurement overview

Our approach consists of a two-terminal Josephson junction, with a rectangular section of quantum well located between two superconducting leads (Figure 5.1). At a given bulk carrier density, the presence or absence of helical edge channels influences the supercurrent density profile across the width of the junction. In the simplest case the supercurrent density is uniform throughout the device, and edge

channels are indistinguishable from bulk channels (Figure 5.1a). This behavior would be expected for a non-topological junction (quantum well width smaller than d_C), or in a topological junction (quantum well width larger than d_C) far from the bulk insulating regime.

In a topological junction, decreasing the bulk carrier density brings the device closer to the QSH insulator regime (Figure 5.1b). Scanning SQUID measurements suggest that over a range of bulk densities the QSH edge channels coexist with bulk states, and can carry considerably more edge current than would be expected for a non-topological conductor [90]. In the two-terminal configuration, this helical edge contribution appears as peaks in the supercurrent density at each edge. When the bulk density becomes sufficiently low, these edge peaks are the only features in the supercurrent density (Figure 5.1c). Then the supercurrent is carried solely along the helical edges, and the system is in the regime of the quantum spin Hall superconductor.

Placing such a Josephson junction in a perpendicular magnetic field B provides a way to measure the supercurrent density in the quantum well. In general, the maximum supercurrent that can flow through a Josephson junction is periodically modulated by a magnetic field. Typically, the period of the modulation corresponds to the magnetic flux quantum $\Phi_0 = h/2e$. In our junctions this period matches the area of the HgTe region plus half the area occupied by each contact, a result of the Meissner effect. The particular shape of the critical current interference pattern depends on the phase-sensitive summation of the supercurrents traversing the junction [113]. In the case of a symmetric supercurrent distribution, this integral takes the simple form:

$$I_C^{max}(B) = \left| \int_{-\infty}^{\infty} dx J_S(x) \cos(2\pi L_J B x/\Phi_0) \right|.$$

Here L_J is the length of the junction along the direction of current, accounting for the magnetic flux focusing from the contacts.

It is evident that different supercurrent densities $J_S(x)$ in the junction can give rise to different interference patterns $I_C^{max}(B)$. The flat supercurrent density of a trivial conductor corresponds to a single-slit Fraunhofer pattern $|(\sin(\pi L_J BW/\Phi_0))/(\pi L_J BW/\Phi_0)|$, characterized by a central lobe width of $2\Phi_0$ and side lobes decaying with $1/B$ dependence (Figure 5.1a). As helical edges emerge, this single-slit interference evolves toward the more sinusoidal oscillation characteristic of a SQUID (Figure 5.1b). The central lobe width shrinks to Φ_0 when only edge supercurrents remain, with the side lobe decay determined by the widths of the edge channels (Figure 5.1c). Measuring the dependence of I_C^{max} on B therefore provides a convenient way to measure the distribution of supercurrent in a junction. To quantitatively extract $J_S(x)$ from the measured quantity $I_C^{max}(B)$ we follow an approach developed by Dynes and Fulton, where nonzero $I_C^{max}(B)$ minima are ascribed to an asymmetric supercurrent distribution [30]. Although other effects may lead to nonzero minima in $I_C^{max}(B)$, we

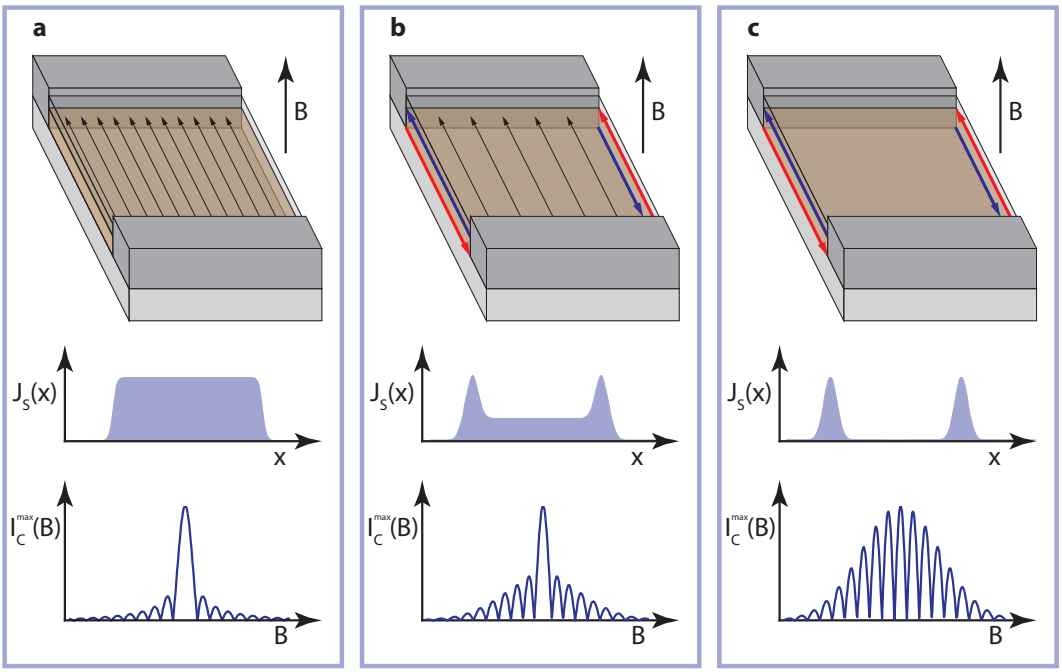

Figure 5.1: Expected two-terminal behavior in different regimes of a topological quantum well. **(a)** When the bulk of a sample is filled with charge carriers, supercurrent can flow uniformly across the junction, corresponding to a flat supercurrent density $J_S(x)$. A perpendicular magnetic field B modulates the maximum critical current I_C^{max}, resulting in a single-slit Fraunhofer interference pattern. **(b)** As the bulk carriers are depleted, the supercurrent density develops peaks due to the presence of the helical edges. This evolution toward edge-dominated transport appears in the interference pattern as a narrowing central lobe width and more pronounced side lobe amplitudes. **(c)** When no bulk carriers remain, the supercurrent is carried only along the helical edges. In this regime the interference results in a sinusoidal double-slit pattern, with an overall decay in B that is determined by the width of the edge channels.

consider here only the possibility of an odd component in $J_S(x)$. Full details of the extraction procedure can be found in Section 5.8.

5.3 Induced superconductivity in the quantum spin Hall regime

To study how supercurrents flow in the QSH regime, we measure a Josephson junction consisting of a 7.5 nm-wide quantum well contacted by titanium/aluminum leads [91]. Our contact lengths are each 1 μm, and the contact separation is 800 nm. The junction width of 4 μm is defined by etched mesa edges. A voltage V_G applied to a global topgate allows us to tune the carrier density in the junction. At each value of V_G and B, the critical current I_C^{max} is determined by increasing the current through the junction while monitoring the voltage across the leads. The behavior observed in this device is reproducable in several other similar junctions, as reported in Section 5.10.

As a function of the topgate voltage, the overall behavior of the junction evolves between two extremes. At more positive gate voltage and higher bulk density, the critical current envelope strongly resembles a single-slit pattern (Figure 5.2a). This type of interference suggests a nearly uniform supercurrent density throughout the sample, confirmed by transformation to the $J_S(x)$ picture (Figure 5.2b). This nearly flat distribution indicates that the quantum well is in the high carrier density regime of an essentially trivial conductor.

At more negative gate voltage and lower bulk density, the critical current envelope becomes close to a sinusoidal oscillation (Figure 5.2c). The shift toward a SQUID-like interference pattern corresponds to the development of sharp peaks in supercurrent density at the mesa edges (Figure 5.2d).

We can track this evolution in a single device by measuring the critical current envelope at a series of gate voltages. As the topgate is varied from $V_G = 1.05$ V to $V_G = -0.45$ V, the maximum critical current decreases from 505 nA to 5.7 nA. At the same time, the overall critical current behavior shows a narrowing of the central interference lobe, from $2\Phi_0$ at positive gate voltages to Φ_0 at negative gate voltages (Figure 5.3a,b). The side lobes additionally become continuously more pronounced, indicating the confinement of supercurrent to channels at the edges of the junction (Figure 5.3c,d). The normal resistance, measured at large bias to overcome superconductivity, increases from 160 Ω to $\sim 3,000\,\Omega$ over the range of this transition (Figure 5.3e). While it is possible to gate further toward depletion, the critical currents become too small to reliably measure and no meaningful supercurrent density can be extracted.

At the most negative gate voltage, $V_G = -0.45$ V, we can estimate the widths of the supercurrent-carrying edge channels using a Gaussian lineshape (Figure 5.3f). Using this method, we find widths of 408 nm and 319 nm for the two edges. Our measurements of edge widths in another device with

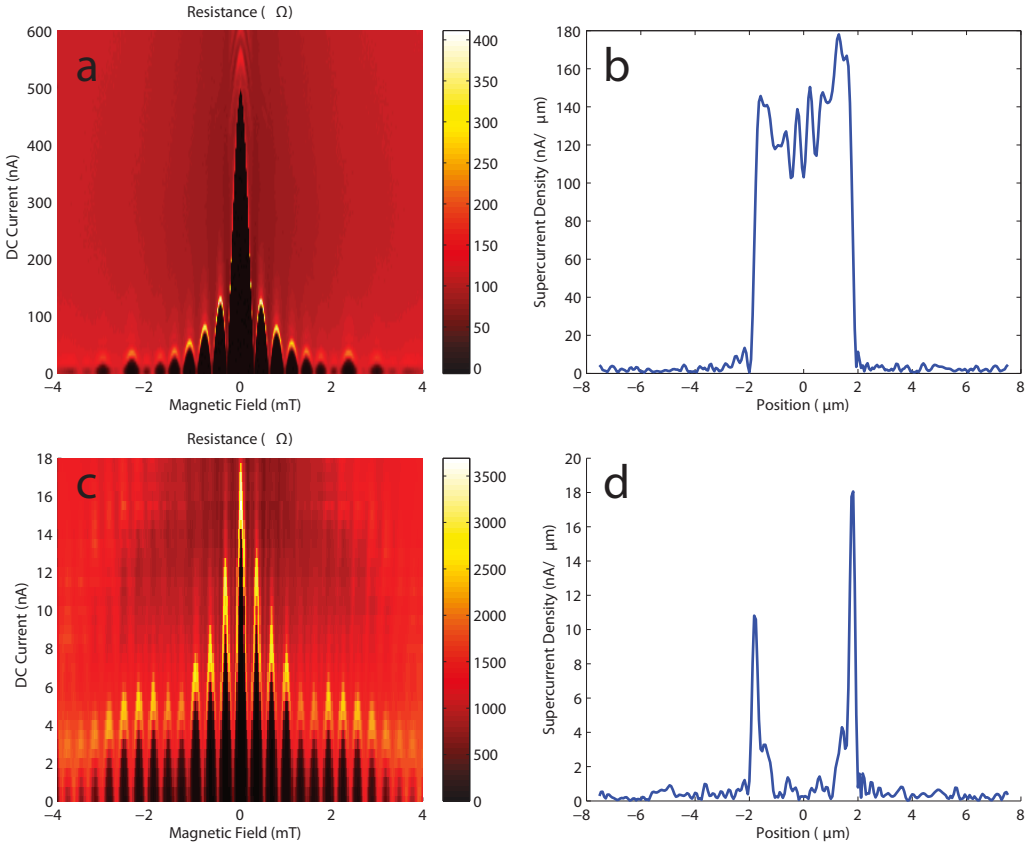

Figure 5.2: General behavior observed in the topological Josephson junction. **(a)** A map of the differential resistance across the junction, measured with the topgate at $V_G = 1.05$ V, shows the single-slit interference characteristic of a uniform supercurrent density. **(b)** The supercurrent density, extracted for $V_G = 1.05$ V, is consistent with trivial charge transport throughout the bulk of the junction. **(c)** When the topgate voltage is lowered to $V_G = -0.425$ V, the differential resistance shows a more sinusoidal interference pattern. **(d)** Using the inteference envelope measured at $V_G = -0.425$ V, the supercurrent density is clearly dominated by the contribution from the edges. In this regime almost no supercurrent passes through the bulk.

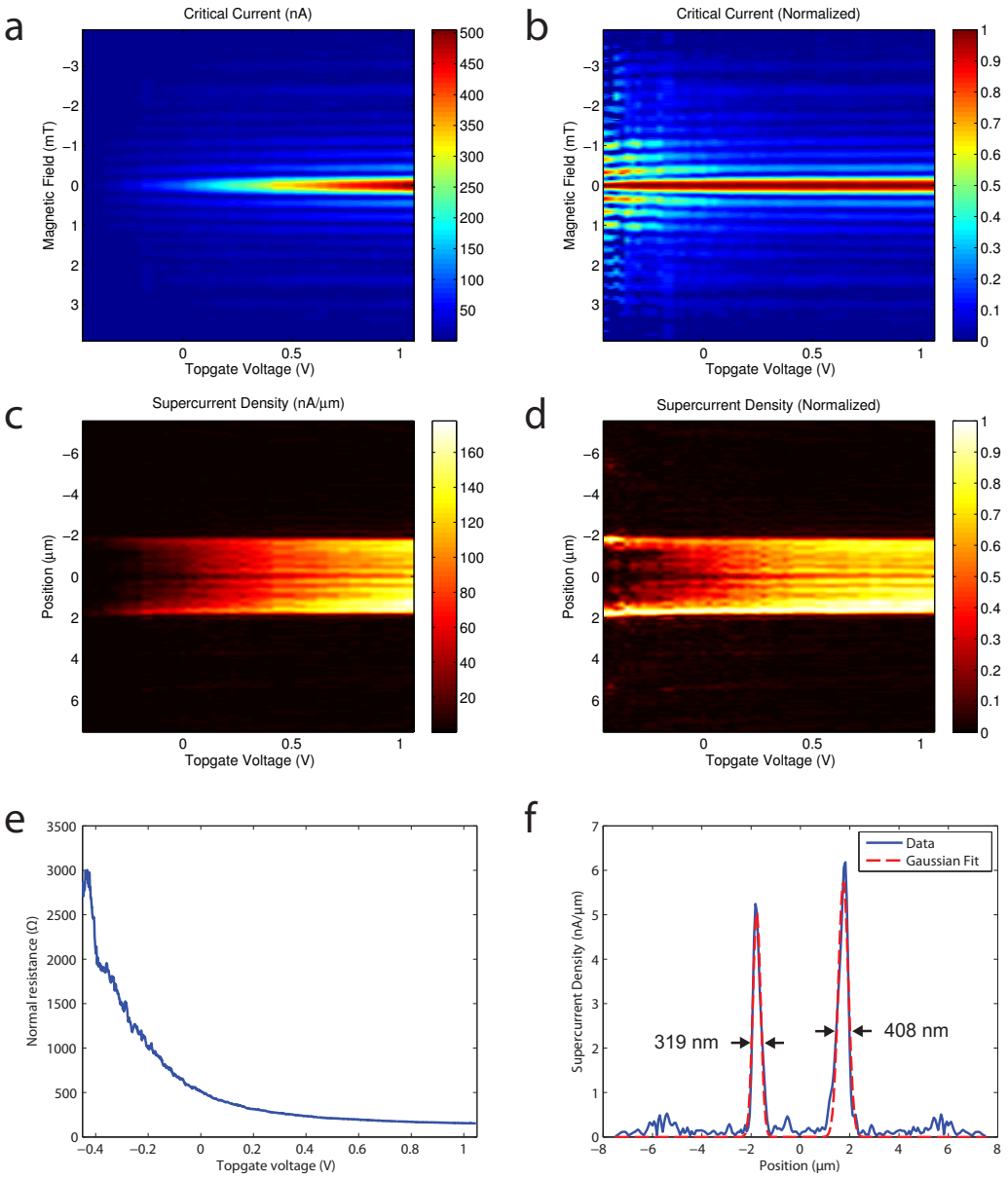

Figure 5.3: Continuous evolution with gating in the topological Josephson junction. **(a)** As the topgate is varied from $V_G = 1.05$ V to $V_G = -0.45$ V, the maximum critical current decreases from 505 nA to 5.7 nA. **(b)** Normalizing the interference patterns to their peak values reveals the evolution toward sinusoidal interference. **(c)** Using the envelope at each gate voltage, the evolution of the supercurrent density can be visualized. **(d)** By normalizing each supercurrent density to its maximum value, the transition from trivial to edge-dominated supercurrent transport can be clearly seen. **(e)** This transition occurs as the normal device resistance increases from 160 Ω to 3,000 Ω. **(f)** At the most negative gate voltage, $V_G = -0.45$ V, the supercurrent density provides a measurement of the edge widths.

similar dimensions, as well as one with a 2 μm mesa width, show edges as narrow as 180 nm (see Section 5.10). These width variations, as well as the normal state resistance that is low compared to the resistance $h/2e^2$ for two ballistic 1D channels, suggest the presence of additional edge modes or of bulk modes coupled too weakly across the junction to carry supercurrent.

5.4 Induced superconductivity in a non-topological quantum well

To provide further evidence that the observed edge supercurrents are topological in nature, we next turn to a heterostructure with a quantum well width of 4.5 nm. In this device, the well width is smaller than the critical width d_C, so that the sample is not expected to enter the QSH regime. Near zero topgate voltage and a normal resistance of 270 Ω, the critical current interference pattern has a maximum of 243 nA and resembles a single-slit envelope (Figure 5.4a,b). Upon energizing the topgate and decreasing the bulk density, the single-slit pattern persists. In contrast to the wide well sample, this behavior corresponds to a supercurrent density that remains distributed throughout the junction even as the normal resistance rises to several kΩ (Figure 5.4c-f). Because the edge supercurrents are present only when the well width is larger than d_C, we conclude that our observations provide evidence for induced superconductivity in the helical QSH edge states.

By studying Fraunhofer interference, our measurements provide detailed information about the supercurrent distribution in HgTe quantum wells. In the quantum spin Hall regime, this interferometry confirms the existence of topological edge channels associated with the quantum spin Hall insulating state. Our observed supercurrent distributions additionally provide the first direct measurements of the helical edges' spatial extent. In general, our application of this Fourier imaging technique to HgTe quantum wells could be widely adopted as a method to elucidate the microscopic structure of topological materials. In our devices, the observation of Josephson supercurrents through the helical edge channels establishes the HgTe/HgCdTe system as a platform in which to pursue topological superconductivity and Majorana bound states, whether through following existing theoretical proposals or those yet to be formulated [50, 82, 103].

5.5 Device characteristics

Devices were fabricated on two different HgTe/HgCdTe heterostructures, with layer structures shown in Figure 5.5. Wafer I contained a 7.5 nm quantum well with an electron density of $3.6 \times 10^{11}/\text{cm}^2$ and a mobility of $300,000\ \text{cm}^2/\text{Vs}$. Wafer II contained a 4.5 nm quantum well with an electron density of $3.5 \times 10^{11}/\text{cm}^2$ and a mobility of $100,000\ \text{cm}^2/\text{Vs}$.

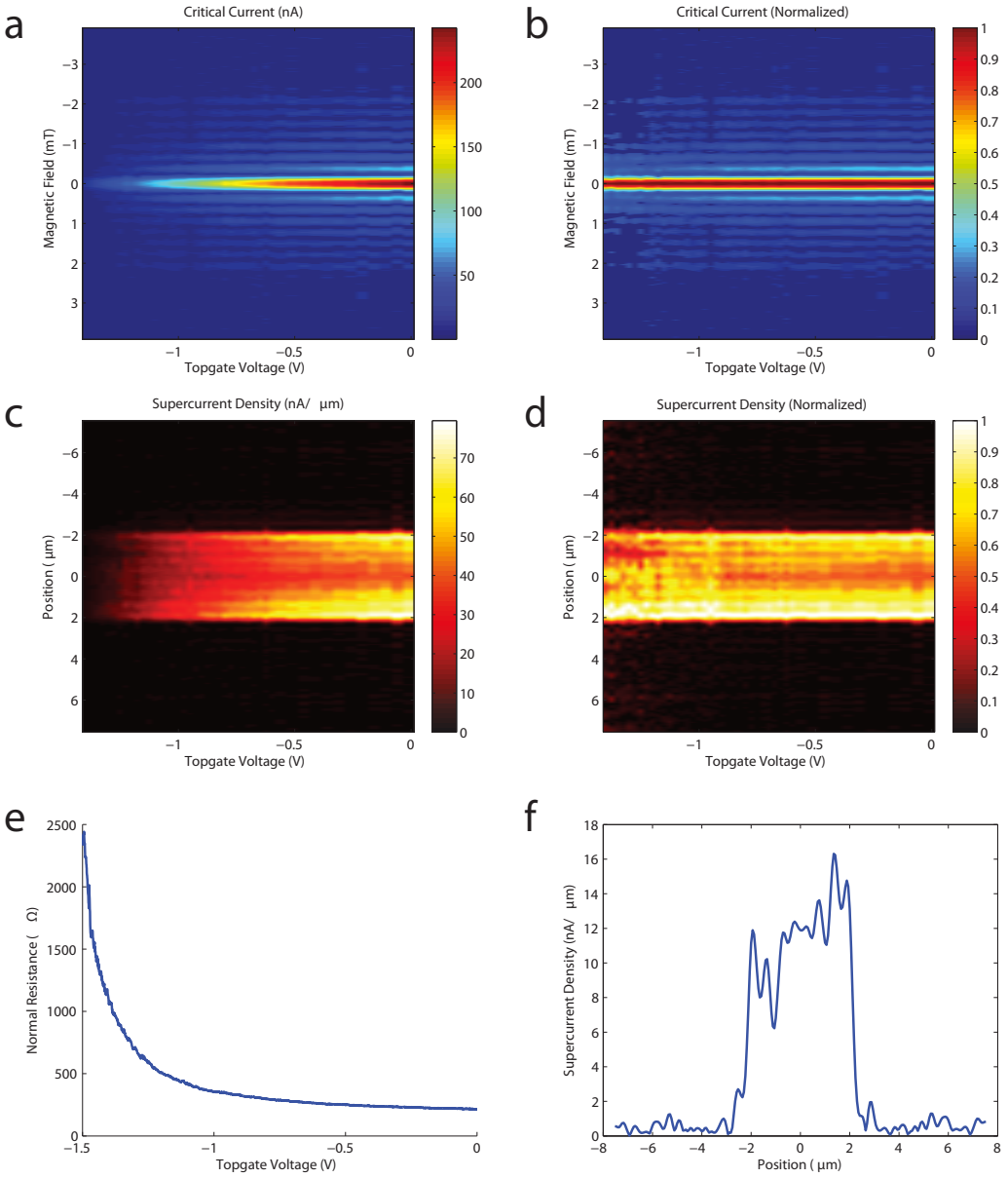

Figure 5.4: Continuous evolution with gating in the non-topological Josephson junction. **(a)** As the topgate is varied from $V_G = 0$ V to $V_G = -1.5$ V, the maximum critical current decreases from 243 nA to 4.4 nA. **(b)** Normalizing the interference patterns to their peak values shows the stability of the single-slit pattern over a wide range of gating. **(c)** Using the envelope at each gate voltage, the evolution of the supercurrent density can be visualized. **(d)** Normalizing each supercurrent density to its maximum value shows that the supercurrent remains distributed throughout the device. **(e)** This roughly uniform supercurrent distribution remains even as the device resistance increases from 215 Ω to almost 2,500 Ω. **(f)** A linetrace of the supercurrent density close to depletion further demonstrates that the supercurrent flows throughout the device.

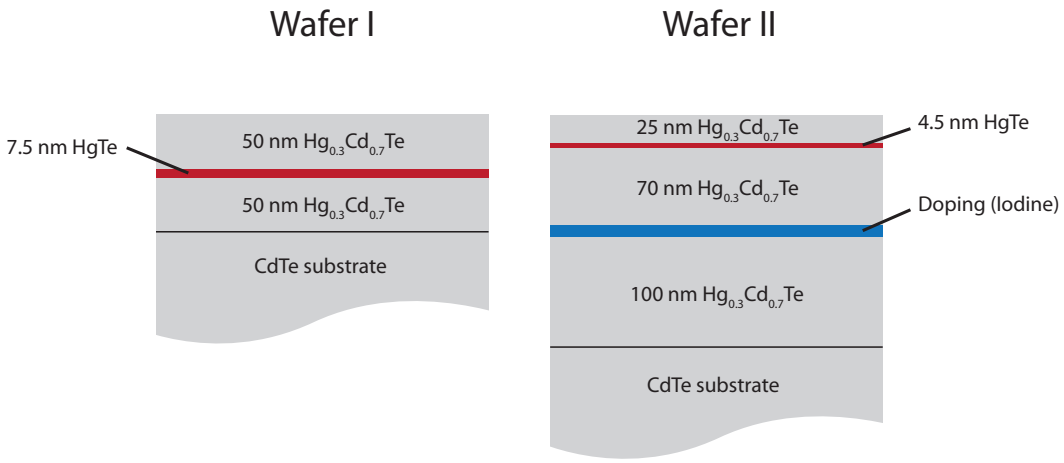

Figure 5.5: Schematics of the heterostructures used in the experiment. The quantum well thicknesses were 7.5 nm for Wafer I and 4.5 nm for Wafer II.

Device processing consisted of the following steps. Mesas were defined by etching with an Ar ion source, and were 100 nm in height. Contacts consisted of 10 nm of titanium under 180 nm of aluminum, deposited by thermal evaporation after in situ cleaning with an Ar ion source. A 50 nm layer of aluminum oxide deposited by atomic layer deposition isolated the mesa and contacts from the topgate, which consisted of 10 nm of titanium under 250 nm of gold. An SEM image of a junction is depicted in Figure 5.6.

5.6 Critical current measurement

Measurements were performed in a dilution refrigerator with a base temperature of 10 mK, and an electron temperature of 20 mK measured using standard Coulomb blockade techniques. At each voltage V_G on the topgate, the magnetic field was stepped through $B = 0$ mT over a range of 8 mT. At each value of magnetic field, the DC current I_{DC} through a junction was then increased while monitoring the DC voltage drop V_{DC} across the junction. A voltage threshold was used to determine the critical current; the point beyond which V_{DC} was increasing and above the threshold voltage was recorded as the critical current $I_C^{max}(B, V_G)$. Our threshold was set at 1 μV, several standard deviations above the noise level. There is an artificial offset introduced by this method when the critical current falls to zero. In our analysis these artificial offset currents are reported as zero instead of the value given by the threshold method.

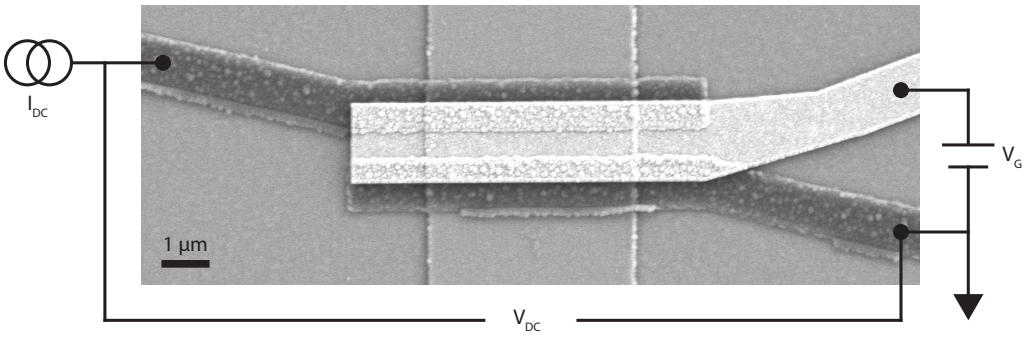

Figure 5.6: A scanning electron micrograph showing the layout of the junctions. A mesa 4 microns in width was contacted by Ti/Al leads. The voltage drop V_{DC} across these leads was monitored as a function of the DC current I_{DC} flowing between them. A voltage V_G applied to a topgate was used to tune the electron density in the device.

5.7 Normal resistance and strength of the induced superconductivity

The critical current I_C and normal state resistance R_N of an ideal device are related to the aluminum superconducting gap Δ by the formula $eI_CR_N/\pi = \Delta$[10]. In reality, measurement of I_C and R_N can yield a product eI_CR_N/π that is smaller than Δ. This situation can arise if, for example, the critical current is smaller than expected due to imperfect contact between the aluminum and modes in the HgTe quantum well. The measured product $\Delta^* = eI_CR_N/\pi$ therefore provides a gauge of how strongly superconductivity is induced into the quantum well. In order to calculate this quantity it is necessary to know the normal resistance of modes contributing to the supercurrent, as well as their critical current.

To measure the normal resistance of our device, at each voltage V_G on the topgate we applied a DC voltage bias of 750 μV between the aluminum leads while measuring the differential resistance R using an AC current bias of 5 nA. This measurement avoids features related to superconductivity through application of the DC bias much larger than the aluminum superconducting gap. However, one must exercise caution in equating these R values directly to the normal resistance R_N of modes which carry supercurrent, because the large DC bias can provide sufficient energy for transport via bulk states that would otherwise be inaccessible near zero bias. Therefore, the reported R is likely to be lower than the normal resistance of the modes actually available for low bias transport, complicating an estimation of the strength of superconductivity induced in our device.

Despite this complication, we can still analyze extreme possibilities for the strength of the induced

superconductivity. In the case that only two helical edge channels contribute to the supercurrent the normal resistance of the device is $h/2e^2$. If the normal transport occurs ballistically, this is the maximum normal resistance that can be assigned to superconducting modes. Then using the measured $I_C = 5.7$ nA at $V_G = -0.45$ V, the product $\Delta^* = eI_C \cdot (h/2e^2)/\pi = 23$ μeV provides an upper bound on the strength of the induced superconductivity.

5.8 Analysis of current density profile

In a Josephson junction immersed in a perpendicular magnetic field B, the magnitude of the maximum critical current $I_C^{max}(B)$ depends strongly on the supercurrent density between the leads. For example, a uniform supercurrent density generates single-slit Fraunhofer interference, while a sinusoidal double-slit interference pattern arises from two supercurrent channels enclosing the junction area. In the following discussion we elaborate on this correspondence, outlining the quantitative way in which we convert our measured interference patterns to their originating supercurrent density profiles. We assume throughout that the current density varies only along the x direction, and that the supercurrent is directed along the orthogonal y direction. The junction then has a length L in the y direction, and the leads each have a length L_{Al}. Our method follows the approach developed by Dynes and Fulton [30].

At a fixed magnetic field, the total critical current through the Josephson junction is a phase-sensitive summation of supercurrent over the width of the junction. Suppose we have a supercurrent density profile $J_S(x)$. Then its complex Fourier transform yields a complex critical current function $\mathscr{I}_C(\beta)$,

$$\mathscr{I}_C(\beta) = \int_{-\infty}^{\infty} dx J_S(x) e^{i\beta x}, \tag{5.1}$$

where the normalized magnetic field unit $\beta = 2\pi(L+L_{Al})B/\Phi_0$, and the magnetic flux quantum $\Phi_0 = h/2e$.

The experimentally observed $I_C^{max}(\beta)$ is the magnitude of this summation: $I_C^{max}(\beta) = |\mathscr{I}_C(\beta)|$. Therefore to extract the supercurrent density from $I_C^{max}(\beta)$ it is necessary to first recover the complex critical current $\mathscr{I}_C(\beta)$.

This reduces to a particularly simple problem in the case of an even current density, $J_E(x)$, representing a symmetric distribution. The odd part of $e^{i\beta x}$ vanishes from the integral, and equation (1) becomes $\mathscr{I}_C(\beta) = I_E = \int_{-\infty}^{\infty} dx J_E(x) \cos \beta x$. Since $J_E(x)$ is real and positive, we see that $\mathscr{I}_C(\beta)$ is also real, and it typically alternates between positive and negative values at each zero-crossing. Because $I_C^{max}(\beta) = |\mathscr{I}_C(\beta)|$, we can therefore recover the exact $\mathscr{I}_C(\beta)$ by flipping the sign of every other lobe of the observed $I_C^{max}(\beta)$.

Now suppose that on top of this even function, the current distribution has a small but non-vanishing odd component, $J_O(x)$, with its Fourier transform $I_O(\beta) = \int_{-\infty}^{\infty} dx J_O(x) \sin \beta x$. Then (1) gives

$$\mathscr{I}_C(\beta) = I_E(\beta) + iI_O(\beta). \tag{5.2}$$

The observed critical current $I_C^{max}(\beta) = \sqrt{I_E^2(\beta) + I_O^2(\beta)}$ is therefore dominated by $I_E(\beta)$ except at its minima points. Approximately, $I_E(\beta)$ is obtained by multiplying $I_C^{max}(\beta)$ with a flipping function that switches sign between adjacent lobes of the envelope function (Figures 5.7,5.8a). When $I_E(\beta)$ is minimal, the odd part $I_O(\beta)$ dominates the critical current. $I_O(\beta)$ can then be approximated by interpolating between the minima of $I_C^{max}(\beta)$, and flipping sign between lobes (Figure 5.8b). A Fourier transform of the resulting complex $\mathscr{I}_C(\beta)$, over the sampling range b of β, yields the current density profile (Figure 5.9):

$$J_S(x) = \left| \frac{1}{2\pi} \int_{-b/2}^{b/2} d\beta \mathscr{I}_C(\beta) e^{-i\beta x} \right|. \tag{5.3}$$

5.9 Gating of resistance and supercurrent

To study the variation of the normal resistance as a function of the bulk carrier density, we swept the topgate voltage in the topological junction (main text) from $V_G = 1.05$ V to $V_G = -3$ V. Over this gate range, the differential resistance was measured using an AC excitation of 5 nA. We additionally maintained a constant DC voltage bias of 750 μV across the junction to avoid features related to superconductivity. The resulting normal resistance measurement displays two relatively conductive regimes separated by a resistance plateau peaking near 6-8 kΩ (Figure 5.10a). This behavior is consistent with previous transport measurements of the QSH effect, where the QSH insulator state appears as a resistance peak when samples are gated from n-type to p-type regimes [62]. The value of the resistance plateau is lower than the expected resistance $h/2e^2$ for two ballistic 1D channels, suggesting that additional bulk modes are present. Near $V_G = -3$ V, our junction resistance saturates at 3 kΩ and we observe no superconductivity. This behavior can be explained by the formation of an n-p-n junction, where barriers between regions of different carrier type can block the transmission of supercurrent.

As we tune the topgate to more negative voltages, the maximum critical current of our junction decreases (Figure 5.3a). The electron temperature $T = 20$ mK provides an estimate $2ek_BT/\hbar \approx 1$ nA for the smallest critical currents that can still be reliably measured. For the topological junction

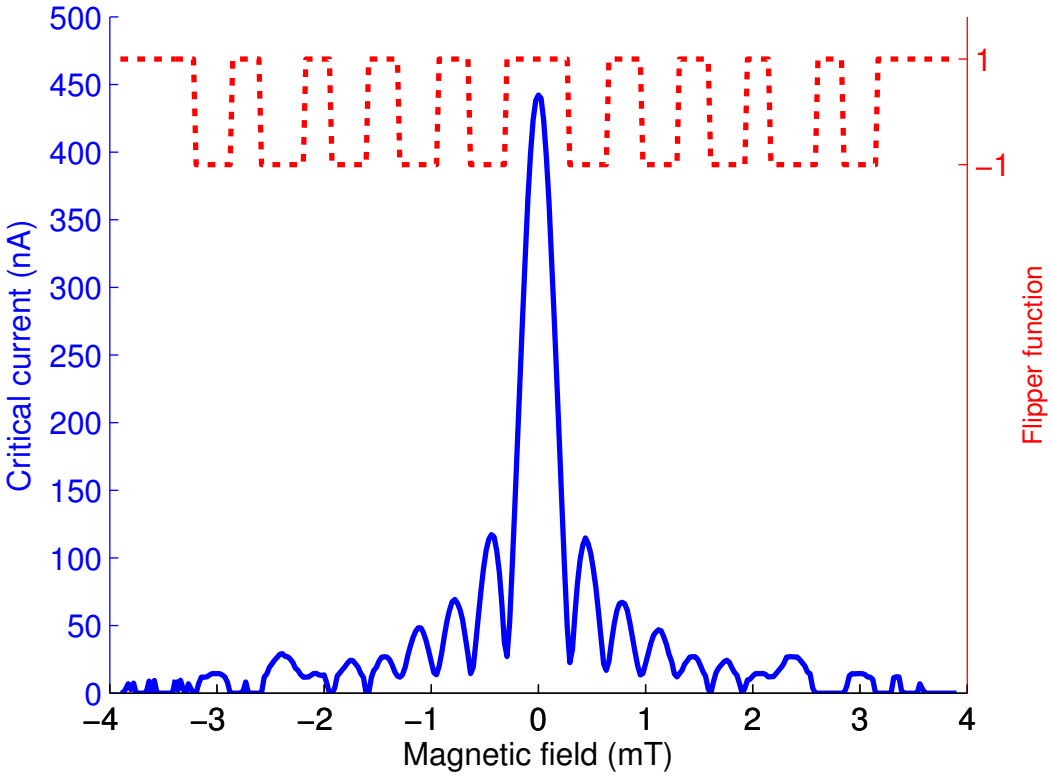

Figure 5.7: Recovering the critical current phase. When the current distribution is mostly symmetric, the experimentally observed critical current envelope (blue line) approaches zero between peaks. In such cases a flipping function (red dashed line) that changes sign at each node of the envelope enables the recovery of $\mathscr{I}_C(B)$ from $I_C^{max}(B)$.

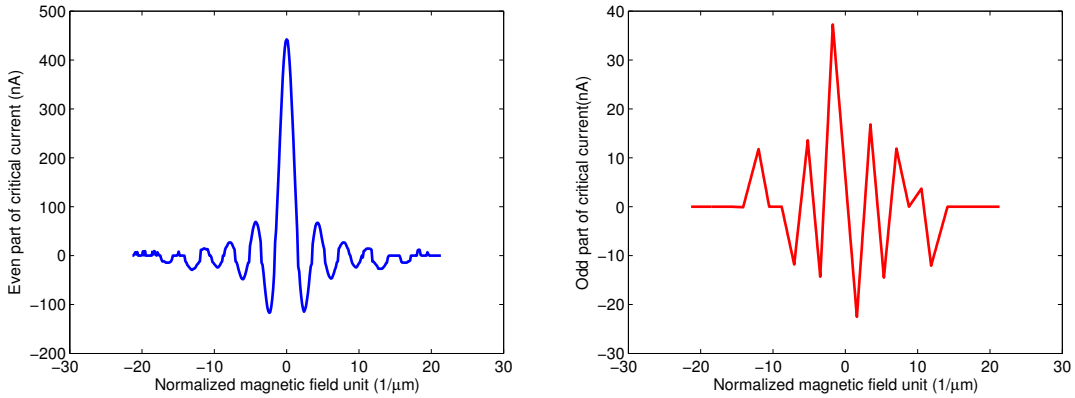

Figure 5.8: Recovered complex critical current. The left plot shows the recovered critical current $I_E(\beta)$ that corresponds to the even part of the current density profile $J_E(x)$. The right plot shows the recovered critical current $I_O(\beta)$ that corresponds to the odd part of the current density profile $J_O(x)$.

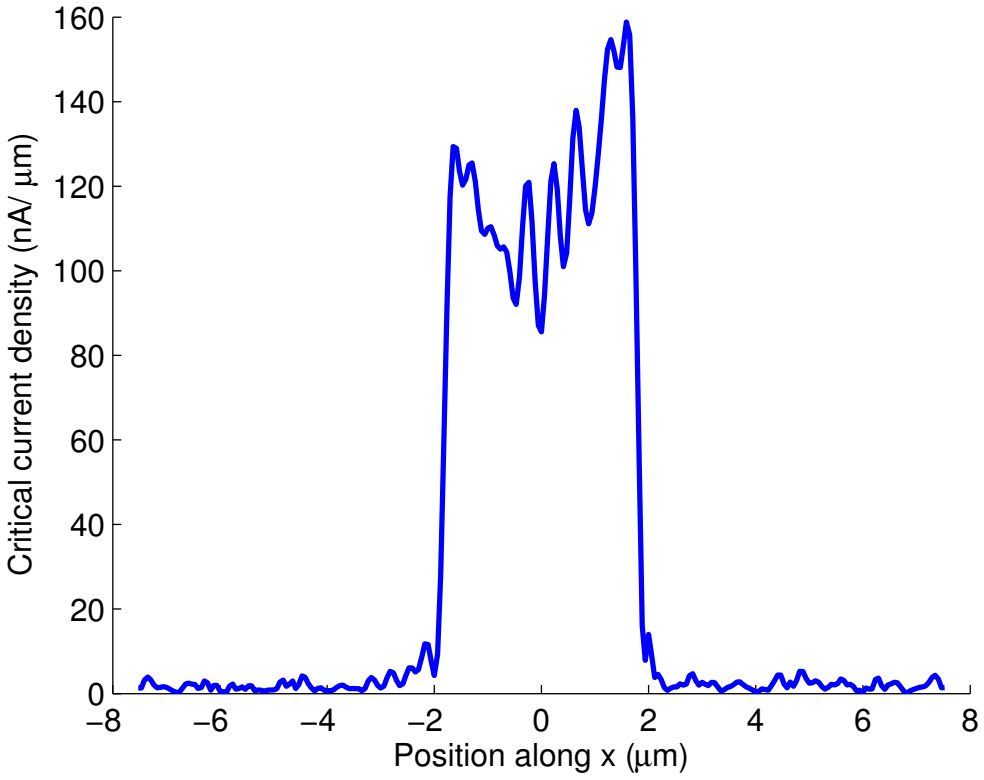

Figure 5.9: The current density profile $J_S(x)$ that corresponds to the envelope in Figure 5.7.

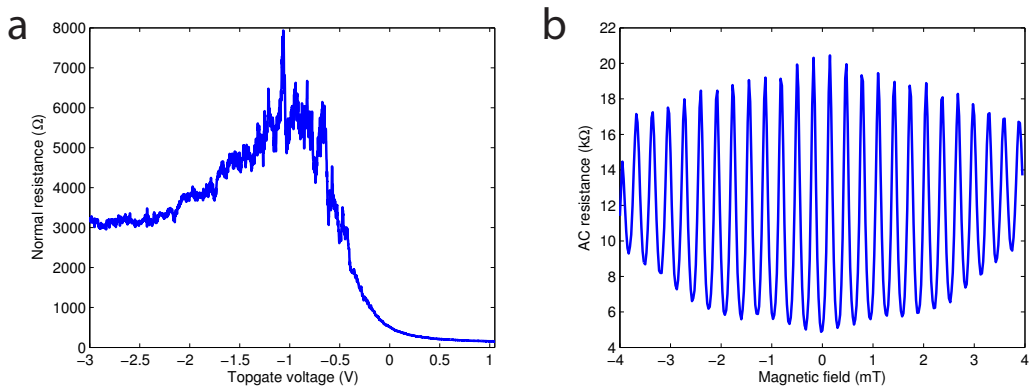

Figure 5.10: Additional data for the topological junction discussed in the main text, as the carrier density in the HgTe is depleted even further. **(a)** As a function of the topgate voltage the normal AC resistance peaks near 6-8 kΩ, consistent with the QSH effect in the presence of several additional bulk modes. **(b)** The junction's AC resistance as a function of magnetic field, measured with the topgate voltage at $V_G = -0.7$ V and with no DC current bias. Even though the resistance minima are far from 0 Ω, the resistance oscillates with a period corresponding to $\Phi_0 = h/2e$. This periodic behavior is consistent with the superconducting interference observed at higher densities, and suggests that supercurrent transport persists well into the QSH regime.

shown in the main text (Figures 5.2, 5.3), this limit is reached above a topgate voltage of $V_G = -0.45$ V. However, even beyond this point clear magnetoresistance oscillations are still apparent. In Figure 5.10b these oscillations are plotted for $V_G = -0.7$ V. The magnetic field period corresponds to the magnetic flux quantum $\Phi_0 = h/2e$ observed throughout the gating of the device, suggesting that supercurrent transport persists well into the QSH regime.

5.10 Additional devices

In addition to the two devices presented in the main text, we also measured several different junction geometries fabricated using the 7.5 nm quantum well heterostructure. One of these junctions had a width of 2 microns, but was otherwise identical to the topological device presented in the main text. This device also showed a transition from uniform bulk supercurrent to edge-dominated supercurrent, concurrently with the normal resistance rising from 300 ohms to 4, 000 ohms (Figure 5.11). The size of the magnetic field period in this device is 0.68 mT, consistent with the overall device area of 2 microns $\times$ (800 nm + 1 micron). From the supercurrent density profile in the QSH regime, we extract edge widths of 180 nm and 197 nm.

The other device, a 4 micron wide junction, was also identical to the topological junction from

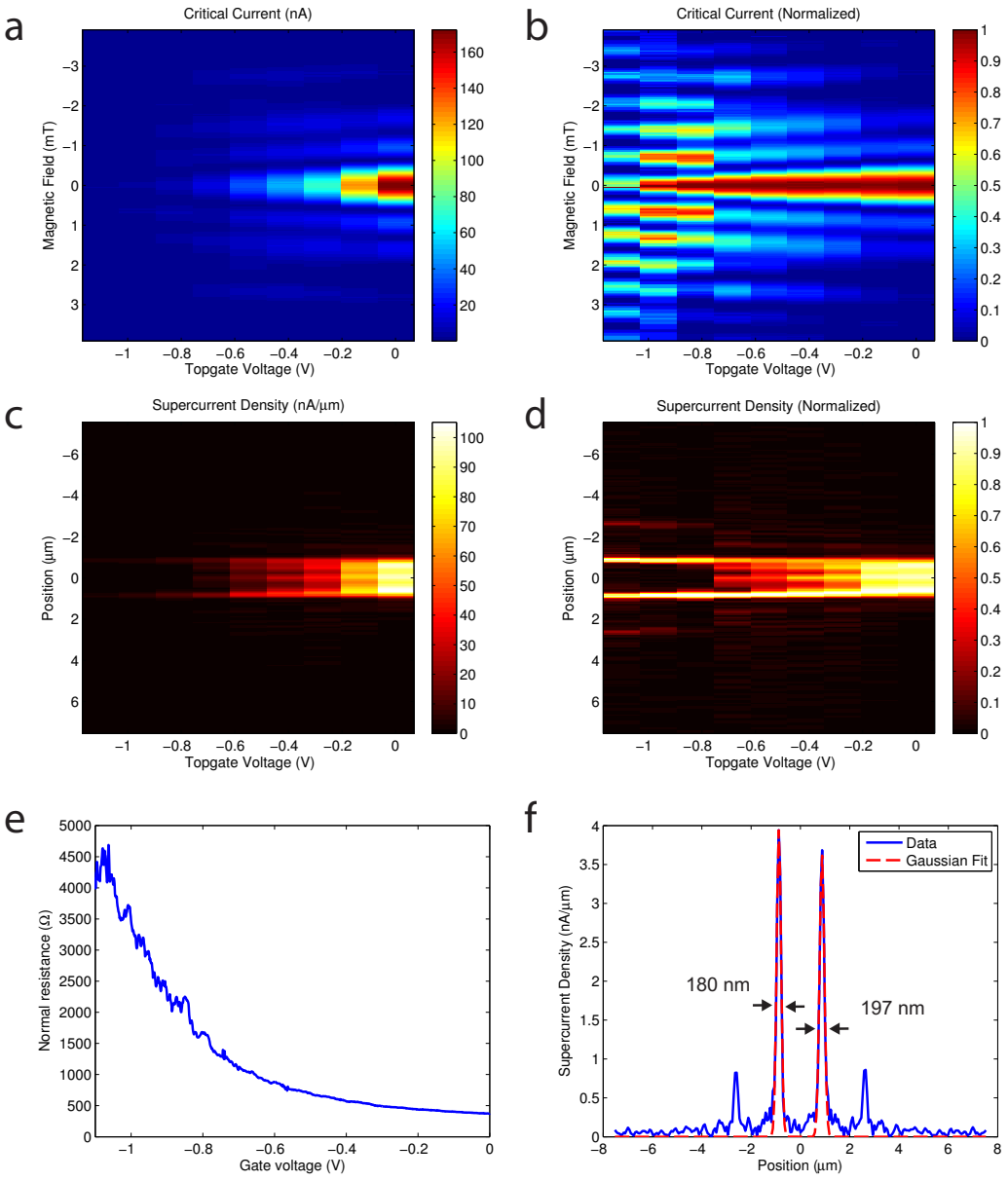

Figure 5.11: Data from a Josephson junction fabricated using Wafer I, the 7.5 nm quantum well. This junction was identical to the one presented in the main text, except that the width of the mesa is 2 microns. **(a)** A map of the critical current envelope as a function of topgate voltage shows that this device has a magnetic field period of 0.68 mT, consistent with the overall area of the device. **(b)** After normalization the interference patterns show the evolution of this device into the QSH regime. The decay of the interference envelope over roughly 4 mT in the QSH regime is determined by the widths of the edge channels. **(c, d)** The supercurrent density shows the confinement of supercurrent to edge modes as the bulk density is depleted. **(e)** The normal resistance of the junction as a function of the topgate voltage. **(f)** Edge widths extracted from the supercurrent density at the farthest negative gate voltage (-1.1 V).

the main text except that the topgate was only 200 nm long and was threaded between the contacts. Although this topgate did not fully cover the junction, the behavior observed in this device was still consistent with the other topological devices (Figure 5.12). This suggests that the gate effect was approximately uniform across the area between the contacts. When the normal resistance of the device was $4,000$ ohms, supercurrent transport was observed in this device through edges with widths of 208 nm and 214 nm. Even after supercurrents became too small to measure, the normal resistance of this device approached the expected value of $h/2e^2$ for transport through two ballistic one-dimensional edge modes.

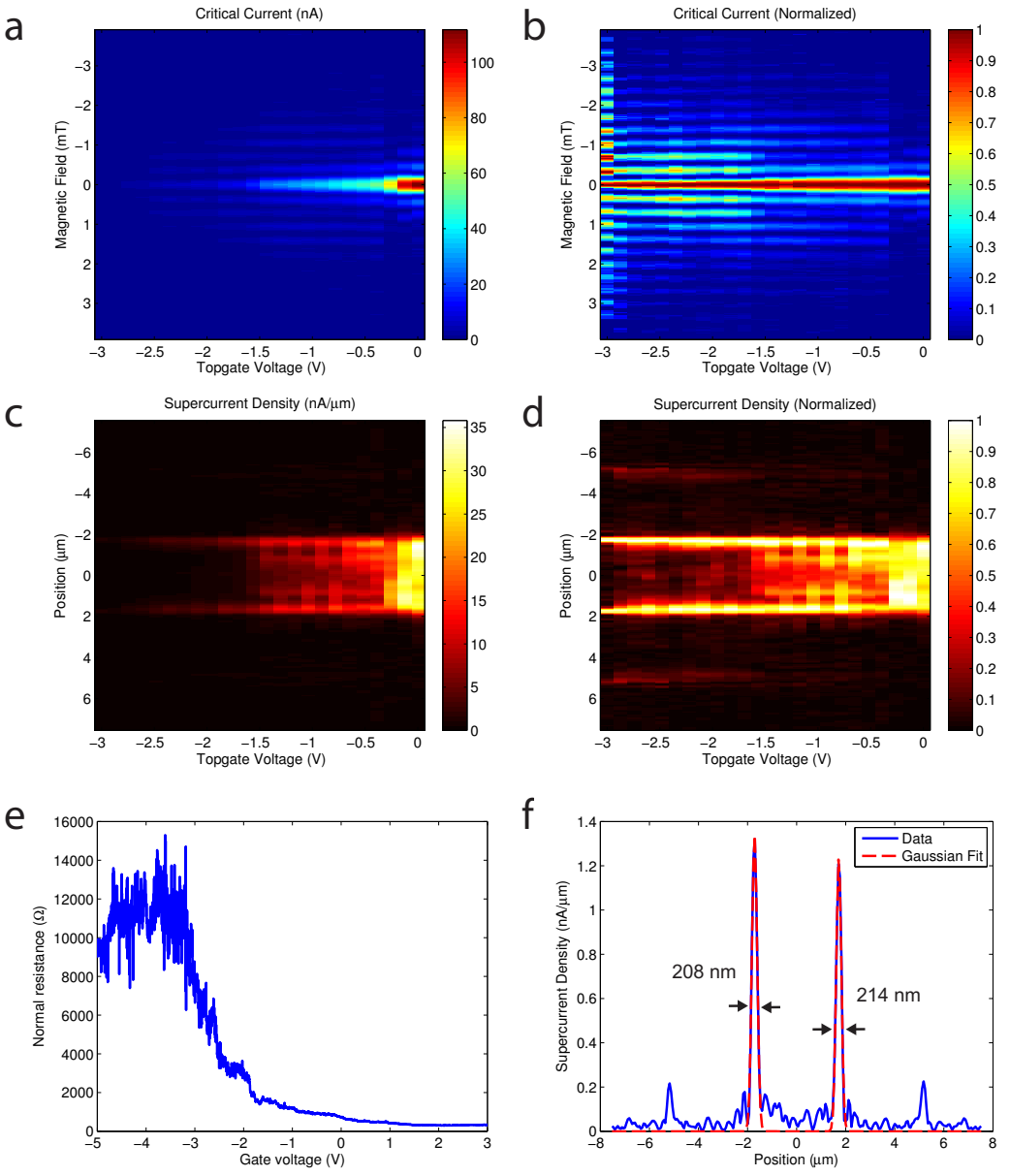

Figure 5.12: Data from a Josephson junction fabricated using Wafer I, the 7.5 nm quantum well. This junction was identical to the one presented in the main text, except that the topgate was 200 nm and centered between the contacts. **(a,b)** Consistent with other topological devices, the critical current envelope tranforms from a single-slit to a sinusoidal pattern as the density is decreased. The decay of the interference lobes is over roughly 4 mT at the most negative gate voltage. **(c, d)** The supercurrent density shows the confinement of supercurrent to edge modes as the bulk density is depleted. **(e)** The normal resistance of the device, extending beyond the $4,000$ ohms where the smallest supercurrents were observed. The resistance approaches the expected value for transport through two ballistic QSH edges. **(f)** Edge widths extracted from the supercurrent density at the farthest negative gate voltage.

6

Controlled finite momentum pairing and spatially varying order parameter in HgTe quantum wells

Conventional *s*-wave superconductivity is understood to arise from singlet pairing of electrons with opposite Fermi momenta, forming Cooper pairs whose net momentum is zero [7]. Several recent studies have focused on structures where such conventional *s*-wave superconductors are coupled to systems with an unusual configuration of electronic spin and momentum at the Fermi surface. Under these conditions, the nature of the paired state can be modified and the system may even undergo a topological phase transition [33, 102]. Here we present measurements and theoretical calculations of several HgTe quantum wells coupled to either aluminum or niobium superconductors and subject to a magnetic field in the plane of the quantum well. By studying the oscillatory response of Josephson interference to the magnitude of the in-plane magnetic field, we find that the induced pairing within the quantum well is spatially varying. Cooper pairs acquire a tunable momentum that grows with magnetic field strength, directly reflecting the response of the spin-dependent Fermi surfaces to the in-plane magnetic field. In addition, in the regime of high electron density, nodes in the induced superconductivity evolve with the electron density in agreement with our model based on

the Hamiltonian of Bernevig, Hughes, and Zhang [12]. This agreement allows us to quantitatively extract the value of $\tilde{g}/v_F$, where $\tilde{g}$ is the effective g-factor and v_F is the Fermi velocity. However, at low density our measurements do not agree with our model in detail. Our new understanding of the interplay between spin physics and superconductivity introduces a way to spatially engineer the order parameter, as well as a general framework within which to investigate electronic spin texture at the Fermi surface of materials.

6.1 Unconventional superconductivity with finite momentum pairing

Below a critical temperature and magnetic field, certain materials undergo a phase transition to the superconducting state. Macroscopically identified through effects such as zero resistivity and the Meissner effect [80], superconductors may further be understood microscopically as arising due to pairing of electrons occupying opposite points on the Fermi surface and having opposite spin. Within a conventional setting this interaction results in Cooper pairs with zero net momentum. However, in certain materials the presence of both magnetic order and superconductivity can lead to intrinsically nonzero pairing momentum as the system enters the Fulde-Ferrell-Larkin-Ovchinnikov (FFLO) state [35, 68]. Studies of both $CeCoIn_5$ and κ-(BEDT-TTF)$_2$Cu(NCS)$_2$ under large external magnetic fields found evidence for coupled magnetic order and superconductivity, although in each material the field strength needed was in excess of 10 T [57, 78].

Exotic superconductivity has recently come under additional investigation through the goal of combining $s-$wave superconductors with materials whose properties are rarely found among the conventional superconductors. For example, inducing pairing from an s-wave superconductor into a material with strong spin-orbit coupling and reduced dimensionality has been recently considered as a viable platform within which to achieve triplet pairing [88, 96] and topological superconductivity [33, 102], or to engineer a Josephson ϕ_0-junction [27, 130]. Moreover, when a ferromagnetic layer is sandwiched by two superconductors, pairs traversing the junction acquire momentum due to the exchange field within the ferromagnet [17, 24]. Measurements of critical current oscillations in such superconductor-ferromagnet-superconductor (SFS) junctions have provided evidence for both π-junctions and nonzero pairing momentum [32, 65, 100, 107], although the magnitude of the momentum was effectively untunable due to the typically large exchange fields.

Here we report on coupling between superconducting leads and a two-dimensional electron system realized within HgTe/HgCdTe heterostructures in the inverted regime. Due to the interplay between superconductivity, band structure, and the applied magnetic field, we find that the order parameter has an oscillatory component derived from the finite momentum of paired electrons, and that this

momentum can be continuously tuned between conventional and unconventional regimes. Our use of only relatively small external magnetic fields (≤ 4 T) and micron-scale device dimensions introduces a new regime in the exploration of the interplay between superconductivity and spin physics.

6.2 Interference measurements with a finite parallel magnetic field B_x

To study the effect of magnetic field and band structure on electron pairing, we place two superconducting leads on opposite boundaries of a rectangular section of quantum well. Devices were fabricated at varying angles with respect to the cleavage edges of the crystal (the $[110]$ and $[1\bar{1}0]$ axes). The angular alignment corresponds to a rotation angle θ with respect to the principal crystal axis $[100]$, with θ defined modulo $\pi/2$ (Figure 6.1A, see Section 6.6). The width W between the two leads is 800 nm and the length L of the resulting Josephson junction is 4 microns. We study the influence of either niobium or aluminum superconductors by applying a small AC current bias between the two leads while measuring the resultant AC voltage [91]. The aluminum thickness is 15 nm in order to sustain superconductivity in moderate parallel magnetic fields (Section 6.7) [81], while the niobium thickness is 130 nm. Josephson interference is generated by application of small (up to $\sim$ 10 mT) magnetic fields in the z direction [113]. Throughout, the in-plane coordinate axes are referred to as x and y, respectively oriented perpendicular and parallel to the supercurrent flow between leads. The addition of a normal metal topgate allows us to study superconductivity over a range of density in the electron-doped regime. Previous experiments have also investigated the behavior of devices as the electron density is further depleted into the quantum spin Hall regime [43, 62]. In the regime of high electron density and with no parallel magnetic field, our junctions display Josephson interference consistent with uniform supercurrent transport through the bulk of the quantum well, shown in Figure 6.1B for a device with aluminum leads.

We primarily study differential resistance with zero applied DC current, due to the efficiency of such measurements in illuminating the structure of the interference pattern. Lower resistance relative to the normal device resistance typically corresponds to elevated critical current (Section 6.8). In an aluminum-based junction, with the topgate voltage set to 0.5 V and with angle $\theta = \pi/4$, increasing the magnetic field in the x direction strongly modulates the Josephson interference (Figure 6.1C). Two distinct regions of decreased resistance are separated by a nodal field of approximately $B_x = 1.1$ T, corresponding to the suppression of induced superconductivity. At each value of the parallel field, we extract the minimum junction resistance as a measure of the strength of superconductivity at that particular field. Plotting these minimum junction resistances highlights the oscillatory effect of parallel field on superconductivity, with the nodal field marked by an arrow (Figure 6.1D). The suppression

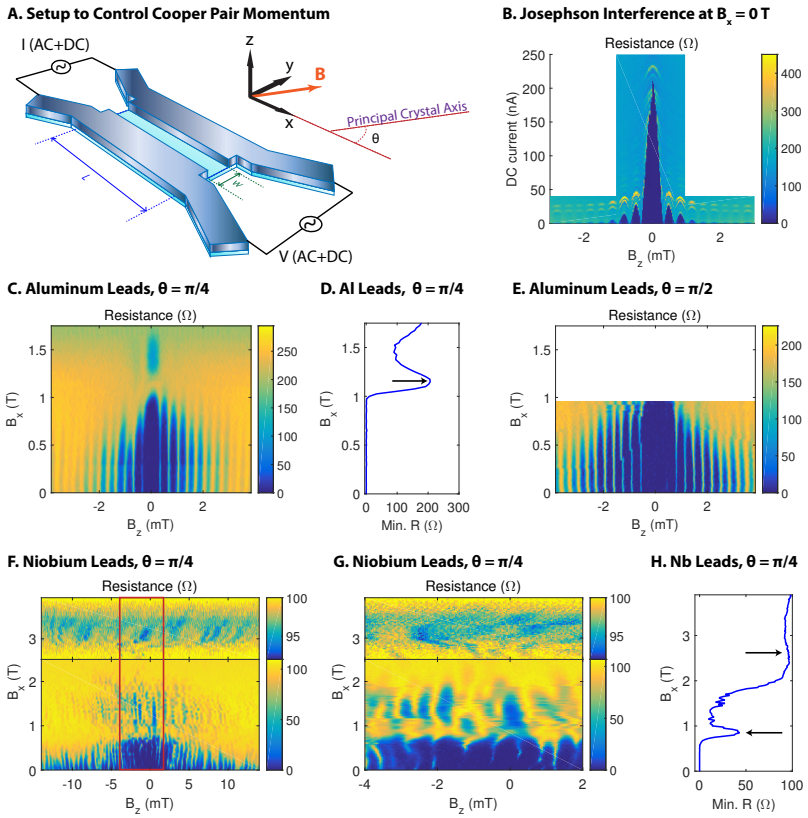

Figure 6.1: Experimental control of the order parameter and of pairing momentum. **(A)** Two superconducting leads, composed of either aluminum or niobium, couple to a rectangular section of HgTe quantum well to form a Josephson junction. The width W separating the leads is always 800 nm, while the length L of the junction is always 4 microns. The resistance of the junction is monitored by applying a small AC current bias (typically $\sim$ 1 nA) and concurrently measuring the resulting AC voltage. Further sourcing DC current allows measurement of critical currents and normal device resistance. The external magnetic field $\vec{B}$ contains a small z component to generate Josephson interference, while here the larger x component couples significantly to the spin-degree of freedom. Junctions may be oriented at an angle θ with respect to the $[100]$ principal crystal axis, modulo $\pi/2$. **(B)** In the electron-doped regime, the devices show Josephson interference consistent with transport through a doped bulk. In all subsequent measurements, zero DC current is applied. **(C)** The differential resistance of a junction with aluminum leads oscillates due to Josephson interference as the perpendicular field varies. Increasing the parallel field modulates the strength of induced superconductivity. **(D)** Plotting the minimum resistance at each value of B_x demonstrates the presence of a nodal resistance maximum near $B_x = 1.1$ T. **(E)** In an aluminum-based device oriented with $\theta = \pi/2$, increasing the parallel field similarly modifies the resistance. **(F)** In a junction with niobium leads, a similar modulation of the resistance occurs. **(G)** A more detailed study of the space outlined in red in (F) highlights three regions of decreased resistance separated by bands of high resistance near $B_x = 0.9$ T and $B_x = 2.7$ T. In both (F) and (G), the decreased resistance above 2.5 T is highlighted via a stretched color scale. **(H)** The minimum resistance at each value of B_x further shows the oscillatory nature of the superconductivity as the parallel field increases. Successively higher nodes (marked by arrows) occupy broader regions of parallel field, while superconductivity also weakens as the parallel field increases.

of superconductivity at the nodal field directly results from the finite momentum of induced Cooper pairs.

In an aluminum-based junction, with the topgate set to 0 V and oriented with $\theta = \pi/2$, a similar modulation of superconductivity occurs as the parallel field B_x grows (Figure 6.1E, see Section 6.9-6.10). Although the aluminum leads can sustain superconductivity up to 1.75 T, we only measure this device up to $B_x = 1$ T due to constraints on the range of our vector magnet (see Section 6.6).

The resistance of a device with niobium leads and $\theta = \pi/4$ is similarly modulated upon application of a parallel field, with multiple nodes visible as B_x increases to 4 T (Figure 6.1F). For these measurements the topgate voltage was set to 0 V. A more detailed measurement highlights the presence of three distinct regions of decreased resistance, separated by bands of high resistance occurring near $B_x = 0.9$ T and $B_x = 2.7$ T (Figure 6.1G). We again extract the minimum junction resistance at each particular parallel field value, demonstrating the oscillatory effect of parallel field on superconductivity (Figure 6.1H). Nodes of the oscillation, marked by arrows, correspond to local maxima in the overall junction resistance.

Despite the differences in fabrication of our devices, the nodal structure is both robust and occurs at nearly the same parallel field magnitudes. These observations suggest that the induced pairing momentum originates in the heterostructures and not the bulk superconductors, and is insensitive to details of the crystal orientation. Since superconductivity arises from pairing of electrons with opposing spins and momenta, it is therefore necessary to examine the nature of both Zeeman coupling and spin-orbit coupling within the quantum well.

6.3 Theoretical model of the proximity effect

We model our devices by considering first the quantum well region in the absence of the superconductors, for which a four-band theoretical Hamiltonian H_1 was proposed as a way to describe the topology of the band structure [12]. We adopt a version of this model to include both the external magnetic field and possible contributions from spin-orbit coupling [63, 99, 123]. The key prediction of the band structure modeling is that the Zeeman coupling from the external field B_x modifies the Fermi surfaces in a manner which depends on the nature of the spin-orbit coupling (Section 6.11). As a consequence, the induced superconducting order parameter is expected to oscillate in space, due to a pairing momentum shift with magnitude of order $\hbar\Delta k \approx \tilde{g}\mu_B B_x/v_F$, whose orientation also depends on the spin-orbit coupling. Here $\tilde{g}$ is the in-plane g-factor, and v_F is the Fermi velocity.

To theoretically investigate the proximity effect in our quantum wells, we consider a model in which the two-dimensional electron gas (2DEG), assumed to have uniform electron density, is contacted

by a pair of superconducting leads with a controlled phase difference between them, and we seek to calculate the maximum supercurrent that can be carried between the strips (Figure 6.3A, see Section 6.12-6.15 for details not presented here). Our model calculations cannot predict the absolute value of the critical current, but they should give the correct dependence on parameters such as the strength and direction of the magnetic field. We assume a Hamiltonian $H = H_1 + H_2$, where H_2 is the coupling between the superconductors and the 2DEG, described by a pairing Hamiltonian of the form

$$H_2 = -\int dxdy \left[\Delta(x,y)\Psi^\dagger(x,y) + \Delta^*(x,y)\Psi(x,y)\right]. \tag{6.1}$$

Here $\Psi(x,y) \equiv \psi_\uparrow(x,y)\psi_\downarrow(x,y)$ is an operator which annihilates a singlet pair of electrons in the 2DEG at the point (x,y), while the pair potential $\Delta(x,y)$ is a complex number that depends on the phase of the superconductor and the tunneling amplitude at that point.

We assume that the contacts between the 2DEG and the superconductors occur at the edges of the superconductors, located at $y = 0$ and $y = W$, so that we may write

$$\Delta(x,y) = \lambda_1(x)\delta(y) + \lambda_2(x)\delta(y-W) \equiv \Delta_1(x,y) + \Delta_2(x,y), \tag{6.2}$$

with $-L/2 < x < L/2$. We assume that the magnitude of the coupling is constant along each lead, but the phase will vary if there is a perpendicular magnetic field $B_z \neq 0$. We choose a gauge where the vector potential points in the x direction, with $A_x = -B_z(y - W/2)$, so that the vector potential vanishes along the midline of the 2DEG. If the superconducting strips have identical widths W_{SC}, then the couplings λ_j will have the form

$$\lambda_j(x) = |\lambda_j|\, e^{2\pi i \phi_j(x)}, \tag{6.3}$$

$$\phi_j(x) = \phi_j(0) + \frac{(-1)^{j-1} x B_z (W + W_{sc})}{2\Phi_0}, \tag{6.4}$$

with $j = 1, 2$.

To lowest order in the couplings λ_j, the portion of the total energy that depends on the phase difference between the two superconducting leads can be written in the form:

$$E = -\int dx_2 \left[\lambda_2^*(x_2) \left\langle \Psi(x_2, W)\right\rangle_1 + c.c.\right], \tag{6.5}$$

where $\left\langle \Psi(x,y)\right\rangle_1$ is the order parameter at point (x,y) induced by the superconductor $j = 1$. In

turn, this may be written in the form

$$\langle \Psi(x,y) \rangle_1 = \int dx_1 \lambda_1(x_1) F(x, x_1, y), \tag{6.6}$$

where F is the propagator from point $(x_1, 0)$ to point (x, y) for an induced Cooper pair. Depending upon the relative magnitudes of spin-orbit coupling and the Zeeman coupling, the propagator F may take various forms (see Section 6.14). Here we consider both structural inversion asymmetry (SIA), referring to asymmetry of the quantum well in the z direction [18], and bulk inversion asymmetry (BIA), referring to inversion asymmetry of the underlying crystal lattice [29]. In the limit where either SIA or BIA is strong compared to the Zeeman coupling, the pair momentum shift orientation is independent of position on the Fermi surface. The shift occurs along an angle α with respect to the x axis, and the propagator is

$$F(x, x_1, y) = \frac{k_F}{8\pi^2 v_F} \cdot \frac{e^{i\gamma} + e^{-i\gamma}}{(x - x_1)^2 + y^2}, \gamma = \Delta k \left(\sin(\alpha) y + \cos(\alpha)(x - x_1) \right). \tag{6.7}$$

In Figure 6.2, we calculate the order parameter $\langle \Psi(x,y) \rangle_1$ for several different limiting cases. When SIA dominates the spin-orbit coupling, a magnetic field B_x induces pairing momentum in the y direction, and the order parameter also oscillates in the y direction (Figure 6.2A). When $\Delta k W = \pi/2$, the first node of the oscillation coincides with the line $y = W$ corresponding to the width of the junction. Increasing the parallel field so that $\Delta k W = 3\pi/2$ leads to coincidence of the second node and the junction width (Figure 6.2B).

If BIA instead dominates the spin-orbit coupling, when $\theta = 0$ the parallel magnetic field induces order parameter oscillations in the x direction (Figure 6.2C). These oscillations arise due to the finite length of the Josephson junction, with amplitudes that are largest near the ends of the mesa. In contrast to the limit of large SIA, with dominant BIA the nodes of the order parameter never coincide with the junction width. Oscillations in the order parameter instead occur with greater frequency along the x direction as the magnetic field increases.

Finally, when the Zeeman coupling dominates the spin-orbit coupling, the pair momentum shift magnitude is isotropic in-plane, but the orientation lies parallel to the direction of Cooper pair propagation. In this limit the propagator is

$$F(x, x_1, y) = \frac{k_F}{8\pi^2 v_F} \cdot \frac{e^{i\gamma} + e^{-i\gamma}}{(x - x_1)^2 + y^2}, \gamma = \Delta k \sqrt{(x - x_1)^2 + y^2}. \tag{6.8}$$

Here the induced order parameter oscillates along both the x and y directions (Figure 6.2D). Al-

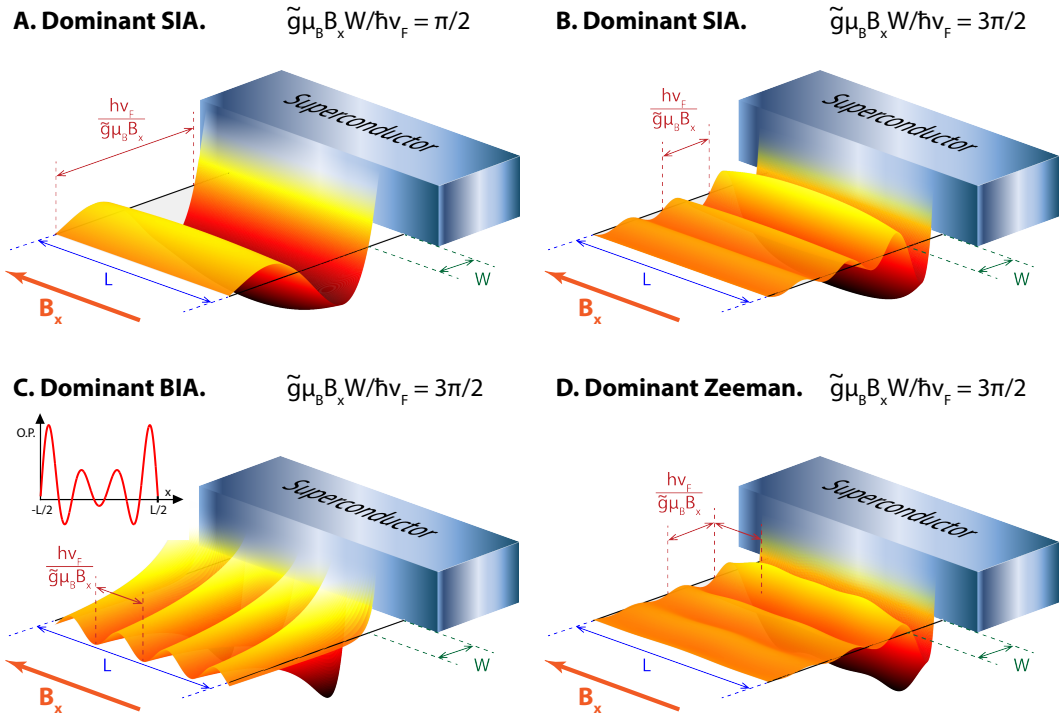

Figure 6.2: Theoretical prediction for the spatially varying order parameter $\langle \Psi(x,y) \rangle_1$ near a single superconducting lead, with $B_z = 0$. **(A)** With dominant SIA, application of an in-plane magnetic field B_x induces oscillations of the order parameter in the y direction, with wavelength $hv_F/\tilde{g}\mu_B B_x$. When $\tilde{g}\mu_B B_x W/\hbar v_F = \pi/2$ the first node of the order parameter occurs a distance W from the superconductor. **(B)** As the magnitude of magnetic field increases, the wavelength of order parameter oscillations decreases. When $\tilde{g}\mu_B B_x W/\hbar v_F = 3\pi/2$, the second order parameter node lies a distance W from the superconductor. **(C)** If instead BIA dominates, the order parameter oscillations occur in the x direction. As the magnetic field increases, the frequency of oscillations increases. In the inset, a linecut of the order parameter a distance W from the superconductor demonstrates that oscillations are an end effect, with amplitudes which decay into the bulk of the 2DEG. **(D)** With weak spin-orbit coupling, the parallel field B_x introduces order parameter oscillations in both directions.

though the shape of the order parameter resembles the limit of strong SIA, the possibility to oscillate in all in-plane directions prevents a node from forming along a line of constant y.

6.4 Modeling interference patterns with finite B_x

We can link the order parameter oscillations to the Josephson energy E by integrating over the second superconducting lead at position $y = W$, as in equation (6.5). By then differentiating with respect to the phase difference $\phi_2(0) - \phi_1(0)$ we find the current-phase relation of the junction, which is then maximized with respect to the phase difference to obtain the critical current.

When SIA dominates the spin-orbit coupling, the critical current periodically disappears when the nodal condition $\Delta k W = (2n + 1)\pi/2$ is satisfied (Figure 6.3B). This suppression of the critical current arises when singlet pairs injected at one lead evolve to become triplet pairs at the location of the second lead. The conversion to triplet pairing corresponds to nodes of the induced singlet order parameter; when these nodes coincide with the positions of the leads, the supercurrent is completely suppressed. Microscopically, these oscillations of the order parameter correspond to finite momentum pairing of electrons, as diagrammed in the inset of Figure 6.3B. In the limit of strong SIA, the Fermi surfaces oppositely shift in the y direction, so that Cooper pairs form internally to each surface with finite wavevector $\Delta k \hat{y}$. Furthermore, as the parallel magnetic field B_x increases beyond the nodal field $B_{\text{node}} = \frac{\pi}{2} \cdot \frac{\hbar v_F}{\tilde{g} \mu_B W}$, we observe evidence that the junction transitions into a π-junction (Section 6.17).

The predicted interference with strong SIA resembles the nodal pattern we observe experimentally. However, in both aluminum and niobium-based devices we also observe that superconductivity weakens as the parallel field increases, in contrast with the cosine dependence predicted by our model. We believe that this effect results from spatially inhomogeneous screening of the parallel field at the edges of superconducting leads. The superconductor repels the in-plane field and slight roughness at the edges results in a weak magnetic field along the z direction that is positive at some locations and negative at others. This screening leads to a spatially varying random component of the phase that grows linearly with the in-plane field. Hence, we introduce a random phase $\chi \propto (R_1(x_1) - R_2(x_2))\, B_x$, where the random variables $R_1(x_1)$ and $R_2(x_2)$ correspond to fluctuations in the direction of the parallel field at each interface (see Section 6.16 for details). With this randomness, the calculated critical currents diminish in magnitude as the in-plane field increases, in agreement with our experimental observation (Figure 6.3C).

Considering, instead, BIA as the dominant source of spin-orbit coupling, when the junction is aligned to the [100] or [010] crystal direction, the order parameter oscillates in the x direction. This oscillation corresponds to shifting of the Fermi surfaces oppositely along x, so that Cooper pairs form

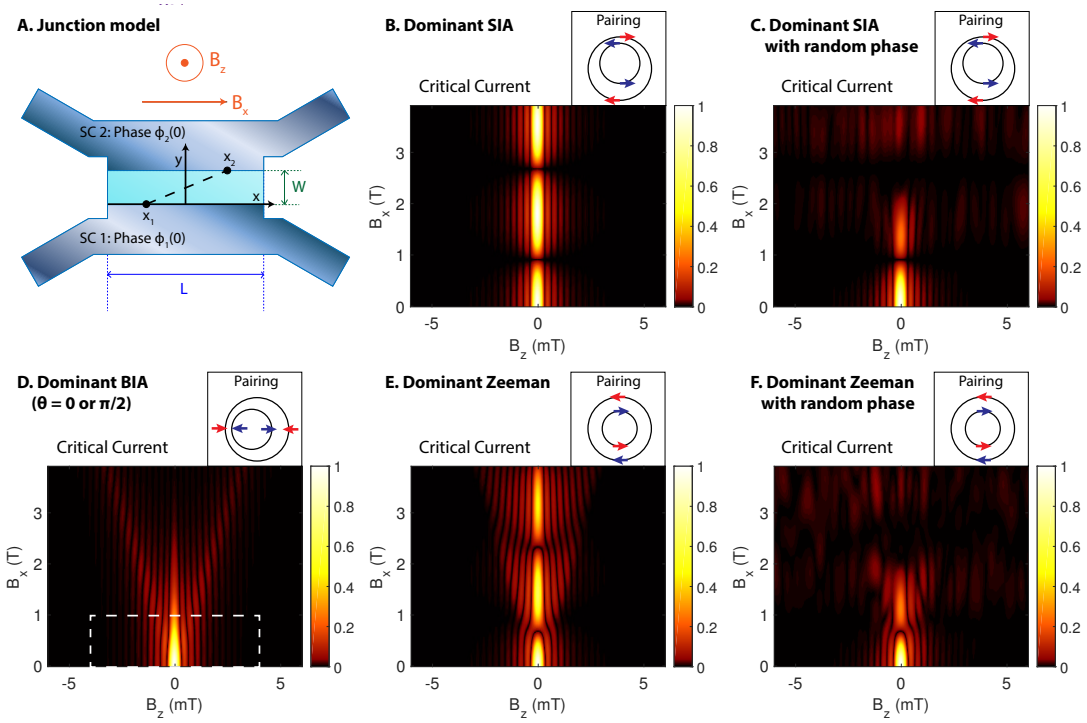

Figure 6.3: Modeling Josephson interference between two superconducting leads. **(A)** With two leads, paired electrons may traverse the junction beginning at a point x_1 in the lower superconducting lead (SC 1). The pairing amplitude at the point x_2 in the upper lead (SC 2) takes account of the phase accumulated due to finite pairing momentum within the HgTe quantum well. **(B)** With SIA dominant, the external magnetic field B_x increases the pairing wavevector Δk only in the y direction. At certain values $\Delta k = (2n+1)\pi/(2W)$, n integer, the superconducting interference disappears. A diagram schematically depicts the expected Fermi surfaces and Cooper pairing, where arrows denote spin direction and pairs are each colored blue or red. Similar diagrams throughout this figure indicate the expectation for pairing and Fermi surfaces as the model parameters change. **(C)** Randomness at the interface between the quantum well and superconductors may arise due to structural imperfections. The random phase causes superconductivity to weaken as the parallel field increases. **(D)** For junctions aligned to a principal crystal axis, dominant BIA leads to a pairing wavevector Δk that grows in the x direction as B_x increases. The critical current maxima then occur at increasingly large values of $|B_z|$ as B_x grows. Fabricating devices at varying angles with respect to the crystal is expected to modify the interference when BIA dominates. The region outlined in dashed white corresponds to the measured region in Figure 6.1E. **(E)** With dominant Zeeman coupling, the pairing magnitude is isotropic in-plane and the interference grows as a hybrid of the SIA and BIA cases. Characteristically, interference fringes repeatedly combine to form the central fringe at each successive node in the parallel field. Additionally, with zero perpendicular field, superconductivity disappears at values of parallel field that are smaller than the nodal magnetic field in the case with dominant SIA. **(F)** Including randomness leads to a similar picture to (C), while retaining the combining of fringes characteristic of dominant Zeeman coupling.

internally to each surface with wavevector $\Delta k\hat{x}$ (Figure 6.3D). Since the real-space supercurrent density and the Josephson critical current can be regarded as Fourier conjugates [30], this pairing momentum results in finite weight of the interference at a particular magnitude of B_z that grows linearly with the parallel field, forming a 'V' shape. In our measurements of the device oriented with $\theta = \pi/2$, this splitting would be seen in the limit of strong BIA, but is not observed experimentally (Figure 6.3E, Section 6.10). Additionally, when junctions are fabricated at an angle $\theta = \pi/4$, with strong BIA the behavior is expected to shift from that shown in Figure 6.3D to the nodal structure in Figure 6.3B. Since we instead observe behavior that does not depend on the crystal orientation, we conclude that BIA in our heterostructure is relatively weak. This conclusion agrees with a previous measurement of Shubnikov-de Haas oscillations in a HgTe quantum well, which was found to be consistent with strong SIA and weak BIA [39].

In the limit of overall weak spin-orbit coupling, the order parameter oscillates in both in-plane directions. Zeeman coupling at finite values of B_x leads to two concentric Fermi surfaces with opposite spin polarization, so that pairing occurs between surfaces with momentum in all in-plane directions (Figure 6.3E). Increasing the parallel magnetic field causes the interference to both spread in B_z and periodically oscillate, a hybrid of the two above cases. Characteristically, at each node the two interference fringes adjacent to the central fringe combine to form the subsequent central fringe, a direct result of the inability to form nodes in the order parameter along lines of constant y. Although it is possible that this behavior is present in the device with niobium leads, the nodal pattern is more consistent with strong SIA with aluminum leads at high density. In the limit of overall weak spin-orbit coupling, with the random phase χ the modeled interference successfully reproduces many aspects of the behavior observed in the niobium device, but is still inconsistent with the aluminum devices (Figure 6.3F).

6.5 Density dependence

As an additional study into the nature of electron pairing momentum, we explore the evolution of the minimum junction resistance at different parallel field B_x values, while energizing the global topgate to modify the bulk electron density. Devices used for these measurements were aligned such that $\theta = \pi/4$, corresponding to the devices of Figure 6.1C,D,F-H. At the most positive gate voltage, as the magnetic field is increased the niobium device displays the node of increased resistance near $B_x = 0.9$ T (Figure 6.4A). As before, an additional node is present near $B_x = 2.7$ T. When the top gate voltage is lowered to -5 V, the field magnitude of the lower node increases, first slowly and then more rapidly. In the device with aluminum leads, a similar nodal structure is observed, with the magnitude of the

nodal field weakly increasing as the top gate voltage is lowered from 0.5 V to 0 V (Figure 6.4B). Due to a doping layer in the heterostructure of the niobium device, more negative gate voltage is required in this device to achieve depletion (see Section 6.6).

The dependence of the nodal field magnitude on density can be calculated within the framework of our model based on BHZ theory, here assuming the presence of SIA due to a perpendicular electric field equal to 10 mV/nm (Section 6.11). Since the magnitude of the induced Cooper pair momentum is approximately $\hbar\Delta k \approx \tilde{g}\mu_B B_x/v_F$, the dependence of both $\tilde{g}$ and v_F on the electron density will directly influence the magnitude of the parallel field needed to satisfy the nodal condition $\Delta k W = (2n+1)\pi/2$. Due to the inverted nature of the bands, the g-factors in the conduction bands are expected to evolve from -20.5 toward zero as the Fermi wavevector decreases [63], while the expected magnitudes of the Fermi velocities first decrease slightly and then more rapidly fall to zero (Figure 6.4C, D). With these considerations we expect the magnitudes of the induced pairing wavevectors at 1 T to fall to zero from values near $1.2/\mu$m as the Fermi wavevector decreases (Figure 6.4E). As a result, the magnetic field needed to satisfy the nodal condition increases as the electron density decreases, finally diverging at zero electron density (calculated in black dotted lines in Figure 6.4A-B). Although the overall evolution agrees well with the expectation from BHZ theory, we find that our measurements on niobium and aluminum devices respectively yield values of $\tilde{g}/v_F$ that are approximately 1.9 and 1.4 times greater than those expected theoretically (see Section 6.11).

Several aspects of the density-dependent data do not fall into the modeling framework discussed above, and are interesting for further consideration. First, we expect that the position of the node associated with induced Cooper pair momentum should occur at higher parallel magnetic field as the density is reduced, a behavior that we observe only at high density. As the density is further reduced, the magnitude of the nodal field eventually begins to decrease, an element of our model that is not present and remains to be understood, but could possibly be explained by a finite g-factor at zero density. Second, in the aluminum device, the region of reduced resistance occuring above the first node appears to be strongest near top gate voltages equal to -0.9 V and 0.5 V. We observe that these two regions of reduced resistance are connected by a region in which the resistance is more weakly reduced, but we have no reason to expect that the reduction in resistance above the first node should vary as the density decreases.

Our measurements demonstrate that a parallel magnetic field can be used both to tune the momentum of Cooper pairs in a material and to clarify the nature of spin-orbit coupling in that material. A major current goal of condensed matter physics is to understand the nature of the superconductivity that results when electron pairing is combined with materials possessing exotic spin textures. Therefore our new understanding that the superconducting order parameter can be engineered in space may

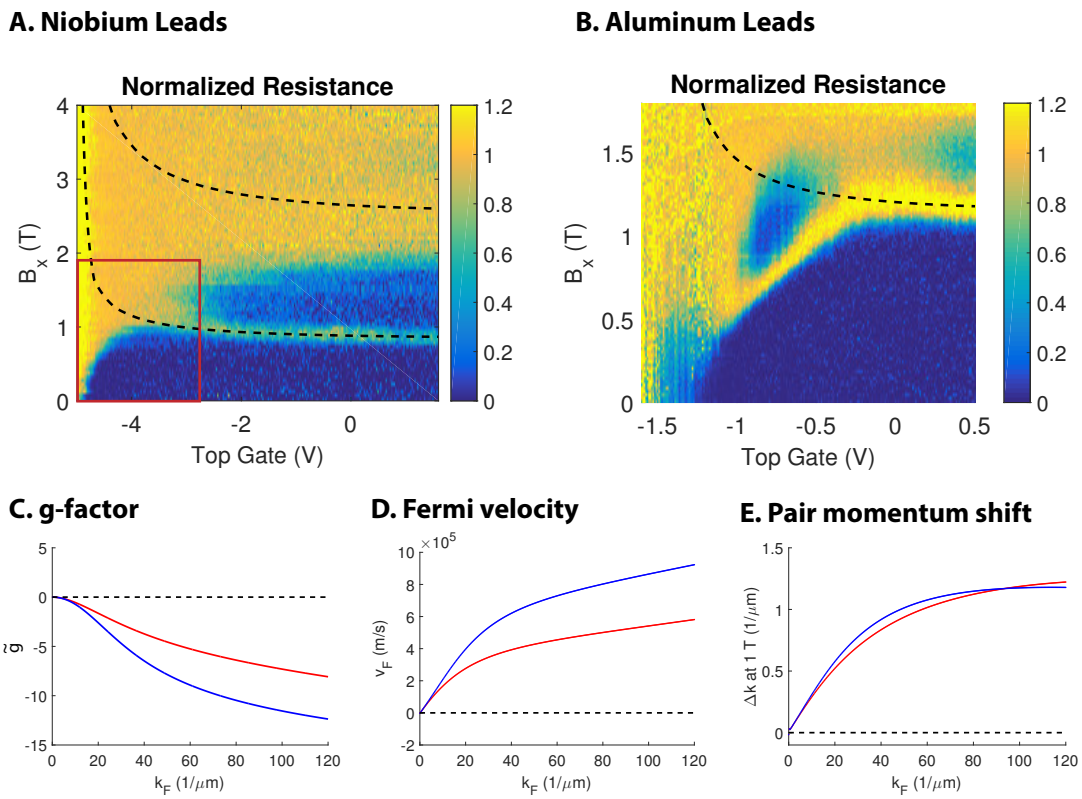

Figure 6.4: The evolution of minimum differential resistance as density and parallel magnetic field B_x vary. Differential resistance measurements are normalized at each point by the normal junction resistance. **(A)** At the highest gate voltage in the niobium junction, increasing the magnetic field leads to periodic high-resistance nodes separating regions of decreased resistance. As the gate voltage is decreased, the magnetic field at the first node rises to larger values of B_x. **(B)** The aluminum junction behaves similarly to the niobium junction, although the measurement is limited to a smaller region outlined in red in (A). At low density, the magnitude of the nodal magnetic field begins to decrease as the density is lowered, a feature which remains to be understood. **(C)** The values of B_x at which we expect nodes to appear are sensitive to the density dependence of both the in-plane g-factors and the Fermi velocities, calculated here assuming that SIA is due to an electric field of 10 mV/nm. Blue and red curves correspond to the inner and outer Fermi surfaces, respectively. As the magnitude of the Fermi wavevector k_F decreases, the in-plane g-factors shift from -20.5 toward zero. **(D)** Meanwhile the magnitudes of the Fermi velocities decrease to zero. **(E)** The pairing momenta induced at 1 T consequently decrease to zero from approximately 1.2/μm. Since there can be no induced momentum at zero density, the nodal magnetic field diverges as the density is lowered. The nodal magnetic field, averaged over the two Fermi surfaces, is calculated using BHZ theory and plotted as dashed black lines in (A) and (B).

be utilized to investigate spin physics within a broad range of materials including InAs-based quantum wells or the surfaces of three-dimensional topological insulators. Our method to tune the Josephson energy could find additional application in the field of quantum information processing, where direct control of the energy levels in a single superconducting qubit could provide a powerful tool for the investigation and optimization of qubit coherence.

6.6 Wafer characteristics and General Measurements

Junctions were fabricated using HgTe/HgCdTe heterostructures grown in the $[001]$ crystal direction (the z direction), composed as shown in Figure 6.5. Wafer I contained an 8 nm quantum well with an electron density of $13.5 \times 10^{11}/\text{cm}^2$ and a mobility of $390,000\ \text{cm}^2/\text{Vs}$. Wafer II contained a 7.8 nm quantum well with an electron density of $2.9 \times 10^{11}/\text{cm}^2$ and a mobility of $790,000\ \text{cm}^2/\text{Vs}$. Josephson junctions fabricated on these wafers were aligned at varying angles with respect to the $[110]$ and $[1\bar{1}0]$ cleavage edges of the crystal, but we do not know which is which in our samples. Therefore, we can only specify that the angular alignment corresponds to a rotation angle θ with respect to the $[100]$ crystal axis, modulo $\pi/2$. Although we do not know which principal axis θ is referenced to experimentally, our model predicts the same results when θ is referenced to either. The x and y axes always lie respectively perpendicular and parallel to the direction of current flow in devices (see Figure 6.1).

Throughout the remainder of this chapter, devices are referred to in the following manner. Device A was fabricated by depositing aluminum leads onto a mesa etched into Wafer I, and was oriented at an angle $\theta = \pi/4$. Devices B, C, and D were concurrently fabricated by depositing aluminum leads on Wafer II, and were respectively oriented at different angles $\theta = 0, \pi/2$, and $\pi/4$. Device E was fabricated using Wafer I, contained niobium leads, and was oriented at $\theta = \pi/4$. Device F was fabricated using Wafer I, contained aluminum leads, and was oriented at $\theta = \pi/4$. Note that data from devices C, D and E were reported in the main text.

Devices were processed as follows. To define the ends of the junctions, mesas 100 nm in height were etched using an argon ion source. To fabricate superconducting contacts, the contact area was etched enough to expose the quantum well using argon milling. Without breaking vacuum, the contact material was then deposited. For devices A-D and F, 5 nm of titanium was deposited by thermal evaporation, followed by thermal evaporation of 15 nm of aluminum. For device E, 10 nm of titanium was deposited by e-beam evaporation, followed by 130 nm of niobium deposited by DC magnetron sputtering. Next, a 50 nm layer of aluminum oxide was grown using atomic layer deposition, to isolate the final topgate layer (10 nm of titanium and 250 nm of gold) from the underlying junctions.

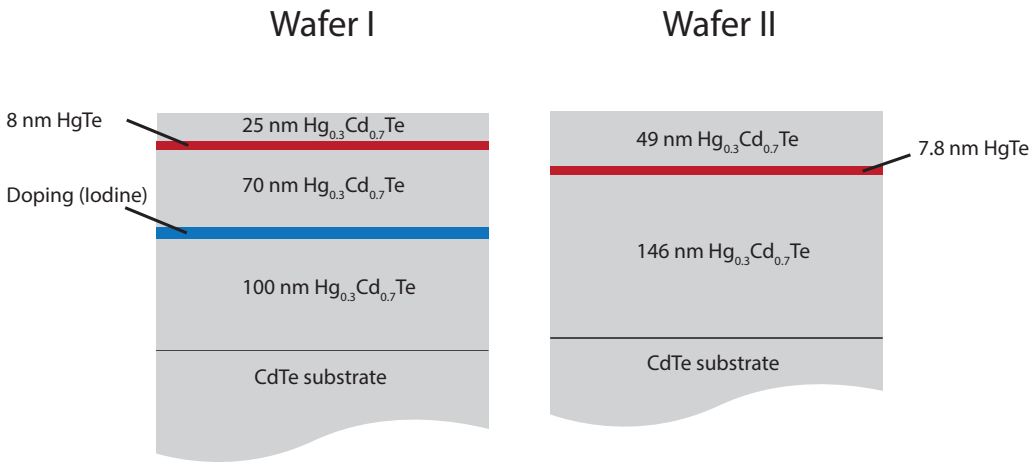

Figure 6.5: Composition of the heterostructures used in the experiment, labeled Wafer I and Wafer II. Both wafers consist of a HgTe quantum well surrounded by barriers of $Hg_{0.3}Cd_{0.7}Te$. In Wafer I, a layer containing iodine dopants lies 70 nm below the quantum well. Both wafers were grown on CdTe substrates, in the $[001]$ crystal direction.

Measurements were performed primarily in a dilution refrigerator outfitted with a $6-1-1$ vector magnet capable of applying up to 6 T in one direction, and 1 T in the two remaining directions. Experiments were carried out at the mixing chamber base temperature of 50 mK. Unless otherwise mentioned, all measurements occurred in this system. Two measurements were performed in a separate dilution refrigerator with a base temperature of 10 mK.

As either the external magnetic field or the topgate voltage was varied, the differential four-terminal resistance of junctions was monitored using standard lock-in techniques. To determine critical currents or to provide bias sufficient to measure the normal resistance of the junctions, sometimes a DC current bias was applied to the junctions. Otherwise all measurements occurred with no DC current bias.

6.7 Characterization of Thin Aluminum Leads

The resistance of thin aluminum leads was characterized as a function of magnetic field in both the x direction and the y direction (Figure 6.6). In each plot, red and blue color coding corresponds to the two leads of a single junction. Different junctions were used in the two plots, demonstrating the consistency of the fabrication process. The critical parallel field of the 15 nm aluminum films was consistently above 1.5 T, in agreement with a previous study of thin aluminum [81]. The data

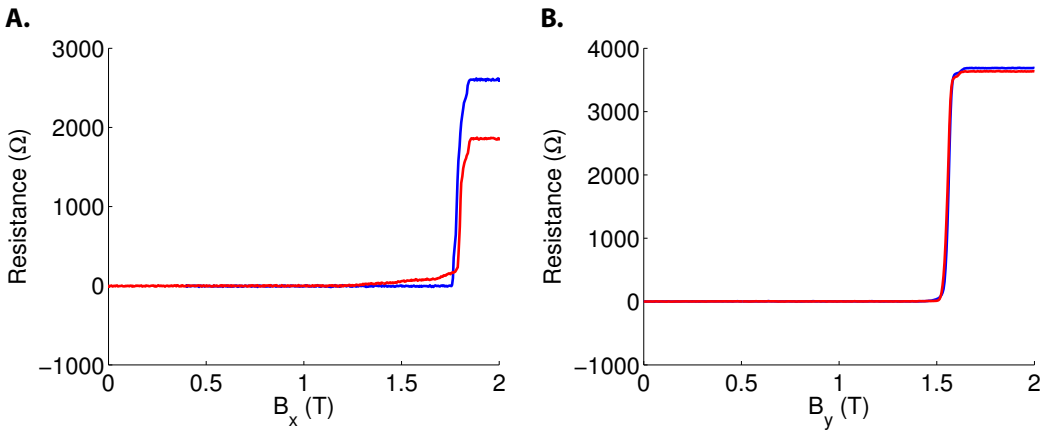

Figure 6.6: Resistances of junction leads as the parallel magnetic field is increased in the x and y directions, for junctions with aluminum leads. The critical field in the plane of the leads is consistently above 1.5 T.

presented in Figure 6.6B was collected at a temperature of 10 mK in the system discussed previously.

6.8 Critical Current of a Josephson Junction Under External Parallel Magnetic Field

Here we present measurements of the critical current in device D, for different values of the external magnetic field. When compared to corresponding measurements of differential resistance without any applied DC current (Figure 6.8E and Figure 6.9E), it is apparent that both measurement modes reveal the same basic behaviors.

In the measurements of critical current presented here, increasing the external field in either the x or y direction results in a decrease of the maximum critical current (Figure 6.7A, B). This decrease occurs more rapidly for B_y, where the critical current becomes too small to reliably measure when B_y exceeds 0.44 T. B_x, however, must exceed 1.1 T before critical currents become immeasurably small.

Upon normalization of the interference pattern at each separate value of parallel field, the asymmetry between the two directions becomes more pronounced (Figure 6.7C, D). At all values of B_x, the shape of the Josephson interference remains essentially unaffected. By contrast, as B_y increases the critical current splits into two separate maxima which occur at larger values of $|B_z|$. In Section 6.16 we model the effect of the in-plane field B_y, which we expect to induce a finite x component of the pairing wavevector that grows linearly with B_y. In junctions with finite length and with $B_z = 0$, this pairing momentum in the x direction leads to oscillations in the order parameter which are most pronounced near the ends of the junction. As a consequence, we expect that as B_y increases, the max-

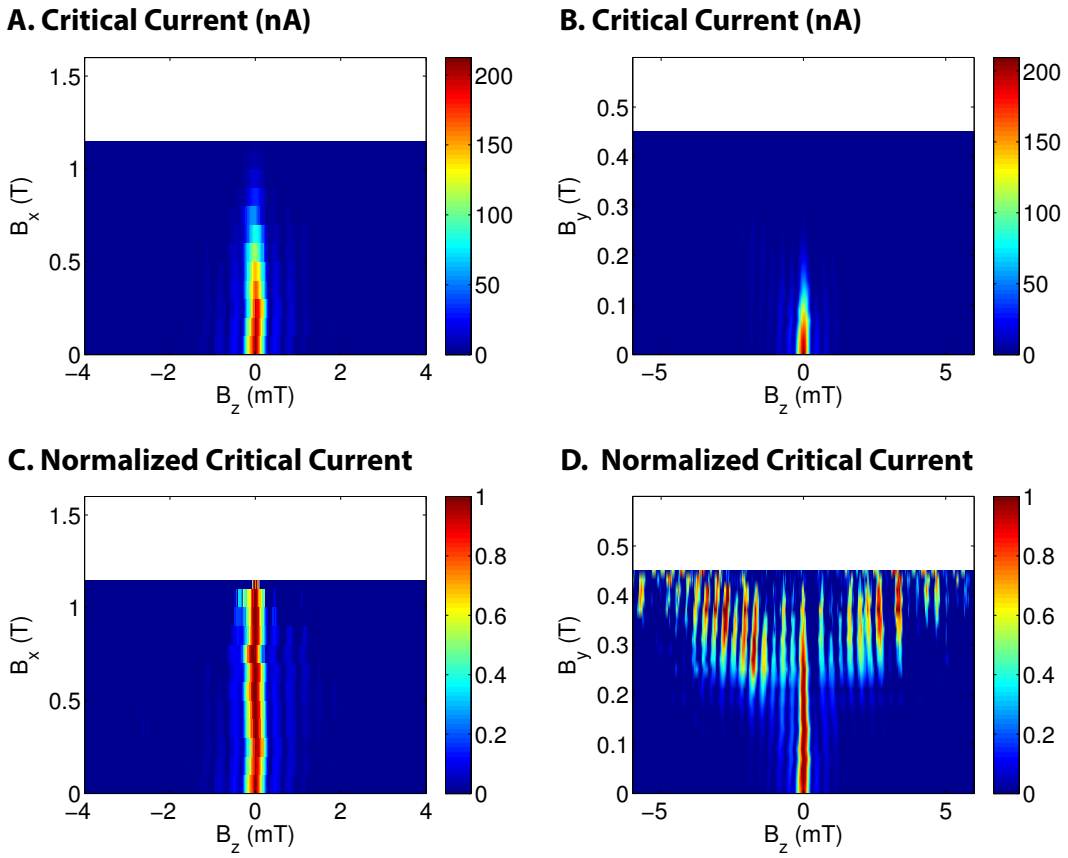

Figure 6.7: The critical current as a function of perpendicular magnetic field B_z, as parallel components of the magnetic field are varied. The data presented here was taken using the device with aluminum leads presented in the main text (device D). **(A, B)** As the parallel magnetic field in either the x or y direction is increased, the magnitude of the maximum critical current decreases. This decrease occurs more rapidly in y direction than in the x direction. **(C)** Normalizing the Fraunhofer interference at each value of B_x shows that the shape of the interference pattern remains essentially unaffected until it becomes immeasurably small. **(D)** In the B_y direction, normalization reveals a dramatically different behavior of the Fraunhofer interference, where critical current maxima occur at higher values of B_z as B_y is increased. Concurrently, the weight of the critical current at $B_z = 0$ mT decreases to 0. These observations match those deduced through measurements of the differential resistance as the parallel magnetic field varies in either the x or y direction. Therefore both differential resistance and critical current measurements reflect the same basic phenomenon.

imum critical currents in our junctions will occur at values of $|B_z|$ that grow linearly with B_y. With only the parallel field B_x present, however, the induced pair momentum is expected to lie along the y direction. In this case no such wavevector in the x direction is observed.

6.9 Josephson Junctions Rotated with Respect to the Crystal

Measurements of the differential resistance were performed on junctions oriented at different angles with respect to the crystal lattice, in order to determine whether bulk inversion asymmetry (BIA) plays a significant role in the momentum acquired by Cooper pairs. As previously mentioned, these devices A-E have orientation $\theta = \pi/4, 0, \pi/2, \pi/4$, and $\pi/4$ respectively. Devices A-D use aluminum leads, while device E uses niobium leads. For each set of the devices, we explored behaviors resulting from a parallel magnetic field applied in the x direction or in the y direction, which in the previous section were shown for device D to differ.

Even as the angle θ varies among devices, the manner in which superconductivity evolves due to the applied field B_x remains qualitatively unchanged at high density (Figure 6.8). Devices B-D, fabricated on a single piece of wafer, show quantitative agreement in the value of B_x at which a superconducting node appears. Devices A and E were separately fabricated on Wafer I, and show slight quantitative differences but nevertheless the same shape. The appearance of these nodes in the interference evolution, with no dependence on the crystal orientation, signals that structural inversion asymmetry (SIA) dominates the behavior of our quantum wells in the electron-doped regime (Section 6.11-6.14).

With the parallel field applied in the y direction and at high density, the interference pattern splits, forming a 'V' shape as B_y increases that is qualitatively identical for all values of θ (Figure 6.9). The slope of the two arms of the 'V' varies among devices, but is similar for devices B-D which were fabricated concurrently. The most dramatic effect is seen for device E with 130 nm thick niobium leads, in which the slope is approximately 7 times smaller than the other devices.

From the above measurements one can conclude that the basic differences in interference as B_x or B_y is increased have little to do with the orientation of the crystal lattice. The most striking difference is found among the data with the magnetic field oriented along the y direction, in which the thickness of the leads correlates to the slope of the interference splitting. This behavior, which results from magnetic flux penetrating the area dL formed by the length L of the junction and the height difference d between the center of the quantum well and the center of the leads, is modeled in Section 6.16.

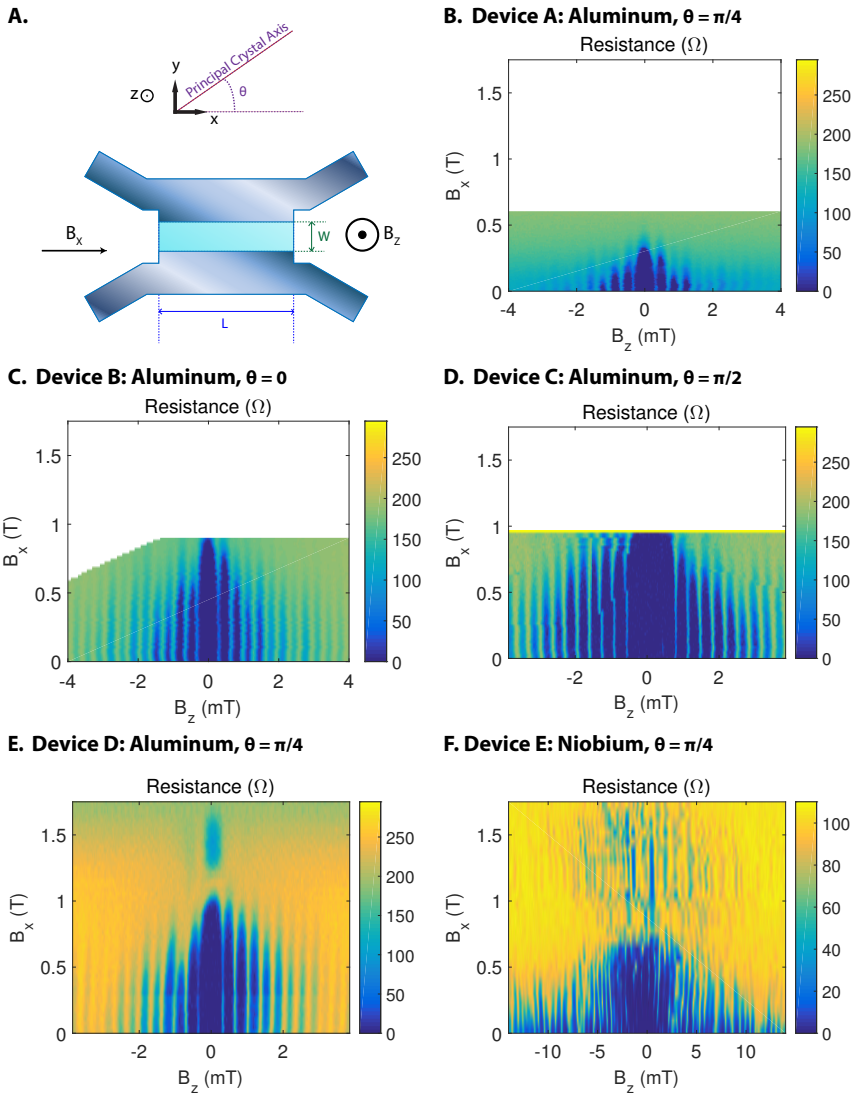

Figure 6.8: Josephson interference as the magnetic field B_x is increased. **(A)** Junctions were oriented at an angle θ, modulo $\pi/2$, with respect to the $[100]$ axis of the crystal. Devices generating data in (C-E) were concurrently fabricated with respect to the same crystal cleavage edge. Devices in (B) and (F) were separately fabricated. All junctions had aluminum leads except for in (F), where niobium leads were used. **(B)** For a junction oriented at $\theta = \pi/4$ with respect to the crystal, the differential resistance is monitored as both the perpendicular field B_z and the parallel field B_x are altered. As B_x increases, the position of nodes in the interference pattern does not change, but the interference gradually disappears. **(C)** A junction oriented at $\theta = 0$ and **(D)** a junction oriented at $\theta = \pi/2$ with respect to the crystal show qualitatively identical behavior. **(E)** A further junction aligned at $\theta = \pi/4$ shows the same behavior, as previously presented in the main text. **(F)** Also in the main text, the junction with niobium leads is oriented with $\theta = \pi/4$ and shows interference which remains strongly weighted at $B_z = 0$ T. The observations on aluminum devices are all consistent with dominant SIA in the quantum well.

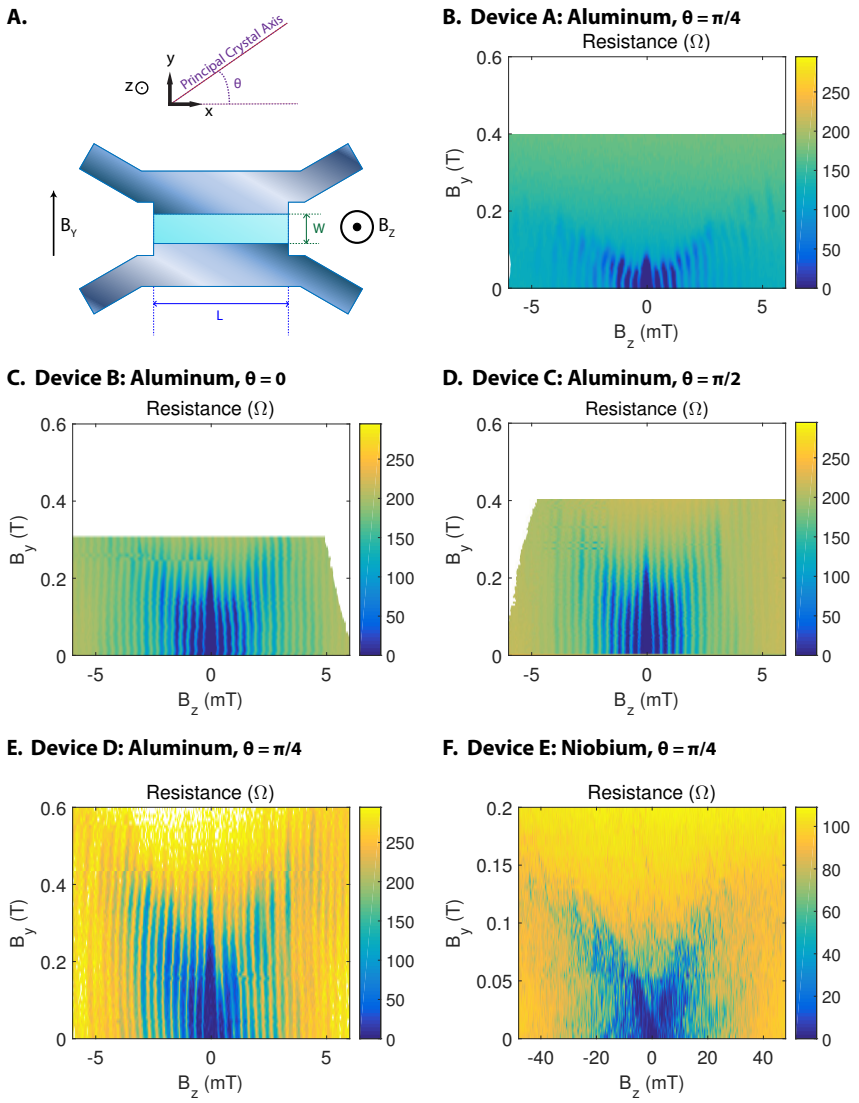

Figure 6.9: Josephson interference as the magnetic field B_y is increased. **(A)** Junctions were oriented at an angle θ, modulo $\pi/2$, with respect to the $[100]$ axis of the crystal. As in Figure 6.8, devices generating data in (C-E) were concurrently fabricated with respect to the same crystal cleavage edge, and devices in (B) and (F) were separately fabricated. **(B)** With the junction aligned such that $\theta = \pi/4$, the differential resistance is monitored as a function of the perpendicular field B_z and the parallel field B_y. Increasing B_y rapidly causes the weight of interference fringes to shift to larger B_z values, forming a `V' shape. The interference evolves more rapidly due to a parallel field in the y direction than in the x direction due to the fact that leads are spatially displaced in z with respect to the quantum well. **(C)** Orienting a junction at $\theta = 0$ introduces no qualitative change to the behavior, as is also the case with **(D)** a junction oriented at $\theta = \pi/2$. Junctions from the main text with **(E)** aluminum and **(F)** niobium leads are presented, also displaying similar behavior. The enhanced scale of B_z in the niobium-based junction is due to the increased thickness of the leads.

6.10 Evolution of Interference Lobes as the Parallel Magnetic Field B_x Increases, in a Device with $\theta = \pi/2$

In the previous section, it was observed that at particular values of the parallel magnetic field B_x, nodes of suppressed superconductivity occur in our Josephson junctions. Additionally, this evolution of the Josephson interference with the parallel field B_x does not depend on the device orientation with respect to the crystal. The appearance of nodes with lack of θ dependence already suggests that the effect of bulk inversion asymmetry (BIA) in our devices is small, and that structural inversion asymmetry (SIA) dominates (Section 6.11- 6.14). Still, the evolution of critical currents, in particular the maximum critical current of interference lobes occurring at nonzero perpendicular field, can provide further evidence that BIA is weak. When $\theta = \pi/2$, in the limit of strong BIA these side lobe maximum critical currents are expected to grow as the parallel field B_x is increased from zero (Figure 6.3D). However, if SIA is strong, these critical currents are expected to monotonously decay as the parallel field increases up to the first node.

In Device C, oriented at $\theta = \pi/2$, we study the evolution of the first three side lobes adjacent to the central lobe (Figure 6.10A). A measurement of the critical currents of these lobes indicates that all lobes are largest when $B_x = 0$ T (Figure 6.10B). We extract the maximum critical current for each side lobe, plotted in Figure 6.10C for each lobe. All critical currents are largest when $B_x = 0$ T, and all decay monotonously until becoming indistinguishable from zero. This evolution of the side lobe critical currents provides additional evidence consistent with weak BIA in our devices.

6.11 Four-Band Model and Spin-Orbit Effects in the Quantum Well

A four-band model has been developed starting from $k \cdot p$ theory, and subsequently used to describe the topology of HgTe quantum wells [12]. Here we adopt an elaboration on this model, where bulk inversion asymmetry (BIA), structural inversion asymmetry (SIA), and coupling to an external magnetic field are included. The four bands originate in the $s-$ and $p-$like bands of the underlying crystals, so that the basis states are written as $|E1, m_J = +1/2\rangle$, $|H1, m_J = +3/2\rangle$, $|E1, m_J = -1/2\rangle$, and $|H1, m_J = -3/2\rangle$. In this notation, $E1$ refers to electron-like states with angular momentum 1/2, while $H1$ refers to hole-like states with angular momentum 3/2. The Hamiltonian describing the

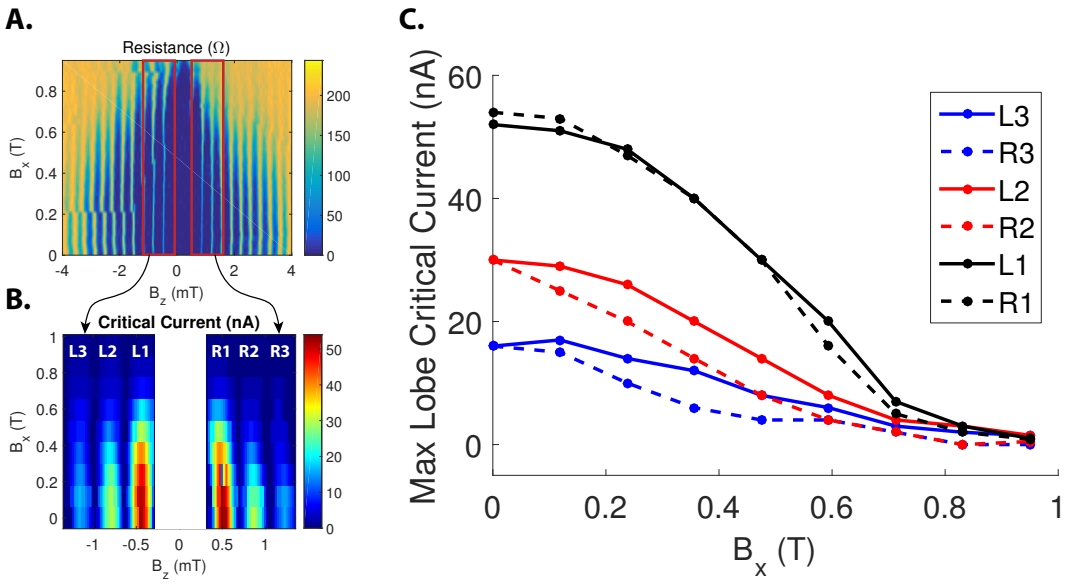

Figure 6.10: Evolution of critical currents, in Device C, oriented such that $\theta = \pi/2$. Data was taken with the top gate voltage set to 0 V. **(A)** The differential junction resistance, measured with no applied DC current, evolves consistently with the absence of BIA in the device. **(B)** The critical currents in the interference side lobes adjacent to the central lobe decay as the parallel field B_x increases from zero. The region of the critical current measurement is outlined in red in (A). Each side lobe is labeled in white. **(C)** The extracted maximum critical current for each side lobe. Within each lobe, the critical current decreases from its maximum value at $B_x = 0$ T.

system is then [63, 99, 123]:

$$H_1 = \epsilon\left(\hat{k}^2\right) + M\left(\hat{k}^2\right)s_z + A\hat{k}_x s_x\sigma_z - A\hat{k}_y s_y + h\left(\cos(2\theta^{th})\sigma_y + \sin(2\theta^{th})\sigma_x\right)s_y + R_0\tfrac{s_z+1}{2}\left(\hat{k}_x\sigma_y - \hat{k}_y\sigma_x\right) - \mu_B\cdot\vec{B}\cdot\vec{M} \tag{6.9}$$

where

$$\epsilon\left(\hat{k}^2\right) = C - D\left(\hat{k}_x^2 + \hat{k}_y^2\right), M\left(\hat{k}^2\right) = M - B\left(\hat{k}_x^2 + \hat{k}_y^2\right) \tag{6.10}$$

and

$$M_x = g_{||}\sigma_x\frac{1+s_z}{2},\ M_y = g_{||}\sigma_y\frac{1+s_z}{2},\ M_z = g_{E\perp}\sigma_z\frac{1+s_z}{2} + g_{H\perp}\sigma_z\frac{1-s_z}{2}. \tag{6.11}$$

The first four terms are those present in the original theory of Bernevig, Hughes, and Zhang. The fifth term describes the magnitude h of the BIA and the angle θ^{th} between the x axis and the $[100]$ crystal direction. The sixth term includes SIA with strength $R_0/(e\mathcal{E})$, where $\mathcal{E}$ is the magnitude of an electric field oriented along the z axis. Coupling to the external magnetic field occurs anisotropically and is different for $E1$ and $H1$ states due to the inability of magnetic field to couple $m_J = \pm 3/2$ to first order. The value of the parallel g-factor $g_{||}$ and perpendicular g-factors $g_{E\perp}$ and $g_{H\perp}$, along with all other parameter values, are listed in Table 6.1. The in-plane wavevectors are $\hat{k}_x = i\partial_x$ and $\hat{k}_y = i\partial_y$.

The bare effect of a parallel magnetic field is visualized by setting $h = 0$ and $R_0 = 0$ and calculating the conduction band spectrum, under various values of $\vec{B}$ (Figure 6.11A-C). In each plot, the bands are plotted up to the Fermi energy, which varies in order to demonstrate various limiting cases of weak or strong spin-orbit coupling. The Fermi surfaces are projected onto a plane below the bands, with the spin texture plotted at various points on the Fermi surfaces. The x and y components of the spin vectors are equal respectively to $\langle\sigma_x\left(1+s_z\right)/2\rangle$ and $\langle\sigma_y\left(1+s_z\right)/2\rangle$, the spin expectation values projected onto the $E1$ bands.

With no external magnetic field, the conduction band is doubly degenerate due to the presence of the spin degree of freedom, modeled here up to a Fermi energy equal to 20 meV. Changing the magnetic field to 3 T in the x direction lifts this degeneracy due to the Zeeman effect, resulting in two concentric Fermi surfaces centered at $\vec{k} = 0$. Within the outer Fermi surface, spins point toward $-x$, due to the negative value of $g_{||}$. Within the inner Fermi surface, spins are oppositely oriented.

A (eV·Å)	B (eV·Å^2)	D (eV·Å^2)	M (eV)	h (eV)	θ^{th}	$R_0/(e\mathcal{E})$ (nm^2)	$\mathcal{E}$ (mV/nm)	$g_{E\perp}$	$g_{H\perp}$	$g_{\|\|}$
3.645	−68.6	−51.2	−0.010	0, 0.0016	0	−15.6	0, 10	22.7	−1.21	−20.5

Table 6.1: List of parameters used to model the band structure. Parameters correspond to a quantum well in the inverted regime, with a well width of 70 Å.

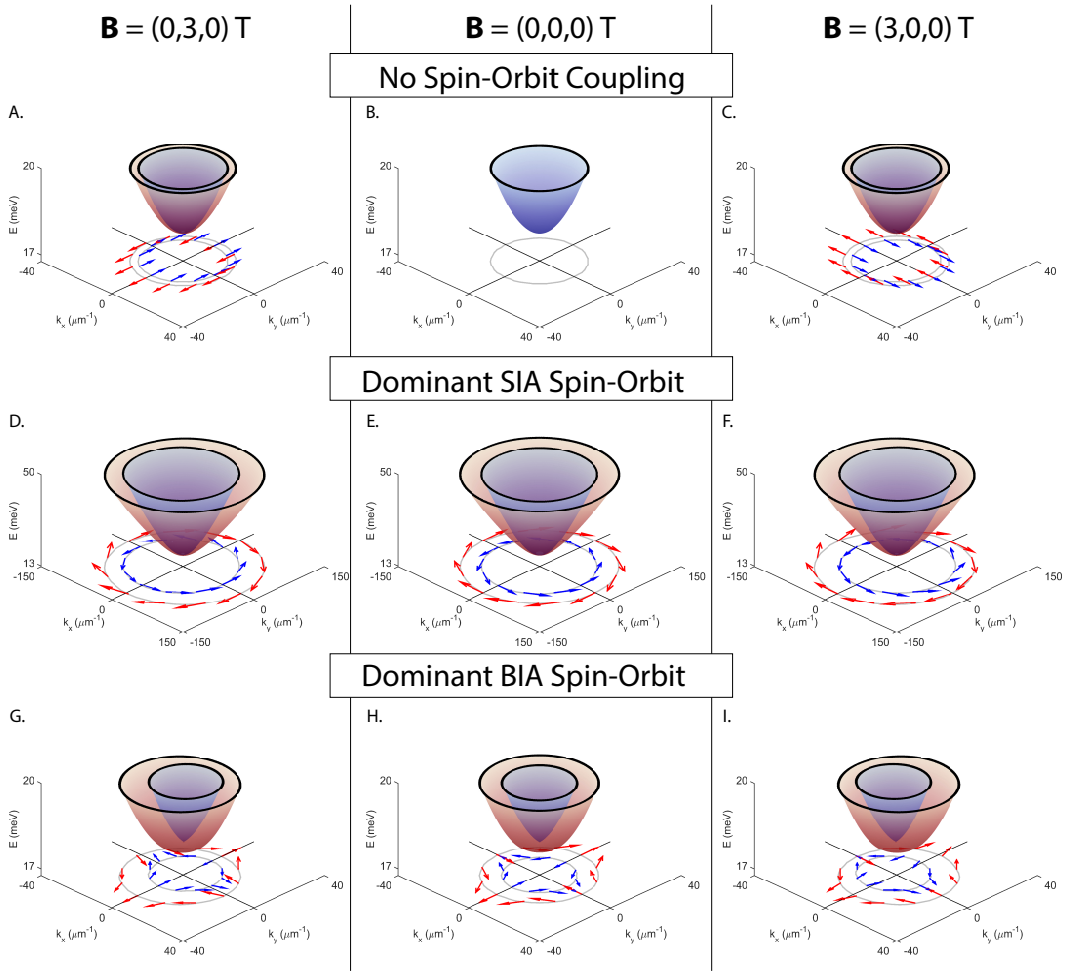

Figure 6.11: Modeling of the conduction band structure under various spin-orbit and parallel magnetic field conditions. **(A-C)** When spin-orbit coupling is absent, the addition of a 3 T parallel magnetic field simply polarizes spins in a direction determined by the sign of the in-plane g-factor, $g_{||}$. With no exernal magnetic field, the two spin bands are degenerate (B). **(D-F)** Dominant structural inversion asymmetry causes axially symmetric spin-splitting to occur at finite momentum (E). This type of spin-orbit coupling causes the bands to shift orthogonally to the external magnetic field (D, F), leading to nonzero Cooper pair momentum in the shift direction. **(G-I)** Dominant bulk inversion asymmetry with $\theta^{th} = 0, \pi/2$ acts oppositely to structural inversion asymmetry, so that external magnetic fields cause bands to shift parallel to the external magnetic field. This type of shift is not observed experimentally in our devices.

Application of a 3 T magnetic field in the y direction identically splits the bands, although the spins in this case orient along $\pm y$. It can be seen that with no spin-orbit coupling and an applied in-plane magnetic field, pairs may form with nonzero wavevector in any in-plane direction.

Including dominant SIA (equivalent to a perpendicular electric field of 10 mV/nm) with no BIA modifies the expectation for the band structure (Figure 6.11D-F). Even without any external magnetic field, in this case the bands are spin-split for all nonzero wavevectors. The axial symmetry of the spin-orbit coupling results in the spin texture shown in Figure 6.11E, modeled up to a higher Fermi energy of 50 meV to highlight the limit of strong SIA. Now coupled with an external magnetic field, these factors result in a behavior that is different from the case with no spin-orbit coupling. When magnetic field is applied in the x (y) direction, the two Fermi surfaces shift oppositely in the y (x) direction. Consistent with our observations on aluminum-based junctions in the electron-doped regime, this shift implies that a magnetic field in the x direction introduces a pairing wavevector in the y direction. Also superficially consistent with our data, a magnetic field in the y direction leads to a pairing wavevector in the x direction. However, the magnitude of this wavevector alone is too small to explain the experimental evolution of interference as B_y is increased. A full explanation of this effect is presented in Section 6.16. Finally, the lack of dependence of SIA on the angle θ^{th} is consistent with our measurements (Figures 6.8 and 6.9).

In the remaining case, the effect of dominant BIA with no SIA is investigated in Figure 6.11G-I, for an angle $\theta^{th} = 0$ and up to a Fermi energy of 20 meV. Similarly to the case of strong SIA, with no external magnetic field present the bands are spin-split at nonzero wavevectors. However, the texture of spins at the Fermi surfaces displays tetrahedral symmetry in this case. As a result, when parallel magnetic field is present in the x (y) direction, the two Fermi surfaces shift oppositely in the x (y) direction. This shifting is orthogonal to the shifts present with strong SIA, and does not agree with our interference measurements on devices aligned with $\theta = 0$ or $\pi/2$. Furthermore, the shift direction rotates by $\pi/2$ as the angle θ^{th} becomes $\pi/4$. This prediction that the direction of induced Cooper pair momentum should depend on θ^{th} is also inconsistent with our results.

Finally, in the main text, we model the evolution with density of the in-plane g-factor $\tilde{g}$, the Fermi velocity v_F, and the pair momentum shift $\Delta k \approx \tilde{g}\mu_B B_x/\hbar v_F$, under the assumption that BIA is absent and SIA is dominant (equivalent to a perpendicular electric field of 10 mV/nm). At each density, a particular value of the magnetic field satisfies the condition $\Delta k W = \pi/2$, leading to a node in the induced superconductivity in the junction. We find that the evolution with density of this nodal magnetic field value agrees with our model at high densities. In niobium and aluminum devices respectively, the value of the nodal magnetic field is consistent with values of of $\tilde{g}/v_F$ that are approximately 1.9 and 1.4 times greater than those expected theoretically. Using different values for

the electric field only weakly modifies this conclusion. For example, if the SIA was instead equivalent to a perpendicular electric field of 40 mV/nm, we would find values of of $\tilde{g}/v_F$ approximately 2.1 and 1.5 times greater than the theoretical expectation, only a $\sim 10\%$ difference.

6.12 Model of a Two-Dimensional Electron Gas Contacted by Superconducting Leads

In the following sections, we model the coupling of superconducting leads to our quantum well. We consider a geometry in which a two-dimensional electron gas (2DEG) is contacted by a pair of superconducting leads with a controlled phase difference between them, and we seek to calculate the maximum supercurrent that can be carried between the strips. The following is a more complete derivation of the pair propagator F used in the main text to carry out this goal. We assume a Hamiltonian $H = H_0 + H_2$, where H_0 is the Hamiltonian for the 2DEG in the absence of the superconductor, and H_2 is the coupling between the superconductors and the 2DEG, described by a pairing Hamiltonian of the form

$$H_2 = -\int dxdy \left[\Delta(x,y)\Psi^\dagger(x,y) + \Delta^*(x,y)\Psi(x,y)\right]. \tag{6.12}$$

Here $\Psi(x,y) \equiv \psi_\uparrow(x,y)\psi_\downarrow(x,y)$ is an operator which annihilates a singlet pair of electrons in the 2DEG at the point (x,y), while the pair potential $\Delta(x,y)$ is a complex number that depends on the phase of the superconductor and the tunneling amplitude at that point.

We assume that the contacts between the 2DEG and the superconductors occur at the edges of the superconductors, located at $y = 0$ and $y = W$, so that we may write

$$\Delta(x,y) = \lambda_1(x)\delta(y) + \lambda_2(x)\delta(y-W) \equiv \Delta_1(x,y) + \Delta_2(x,y), \tag{6.13}$$

with $-L/2 < x < L/2$. We assume that the magnitude of the coupling is constant along each lead, but the phase will vary if there is a perpendicular magnetic field $B_z \neq 0$. We choose a gauge where the vector potential points in the x direction, with $A_x = -B_z(y - W/2)$, so that the vector potential vanishes along the midline of the 2DEG. If the superconducting strips have identical widths W_{SC}, then the couplings λ_j will have the form

$$\lambda_j(x) = |\lambda_j|\, e^{2\pi i \phi_j(x)}, \tag{6.14}$$

$$\phi_j(x) = \phi_j(0) + \frac{(-1)^{j-1} x B_z (W + W_{sc})}{2\Phi_0}, \tag{6.15}$$

with $j = 1, 2$. The phases in equation (6.15) are determined by the condition that there should be no net current flow along the length of the superconducting strips, so the phase gradient in each superconductor should be canceled by the vector potential along the center line of the superconductor.

We assume that B_z is sufficiently weak that the cyclotron radius $R_c = \hbar k_F / e B_z$ is large compared to W (typically in our devices $R_c \approx 10\ \mu$m, which is large compared to $W = 800$ nm). In this case, we may ignore the effect of B_z on the trajectories of electrons in the 2DEG. Moreover, since we have chosen the vector potential to vanish along the midline of the 2DEG, an electron crossing from $y = 0$ to $y = W$ will acquire no net phase due to the vector potential. We also ignore, for the moment, any orbital effects of the parallel field $B_{||}$. Thus the 2DEG Hamiltonian H_0 will include the Zeeman coupling to $B_{||}$, as well as the spin-orbit coupling, but will not include terms due to the magnetic field in the kinetic energy.

To lowest order in the couplings λ_j, the portion of the total energy that depends on the phase difference between the two superconducting leads can be written in the form:

$$E = -\int dx_2 \left[\lambda_2^*(x_2) \left\langle \Psi(x_2, W) \right\rangle_1 + c.c.\right], \tag{6.16}$$

where $\langle \Psi(x, y) \rangle_1$ is the order parameter at point (x, y) induced by the superconductor $j = 1$. In turn, this may be written in the form

$$\langle \Psi(x, y) \rangle_1 = \int dx_1 \lambda_1(x_1) F(x, x_1, y), \tag{6.17}$$

where F is the propagator from point $(x_1, 0)$ to point (x, y) for an induced Cooper pair. We will determine the form of F in the following section.

As a first approximation, we may ignore the fact that there are boundaries of the 2DEG at $x = \pm L/2$ and that electrons will be reflected at these boundaries (either specularly or diffusely, and possibly with a spin flip). Similarly, we ignore the possibility of single-particle reflection at $y = 0$ or $y = W$, where the superconducting leads touch the 2DEG. Furthermore, we assume that the electron density is constant in the 2DEG, and we ignore any interactions between electrons in the 2DEG. We also ignore scattering by impurities inside the 2DEG. Then the propagator F may be calculated for an infinite, translationally invariant 2DEG, where the momentum of each electron is a good quantum number. We believe that corrections due to reflections at the boundaries will have quantitative effects but will not affect qualitatively the form of our results. Modeling of critical current including

specular reflections at mesa edges will be discussed in Section 6.15 and 6.16.

6.13 Derivation of a General Formula for the Pair Propagator F

As discussed previously, the portion of the total energy that depends on the phase difference between the two superconducting leads can be expressed, to leading order in the coupling constants λ_j, in terms of the pair propagator $F(x, x_1, W)$ of the normal 2DEG from a point $(x, 0)$ under one superconductor to a point (x_1, W) under the other, according to equation (6.16). A more complete calculation should go beyond lowest order and should take into account the finite widths of the superconducting contacts and changes in the local chemical potential resulting from the coupling to the superconductor. The effect of these corrections may be described by introduction of an amplitude for normal reflection where the 2DEG meets the edge of the superconductor, as well as a renormalization of the amplitude for Andreev reflection, which will clearly have an effect on the overall magnitude of the coupling between the two superconductors and therefore on the maximum critical current. Since we do not know the precise strength of the coupling between the 2DEG the superconductors in the first place, we are not interested in this overall magnitude of the critical current, but rather in its dependence of the critical current on the parameters of the system, such as direction and strength of the magnetic field, the sample geometry, and the electron density.

A potential concern for our analysis is that beyond the lowest order in perturbation theory, one should include processes where an electron can undergo multiple reflections between the two superconductors before it is absorbed in an Andreev process at one side or the other. However, processes involving multiple reflections will fall off faster with W than the processes included in equation (6.16), particularly if one takes into account disorder at the superconducting interface. Consequently, we feel justified in neglecting such processes here.

If one uses equation (6.16) to calculate the critical current, one finds that dependences of the critical current on system parameters such as the direction and strength of the magnetic field arise from interference between contributions to the integral from different points x and x_1, which will be particularly sensitive to variations of the phase of $F(x, x_1, W)$ as a function of these variables. We remark that, strictly speaking, calculations beyond lowest-order perturbation theory may lead to dependences of the amplitude for Andreev reflections at the boundaries on the angle of incidence and on the electron energy that differ somewhat from the lowest-order results, which would give, in turn, corrections to the space dependence of the integrand in equation (6.16). However, we do not expect these corrections to have a major effect on the results in the parameter range of interest to us. Moreover, any corrections of this type would depend on details of the coupling between the superconductor and the

2DEG, which are not known in practice.

The function $F(x, x_1, W)$ will depend on what one assumes for the Hamiltonian H_1 of the 2DEG. A four-band model Hamiltonian H_1 for our quantum wells was previously discussed. Since we presently are interested in behavior near the Fermi energy E_F, and within the conduction bands only, in the following we adopt a simplified two-band model Hamiltonian. This Hamiltonian for an electron in the 2DEG with momentum $\vec{k}$ is given by the 2×2 matrix

$$H^0_{\vec{k}} = v_F(k - k_F) + \vec{\beta}(\hat{k}) \cdot \vec{\sigma}, \tag{6.18}$$

$$\beta_j = \tilde{g}\mu_B B_j/2 + \hat{k}_i S_{ij}, \tag{6.19}$$

where B_j are the x and y components of the in-plane magnetic field, $\tilde{g}$ is an effective g-factor, $\hat{k} \equiv \vec{k}/k$, and $\hat{k}_i S_{ij}\sigma_j$ is the spin-orbit coupling term, which we assume to be small compared to the Fermi energy. We have here assumed a single electron band, and assumed that band structure is isotropic in the absence of spin-orbit coupling. We can then write

$$H^0_{\vec{k}} = \sum_\eta \epsilon_{\vec{k}\eta} P^{\hat{k}\eta}, \tag{6.20}$$

with $\eta = \pm 1$. Here $\epsilon_{\vec{k}\eta}$ are the two eigenvalues, and $P^{\hat{k}\eta}$ are projection matrices given by

$$\epsilon_{\vec{k}\eta} = v_F(k - k_F) + \eta \left|\vec{\beta}\right|, P^{\hat{k}\eta} = (1 + \eta\hat{\beta} \cdot \vec{\sigma})/2, \tag{6.21}$$

with $\hat{\beta} \equiv \vec{\beta}/\left|\vec{\beta}\right|$.

We next define a 2×2 matrix function

$$g(\vec{r}, \epsilon) \equiv \frac{1}{(2\pi)^2} \sum_\eta \int d^2k e^{i\vec{k}\cdot\vec{r}} \delta(\epsilon - \epsilon_{\vec{k}\eta}) P^{\hat{k}\eta}. \tag{6.22}$$

Then, letting $\vec{r} = (x - x_1, y)$, the pair propagator $F(x, x_1, y)$ may be expressed as

$$F(\vec{r}) = \int_0^\infty d\epsilon \int_0^\infty d\epsilon' \frac{\mathrm{tr}\left[g(\vec{r}, \epsilon)\sigma^y g^T(\vec{r}, \epsilon')\sigma^y + g(\vec{r}, -\epsilon)\sigma^y g^T(\vec{r}, -\epsilon')\sigma^y\right]}{2(\epsilon + \epsilon')}, \tag{6.23}$$

where T indicates the matrix transpose.

We are interested in the situation where $k_F r \gg 1$, and $|\epsilon| \ll E_F$. Then the integration over the

direction of $\vec{k}$ is dominated by regions close to the end points where $\vec{k}$ is either parallel or antiparallel to $\vec{r}$, and the expression for $g(\vec{r},\epsilon)$ may be approximated by

$$g(\vec{r},\epsilon) \approx \frac{k_F^{1/2}}{(2\pi)^{3/2} v_F r^{1/2}} \sum_\eta \Big[e^{ik_F r} e^{i\epsilon r/v_F} e^{-i\pi/4} e^{-i\delta k_\eta^+ r} P^{\eta +} + e^{-ik_F r} e^{-i\epsilon r/v_F} e^{i\pi/4} e^{i\delta k_\eta^- r} P^{\eta -} \Big] \tag{6.24}$$

where $P^{\eta\pm}$ is equal to $P^{\hat{k}\eta}$, with $\hat{k} = \pm\hat{r} \equiv \pm\vec{r}/r$ and

$$\delta k_\eta^\pm = \frac{\eta \left| \vec{\beta}(\pm\hat{r}) \right|}{v_F}. \tag{6.25}$$

When we substitute the expression for g in formula (6.23) for $F(\vec{r})$, we may ignore the terms proportional to $e^{\pm 2ik_F r}$, as these rapidly oscillating terms will give vanishing contribution to the energy if the width of the contacts between the 2DEG and the superconducting strips are large compared to $1/k_F$. Performing the integrals over ϵ and ϵ' in the remaining terms, one obtains the result

$$F(\vec{r}) \approx \frac{C}{r^2} \sum_{\eta\eta'} N_{\eta\eta'}(\hat{r}) e^{-i\left(\delta k_\eta^+ - \delta k_{\eta'}^-\right) r}, \tag{6.26}$$

with $C = k_F/(8\pi^2 v_F)$, and

$$N_{\eta\eta'}(\hat{r}) = N_{\eta\eta'}(-\hat{r}) = \frac{1 - \eta\eta' \hat{\beta}(\hat{r}) \cdot \hat{\beta}(-\hat{r})}{2}. \tag{6.27}$$

6.14 Special Cases and Limiting Forms of the Pair Propagator

Here we discuss several special cases which lead to limiting forms for the pair propagator $F(\vec{r})$. The above expressions (equations (6.26) and (6.27)) may be simplified in the limit where the Zeeman energy is small compared to the spin-orbit energy splitting. When $B_{||} = 0$, we find that $\hat{\beta}(\hat{r}) = -\hat{\beta}(-\hat{r})$, so that $N_{\eta\eta'} = \delta_{\eta\eta'}$. Furthermore, when $\eta = \eta'$, we see that the exponent in equation (6.26) is equal to zero, so F will have no oscillations as a function of r. If $B_{||}$ is nonzero but still small compared to the spin-orbit splitting, it remains a good approximation to set $N_{\eta\eta'} = \delta_{\eta\eta'}$. In the exponent, however, we have

$$\left(\delta k_\eta^+ - \delta k_\eta^-\right) = \eta \tilde{g} \mu_B \vec{B}_{||} \cdot \vec{\beta}(\vec{r}). \tag{6.28}$$

An important example is the case of pure SIA spin-orbit coupling, where the matrix S has the Rashba form, $S \propto i\tau^y$, where τ^y is a Pauli matrix. In this case we may write

$$\left(\delta k_\eta^+ - \delta k_\eta^-\right) r = \eta \Delta\vec{k} \cdot \vec{r} \tag{6.29}$$

with

$$\Delta\vec{k} = \hat{z} \times \vec{B}_{||} \tilde{g} \mu_B / v_F. \tag{6.30}$$

The oscillations in $F(\vec{r})$ have a simple interpretation in this case. When $B = 0$, the Fermi surface consists of two circles centered about the origin, split by the spin-orbit coupling, with spin orientations shown in Figure 6.3B. Application of a weak in-plane magnetic field will shift the two Fermi circles in opposite directions, by amounts $\pm\Delta\vec{k}/2$. The function $F(\vec{r})$ describes the propagator when a singlet pair of electrons is injected at one point and removed at a second point, separated by $\vec{r}$. For large separations, $F(\vec{r})$ is dominated by pairs of electrons that are close to the Fermi energy, with wave vectors opposite to each other and parallel or antiparallel to $\vec{r}$. Because the two electrons must have opposite spins, they must belong to the same branch of the Fermi surface. Thus, the induced pairs will have total momenta equal to $\pm\Delta\vec{k}$, depending on the branch η. The momentum shifts are manifest in the phase factors $e^{i\eta\Delta\vec{k}\cdot\vec{r}}$, which appear in $F(\vec{r})$ in this case.

In the case of pure BIA coupling, the matrix S is $\propto \tau^z$, in our coordinate system. We may again write the phase accumulation in the form (6.29), but now the direction of $\Delta\vec{k}$ depends on the directions of $\vec{B}_{||}$ relative to the crystal axes.

The formula for $F(\vec{r})$ also becomes simple in the case where the Zeeman energy is large compared to the spin-orbit splitting. In this case, the Fermi surface consists of two concentric circles, with spin that are uniformly aligned on each circle, either parallel or antiparallel to $\vec{B}_{||}$. In order to form a spin singlet, we must choose one electron from each Fermi circle. If we also require that the momenta be parallel or antiparallel to $\vec{r}$, we see that the induced electron pair will have a total momentum equal to $\pm\hat{r}\tilde{g}\mu_B B_{||}/v_F$. Thus we should find that the phase shift is independent of the direction of $\vec{r}$.

These expectations may be confirmed using the formulas derived above. In the case where the Zeeman energy is large compared to the spin-orbit splitting, we find that $\vec{\beta}(\hat{k})$ is independent of $\hat{k}$, and thus $N_{\eta\eta'} = \delta_{\eta,-\eta'}$. Furthermore, $\delta k_\eta^+ - \delta k_{-\eta}^- = \eta\tilde{g}\mu_B B_{||}/v_F$, independent of $\vec{r}$.

6.15 Reflections from the Sample Edges

Taking into account the effects of electron reflections from the ends of the sample, at $x = \pm L/2$, we should rewrite the propagator F in a more general form as

$$\begin{aligned} F(x_2, x_1, W) = F_0(\vec{r}) + F_1 \left[\left(x_2 + \frac{L}{2} \right), \left(x_1 + \frac{L}{2} \right), W \right] \\ + F_2 \left[\left(\frac{L}{2} - x_2 \right), \left(\frac{L}{2} - x_1 \right), W \right], \end{aligned} \tag{6.31}$$

where F_0 is the function given by equation (6.26) for the infinite system, $\vec{r} = (x_2 - x_1, W)$, as before, and F_1 and F_2 describe the contributions of electrons reflected from the left boundary or right boundary respectively. We assume that the length L is long enough that we can neglect the effects of electrons that scatter multiple times from opposite boundaries. Here we will assume that the boundaries at $x = \pm L/2$ are represented by infinite potential barriers, which are perfectly smooth, so that electrons are specularly reflected with no change in spin. The symmetry of our problem will then be such that F_1 and F_2 have identical functional forms, so we need only find the form of F_1. For convenience, we move the left boundary to the line $x = 0$, and we assume that the right boundary is located at $x = \infty$. Using similar reasoning to what we used in the translationally invariant case, we may write F_1 in the form

$$F_1(x_2, x_1, W) = \int_0^\infty d\epsilon \int_0^\infty d\epsilon' \frac{\mathrm{tr}\left[h(x_2, x_1, W, \epsilon) \sigma^y h^T(x_2, x_1, W, \epsilon') \sigma^y + c.c. \right]}{2(\epsilon + \epsilon')} \tag{6.32}$$

where

$$\begin{aligned} h(x_2, x_1, W, \epsilon) = -\frac{k_F^{1/2}}{(2\pi)^{3/2} v_F s^{1/2}} \sum_{\eta_1, \eta_2} [e^{ik_F s} e^{i\epsilon s/v_F} e^{-i\pi/4} e^{-i(\delta k^+_{1,\eta_1} s_1 + \delta k^+_{2,\eta_2} s_2)} P_1^{\eta_1 +} P_2^{\eta_2 +} \\ + e^{-ik_F s} e^{-i\epsilon s/v_F} e^{i\pi/4} e^{i(\delta k^-_{1,\eta_1} s_1 + \delta k^-_{2,\eta_2} s_2)} P_1^{\eta_1 -} P_2^{\eta_2 -}], \end{aligned} \tag{6.33}$$

where $s = [(x_1 + x_2)^2 + W^2]^{1/2}$, $s_1 = s x_1/(x_1 + x_2)$, $s_2 = s - s_1$, and

$$\delta k^\pm_{j,\eta} = \frac{\eta \left| \vec{\beta}(\pm \hat{k}_j) \right|}{v_F}, \tag{6.34}$$

for $j = 1, 2$, with

$$\hat{k}_1 = -\frac{[(x_1 + x_2), -W]}{s}, \hat{k}_2 = \frac{[(x_1 + x_2), W]}{s}. \tag{6.35}$$

Furthermore, we have

$$P_j^{\eta\pm} = (1 + \eta\hat{\beta}(\pm\hat{k}_j) \cdot \vec{\sigma})/2. \tag{6.36}$$

We now turn to one particular example. In order to evaluate expression (6.32) for F_1, we must first evaluate the trace over a product of projection matrices and σ^y. In the case of strong SIA coupling and weak magnetic field, the trace simplifies, and we obtain the result

$$\text{tr}\left[P_1^{\eta_1+} P_2^{\eta_2+} \sigma^y \left(P_1^{\eta_3-} P_2^{\eta_4-}\right)^T \sigma^y\right] = \delta_{\eta_1\eta_3}\delta_{\eta_2\eta_4}\left[\sin^2\theta\delta_{\eta_1\eta_2} + \cos^2\theta\delta_{\eta_1,-\eta_2}\right], \tag{6.37}$$

where $\sin\theta = W/s$. Furthermore for $B_{||}$ in the y direction, we find

$$(\delta k_{j,\eta}^+ - \delta k_{j,\eta}^-)s_j = (-1)^j \eta x_j \frac{\tilde{g}\mu_B B_y}{v_F}. \tag{6.38}$$

Thus, in the case of strong SIA and $B_{||}$ in the y direction, we find

$$F_1(x_2, x_1, W) = \frac{2C\left[\sin^2\theta\cos\Delta k(x_1 - x_2) + \cos^2\theta\cos\Delta k(x_1 + x_2)\right]}{(x_1 + x_2)^2 + W^2}, \tag{6.39}$$

where $\Delta k = \tilde{g}\mu_B B_y/v_F$, and the constant C is the same as in equation (6.26).

6.16 Modeling Josephson Interference

Using the pair propagator $F(\vec{r})$ and equation (6.16), we can calculate the Josephson energy and critical current for our junctions. In the limit of either strong BIA or strong SIA, the Cooper pair momentum shift occurs at an angle α with respect to the x axis and the pair propagator is

$$F(x_2, x_1, W) = \frac{k_F}{8\pi^2 v_F} \cdot \frac{e^{i\gamma} + e^{-i\gamma}}{(x_2 - x_1)^2 + W^2}, \gamma = \Delta k\left(\sin(\alpha)W + \cos(\alpha)(x_2 - x_1)\right). \tag{6.40}$$

As previously noted, in this case pairing occurs internally to each Fermi surface. In the limit of weak

spin-orbit coupling, the pair propagator instead takes the form

$$F(x_2, x_1, W) = \frac{k_F}{8\pi^2 v_F} \cdot \frac{e^{i\gamma} + e^{-i\gamma}}{(x_2 - x_1)^2 + W^2}, \gamma = \Delta k \sqrt{W^2 + (x_2 - x_1)^2}. \tag{6.41}$$

Due to the opposite spin polarization of the two Fermi surfaces, pairing in this limit is expected to occur between Fermi surfaces, in contrast to the limit of large spin-orbit coupling.

The Josephson energy E is obtained in each limit by evaluating equation (6.16). By differentiating the Josephson energy with respect to the phase difference $\phi_1(0) - \phi_2(0)$ we find the current-phase relation of the junction, which is then maximized with respect to the phase difference to obtain the critical current.

In the main text we consider only a parallel field along the x direction. In both aluminum and niobium-based devices we experimentally observe that superconductivity weakens as the parallel field B_x increases, in contrast with the cosine dependence predicted by our theoretical model. We believe that this effect results from spatially inhomogeneous screening of the parallel field at the edges of superconducting leads. The superconductor repels the in-plane field and slight roughness at the edges results in a weak magnetic field along the z direction that is positive at some locations and negative at others. This screening leads to a spatially varying random component of the phase that grows linearly with the in-plane field. Hence, we introduce a random phase $\chi \propto (R_1(x_1) - R_2(x_2))\, B_x$, where the random variables $R_1(x_1)$ and $R_2(x_2)$ correspond to fluctuations in the direction of the parallel field at each interface. The modeled step size in x is 40 nm, with no correlations between adjacent positions. The random phase χ is uniformly distributed between zero and an upper bound whose absolute magnitude is equal to 15% of the maximum phase generated by the intrinsic momentum. With this randomness, the calculated critical currents diminish in magnitude as the in-plane field increases, in agreement with the experimental observation (shown in Figure 6.3C for the case of dominant SIA).

In general, the parallel field $\vec{B}_{||}$ can be oriented anywhere in the plane, which modifies α accordingly in the case that spin-orbit coupling is strong. Additionally, loosening the constraint that $\vec{B}_{||}$ lie parallel to x introduces an artifact wavevector $q_y \approx 2\pi B_{||} \sin(\beta) d/\Phi_0$, where d is the height difference between the centers of the quantum well and of the superconducting leads, and β is the angle between the parallel magnetic field and the x axis. This additional phase arises due to the magnetic flux penetrating the area dL formed between the leads and the quantum well due to this height difference. Importantly, no flux penetrates this area when the parallel component of magnetic field is only in the x direction, so that in this case the pair momentum is solely determined by the Zeeman coupling and the spin-orbit coupling.

The behavior of Josephson interference in our devices essentially involves different mechanisms when the parallel magnetic field lies in the x or y direction. With the above modeling it is clear that this difference is due to the dependence of q_y on the magnetic field angle β, so that the data for the magnetic field B_y reflects primarily the difference in height between the superconducting leads and the quantum well. Since we cannot entirely rule out either dominant Zeeman coupling or dominant SIA, we model both possibilities for this field direction. With dominant SIA and the height difference d set to either 10 nm (Figure 6.12A) or 70 nm (Figure 6.12B), the model agrees well with the experimental observation. The corresponding model without any spin-orbit coupling also agrees, however (Figure 6.12C, D).

Nevertheless, it is clear that with the parallel magnetic field in the y direction, the most prominent feature in the response of the device is driven by the parallel magnetic flux penetrating the area dL and not by effects intrinsic to the heterostructure. Assuming that only this parallel magnetic flux contributes, one can estimate the distance d for each device, accounting for the slight difference in W_{SC} for aluminum and niobium devices (1 μm and 400 nm respectively). For devices A-E, the corresponding distance $d \approx 21, 10, 9, 7$, and 70 nm, in agreement with lithographic dimensions. The similar values of d for devices B-D reflects the fact that these devices were all fabricated concurrently. Device E, in which niobium was used for the leads, has a much larger value of d due to the fact that the niobium thickness was larger than the aluminum thicknesses.

Athough the parallel magnetic flux dominates the response of devices to the field B_y, with purely SIA it is still in principle possible in this direction to extract the intrinsic nature of spin-orbit coupling. Since the wavevectors q_y and Δk add and subtract, the 'V' shape of supercurrent evolution contains two nearly identical slopes, which in our measurements are unobservable due to the concurrent decay of superconductivity. However, normalizing the theoretical critical current magnitude still reveals the possibility to determine the nature of spin-orbit coupling using this parallel field direction (Figure 6.12E).

An additional characteristic common among the data sets is an asymmetry in the interference pattern upon inversion of one component of the applied magnetic field. In Figure 6.12F we show an interference pattern measured on Device F with both positive and negative components B_y and B_z. Here the data appears invariant under inversion of both components of the magnetic field, as we expect from time-reversal symmetry. However, the lack of symmetry under inversion of a single component of the magnetic field suggests that devices lack structural symmetry under rotation by 180 degrees. We may model this asymmetry as arising from a difference in lengths of the two leads on either side of the junction. An exaggeration of this effect, where the interface to one lead is 4 microns and to the other is 4.5 microns, shows increased intensity of interference for positive perpendicular field as compared

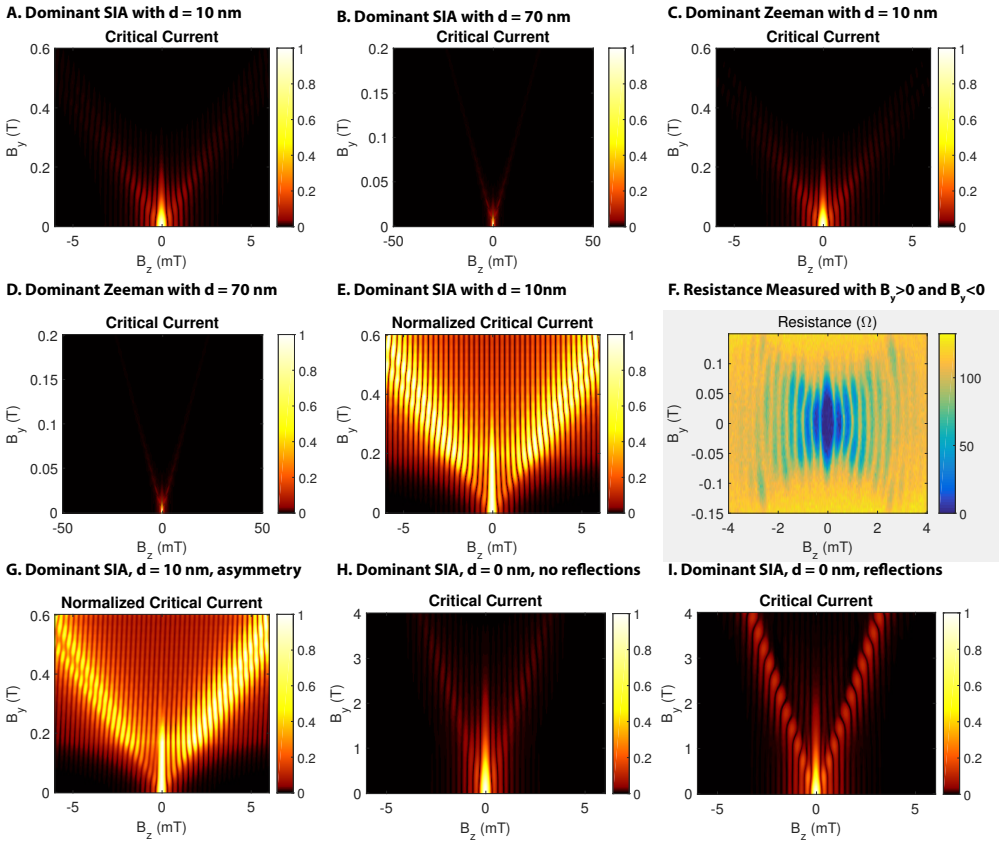

Figure 6.12: Modeling of the critical current as the perpendicular magnetic field B_z (generating flux quanta) and the parallel magnetic field B_y (generating Cooper pair momentum) are varied. **(A)** With dominant SIA and the height difference d between the leads and the quantum well set to 10 nm, the interference evolves consistently with measurements of differential resistance on aluminum devices (devices A-D). **(B)** Increasing d to 70 nm decreases the slope of each arm of the interference pattern consistently with the measurement of a device with thicker niobium leads (device E). **(C, D)** Eliminating spin-orbit coupling leads to a similar picture for both values of d, highlighting the overwhelming extrinsic nature of the pairing momentum induced when the parallel field is applied in the y direction. **E)** Normalizing the critical current at each value of B_y reveals additional features weakly present in the interference with SIA and $d = 10$ nm. Since the extrinsic wavevector q_y adds and subtracts with the wavevector Δk induced due to SIA, two slopes are in principle found in each arm of the interference pattern. However, superconductivity weakens to the extent that such splitting cannot be conclusively observed in our devices. **(F)** The resistance of Device F, measured as both B_y and B_z are tuned to positive and negative values. The measured resistance is observed to be symmetric under inversion of both B_y and B_z, as expected from time-reversal symmetry. Under inversion of either B_y or B_z, however, the resistance is asymmetric. **(G)** Modeling asymmetry in the lengths of superconducting electrodes leads to asymmetry in the interference with respect to inversion of B_z. Plotted here are the expected critical currents for a device with 4 microns and 4.5 microns as the interfacial lengths. **(H)** The expected evolution of interference upon increasing B_y assuming dominant SIA and with $d = 0$. **(I)** Including specular reflections at the mesa ends, assuming the presence of a steep confining potential which does not flip spins upon reflection, quantitatively modifies the interference evolution. However, qualitatively the behavior remains unchanged.

to negative perpendicular field (Figure 6.12G), similar to what is observed experimentally.

Finally, in all of the above modeling we have ignored contributions due to reflections at the ends of the mesa. In Figure 6.12H, we plot the expected evolution of interference upon increasing B_y assuming dominant SIA and with $d = 0$, ignoring the possibility of reflections at mesa boundaries. We may include specular reflections at the mesa boundaries in the model, as discussed in Section 6.15. With these contributions, the interference evolution is quantitatively modified (Figure 6.12I). However, the 'V' shape of the interference evolution is still present, with each arm of the 'V' having the same slope as was obtained by ignoring edge reflections. Hence, we conclude that the contribution of specular reflections preserving the spin direction only quantitatively modifies the expected device behavior. We have not carried out calculations for other boundary conditions, such as diffuse reflection, but we expect that results in these cases would not be qualitatively different from the cases of specular reflection or no reflection at all.

6.17 Evidence for the Transition to a π-Junction

In a conventional Josephson junction with no external magnetic field, the supercurrent I_S is related to the phase difference $\Delta\phi$ between the leads via the Josephson relation $I_S = I_C \sin(\Delta\phi)$. Here I_C is the critical current of the junction. When the induced order parameter oscillates in space, it is possible that this order parameter can have a different sign at the boundary of each superconducting lead. This modifies the current-phase relation by a phase shift of π, so that in such a junction $I_S = I_C \sin(\pi + \Delta\phi)$. These junctions are referred to as π-junctions, and were first explored in systems composed of a ferromagnetic layer sandwiched between two superconductors [100]. A simple experiment which provides evidence of the π phase shift consists of two junctions connected in parallel and sharing the same superconducting leads. If one of the junctions is conventional and the other is a π-junction, then if the junctions also have equal critical currents the total supercurrent must be zero in the absence of external magnetic flux B_z. This contrasts with the standard result for two conventional junctions in series, in which the maximum supercurrent is expected with $B_z = 0$.

In our junctions, applying a finite magnetic field B_x results in finite momentum pairing in the y direction. For a junction with width W, we expect that a π-junction should then be realized when $\frac{\pi}{2} \cdot \frac{\hbar v_F}{\tilde{g}\mu_B W} < B_x < \frac{3\pi}{2} \cdot \frac{\hbar v_F}{\tilde{g}\mu_B W}$, corresponding to the situation where the induced order parameter has a single node inside the junction. To carry out the experiment described above requires that we realize both a π-junction and a conventional junction. To achieve this goal, we have fabricated a device in which a junction with dimensions 800 nm $\times$ 4 μm is wired in parallel with a junction having dimensions 200 nm $\times$ 2 μm (Figure 6.13A). When the condition $\frac{\pi}{2} \cdot \frac{\hbar v_F}{\tilde{g}\mu_B W} < B_x < \frac{3\pi}{2} \cdot \frac{\hbar v_F}{\tilde{g}\mu_B W}$ is

satisfied for the 800 nm junction, the 200 nm junction will still be in the conventional regime. This experiment therefore allows one to detect the π phase shift, and also to verify that the parallel field B_x necessary to achieve the shift depends on the junction width W. All data presented on this device was collected at a temperature of 10 mK in the system discussed previously (Section 6.6).

Due to the screening of the parallel magnetic field by the superconducting leads (described in Section 6.16), we have fabricated our device such that all edges of the leads which lie along the y direction are far from the active areas of the device which contain the quantum well. If this were not the case, the screened field would penetrate the quantum well imhomogeneously, leading to unwanted interference. Instead, the quantum well between the 200 nm and 800 nm junctions is etched away, forming a SQUID geometry. Any screened parallel field penetrates through this central hole, leading to SQUID-like interference between the 200 nm junction and the 800 nm junction. The critical current of this device can be simulated with varying amount of screened flux, using the formalism developed in Section 6.12-6.16. With no screened flux, the expected behavior is simulated in Figure 6.13B. In Figure 6.13C, we plot the same simulation but with experimentally relevant flux screening.

In both simulations, the perpendicular field B_z modulates the critical current. A large period of $\approx$ 1 mT corresponds to the area of the 200 nm junction, while a smaller period of ≈ 0.3 mT corresponds to the area of the 800 nm junction. In the simulation with no screened flux, when the parallel field B_x exceeds ≈ 1.2 T, the critical current develops a sharp minimum at $B_z = 0$. This critical current minimum results from the formation of a π-junction in the 800 nm section of the device. In the simulation which includes screened flux, increasing the parallel field B_x leads to oscillations in the critical current, even at $B_z = 0$. These oscillations arise because the screened flux penetrates the center of the SQUID loop formed by etching the hole between the two junctions. Here, when the parallel field B_x exceeds ≈ 1.2 T, the formation of a π-junction in the 800 nm junction manifests as a π phase shift in the SQUID oscillations. This is due to the fact that when one arm of the SQUID loop is a π-junction, the condition for the maximum supercurrent shifts by $1/2$ flux quantum. To illustrate this effect, a line trace of the simulated critical current at $B_z = 0$ is plotted in Figure 6.13D.

To determine whether the π phase shift is present in our device, we measured the differential resistance with a small amount of DC current (20 nA) applied in order to highlight the positions of the high resistance nodes associated with critical current minima. Upon increasing the perpendicular field B_z, we observe two periods of oscillation corresponding to the areas of the 200 nm and 800 nm junctions (Figure 6.13E). With $B_z = 0$, increasing B_x reveals a series of resistance peaks, corresponding to minima of critical current brought on by the SQUID oscillations. At $B_x = 1.2$ T, only oscillations in B_z corresponding to the 200 nm area are observed, suggesting that in the 800 nm device supercurrent has been completely suppressed. Above this nodal value of B_x, we expect to observe

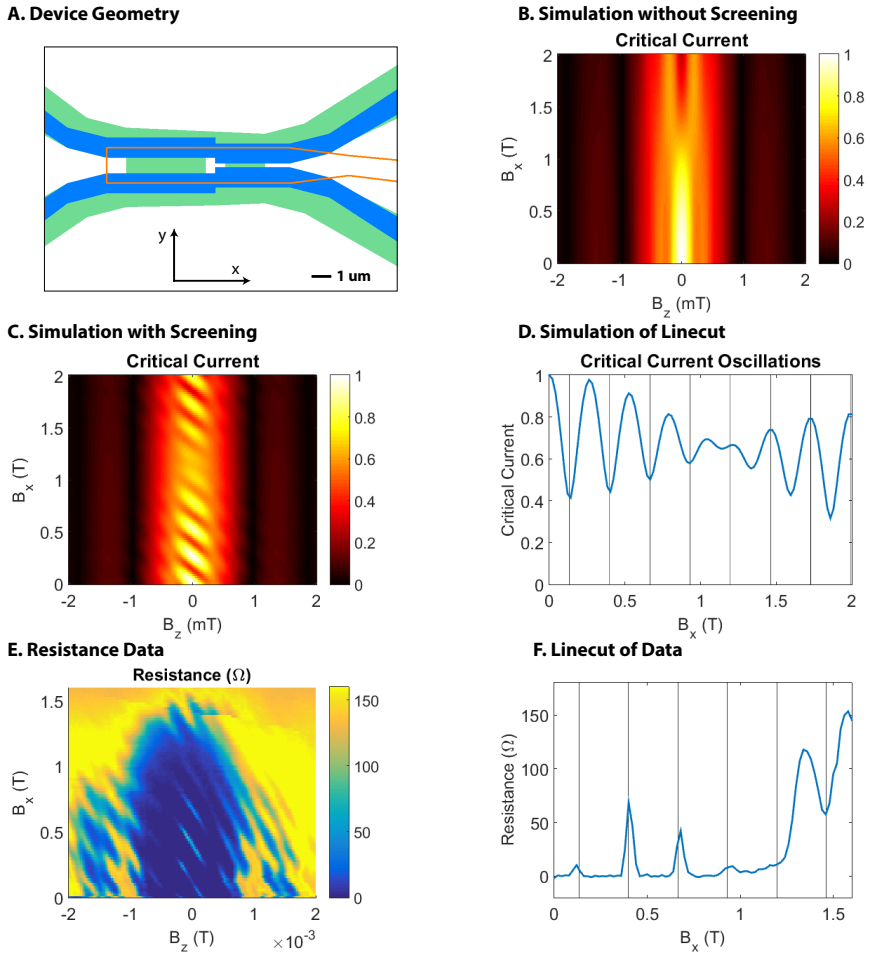

Figure 6.13: Evidence for the transition to a π-junction. **(A)** The device used for these measurements consists of a junction with dimensions 800 nm $\times$ 4 μm wired in parallel with a junction having dimensions 200 nm $\times$ 2 μm. A central area with no quantum well, created by etching, separates the two junctions by 1 μm. **(B)** An external field in both the x and z directions may be simulated, neglecting screening effects from the leads. In this case, application of the magnetic field B_x leads to a pair momentum shift in the y direction. At $B_x = 1.2$ T, the 800 nm junction transitions to a π-junction state. Above this nodal field, the critical current develops a minimum at $B_z = 0$ due to the presence of both a conventional and π-junction in the device. **(C)** Including screening of the magnetic field B_x by the aluminum leads, the simulation shows that increasing B_x while keeping $B_z = 0$ leads to oscillations in the critical current. These are due to flux penetrating the central hole in the device, and are essentially the critical current oscillations of a SQUID loop. **(D)** In this situation, the transition of the 800 nm junction to a π-junction is then expected to manifest as a phase shift in these SQUID oscillations. A linecut of the simulated critical current at $B_z = 0$, as a function of B_x, displays this shift. **(E)** The measured differential resistance of the device, with a DC current bias of 20 nA, shows a node structure which matches the predicted interference. **(F)** Extracting the differential resistance at $B_z = 0$ shows a periodic dependence on B_x at low fields, with the predicted phase shift above $B_x = 1.2$ T.

the predicted phase shift in the SQUID oscillations which signifies the appearance of a π-junction. Plotting the differential resistance as a function of B_x, extracted when $B_z = 0$, we find that the position of nodes does indeed shift by $1/2$ flux quantum (Figure 6.13F). Therefore, we conclude that a π-junction is realized in the 800 nm junction and not in the 200 nm junction, and that the origin of this π-junction lies in oscillations of the induced order parameter brought on by the application of the parallel field B_x.

A

Fabrication procedures for GaAs devices

This appendix describes the processes used to fabricate the GaAs-based devices measured in this thesis. Most of these recipes have by this point become standard, but are listed here for completeness.

A.1 Fabrication Workflow

A.1.1 Mesas

1. Define the etch mask using Shipley 1805 photoresist.
2. Measure the resist thickness using a profilometer.
3. Etch the wafer in a well-mixed solution of H_3PO_4:H_2O_2:H_2O (1:1:25) long enough to hit the target mesa height. The nominal etch rate is $180 - 200$ nm/min, but this can vary slightly between growths and etchant solution preparations. One can deal with the variation via a two-step etch. In the first etch, aim to etch halfway to the target thickness, and then measure the actual etch depth with a profilometer. This procedure gives a measurement of the etch rate, which can then be used to determine the remaining time needed to hit the target thickness.
4. After etching, rinse in DI water.
5. Remove the resist with acetone and rinse in IPA.

6. Measure the mesa height using a profilometer. It is safest to etch through the quantum well layer when making mesas.

A.1.2 Ohmic contacts and bond pads

1. Define the contact areas using AZ5214 photoresist.
2. Evaporate 7 nm Ni, $x/3$ nm Ge, $2x/3$ nm Au, 20 nm Ni, 100 nm Au. Here, x is the depth of the quantum well in nm.
3. Lift off in acetone.
4. Anneal at 120 C (1 minute), 340 C (1 minute), ramp from 340 C to 460 C in 30 seconds, then hold at 460 C for 2 seconds before stopping the heat.

A.1.3 Small gates

Small gates typically range in size from < 1 μm up to 10 μm.

1. Define small gate areas in PMMA 950 A4, using a standard e-beam recipe.
2. After developing, load the sample into a thermal evaporator.
3. Deposit 30 nm PdAu (60:40).
4. Lift off in acetone.

A.1.4 Large optical gates

1. Define the gate areas using AZ5214 photoresist.
2. Evaporate 20 nm Ti and enough Au to climb the mesas.
3. Lift off in acetone.

A.2 List of procedures

A.2.1 Shipley photolithography

1. Spin-coat the sample with Shipley 1805 photoresist at 5000 RPM for 40 seconds.
2. Bake the wafer at 80 C for 5 minutes.

3. Expose for 2.7 seconds on MJB4 in constant power mode. It is advisable to check the lamp intensity before exposure, and scale the exposure time accordingly.

4. Develop the sample in MIF319 for 9 seconds. Take care during this step, since MIF319 contains TMAH.

5. Bake the sample at 100 C for 5 minutes.

A.2.2 AZ5214 image reversal photolithography

This is a photolithography recipe that produces an undercut, enabling lift-off of deposited materials. After development, it should be possible to see the undercut in an optical microscope.

1. Spin-coat the sample with AZ5214 photoresist at 5000 RPM for 40 seconds.

2. Bake the wafer at 100 C for 45 seconds.

3. Expose for 0.4 seconds on MJB4 in constant power mode.

4. Bake the sample for 55 seconds at 120 C.

5. Flood expose the sample for 45 seconds.

6. Develop the sample in AZ726 IR for 20 seconds.

A.2.3 E-beam lithography

These are instructions for a 100 kV Elionix-7000 system, and written specifically for small gate fabrication. If features with lateral dimensions larger than $\approx$ 10 microns are needed, the dose needs to be scaled down due to proximity effects. To lift off layers thicker than 30 nm, insert layers of PMMA 495 C6 as needed before the final PMMA 950 A4 layer. Bake each layer of PMMA at 180 C for $>$ 5 minutes after spin-coating.

1. Spin-coat the sample with PMMA 950 A4 at 4000 RPM for 45 seconds.

2. Expose the pattern. Dose: 2500 μC/cm^2.

3. Develop in MIBK/IPA (1:3) at 0 C for 1 minute.

B

Fabrication procedures for HgTe devices

This appendix describes the processes used to fabricate the HgTe-based devices measured in this thesis. At the highest level, the fabrication workflow for these devices follows the same basic steps as for GaAs-based devices. However, in detail there are many differences, so that a recipe which works perfectly well for GaAs can be disastrously bad for HgTe! As one example, heating the HgTe heterostructure above 80 C tends to rapidly damage the material, so that many photolithography and ebeam processes either cannot be used or must be modified appropriately for use with HgTe. The recipes presented in this appendix will reliably produce Josephson junction devices with yields approaching 100%, but to find the most up-to-date procedures, consult the Yacoby group server.

B.1 Fabrication Workflow

B.1.1 Mesas

1. Define the etch mask using either HSQ or SiO_2/Ti.
2. (Optional) Measure the height of the etch mask before milling using a profilometer.
3. Mill using a DC argon ion source for enough time to etch through the quantum well (usually aim for 100 nm).
4. (Optional) Measure the height of the etch mask after milling using a profilometer.

5. Remove the etch mask by immersing the sample in 1:7 BOE for 7 minutes. Rinse in DI water.

6. Measure the height of the mesa using a profilometer. If you performed the optional steps you can get a sense for if the etch mask is etched at all. Typically for this process it will not be etched.

B.1.2 Bond pads

This procedure will produce large areas of Ti/Au that make good bond pads. If the metal is deposited onto a region where the quantum well has not yet been removed, then there will also be ohmic contact to the quantum well with typical resistances of ≈ 1 kohm$/10,000\ \mu\text{m}^2$.

1. Define large bond pad areas in PMMA, using a low temperature e-beam recipe.

2. After developing, load the sample into a vacuum chamber with a thermal evaporator (and optionally a DC argon source).

3. (Optional) Mill slightly using a DC argon ion source (aim for about 10 nm etch depth). This step is not strictly necessary, but will improve adhesion.

4. Deposit 10 nm of titanium, followed by 50 nm of gold.

5. Lift off in acetone.

B.1.3 Contacts

This procedure will produce contacts that are suitable for inducing superconductivity.

1. Clean the sample with oxygen plasma and spin PMMA.

2. Define contact areas in PMMA, using a low temperature e-beam recipe. These contacts should overlap the bond pads and/or contact the same continuous region of quantum well as the bond pads.

3. After developing, load the sample into a vacuum chamber with a DC argon source and material deposition capability.

4. Mill using a DC argon ion source, aiming to expose the quantum well but not etch through.

5. Deposit the desired materials:

(a) 10 nm titanium, followed by X nm aluminum[1], where $X >$ mesa height. These contacts will climb the mesa but will stop superconducting if the magnetic field applied parallel to the film exceeds 100 mT.

(b) 5 nm titanium, followed by 15 nm aluminum. These contacts probably won't climb the mesa, but will superconduct up to 1.5-2 T applied parallel to the film.

(c) 10 nm titanium, followed by X nm niobium. X can vary and since the niobium is sputtered, the contacts climb mesas. The contacts will superconduct up to applied fields of at least 4 T.

6. Lift off in acetone.

B.1.4 Topgates

Use this procedure to make topgates. It is necessary to deposit a dielectric layer between the gate metal and the substrate to prevent gate leakage.

1. Clean the sample with oxygen plasma.
2. Deposit Al_2O_3 using atomic layer deposition. The thickness of this layer was 50 nm for devices in this thesis, but other thicknesses could be used.
3. Define the gate areas in PMMA, using a low temperature e-beam recipe.
4. Load the sample into an evaporator and deposit 10 nm of titanium, followed by X nm of gold, where $X >$ mesa height to ensure continuity of the gate material. We have typically deposited films with $X = 250$ nm.
5. Lift off in acetone.

B.2 List of Procedures

B.2.1 Creating an HSQ etch mask

Use this procedure to pattern an etch mask composed of HSQ. HSQ is a negative e-beam resist, so areas exposed to the electron beam will be shielded during the etching process. This is a relatively quick method to make mesas. However, sometimes isolated small features ($< 10\ \mu$m) do not stick to the substrate strongly enough, and can be inadvertently removed during development. We have some

[1] All of the aluminum films in this work were deposited by thermal evaporation.

evidence that this problem becomes more pronounced as the resist ages, but more characterization is needed.

- Remove HSQ from refrigerator and place in room temperature fume hood for 30 minutes.
- Spin HSQ onto the substrate at 3000 rpm, for 45 seconds. Bake at 80 C for 4 minutes.
- Spin another layer of HSQ onto the substrate at 3000 rpm, for 45 seconds. Bake at 80 C for 4 minutes.
- Expose the pattern as soon as possible after baking. Dose: 1800 μC/cm^2.
- Develop in 25% TMAH for 17 seconds. Take care during this step, since TMAH is extremely poisonous. Rinse the sample in DI water after developing.
- You are now ready to etch mesas.

B.2.2 Creating a SiO_2/Ti etch mask

This is a liftoff procedure for patterning an etch mask composed of SiO_2/Ti. The titanium may not be strictly necessary, but it is etched extremely slowly by DC argon milling and is easy to deposit, so we use it.

- Define the mesa areas in PMMA, using a low temperature e-beam recipe.
- After development, load the sample into an ebeam evaporator and deposit $\approx$ 100 nm SiO_2.
- Deposit 20 nm of titanium.
- Lift off the etch mask in acetone.
- You are now ready to etch mesas.

B.2.3 Milling the HgTe heterostructure

Use this procedure to remove material from the HgTe heterostructure. For the recipes presented here, the sample should be mounted facing a DC argon source, with the surface of the wafer oriented perpendicular to the argon flux (although angle milling is certainly also possible). We used two different DC argon sources in this thesis, one mounted inside a thermal evaporator, and one inside a sputtering system. The following parameters characterize these two sources:

1. Veeco 3cm DC Ion Source

    - Beam voltage: 500 V
    - Beam current: 50 mA
    - Accelerator voltage: 1000 V
    - Etch rate of HgTe heterostructure: 80 nm/minute

2. Kaufman Ion Source

    - Beam voltage: 400 V
    - Beam current: 23 mA
    - Accelerator voltage: 80 V
    - Etch rate of HgTe heterostructure: 81 nm/minute

B.2.4 Oxygen plasma cleaning

This is a recipe for using an ECR-based reactive ion etcher to clean the surface of the HgTe heterostructure. We have found it essential to clean the surface prior to atomic layer deposition of Al_2O_3. Without this cleaning step there tends to be holes in the growth. The particular etcher that we use is a Nexx RIE.

1. Run the recipe `` `burnin.rcp' `` for 20 minutes, to clean the chamber. If the sample is being cleaned before ALD, this time can be used to preset the ALD machine to the deposition temperature.

2. Load the sample onto the sample chuck, using a drop of Santovac5 vacuum oil on the backside of the wafer to provide a better thermal link to the stage.

3. Run the recipe `` `shipblas.rcp' `` with the following parameters:

    - O_2 flow (sccm): 20
    - Process pressure (mtorr): 15
    - Microwave power (watts): 400
    - RF power (watts): 20
    - Backside helium (torr): 10

- Chuck temperature (C): 25.0
- Tolerance delay (s): 30
- Processing time (s): 300

4. Unload the sample and clean the vacuum oil off the back side using IPA.

B.2.5 Niobium deposition

Niobium was sputtered in a commercially available AJA ATC series UHV hybrid deposition system. The base pressure of the system was in the $10^{-9} - 10^{-8}$ torr range. All of the niobium films in this thesis were deposited using DC sputtering, with the following parameters:

- Ar flow (sccm): 50
- Process pressure (mtorr): 3
- Power (watts): 200

B.2.6 Atomic layer deposition of Al_2O_3

This a recipe for low-temperature atomic layer deposition of Al_2O_3. It was developed for a Cambridge Nanotech Savannah ALD system. It is advisable to wait until the deposition begins before walking away from the system, to make sure that pulses are firing normally. Also, the system is set up to record a screenshot when the recipe finishes.

1. Place a washer onto the center of the stage, and load the sample so that it sits in the center of the washer. This will prevent the sample from accidentally moving into the outlet of the chamber during the pump-down. (If you're feeling lucky, skip the washer.)

2. Pump out the chamber and run the recipe `` `AL2O3 50C 50nm' `` with the following parameters:

0	Flow		20
1	Heater	9	50
2	Heater	8	50
3	Stabilize	9	
4	Wait		60
5	Pulse	0	0.015
6	Wait		20
7	Pulse	3	0.015
8	Wait	10	10
9	Goto	5	500
10	Wait		10

3. Unload the sample.

B.2.7 Low temperature ebeam lithography

These are instructions for a 100 kV Elionix-7000 system. We have found that exposing HgTe heterostructures to standard ebeam doses at 100 kV does not degrade their electronic properties.

1. Spin-coat the sample with PMMA. Spin each layer of PMMA at 4000 RPM for 45 seconds. After spinning each layer of PMMA, bake the sample at 80 C for 10 minutes. For lift-off processes, determine how many layers of PMMA are needed based on the maximum thickness of material that will be deposited, as follows:

   - $\approx$ 30 nm: one layer of PMMA 950 A4.
   - $\approx$ 300 nm: one layer of PMMA 495 C6, followed by one layer of PMMA 950 A4.
   - For thicker films, add more layers of PMMA 495 C6.

   Note that these are just rough guidelines. Also note that PMMA will be etched slightly by argon milling, typically at a rate of $\approx$ 40 nm/minute for the parameters used in this work.

2. Expose the pattern. Dose: 2700 μC/cm^2.

3. Develop in MIBK/IPA (1:3) at 0 C for 1 minute.

C

Cryogenic Apparatus

The measurements described in this thesis were carried out using two dilution refrigerators from Oxford Instruments, an MX400 and an MX50. The MX400 was used primarily for measurements in Chapters 3-5. The MX50, which was retro-fitted with a $6-1-1$ vector magnet, was used for most of the measurements in Chapter 6. The wiring and performance of both of these systems have already been described, by Vivek Venkatachalam in the case of the MX400 [120] and by Mikey Shulman in the case of the MX50 [109].

Here we will not reiterate these descriptions, but rather will focus on two modifications made to the MX400 system. These changes are both aimed at allowing control over more than one component of the external magnetic field. The first change was to construct and install a small magnet which could be mounted on the end of a cold finger. This small magnet can supply up to ≈ 10 mT perpendicular to the sample plane, while a larger magnet surrounding the IVC supplies fields of order 1 T parallel to the sample. This setup allowed us to quickly start investigating the physics presented in Chapter 6.

A more long-term and flexible (but also more costly and initially time-consuming) solution is to use a vector magnet to individually control each component of the magnetic field. This was the second change that we made to the MX400, which is now retrofitted with a $12-3-1$ vector magnet. Below we will briefly describe the operation of this magnet.

C.1 Magnet mounted on a cold finger

A quick way to get small amounts of magnetic field ($\approx$ 10 mT) perpendicular to a sample, while applying large fields (1 T) in-plane, is to wind a small magnet and place it on the end of a cold finger. To do this properly requires a few considerations. First, the cryostat will have limited cooling power, so in order to run at base temperature it will be necessary to use superconducting wire. In order for this wire to remain superconducting, it will need to be well-thermalized below its critical temperature, and the external magnetic field must not exceed the critical field of the wire. Second, with two magnets oriented perpendicular to one another, there will be a torque on the small magnet that should be considered.

Figure C.1 depicts our solution to this problem. Copper wires are used from room temperature until the 4K stage of the cryostat, where solder joints are then used to connect the copper leads to superconducting wire. For the superconducting wire we used 102 μm-diameter T48B-M wire from Supercon, Inc. To avoid making additional solder joints (which could become resistive sources of heat) we used one continuous piece of wire from the 4K stage to the micro-magnet. At each stage of the cryostat, the wires were thermalized by winding around copper spools and securing with GE-varnish (Figure C.1A-B). At the base of the cold finger, the two superconducting leads feed into the micro-magnet, which is held in place by the sample stage and actually protrudes through it slightly (Figure C.1C). This intentional protrusion exists so that the sample, when mounted on a special sample holder with a hole (Figure C.1D) is able to lie flush with the end of the magnet.

The magnet itself consists of a 1 mm-diameter copper core, 1 cm in length, with 10 layers of winding for 1000 turns in total. The end of the magnet nearest the sample terminates in a copper cap that is 200 μm thick, in order to position the sample as close as possible to the end of the magnet. The wire is held in place on the magnet with Stycast. As specified by Supercon, the critical current of the wire at 4.2 Kelvin and in an external magnetic field of 3 T is 7 A. We were able to apply 1 A through the magnet under an external field of 1 T without any problems or heating of the mixing chamber. It is recommended to zero the current through such a coil before performing a helium transfer.

Using this coil, we were able to get $\approx$ 12 mT/A at a distance of $\approx$ 1 mm from the end of the coil, calibrated using the known flux periodicity of a HgTe-based Josephson junction device.

C.2 Vector magnet

Currently, the MX400 is fitted with a $12-3-1$ vector magnet from Oxford instruments. We briefly describe here the aspects of this magnet which are most relevant for operation.

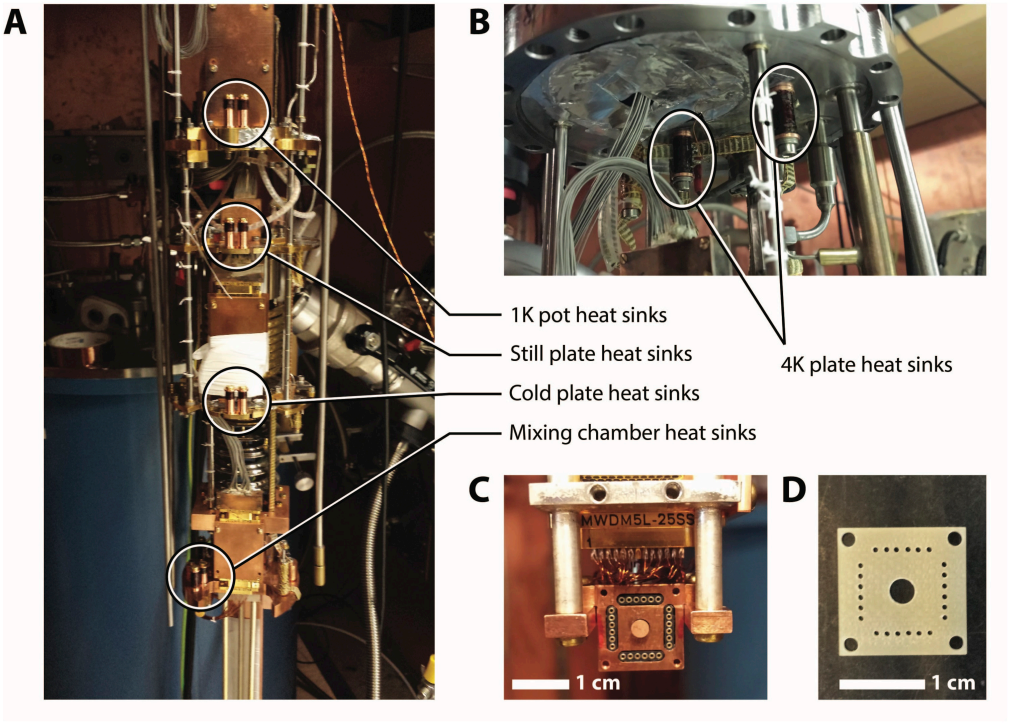

Figure C.1: Wiring and thermalization of the micromagnet. At each stage of the dilution refrigerator, the superconducting wire was wrapped around copper spools and secured with GE-varnish. **(A)** Four stages of thermalization occur from the 1K pot down to the mixing chamber. **(B)** At the 4K plate, there is an additional stage of thermalization. The wiring consists of one continuous superconducting wire from the 4K stage to the magnet. At the 4K stage, the superconducting wire is soldered to copper wires leading to a vacuum feedthrough at the top of the cryostat. **(C)** At the end of the cold finger, the sample stage provides 24 sample wires. The micro-magnet protrudes through the middle of the stage. **(D)** A specialized sample holder allows the back of the sample to lie flush with the end of the micro-magnet. This maximizes the perpendicular field at the top surface of the sample, for a given current through the micro-magnet.

C.2.1 Allowed fields

This section lists the three safe parameter ranges available to the magnet. These should also be listed in the Oxford manual.

1. The maximum field available in the y direction is 1 T. It is possible to orient the magnetic field anywhere within a sphere of radius 1 T, centered at the origin.

2. The maximum field available in the x direction is 3 T. It is possible to orient the magnet anywhere within a circle of radius 3 T in the xz plane.

3. The maximum field available in the z direction is 12 T. Up to 2.5 degree tilt correction is possible over the full 12 T range of the z coil, meaning that it is safe to apply up to 523 mT in the xy plane while the z coil is at 12 T.

C.2.2 Driver

Oxford instruments supplies a Labview-based program which can talk to the magnet power supply and control the field in each direction. When controlling the magnet through Matlab, this Oxford software acts as an unnecessary middleman and slows down communication. Fortunately, it is also possible to communicate directly with the power supply, for example via ethernet. A driver written for this purpose, `smcMercury3axisDirect.m`, can be found on the Yacoby server.

References

[1] Jason Alicea. Majorana fermions in a tunable semiconductor device. *Physical Review B*, 81: 125318, 2010.

[2] Jason Alicea. New directions in the pursuit of Majorana fermions in solid state systems. *Reports on Progress in Physics*, 75:076501, 2012.

[3] C. Altimiras, H. le Sueur, U. Gennser, A. Cavanna, D. Mailly, and F. Pierre. Non-equilibrium edge-channel spectroscopy in the integer quantum hall regime. *Nature Physics*, 6:34–39, 2009.

[4] C. Altimiras, H. le Sueur, U. Gennser, A. Cavanna, D. Mailly, and F. Pierre. Tuning energy relaxation along quantum hall channels. *Phys. Rev. Lett.*, 105(22):226804, Nov 2010. doi: 10.1103/PhysRevLett.105.226804.

[5] C. Altimiras, H. le Sueur, U. Gennser, A. Anthore, A. Cavanna, D. Mailly, and F. Pierre. Chargeless heat transport in the fractional quantum hall regime, Feb 2012.

[6] R. C. Ashoori, H. L. Stormer, L. N. Pfeiffer, K. W. Baldwin, and K. West. Edge magnetoplasmons in the time domain. *Phys. Rev. B*, 45(7):3894–3897, Feb 1992. doi: 10.1103/PhysRevB.45.3894.

[7] J. Bardeen, L. N. Cooper, and J. R. Schrieffer. Microscopic Theory of Superconductivity. *Phys. Rev.*, 108:1175, 1957.

[8] C. W. J. Beenakker. Theory of coulomb-blockade oscillations in the conductance of a quantum dot. *Phys. Rev. B*, 44:1646–1656, Jul 1991. doi: 10.1103/PhysRevB.44.1646. URL http://link.aps.org/doi/10.1103/PhysRevB.44.1646.

[9] C. W. J. Beenakker. Search for Majorana Fermions in Superconductors. *Annual Review of Condensed Matter Physics*, 4:113–136, 2013.

[10] C. W. J. Beenakker and H. van Houten. Josephson current through a superconducting quantum point contact shorter than the coherence length. *Physical Review Letters*, 66:3056, 1991.

[11] B. Andrei Bernevig and Shou-Cheng Zhang. Quantum Spin Hall Effect. *Physical Review Letters*, 96:106802, 2006.

[12] B. Andrei Bernevig, Taylor L. Hughes, and Shou-Cheng Zhang. Quantum Spin Hall Effect and Topological Phase Transition in HgTe Quantum Wells. *Science*, 314:1757–1761, 2006.

[13] Andrew J. Bestwick. *Quantum Edge Transport in Topological Insulators*. PhD thesis, Stanford University, 2015.

[14] A. Bid, N. Ofek, H. Inoue, M. Heiblum, C.L. Kane, V. Umansky, and D. Mahalu. Observation of neutral modes in the fractional quantum hall regime. *Nature*, 466:585–590, July 2010.

[15] Parsa Bonderson, Alexei Kitaev, and Kirill Shtengel. Detecting non-abelian statistics in the $\nu = 5/2$ fractional quantum hall state. *Phys. Rev. Lett.*, 96(1):016803, Jan 2006. doi: 10.1103/PhysRevLett.96.016803.

[16] B. Büttner et al. Single valley Dirac fermions in zero-gap HgTe quantum wells. *Nature Physics*, 7:418–422, 2011.

[17] A. I. Buzdin, L. N. Bulaevskii, and S. V. Panyukov. Critical-current oscillations as a function of the exchange field and thickness of the ferromagnetic metal (F) in an S-F-S josephson junction. *Pis'ma Zh. Eksp. Teor. Fiz.*, 35(4):147–148, 1982.

[18] Yu. A. Bychkov and E. I. Rashba. Properties of a 2D electron gas with lifted spectral degeneracy. *Pis'ma Zh. Eksp. Teor. Fiz.*, 39:66–69, 1984.

[19] Cui-Zu Chang et al. Experimental Observation of the Quantum Anomalous Hall Effect in a Magnetic Topological Insulator. *Science*, 12:167–170, 2013.

[20] D. B. Chklovskii, B. I. Shklovskii, and L. I. Glazman. Electrostatics of edge channels. *Phys. Rev. B*, 46(7):4026–4034, Aug 1992. doi: 10.1103/PhysRevB.46.4026.

[21] H. O. H. Churchill et al. Superconductor-nanowire devices from tunneling to the multichannel regime: zero-bias oscillations and magnetoconductance crossover. *Physical Review B*, 87: 241401(R), 2013.

[22] Anindya Das et al. Zero-bias peaks and splitting in Al-InAs nanowire topological superconductor as a signature of Majorana fermions. *Nature Physics*, 8:887–895, 2012.

[23] John H. Davies. *The Physics of Low-Dimensional Semiconductors*. Cambridge University Press, 1998.

[24] E. A. Demler, G. B. Arnold, and M. R. Beasley. Superconducting proximity effects in magnetic metals. *Physical Review B*, 55(22), 1997.

[25] E. V. Deviatov, A. Ganczarczyk, A. Lorke, G. Biasiol, and L. Sorba. Quantum hall mach-zehnder interferometer far beyond equilibrium. *Phys. Rev. B*, 84:235313, Dec 2011. doi: 10.1103/PhysRevB.84.235313. URL http://link.aps.org/doi/10.1103/PhysRevB.84.235313.

[26] E. V. Deviatov, A. Lorke, G. Biasiol, and L. Sorba. Energy transport by neutral collective excitations at the quantum hall edge. *Phys. Rev. Lett.*, 106:256802, Jun 2011. doi: 10.1103/PhysRevLett.106.256802. URL http://link.aps.org/doi/10.1103/PhysRevLett.106.256802.

[27] Fabrizio Dolcini, Manuel Houzet, and Julia S. Meyer. Topological Josephson ϕ_0 junctions. *Physical Review B*, 92:035428, 2015.

[28] M. Dolev, Y. Gross, R. Sabo, I. Gurman, M. Heiblum, V. Umansky, and D. Mahalu. Characterizing neutral modes of fractional states in the second landau level. *Phys. Rev. Lett.*, 107: 036805, Jul 2011. doi: 10.1103/PhysRevLett.107.036805. URL http://link.aps.org/doi/10.1103/PhysRevLett.107.036805.

[29] G. Dresselhaus. Spin-Orbit Coupling Effects in Zinc Blende Structures. *Phys. Rev.*, 100:580, 1955.

[30] R. C. Dynes and T. A. Fulton. Supercurrent Density Distribution in Josephson Junctions. *Physical Review B: Condensed Matter and Materials Physics*, 3, Number 9:3015–3023, 1971.

[31] A. D. K. Finck et al. Anomalous modulation of a zero-bias peak in a hybrid nanowire-superconductor device. *Physical Review Letters*, 110:126406, 2013.

[32] S. M. Frolov et al. Measurement of the current-phase relation of superconductor/ferromagnet/superconductor pi Josephson junctions. *Physical Review B*, 70, 2004. 144505.

[33] Liang Fu and C. L. Kane. Superconducting Proximity Effect and Majorana Fermions at the Surface of a Topological Insulator. *Physical Review Letters*, 100:096407, 2008.

[34] Liang Fu and C. L. Kane. Josephson Current and Noise at a Superconductor/Quantum-Spin-Hall-Insulator/Superconductor Junction. *Physical Review B*, 79:161408, 2009.

[35] P. Fulde and R. A. Ferrell. Superconductivity in a strong spin-exchange field. *Phys. Rev.*, 135: A550–A564, 1964.

[36] A. Furusaki. Resonant tunneling through a quantum dot weakly coupled to quantum wires or quantum hall edge states. *Phys. Rev. B*, 57:7141–7148, Mar 1998. doi: 10.1103/PhysRevB.57.7141. URL http://link.aps.org/doi/10.1103/PhysRevB.57.7141.

[37] S.M. Girvin and R.E. Prange. *The Quantum Hall Effect*. Springer, 1987.

[38] G. Granger, J. P. Eisenstein, and J. L. Reno. Observation of chiral heat transport in the quantum hall regime. *Phys. Rev. Lett.*, 102(8):086803, Feb 2009. doi: 10.1103/PhysRevLett.102.086803.

[39] Y. S. Gui et al. Giant spin-orbit splitting in a HgTe quantum well. *Physical Review B*, 70:115328, 2004.

[40] F. D. M. Haldane. Model for a Quantum Hall Effect without Landau Levels: Condensed-Matter Realization of the "Parity Anomaly". *Phys. Rev. Lett.*, 61:2015, 1988.

[41] B. I. Halperin. Quantized Hall conductance, current-carrying edge states, and the existence of extended states in a two-dimensional disordered potential. *Phys. Rev. B*, 25:2185–2190, 1982.

[42] B. I. Halperin, Patrick A. Lee, and Nicholas Read. Theory of the half-filled Landau level. *Physical Review B*, 47:7312, 1993.

[43] S. Hart et al. Induced Superconductivity in the Quantum Spin Hall Edge. *Nature Physics*, 10: 638–643, 2014.

[44] S. Hart et al. Controlled finite momentum pairing and spatially varying order parameter in HgTe quantum wells. 2015. URL http://arxiv.org/abs/1509.02940.

[45] M. Z. Hasan and C. L. Kane. Colloquium: Topological Insulators. *Reviews of Modern Physics*, 82:3045–3067, 2010.

[46] Eric A. Hoffmann, Henrik A. Nilsson, Jason E. Matthews, Natthapon Nakpathomkun, Ann I. Persson, Lars Samuelson, and Heiner Linke. Measuring temperature gradients over nanometer

length scales. *Nano Letters*, 9(2):779–783, 2009. doi: 10.1021/nl8034042. URL http://pubs.acs.org/doi/abs/10.1021/nl8034042. PMID: 19159269.

[47] M. Huber, M. Grayson, M. Rother, W. Biberacher, W. Wegscheider, and G. Abstreiter. Structure of a single sharp quantum hall edge probed by momentum-resolved tunneling. *Phys. Rev. Lett.*, 94(1):016805, Jan 2005. doi: 10.1103/PhysRevLett.94.016805.

[48] S. W. Hwang, D. C. Tsui, and M. Shayegan. Experimental evidence for finite-width edge channels in integer and fractional quantum hall effects. *Phys. Rev. B*, 48(11):8161–8165, Sep 1993. doi: 10.1103/PhysRevB.48.8161.

[49] J. K. Jain. *Composite Fermions*. Cambridge University Press, 2007.

[50] Liang Jiang et al. Unconventional Josephson Signatures of Majorana Bound States. *Physical Review Letters*, 107:236401, 2011.

[51] B. D. Josephson. Possible new effects in superconductive tunnelling. *Phys. Lett.*, 1:251, 1962.

[52] C. L. Kane and M. P. A. Fisher. *Perspectives in the Quantum Hall effect*. Wiley, 1997.

[53] C. L. Kane and Matthew P. A. Fisher. Quantized thermal transport in the fractional quantum hall effect. *Phys. Rev. B*, 55(23):15832–15837, Jun 1997. doi: 10.1103/PhysRevB.55.15832.

[54] C. L. Kane and E. J. Mele. Quantum Spin Hall Effect in Graphene. *Physical Review Letters*, 95:226801, 2005.

[55] C. L. Kane and E. J. Mele. Z2 Topological Order and the Quantum Spin Hall Effect. *Physical Review Letters*, 95:146802, 2005.

[56] C. L. Kane, Matthew P. A. Fisher, and J. Polchinski. Randomness at the edge: Theory of quantum hall transport at filling $\nu = 2/3$. *Phys. Rev. Lett.*, 72(26):4129–4132, Jun 1994. doi: 10.1103/PhysRevLett.72.4129.

[57] M. Kenzelmann et al. Coupled Superconducting and Magnetic Order in $CeCoIn_5$. *Science*, 321(5896):1652–1654, 2008.

[58] V. S. Khrapai, S. Ludwig, J. P. Kotthaus, H. P. Tranitz, and W. Wegscheider. Counterflow of electrons in two isolated quantum point contacts. *Phys. Rev. Lett.*, 99:096803, Aug 2007. doi: 10.1103/PhysRevLett.99.096803. URL http://link.aps.org/doi/10.1103/PhysRevLett.99.096803.

[59] A Yu Kitaev. Unpaired Majorana fermions in quantum wires. *Physics-Uspekhi*, 44:131–136, 2001.

[60] Alexei Kitaev. Periodic table for topological insulators and superconductors. *AIP Conf. Proc.*, 1134:22, 2009.

[61] Ivan Knez, Rui-Rui Du, and Gerard Sullivan. Andreev Reflection of Helical Edge Modes in InAs/GaSb Quantum Spin Hall Insulator. *Physical Review Letters*, 109:186603, 2012.

[62] Markus König, Steffen Wiedmann, Christoph Brüne, Andreas Roth, Hartmut Buhmann, Laurens W. Molenkamp, Xiao-Liang Qi, and Shou-Cheng Zhang. Quantum Spin Hall Insulator State in HgTe Quantum Wells. *Science*, 318(5851):766–770, 2007. doi: 10.1126/science.1148047. URL http://www.sciencemag.org/content/318/5851/766.abstract.

[63] Markus König, Hartmut Buhmann, Laurens W. Molenkamp, Taylor Hughes, Chao-Xing Liu, Xiao-Liang Qi, and Shou-Cheng Zhang. The Quantum Spin Hall Effect: Theory and Experiment. *Journal of the Physical Society of Japan*, 77(3):031007, 2008. doi: 10.1143/JPSJ.77.031007. URL http://jpsj.ipap.jp/link?JPSJ/77/031007/.

[64] Markus König et al. Spatially Resolved Study of Backscattering in the Quantum Spin Hall State. *Physical Review X*, 3:021003, 2013.

[65] T. Kontos et al. Josephson Junction through a Thin Ferromagnetic Layer: Negative Coupling. *Physical Review Letters*, 89(13), 2002.

[66] Angela Kou. *Microscopic Properties of the Fractional Quantum Hall Effect*. PhD thesis, Harvard University, 2013.

[67] L. P. Kouwenhoven, B. J. van Wees, N. C. van der Vaart, C. J. P. M. Harmans, C. E. Timmering, and C. T. Foxon. Selective population and detection of edge channels in the fractional quantum hall regime. *Phys. Rev. Lett.*, 64(6):685–688, Feb 1990. doi: 10.1103/PhysRevLett.64.685.

[68] A. I. Larkin and Y. N. Ovchinnikov. Inhomogeneous state of superconductors. *Sov. Phys. JETP*, 20:762–769, 1965.

[69] R. B. Laughlin. Anomalous quantum hall effect: An incompressible quantum fluid with fractionally charged excitations. *Phys. Rev. Lett.*, 50:1395–1398, May 1983. doi: 10.1103/PhysRevLett.50.1395. URL http://link.aps.org/doi/10.1103/PhysRevLett.50.1395.

[70] Eduardo J. H. Lee et al. Zero-bias anomaly in a nanowire quantum dot coupled to superconductors. *Physical Review Letters*, 109:186802, 2012.

[71] Sung-Sik Lee, Shinsei Ryu, Chetan Nayak, and Matthew P. A. Fisher. Particle-hole symmetry and the $\nu = \frac{5}{2}$ quantum hall state. *Phys. Rev. Lett.*, 99:236807, Dec 2007. doi: 10.1103/PhysRevLett.99.236807. URL http://link.aps.org/doi/10.1103/PhysRevLett.99.236807.

[72] Michael Levin, Bertrand I. Halperin, and Bernd Rosenow. Particle-hole symmetry and the pfaffian state. *Phys. Rev. Lett.*, 99:236806, Dec 2007. doi: 10.1103/PhysRevLett.99.236806. URL http://link.aps.org/doi/10.1103/PhysRevLett.99.236806.

[73] Chaoxing Liu et al. Quantum Spin Hall Effect in Inverted Type-II Semiconductors. *Physical Review Letters*, 100:236601, 2008.

[74] A. H. MacDonald. Edge states in the fractional-quantum-hall-effect regime. *Phys. Rev. Lett.*, 64(2):220–223, Jan 1990. doi: 10.1103/PhysRevLett.64.220.

[75] Joseph Maciejko, Taylor L. Hughes, and Shou-Cheng Zhang. The quantum spin hall effect. *Annual Review of Condensed Matter Physics*, 2(1):31–53, 2011. doi: 10.1146/annurev-conmatphys-062910-140538. URL http://www.annualreviews.org/doi/abs/10.1146/annurev-conmatphys-062910-140538.

[76] Joseph Maciejko et al. Kondo effect in the helical edge liquid of the quantum spin Hall state. *Phys. Rev. Lett.*, 102:256803, 2009.

[77] J. Martin, S. Ilani, B. Verdene, J. Smet, V. Umansky, D. Mahalu, D. Schuh, G. Abstreiter, and A. Yacoby. Localization of fractionally charged quasi-particles. *Science*, 305(5686):980, 2004.

[78] H. Mayaffre et al. Evidence of Andreev bound states as a hallmark of the FFLO phase in κ-(BEDT-TTF)$_2$Cu(NCS)$_2$. *Nature Physics*, 10:928–932, 2014.

[79] Douglas McClure. *Interferometer-Based Studies of Quantum Hall Phenomena*. PhD thesis, Harvard University, 2012.

[80] W. Meissner and R. Ochsenfeld. Ein neuer Effekt bei Eintritt der Supraleitfahigkeit. *Naturwissenschaften*, 21 (44):787–788, 1933.

[81] R. Meservey and P. M. Tedrow. Properties of Very Thin Aluminum Films. *Journal of Applied Physics*, 42:51, 1971.

[82] Shuo Mi et al. Proposal for the detection and braiding of Majorana fermions in a quantum spin Hall insulator. *Physical Review B*, 87:241405(R), 2013.

[83] Hongki Min et al. Intrinsic Rashba spin-orbit interactions in graphene sheets. *Phys. Rev. B*, 74:165310, 2006.

[84] Gregory Moore and Nicholas Read. Nonabelions in the fractional quantum Hall effect. *Nuclear Physics B*, 360:362–396, 1991.

[85] V. Mourik et al. Signatures of Majorana Fermions in Hybrid Superconductor-Semiconductor Nanowire Devices. *Science*, 336:1003–1007, 2012.

[86] Chetan Nayak et al. Non-abelian anyons and topological quantum computation. *Reviews of Modern Physics*, 80:1083–1159, 2008.

[87] A. H. Castro Neto, F. Guinea, N. M. R. Peres, K. S. Novoselov, and A. K. Geim. The Electronic Properties of Graphene. *Reviews of Modern Physics*, 81:109–162, 2009.

[88] Predrag Nikolic, Tanja Duric, and Zlatko Tesanovic. Fractional Topological Insulators of Cooper Pairs Induced by the Proximity Effect. *Physical Review Letters*, 110:176804, 2013.

[89] E. G. Novik et al. Band structure of semimagnetic $Hg_{1-y}Mn_yTe$ quantum wells. *Phys. Rev. B*, 72:035321, 2005.

[90] Katja C. Nowack et al. Imaging currents in HgTe quantum wells in the quantum spin Hall regime. *Nature Materials*, Advance Online Publication, 2013.

[91] Jeroen B. Oostinga et al. Josephson Supercurrent through the Topological Surface States of Strained Bulk HgTe. *Phys. Rev. X*, 3:021007, 2013.

[92] Loren Pfeiffer and K. W. West. The role of MBE in recent quantum Hall effect physics discoveries. *Physica E*, 20:57–64, 2003.

[93] A. Pfeuffer-Jeschke. *Bandstruktur und Landau-Niveaus quecksilberhaltiger II-VI Heterostrukturen*. PhD thesis, University of Würzburg, 2000.

[94] Xiao-Liang Qi and Shou-Cheng Zhang. Topological insulators and superconductors. *Reviews of Modern Physics*, 83:1057–1110, 2011.

[95] N. Read and Dmitry Green. Paired states of fermions in two dimensions with breaking of parity and time-reversal symmetries and the fractional quantum Hall effect. *Physical Review B*, 61:10267–10297, 2000.

[96] Christopher R. Reeg and Dmitrii L. Maslov. Proximity-induced triplet superconductivity in Rashba materials. 2015. URL http://arxiv.org/abs/1508.03623.

[97] Leonid P. Rokhinson, Xinyu Liu, and Jacek K. Furdyna. The fractional a.c. Josephson effect in a semiconductor-superconductor nanowire as a signature of Majorana particles. *Nature Physics*, 8:795–799, 2012.

[98] Andreas Roth et al. Nonlocal Transport in the Quantum Spin Hall State. *Science*, 325:294–297, 2009.

[99] D G Rothe et al. Fingerprint of different spin-orbit terms for spin transport in HgTe quantum wells. *New Journal of Physics*, 12:065012 (22pp), 2010.

[100] V. V. Ryazanov et al. Coupling of Two Superconductors through a Ferromagnet: Evidence for a π Junction. *Physical Review Letters*, 86:2427–2430, 2001.

[101] Shinsei Ryu et al. Topological insulators and superconductors: tenfold way and dimensional hierarchy. *New Journal of Physics*, 12, 2010.

[102] Jay D. Sau, Roman M. Lutchyn, Sumanta Tewari, and S. Das Sarma. Generic new platform for topological quantum computation using semiconductor heterostructures. *Physical Review Letters*, 104:040502, 2010.

[103] Jay D. Sau et al. Non-Abelian quantum order in spin-orbit-coupled semiconductors: Search for topological Majorana particles in solid-state systems. *Physical Review B*, 82:214509, 2010.

[104] Thomas L. Schmidt, Stephan Rachel, Felix von Oppen, and Leonid I. Glazman. Inelastic Electron Backscattering in a Generic Helical Edge Channel. *Physical Review Letters*, 108:156402, 2012.

[105] Andreas P. Schnyder et al. Classification of topological insulators and superconductors in three spatial dimensions. *Physical Review B*, 78:195125, 2008.

[106] Andreas P. Schnyder et al. Classification of Topological Insulators and Superconductors. *AIP Conf. Proc.*, 1134:10, 2009.

[107] Hermann Sellier et al. Temperature-induced crossover between 0 and pi states in S/F/S junctions. *Physical Review B*, 68, 2003. 054531.

[108] M. D. Shulman et al. Demonstration of Entanglement of Electrostatically Coupled Singlet-Triplet Qubits. *Science*, 336:202–205, 2012.

[109] Michael Shulman. *Entanglement and Metrology with Singlet-Triplet Qubits*. PhD thesis, Harvard University, 2015.

[110] Ady Stern and Bertrand I. Halperin. Proposed experiments to probe the non-abelian $\nu = 5/2$ quantum hall state. *Phys. Rev. Lett.*, 96(1):016802, Jan 2006. doi: 10.1103/PhysRevLett.96.016802.

[111] S. Takei, M. Milletarì, and B. Rosenow. Nonequilibrium electron spectroscopy of luttinger liquids. *Phys. Rev. B*, 82:041306, Jul 2010. doi: 10.1103/PhysRevB.82.041306. URL http://link.aps.org/doi/10.1103/PhysRevB.82.041306.

[112] D. J. Thouless, M. Kohmoto, M. P. Nightingale, and M. den Nijs. Quantized hall conductance in a two-dimensional periodic potential. *Phys. Rev. Lett.*, 49:405, 1982.

[113] Michael Tinkham. *Introduction to Superconductivity*. Dover Publications, Inc., 2004.

[114] D. C. Tsui, H. L. Stormer, and A. C. Gossard. Two-dimensional magnetotransport in the extreme quantum limit. *Phys. Rev. Lett.*, 48:1559–1562, May 1982. doi: 10.1103/PhysRevLett.48.1559. URL http://link.aps.org/doi/10.1103/PhysRevLett.48.1559.

[115] K. v. Klitzing, G. Dorda, and M. Pepper. New Method for High-Accuracy Determination of the Fine-Structure Constant Based on Quantized Hall Resistance. *Physical Review Letters*, 45:494–497, 1980.

[116] B. J. van Wees, E. M. M. Willems, C. J. P. M. Harmans, C. W. J. Beenakker, H. van Houten, J. G. Williamson, C. T. Foxon, and J. J. Harris. Anomalous integer quantum hall effect in the ballistic regime with quantum point contacts. *Phys. Rev. Lett.*, 62(10):1181–1184, Mar 1989. doi: 10.1103/PhysRevLett.62.1181.

[117] B. J. van Wees et al. Quantized Conductance of Point Contacts in a Two-Dimensional Electron Gas. *Physical Review Letters*, 60:848–850, 1988.

[118] Jukka I. Väyrynen, Moshe Goldstein, and Leonid I. Glazman. Helical edge resistance introduced by charge puddles. *Phys. Rev. Lett.*, 110:216402, 2013.

[119] Jukka I. Väyrynen, Moshe Goldstein, Yuval Gefen, and Leonid I. Glazman. Resistance of helical edges formed in a semiconductor heterostructure. *Phys. Rev. B*, 90:115309, 2014.

[120] Vivek Venkatachalam. *Single Electron Probes of Fractional Quantum Hall States*. PhD thesis, Harvard University, 2012.

[121] Vivek Venkatachalam et al. Local thermometry of neutral modes on the quantum Hall edge. *Nature Physics*, 8:676–681, 2012.

[122] Klaus von Klitzing. Developments in the quantum Hall effect. *Philosophical Transactions of the Royal Society A*, 363:2203–2219, 2005.

[123] L Weithofer and P Recher. Chiral Majorana edge states in HgTe quantum wells. *New Journal of Physics*, 15:085008, 2013.

[124] R. T. Weitz et al. Broken-Symmetry States in Doubly Gated Suspended Bilayer Graphene. *Science*, 330:812–816, 2010.

[125] X. G. Wen. Electrodynamical properties of gapless edge excitations in the fractional quantum hall states. *Phys. Rev. Lett.*, 64(18):2206–2209, Apr 1990. doi: 10.1103/PhysRevLett.64.2206.

[126] R. Willett, J. P. Eisenstein, H. L. Störmer, D. C. Tsui, A. C. Gossard, and J. H. English. Observation of an even-denominator quantum number in the fractional quantum hall effect. *Phys. Rev. Lett.*, 59(15):1776–1779, Oct 1987. doi: 10.1103/PhysRevLett.59.1776. AB.

[127] Roland Winkler. *Spin-Orbit Coupling Effects in Two-Dimensional Electron and Hole Systems*. Springer Tracts in Modern Physics, 2003.

[128] A. Yacoby, H.F. Hess, T.A. Fulton, L. Pfeiffer, and K. West. Electrical imaging of the quantum hall state. *Solid State Communications*, 111:1–13, 1999.

[129] Yugui Yao et al. Spin-orbit gap of graphene: First-principles calculations. *Phys. Rev. B*, 75: 041401(R), 2007.

[130] Tomohiro Yokoyama, Mikio Eto, and Yuli V. Nazarov. Anomalous Josephson effect induced by spin-orbit interaction and Zeeman effect in semiconductor nanowires. *Physical Review B*, 89:195407, 2014.

[131] Haijun Zhang and Shou-Cheng Zhang. Topological insulators from the perspective of first-principles calculations. *Physica Status Solidi RRL*, 7:72–81, 2013.

[132] N. B. Zhitenev, R. J. Haug, K. v. Klitzing, and K. Eberl. Time-resolved measurements of transport in edge channels. *Phys. Rev. Lett.*, 71(14):2292–2295, Oct 1993. doi: 10.1103/PhysRevLett.71.2292.

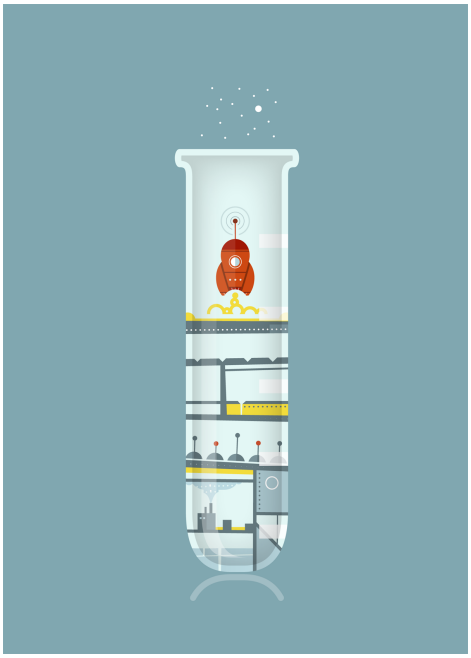

This thesis was typeset using LaTeX, originally developed by Leslie Lamport and based on Donald Knuth's TeX. The body text is set in 11 point Egenolff-Berner Garamond, a revival of Claude Garamont's humanist typeface. The above illustration, *Science Experiment 02*, was created by Ben Schlitter and released under CC BY-NC-ND 3.0. A template that can be used to format a PhD dissertation with this look & feel has been released under the permissive AGPL license, and can be found online at github.com/suchow/Dissertate or from its lead author, Jordan Suchow, at suchow@post.harvard.edu.